THÈSE

En vue de l'obtention du

DOCTORAT DE L'UNIVERSITÉ DE TOULOUSE

Délivré par : *l'Université Toulouse 3 Paul Sabatier (UT3 Paul Sabatier)*

Présentée et soutenue le *14 mars 2019* **par :**

Erick MORA RAMIREZ

Radiopharmaceutical dosimetry in targeted radionuclide therapy

---

JURY

Glenn FLUX	Directeur de Recherche	Rapporteur
Jean-Philippe VUILLEZ	PU-PH, Université Grenoble I	Rapporteur
Frédéric COURBON	PU-PH, Université Toulouse III	Examinateur
Ludovic FERRER	Physicien Médical	Examinateur
Emmanuelle CASSOL	MCU-PH, Université Toulouse III	Examinatrice
Manuel BARDIÈS	DR INSERM, CRCT Toulouse	Directeur

École doctorale et spécialité :
GEET : Radio-physique et Imagerie Médicales
Unité de Recherche :
Centre de Recherches en Cancérologie de Toulouse (INSERM UMR 1037, Équipe 15)
Directeur de Thèse :
Manuel BARDIÈS
Rapporteurs :
Glenn FLUX et *Jean-Philippe VUILLEZ*

REMERCIEMENTS

Tout d'abord, je voudrais remercier le Tout-Puissant de m'avoir permis d'atteindre ce moment de ma vie, dont j'ai rêvé pendant de nombreuses années et qui est finalement devenu une réalité grâce à lui. A la Vierge des Anges pour avoir pris soin de moi sur cette route.

A ma belle épouse, Viviana Meoño Alvarado, MERCI de m'avoir aidé dans tant de choses, d'être mon amie, ma confidente, d'avoir accepté de partager cette aventure à Toulouse. Merci macha, je t'aime beaucoup, je t'en suis éternellement reconnaissant.

Pour mon fils, Alejandro Mora Cruz, vous avez été l'une des plus grandes sources d'inspiration dans ma vie pour toujours aller de l'avant. Je t'aime nano.

À ma mère, mes frères, ma sœur, ma tante Gis et le reste de ma famille, merci d'être toujours à mes côtés. Je les aime beaucoup.

À la famille Meono-Alvarado, Don Mario, Dona Lidieth, Monica, Marito. Merci pour tout, je vous en suis éternellement reconnaissant.

Je tiens à remercier Ph.D. Ralph García Vindas et le M.Sc. Patricia Mora Rodríguez pour avoir pensé à moi pour réaliser ces études afin de collaborer avec le projet Ciclotrón - Radiofarmacia - PET/CT de l'Université du Costa Rica. Merci de votre confiance et de votre soutien.

Aux Assemblées de l'École de physique et de l'École des technologies de la santé, au Système d'études postuniversitaires (SEP) et au Bureau des Affaires Internationales de l'Université du Costa Rica, pour m'avoir soutenu avec cette bourse, pour tous les efforts qui ont été faits afin que je puisse être ici.

Au Dr. Isabel Berrocal Gamboa, M.Sc. José Carvajal Mejías et Lic. Mario Meoño Alvarado, qui m'ont servi de garants devant l'Université du Costa Rica, je vous remercie pour votre confiance et votre soutien. Je vous en suis éternellement reconnaissant.

A l'Institut Français d'Amérique Centrale (IFAC) à tout le personnel qui y travaille, je vous remercie pour la bourse que vous m'avez accordée. Un merci particulier à Yadira Vargas pour son soutien inconditionnel durant ces études.

Je tiens à remercier mon Directeur de Thèse Manuel Bardiès du fond du cœur, de m'avoir accepté dans son équipe, de m'avoir donné l'opportunité de développer mes études doctorales. Merci pour tout Manu, j'ai appris le français avec un bon accent, j'ai appris beaucoup de culture française et j’ai pu apprécier la beauté de ce pays. J'espère que j'ai rétribué avec beaucoup de travail toute la confiance que vous m'avez donnée. Pour moi, vous êtes un grand professeur et un exemple académique à suivre, je vous en serai éternellement reconnaissant.

À tous les membres permanents de l'équipe, à Marie-Claude Bordage pour avoir toujours accepté une bonne tasse de café et m'avoir apporté le soutien nécessaire concernant l'administration universitaire française. À Emmanuelle Cassol pour toutes ces heures où nous avons pu discuter de divers sujets de médecine nucléaire, pas seulement ceux liés à la thèse, j'ai beaucoup appris de ces conversations. À Luc Simon, à Laure Vieillevigne, merci d'être là, l'équipe ne serait pas la même sans vous. À tous les autres membres de l'équipe, merci.

À tout le personnel administratif de la CRCT, en particulier Sébastien Gibert, Laurence Granier et Marie-Hélène Lalaux, merci pour toute l'aide que vous m'avez apportée durant mon séjour.

À Anne-Sophie Salabert, merci beaucoup pour toute la confiance que vous m'avez accordée afin de pouvoir développer les calculs dosimétriques du médicament qui a été développé dans le CHU-PURPAN. Je vous suis éternellement reconnaissant.

Au Service de Médecine Nucléaire de l'Institut de Cancérologie de Montpellier (ICM), en particulier à Lore Santoro et Emmanuel Deshayes, pour toute la gentillesse qu'ils ont eue avec moi pendant mon séjour au service. Merci de m'avoir donné l'occasion de travailler avec vous pour moi a été un honneur, un plaisir et un grand apprentissage, je vous serai éternellement reconnaissant. Aussi je voudrais dire merci à Soufiane Chouaf et Dorian Trauchessec pour votre aide pendant ce travail.

Aux docteurs Eduardo Savio, Florencia Zoppolo, Ingrid Kreimerman et toute l'équipe du CUDIM pour m'avoir donné l'occasion d'effectuer des calculs dosimétriques des deux médicaments développés dans leur centre, ce fut pour moi un honneur et un plaisir de collaborer avec vous. Je vous suis éternellement reconnaissant.

À Sara Beilla MERCI pour tout le soutien que tu m'as donné ici, tu étais comme un ange pour moi, tu m'as beaucoup aidé quand j'en avais le plus besoin, je serai toujours redevable envers toi. Merci pour tous vos conseils. Gros câlin.

À Sara Marcatili, merci pour tout le temps que je consacre à répondre à mes questions, et pour les conseils donnés.

À Antonis Tsologiannis, merci de partager vos idées avec moi. Gros câlin.

À Gustavo Costa merci de m'avoir donné le conseil de m'installer ici à Toulouse et de m'aider dans certains moments difficiles. Merci de m'avoir appris à voir le café différemment. Merci pour toute l'aide que tu m'as donnée avec GATE. Gros câlin.

À Richard Brown, merci d'être le végétarien que tu es, de m'avoir écouté et de m'avoir donné des conseils, merci de m'avoir accueilli chez toi, je me sentais comme le mien, merci pour tout mon ami. Gros câlin.

À Frédéric Chatrie, merci de m'avoir appris à skier, pour tes conseils, ton aide. Gros câlin.

À Jonathan Tranel, merci d'avoir toujours pensé à moi pour une randonnée, j'ai vraiment apprécié beaucoup de paysages que nous avons pu traverser. Merci pour ton aide.

À Julien Bordes, merci de m'avoir fait me sentir chez moi, mon frère français, de m'avoir écouté, de m'avoir conseillé et de m'avoir montré un peu la culture française. Gros câlin.

À Tony Younes, mon frère libanais, merci pour tout, surtout pour les conversations au CRCT, pour les rires et les bonnes blagues, pour m'avoir fait me sentir chez moi, pour m'avoir écouté, pour m'avoir donné vos conseils et pour m'avoir montré un peu de la culture libanaise. Un gros câlin.

À Maxime Chauvin, merci pour tout ce que j'ai appris de vous, pour avoir partagé tant de bons moments et de bonnes conversations. Merci pour vos enseignements Python et GATE. Gros câlin.

À Ana Rita Pereira, merci de m'avoir écoutée, de m'avoir conseillée et de m'avoir aidée.

À Juan Camilo Ocampo Ramos, Parce, mon frère colombien, merci pour les rires et les bonnes blagues, pour toutes les conversations que nous avons eues, pas seulement académiques, toutes ont été très utiles, je vous suis éternellement reconnaissant, j'ai beaucoup appris de vous. Gros câlin.

À Joey Labour, j'espère pouvoir bientôt célébrer la fin de vos études. Un gros câlin.

À Gunjan Kayal, ma sœur indienne, merci de partager votre culture, votre nourriture, de m'écouter et tous vos conseils, j'espère pouvoir bientôt célébrer la fin de vos études. Un gros câlin.

À Jerémy Lester et Alex Vergara, merci pour tous ces moments partagés.

À toutes ces personnes formidables que j'ai rencontrées au quatrième étage de la CRCT (Salvatore, Sabina, Maha, Carlos, Clara, Laura, Vincent, Mme. Weulersse, Léa), merci pour tous ces moments partagés.

À toutes mes chers compatriotes à Toulouse Maria, Salome, Estefanny, Esteban Vargas, Esteban Gonzalez, Esteban Muñoz, Sebastien, Alfonso, Kerry, Aaron, Juan Jose, Miguel, Jean-Carlo Augusto et a aussi à mes chers amies françaises Muriel, Olivier, Clara et Benoit……..PURA VIDA!!!!!!.

Contents

Chapter 1: Theoretical framework

Chapter 2: Dosimetry for new radiopharmaceuticals

Chapter 3: SPECT/CT calibration and workstation's evaluation

Chapter 4: Patient data evaluation on commercial workstations

Appendix

Scientific Production

List of figures

List of figures chapter 1

List of figures chapter 2

List of figures chapter 3

List of figures chapter 4

List of figures Appendix: Chapter 3 and Chapter 4

List of Tables

List of tables chapter 1

List of tables chapter 2

List of tables chapter 3

List of tables chapter 4

List of tables appendix: Chapter 2 and Chapter 4

List of abbreviations and acronyms

1stTx	First treatment cycle
2D	Two dimensions
2ndTx	Second treatment cycle
3D	Three dimensions
^{18}F	Radionuclide flour-18
^{11}C	Radionuclide carbon-11
ADC	Absorbed Dose Coefficients
AF	Absorbed Fraction
CEDF	Contribution to the Effective Dose Factor
CSG	Constructive solid geometry
CT	Computed tomography
DOTATOC	[DOTA^0, Tyr^3]-octreotide
DOTATATE	[DOTA^0, Tyr^3]-octreotate
EANM	European Association of Nuclear Medicine
EBRT	External beam radiotherapy
FAX	Female adult voxel
FNM	Radiopharmaceutical Fluoroethylnormemantine
FWHM	Full with half maximum
GEP-NET	Gastroenteropancreatic neuroendocrine tumours
GM	Geometric mean
HU	Hounsfield unit
IAEA	International Atomic Energy Agency
ICRP	International Commission on Radiological Protection
MAX	Male adult voxel
MEGP	Medium energy general-purpose collimator
MIRD	Medical Internal Radiation Dose Committee
MRI	Magnetic resonance images
MRM	Magnetic resonance microscopy
MRT	Molecular radiotherapy
NA	Noradrenaline transporter
NaI(Tl)	Sodium iodine crystal active with thallium
NET’s	Neuroendocrine tumours
NHL	Non-Hodgkin lymphoma
NURBS	Non-uniform rational B-splines
ORTEC	Multichannel analyser equipment
PET	Positron emission tomography
PET/CT	Positron emission tomography/Computed tomography
PRRT	Peptide receptor radionuclide therapy
PRD	Percentage of relative difference
RB	Remainder of the body
RM	Red bone marrow
ROIs	Regions of interest

RWEDC	Risk-Weighted Effective Dose Coefficient
SAF	Specific Absorbed Fraction
SAM	*S*-adenosyl Methionine
SNMMI	Society of Nuclear Medicine & Molecular Imaging
SRF101	Sulforhodamine 101
SPECT	Single photon emission tomography
SPECT/CT	Single photon emission tomography/Computed tomography
SS	Somatostatin
TACs	Time activity curves
TIA	Time-integrated activity
TIAC	Time-integrated activity coefficient
TRT	Targeted radionuclide therapy
USNRC	United States Nuclear Regulatory Commission
VHP	Visible human project
VOIs	Volumes of interest

Dosimétrie des radiopharmaceutiques en radiothérapie interne vectorisée

Resumé

La médecine nucléaire est une spécialité médicale dont l’une des applications est l’étude de la physiologie des organes et du métabolisme de divers types de tumeurs. Les produits pharmaceutiques liés à un isotope radioactif (médicament radio-pharmaceutique, MRP) sont étudiés en préclinique avant d’être utilisés chez l’homme. Les rongeurs sont généralement utilisés pour étudier la bio-cinétique du traceur dans un groupe d'organes prédéfinis. L'extrapolation des résultats de ces études de l’animal à l'homme permet d'avoir une estimation du comportement des MRP et de l’irradiation délivrée en clinique. Trois nouveaux MRP ont été mis au point, l'un en France (CHU-Hôpital Purpan) et deux en Uruguay (CUDIM). Deux visent à étudier le cerveau et un vise à diagnostiquer le cancer de la prostate. Dans ce travail, l'extrapolation des résultats précliniques est présentée, les doses absorbées et efficaces sont estimées en utilisant les logiciels OLINDA/EXM V1.0, V2.0 et IDAC2.1. Les différences entre les résultats de chaque programme sont discutées.

Au niveau clinique, les protocoles dosimétriques incluent la détermination du facteur d'étalonnage, la segmentation, le recalage, l'ajustement des courbes et le calcul de la dose absorbée. Dans ce travail, l’étalonnage développé pour un SPECT/CT est présenté en utilisant différentes sources d’étalonnage et différentes géométries. L’influence de la méthode de reconstruction sur la détermination du facteur d’étalonnage et les courbes du facteur de récupération sont présentées.

Par ailleurs, quatre logiciels commerciaux sont comparés sur la base des informations cliniques de deux patients atteints de tumeurs gastro-entéro-pancréatiques d’origine neuroendocrine et traitées au ^{177}Lu-DOTATATE. Deux cycles de traitement pour chaque patient ont été utilisés afin d’estimer les temps de résidence des reins, du foie, de la rate, de la moelle osseuse et du corps entier. Le calcul des doses absorbées a été initialement réalisé à l'aide de OLINDA/EXM V1.0 & V2.0, en ajustant la masse de chaque organe/tissu. Dans le cas de la moelle osseuse, une nouvelle méthodologie est présentée pour estimer la dose absorbée sans qu'il soit nécessaire de procéder à des mesures de corps entier. Il est possible de constater que le recalage des images a un impact sur la détermination de la dose absorbée. Les résultats sont donc calculés en employant d'un outil permettant de recaler indépendamment chaque organe et non pas toute l'image du champ de vue.

Différents algorithmes de calcul ont été utilisés pour déterminer la dose absorbée délivrée aux patients, par exemple le modèle de sphère d’OLINDA/EXM V2.0, les méthodes de convolution et le dépôt d’énergie local de PLANET®Onco Dose de Dosisoft. Les résultats trouvés avec les différents outils sont comparés et discutés.

Mots clés : Dosimétrie, Radiothérapie Interne Vectorisée, Médicine Nucléaire

Radiopharmaceutical dosimetry in targeted radionuclide therapy

Abstract

Nuclear medicine is a medical specialty in which one of whose applications is the study of the physiology of organs and the metabolism of various types of tumours. Pharmaceuticals labelled with radionuclides (radiopharmaceuticals) are studied at pre-clinical level before being used in humans. Rodents are generally used to study the biokinetics of tracer in a group of predefined organs. The extrapolation of the results of these studies from animals to humans provides an estimate of the behaviour of the radiopharmaceuticals and the irradiation delivered clinically. Three new radiopharmaceuticals were developed, one in France (CHU-Hôpital Purpan) and two in Uruguay (CUDIM). Two aim to study the brain and one aims to diagnose prostate cancer. In this work, extrapolation of pharmacokinetics preclinical results to the human is presented; absorbed and effective doses are estimated using OLINDA/EXM V1.0, V2.0 and IDAC2.1 software. The differences between the results of each program are discussed.

At a clinical level, dosimetric protocols include calibration factor determination, segmentation, registration, curve fitting, and calculation of absorbed dose. In this work, the calibration developed for a SPECT/CT is presented using different calibration sources and different geometries. The influence of the reconstruction method in the determination of the calibration factor and the recovery coefficient curves are shown.

In addition, four commercial software are compared based-on clinical information of two patients with gastro-entero-pancreatic tumours of neuroendocrine origin treated with ^{177}Lu-DOTATATE. Two cycles of treatment for each patient were used to estimate residence times for the kidneys, liver, spleen, bone marrow and whole body. Calculation of absorbed dose was initially developed using OLINDA/EXM V1.0 & V2.0, adjusting the mass of each organ/tissue. In the case of the bone marrow, a novel methodology is presented to estimate the absorbed dose without the need for whole-body measurements. It can be seen that the registration of the images has an impact on the determination of the absorbed dose. The results are thus calculated by employing a tool allowing to register independently each organ and not all the image of the field of view.

Different calculation algorithms were used to determine the absorbed dose delivered to patients, for example the OLINDA/EXM V2.0 sphere model, convolution and local energy deposition methods of PLANET®Onco Dose from Dosisoft. The results found with the different tools are compared and discussed.

Keywords: Dosimetry, Targeted Radionuclide Therapy, Nuclear Medicine

Introduction générale (FR)

La médecine nucléaire est une spécialité médicale dont les applications, essentiellement diagnostiques, permettent l'étude de la physiologie des organes et le métabolisme de divers types de tumeurs. La radiothérapie interne vectorisée (RIV) est une approche thérapeutique de la Médecine Nucléaire. Le but de la RIV est de transporter le radionucléide vers la tumeur. Il faudra donc considérer différents types de molécules vectrices, leur affinité pour les tumeurs, différents isotopes radioactifs et la manière de lier l'isotope à la molécule vectrice. La RIT possède plusieurs catégories, en fonction du type de molécules vectrices utilisées (radioimmunothérapie, radiopeptidethérapie), ou selon l'isotope sélectionné (i.e. irathérapie).

L'efficacité du traitement dépendra de nombreux facteurs, dont du type de rayonnement. Les radionucléides choisis sont généralement ceux qui ont la propriété d'émettre des particules alpha ou bêta, voire Auger, qui ont un parcours réduit dans la matière et qui permettent de délivrer une irradiation localisée autour du point d'émission. Selon la pénétration de ces particules dans la matière, un effet de feu croisé est attendu, dépendant de la portée des radiations et de la taille de la tumeur, ce qui permet théoriquement d'augmenter l'efficacité de la thérapie. Pour les émetteurs de particules alpha, on peut de plus bénéficier d'un transfert linéique d'énergie (TEL) élevé de ce type de particules, qui entraine une augmentation de l'efficacité de l'irradiation pour une même énergie délivrée. Enfin, si les isotopes possèdent une émission gamma, il sera possible de générer des images permettant de suivre le devenir du vecteur radioactif dans le patient.

La place de la dosimétrie en RIV est en constant débat (Chiesa et al., 2017; Flux et al., 2017; Giammarile et al., 2017), entre la nécessité de « *documenter »* l'irradiation délivrée et la possibilité « *d'optimiser* » le traitement. Son développement au niveau dosimétrie clinique est contrasté mais indéniable. L'article 56 (Optimisation) de la directive 2013/59/Euratom du Conseil (Conseil de l'Union européenne 2014), stipule explicitement que *"Pour toutes les expositions médicales de patients à des fins radiothérapeutiques, les expositions de volumes cibles sont planifiées individuellement et leur délivrance est dûment vérifiée en tenant compte que les doses aux volumes et tissus non cibles doivent être aussi faibles que raisonnablement possible et compatibles avec l'objectif radiothérapeutique de l'exposition"*.

La méthodologie est disponible – mais implémenté de façon inégale en clinique, selon les pays et les centres cliniques. De fait, un bon indicateur du développement spectaculaire et récent de la dosimétrie clinique est la mise sur le marché de solutions commerciales. Il est désormais possible d'effectuer des dosimétries personnalisées, tenant compte de la pharmacocinétique du médicament radiopharmeceutique (MRP) et propre à chaque patient et de sa morphologie.

Pour ce qui concerne la dosimétrie dans un contexte diagnostique, elle est essentiellement réalisée lors de la mise au point de nouveaux traceurs, afin de déterminer des ordres de grandeur de la faible l'irradiation délivrée. On parle alors de dosimétrie de référence.

Ce travail de thèse est axé sur la dosimétrie clinique et préclinique des radiopharmaceutiques :

- Nous avons dans un premier temps établi les doses absorbées de référence pour trois nouveaux médicaments radiopharmaceutiques à visée diagnostique, en extrapolant les données précliniques à l'être humain, à l'aide de trois logiciels permettant de comparer les résultats.
- Par la suite, nous avons étudié quatre solutions dosimétriques commerciales, à l'aide d'expériences réalisées sur fantômes et de traitement de données cliniques. Pour les 4 solutions commerciales étudiées, les similitudes et les différences sont présentées. La comparaison s'est avérée difficile, car les différentes solutions commerciales proposent des implémentations différentes de la dosimétrie clinique, ce qui limite parfois l'évaluation ou la comparaison des performances.

Dans le premier chapitre de ce travail, différentes approches de radiothérapie interne vectorisée sont mentionnées. Selon le type de molécule vectrice, on peut les diviser en différents groupes :

- Le cas où l'isotope est également le vecteur (^{131}I, ^{223}Ra),
- Le cas où le vecteur participe au métabolisme tumoral (mIBG),
- Les thérapies utilisant des peptides (radiopeptidothérapie, en anglais peptide receptor radionuclide therapy ou PRRT),
- Les thérapies utilisant des anticorps (radioimmunothérapie - RIT),
- La radiothérapie interne sélective (RIS) : utilise des microsphères radioactives (^{90}Y ou ^{166}Ho) placées au contact des cibles tumorales. Cette technique est utilisée de plus en plus pour la thérapie des tumeurs hépatiques. Il s'agit d'un groupe spécial de thérapies qui n'utilisent pas de MRP mais des dispositifs médicaux (DM). Les radiologues interventionnels effectuent une évaluation angiographique à la recherche du vaisseau qui nourrit les tumeurs, puis placent les microsphères au contact des régions à traiter.

Dans le cas des radiopeptidothérapies, les radionucléides les plus utilisés sont l'indium 111 (^{111}In), l'yttrium 90 (^{90}Y) et le lutécium 177 (^{177}Lu). Ils sont liés à un peptide, par exemple au DOTATATE et le DOTATOC, qui sont les plus utilisés. L'indium a été initialement utilisé parce que des images pouvaient être générées et, en même temps, la tumeur pouvait être traitée. Cependant, son efficacité thérapeutique s'est avérée bien moindre que celle des autres isotopes. L'yttrium a commencé à être utilisé avec succès, mais des toxicités importantes ont été rapportées. Par ailleurs, les images qui sont générées par rayonnement de freinage sont de qualité réduite. Par conséquent, la quantification n'est pas facile à réaliser.

Dans le cas du ^{177}Lu, la réponse thérapeutique est très bonne et des images peuvent être réalisées avec suffisamment de qualité pour permettre une bonne estimation des doses absorbées.

Dans le cas des RIT, l'anti-CD20 a été utilisé pendant de nombreuses années (mais pas en Europe) avec le produit commercial Bexxar (^{131}I-tositumomab) puis a été abandonné. Le Zevalin (^{90}Y-ibritumomab tiuxétan) a été introduit sur le marché (Europe et USA). Les deux médicaments ont été utilisés pour le traitement des lymphomes. Dans le cas du lymphome non hodgkinien, le ^{131}I-rituximab en conjonction avec rituximab, est l'un des anticorps les plus utilisés de nos jours (Gill et al., 2017; McQuillan et al., 2015).

Différents concepts dosimétriques utilisés dans les chapitres suivants de ce travail sont introduits. Une attention particulière est portée aux techniques de quantification planaire et TEMP qui sont utilisées en dosimétrie clinique, ainsi qu'aux techniques de correction des effets qui dégradent les images et limitent la possibilité de quantification de l'activité.

Dans le deuxième chapitre de ce travail, l’étude de trois nouveaux produits radiopharmaceutiques diagnostiques est présentée. L’introduction de produits radiopharmaceutiques dans l'environnement clinique nécessite au préalable des études précliniques (cellulaire et petit animal). Dans ce contexte, différents animaux sont utilisés pour établir la biodistribution et la biocinétique : des rongeurs, différents types de singes, de chiens et des porcs. L'idée est de rechercher l'animal qui présente la plus grande similitude avec l'être humain, du point de vue de la physiologie de l'organe étudié. Dans le cas de MRP à usage diagnostic, l’irradiation délivrée est faible, mais doit toutefois être évaluée afin de permettre l’obtention de l’autorisation de mise sur le marché (AMM). L'extrapolation des résultats de pharmacocinétique de l’animal à l'humain permet d’estimer l’irradiation délivrée en clinique.

Un premier MRP a été développé en France (CHU-Hôpital Purpan) et deux autres en Uruguay (CUDIM). Deux d'entre eux ont pour objectif d'étudier des maladies cérébrales et le dernier de diagnostiquer le cancer de la prostate. Une étude dosimétrique basée sur les études précliniques a été réalisée pour ces trois radiopharmaceutiques.

L'étude dosimétrique du MRP développé en France s’est basée sur des images TEP/TDM de rats, en déterminant la biodistribution et la biocinétique du produit. Nous avons déterminé un modèle biocinétique qui représente les courbes d'activité en fonction du temps pour divers organes. Ce modèle biocinétique a été utilisé pour déterminer les temps de résidence. Pour les organes dans lesquels ce modèle n’était pas adapté, l’intégration de l’activité au cours du temps a été réalisée par la méthode des trapèzes.

Dans le cas des deux MRP développés en Uruguay, l’étude dosimétrique a été réalisée en quantifiant l'activité directement à partir des comptages de la radioactivité présente dans des échantillons (organes, tissus) prélevés après dissection. Dans les 2 cas, l’intégration de l’activité au cours du temps a été réalisée par la méthode des trapèzes afin de déterminer les temps de résidence.

L'extrapolation des résultats précliniques à l'humain a été réalisée par pondération des masses des organes entre les deux espèces. L'un des MRP est utilisé pour étudier le cancer de la prostate. Pour ce produit, il est possible de déterminer que la voie d'excrétion est urinaire. L'extrapolation des données pharmacocinétiques a été réalisée en tenant compte ou non de la vidange de la vessie à différents moments après l'injection. Pour les MRP utilisés pour étudier les maladies cérébrales, dans un cas la voie d'excrétion est fécale, et dans l'autre c'est urinaire (la vidange de la vessie n'a pas été étudié).

Les modèles dosimétriques de référence proposés par la Commission Internationale de Protection Radiologique (CIPR) ont été utilisés pour déterminer les masses des organes chez l'homme. Les doses absorbées et efficaces ont été estimées à l'aide des trois programmes OLINDA/EXM V1.0, V2.0 et IDAC2.1. Il est possible d'expliquer les différences entre les résultats obtenus par des différences entre les modèles dosimétriques utilisés, la manière dont le calcul des doses absorbées et efficaces est implémenté, et les différents codes utilisés pour le calcul des valeurs S.

Dans le troisième chapitre, la dosimétrie clinique en RIV est étudiée. Les différentes étapes de la dosimétrie clinique dans ce contexte incluent la détermination du facteur d'étalonnage des systèmes d'imagerie, l'acquisition et la reconstruction des images, la segmentation des volumes d'intérêt et leur repositionnement sur les différentes images acquises à différents temps, l'ajustement des courbes d'activité-temps, la détermination des temps de résidence et le calcul de la dose absorbée. Cependant, chacune de ces étapes peut être abordée de plusieurs manières.

Généralement, les protocoles de dosimétrie clinique sont implémentés dans des établissements qui disposent de ressources, notamment de personnel spécialisé, de l'infrastructure nécessaire et de programmes de calcul permettant de déterminer la dose absorbée par un organe ou une tumeur en particulier. Malheureusement, les solutions logicielles de dosimétrie clinique étant le plus souvent développées localement, elles ne sont généralement pas accessibles à la communauté internationale.

En dehors des solutions académiques, il existe aujourd'hui des programmes commerciaux dans lesquels divers protocoles dosimétriques sont disponibles. Par exemple, on peut trouver des protocoles planaires, TEMP/ TDM ou hybrides, qui exigent un nombre minimum (mais variable !) de points de mesure pour chaque patient afin de déterminer les courbes d'activité temps. Certains d'entre eux disposent d'outils pour effectuer la reconstruction des images, en utilisant différentes méthodes de correction des effets limitent la quantification de l'activité. D'autres ne disposent pas de ce type d'outils et leur objectif principal est la détermination de la dose absorbée à partir d'images reconstruites. Pour effectuer cette tâche, chaque programme établit comment entrer un facteur d'étalonnage (coups/Bq ou équivalent). Différents outils de recalage et de segmentation d'images sont généralement disponibles. Enfin, certains codes requièrent uniquement le temps de résidence. Le calcul de la dose absorbée est alors réalisé sur un autre code spécifique, fourni ou non dans la solution dosimétrique. D'autres, en plus d'estimer les temps de residence, peuvent calculer la dose absorbée directement de différentes façons.

Le facteur d'étalonnage est un paramètre qui doit être entré afin d'estimer l'activité à un certain point de mesure. Ce point a été étudié par de nombreux groupes de recherche et dépend de différentes géométries des sources utilisées et de fantômes, dont les données sont disponibles dans la littérature. Il existe une relation entre les paramètres d'acquisition, de reconstruction et de correction des images, tant pour l'estimation du facteur d'étalonnage que pour la détermination de l'activité chez les patients.

Dans les études séquentielles, le positionnement du patient est un facteur important lors du recalage des différentes structures. Mais dans la pratique clinique, il est possible que le positionnement du patient ne soit pas identique à 100% pour toutes les études acquises. Les mouvements des organes entre deux images acquis à différents temps peuvent se produire en raison de la respiration, le changement de position et même au cours de l’acquisition des images, par des mouvements du patient. Tous ces aspects affectent la quantification des structures étudiées. Les techniques de segmentation et de recalage d'images disponibles aujourd'hui permettent de réduire les erreurs introduites dans les études cliniques séquentielles.

La détermination de la pharmacocinétique du MRP peut se révéler difficile car les points (temps) de mesures disponibles sont généralement peu nombreux, entre autres du fait de l'état clinique du patient qui ne permet pas toujours d’acquérir des images aussi souvent que souhaité. L'ajustement de la courbe activité-temps est aussi dépendante de l’algorithme sélectionné – et de la possibilité d’évaluer l’incertitude associée au calcul des paramètres pharmacocinétiques.

Enfin, les différents algorithmes de calcul de la dose absorbée peuvent générer des résultats différents, selon le type d’approche considérée lors du calcul.

Les résultats sont d'abord présentés pour un étalonnage en mode planaire, recommandé par GE pour la mise en œuvre de son programme de dosimétrie. Un étalonnage TEMP/TDM est également effectué par la suite pour l’ensemble des solutions logicielles. De plus, l’étalonnage par TEMP/TDM est présenté où différentes sources d'étalonnage et différentes géométries sont considérées, différents aspects liés à la méthode de reconstruction, par exemple : le nombre d'itérations, les sous-ensembles et les méthodes de correction qui peuvent être implémentés. Une variation du facteur d'étalonnage peut être établie en apportant des changements à chacun d'eux.

De plus, les courbes des facteurs de récupération ont été étudiées pour un fantôme de sphères avec et sans activité de fond.

Un artefact connu sous le nom de « *Gibbs-like* » est représenté dans plusieurs géométries (dont les résultats sont disponibles dans les annexes de ce chapitre), ce qui est lié à la correction de la réponse du collimateur et à l'augmentation du nombre de mises à jour (itérations - sous-ensembles).

Dans ce travail, la radiopeptidothérapie au ^{177}Lu a été utilisée pour évaluer solutions logicielles commerciales de dosimétrie clinique : Dosimetry Toolkit (DTK) qui est une application de Xeleris® de GE, Hybrid Dosimetry Module™ (HDM) d’HERMES, STRATOS qui fait partie de IMALYTICS, la station de travail pour la recherche de Phillips et PLANET® Onco Dose (PDOSE) de Dosisoft.

Afin de valider le facteur d'étalonnage pour HDM, STRATOS et PDOSE, une évaluation globale est effectuée pour une géométrie spécifique (fantôme) sur la capacité de chaque logiciel à déterminer le temps de résidence, ce critère étant donc sélectionné à des fins de comparaison. Un autre critère d'évaluation était la détermination de l'activité à chaque point de mesure. Pour le fantôme, une bouteille a été remplie d’eau avec une solution de ^{177}Lu. Cette bouteille a été placée à l’intérieur d’un autre fantôme, le NEMA 2012/IEC 2008 PET. Cinq points de mesure ont été obtenus pour générer une courbe de désintégration radioactive représentative du ^{177}Lu. La variation de la position du fantôme a permis d'étudier l'influence du recalage rigide d'images séquentielles sur la détermination du temps de résidence (dans un cas favorable), pour chaque logiciel et différents facteurs de calibration. Les images ont été reconstruites dans HERMES, puis chargées et analysées dans HDM, STRATOS et PDOSE. Les flux de travail de chaque solution ont été étudiés pour comprendre leurs forces et faiblesses. Sur la base des résultats obtenus à partir des temps de résidence et de l'activité pour chaque point de mesure, deux facteurs d'étalonnage ont été sélectionnés pour être utilisés dans les dosimétries avec les données des patients.

Dans le quatrième chapitre, les données cliniques de deux patients (un homme et une femme) atteints de tumeurs gastro-entéro-pancréatiques d'origine neuroendocrinienne traitées au ^{177}Lu-DOTATATE ont été utilisées. Pour chaque patient, deux cycles de traitement ont été utilisés pour estimer les temps de résidence et les doses absorbées dans les reins, le foie, la rate, la moelle osseuse et le corps entier en utilisant les différentes stations de travail dosimétriques/solutions logicielles commerciales. L’activité administrée était d’environ 7,2 GBq par cycle pour chaque patient.

Les dosimétries ont été réalisées sur les bases d’acquisitions TEMP/TDM. Seuls Xeleris® et HERMES permettent de reconstruire les images. Les images des patients ont été reconstruites indépendamment et par différents utilisateurs avec Xeleris® et HERMES. Les images reconstruites avec Xeleris® ne sont analysées qu’avec DTK, mais les images reconstruites avec HERMES sont chargées et analysées avec HDM, STRATOS et PDOSE.

Dans toutes les stations de travail, la même méthode du recalage des images a été utilisée. Dans le cas du recalage d'images, pour DTK, HDM et STRATOS la méthode a été appliquée en utilisant l'image entière du champ de vision. Dans le cas de PDOSE la méthode appliquée a été optimisée au niveau de chaque organe. Dans le cas de DTK la segmentation a été automatique. Pour HDM, STRATOS et PDOSE la segmentation manuelle a été utilisée.

Les méthodes d'ajustement des courbes d'activité - temps implémentées dans les logiciels sont différentes, il n'est donc pas possible d'appliquer une méthode commune. Nous avons donc utilisé la méthode la plus optimale disponible dans chaque solution logicielle. Une seule station de travail dispose d'une méthode permettant de valider de manière objective la méthode d’ajustement sélectionnée.

En ce qui concerne la méthode de calcul dosimétrique, on constate que pour le ^{177}Lu la plus grande contribution à la dose absorbée locale est due à l'émission bêta, et que pour tous les organes la contribution gamma lui est en général inférieure de deux ordres de grandeur.

Les doses absorbées ont été estimées à l'aide des outils disponibles dans chaque logiciel. Ce calcul est effectué pour le foie, la rate et les reins. Dans le cas de DTK et HDM, un calcul est effectué en utilisant OLINDA/EXM V1.0 et V2.0, respectivement, puisque les deux logiciels y exportent leurs résultats. De plus, les doses sont ajustées en fonction de la masse de chaque organe. Dans le cas du PDOSE, on utilise la méthode du dépôt local d'énergie et dans le cas du STRATOS, on effectue un calcul par convolution. Enfin, tous les logiciels peuvent estimer les temps de résidence.

La comparaison des logiciels se fait en utilisant les résultats de la segmentation (masse des organes), les temps de résidence et les doses absorbées. En tenant compte de l'ajustement par les masses des organes/tissus, les calculs de dose absorbée suivent directement les calculs de temps de résidence.

On voit donc que les masses sont variables d'un patient à l'autre, mais moins variables d'un cycle à l'autre et elles dépendent peu de la station de travail utilisée pour la segmentation (écart type relatif faible).

On constate que les temps de résidence sont très variables d'un patient à l'autre, d'un facteur supérieur à 10 par exemple entre l'homme et la femme pour le foie. Ces facteurs sont également variables d'un cycle à l'autre pour le même patient (exemple du temps de résidence au foie pour la patiente), mais somme toute peu variable d'une station de travail à l'autre.

Pour la patiente, la dose absorbée moyenne au foie a diminué de près 50% entre les 2 cycles. Pour cet organe, de multiples métastases sont visibles. Il est probable que ces lésions captent moins de MRP, ce qui entraîne une diminution de la dose absorbée. Les doses absorbées moyennes pour la rate sont plus élevées que pour les reins, justifié par les différences de valeurs S associées à cet organe pour le ^{177}Lu. Les résultats de dose absorbée moyenne pour les reins sont du même ordre de grandeur que ceux rapportés par Sundlöv (Sundlöv et al. 2017), pour la dose absorbée rénale médiane = 4,5Gy/fraction, pour 51 patients (199 cycles de traitement).

Dans le cas de l'estimation de la dose absorbée dans la moelle osseuse et conformément au schéma du MIRD, il convient de tenir compte à la fois de l'auto-absorption et du rayonnement croisé. Dans le cas de l'auto-absorption, l'estimation de la dose absorbée peut être donnée au moyen de mesures sanguines ou d'images des vertèbres L_2 à L_4. En principe, les deux méthodes devraient être comparables, bien que certains auteurs aient (Beykan et al., 2018) récemment mentionné que ce n'était peut-être pas le cas pour le peptide étudié. Dans le cas du rayonnement croisé (contribution gamma), la contribution des différents organes sources et du corps entier doit être estimée. Pour ces patients, il n'a pas été possible de compter sur les mesures de corps entier. Une nouvelle approche qui permet d'estimer la dose absorbée sans avoir besoin d'utiliser de mesures du corps entier est présentée. Les résultats obtenus sont comparables à d'autres résultats de la littérature (Forrer et al., 2009).

La dernière section du présent document est consacrée à la conclusion générale, aux questions encore en suspens et aux perspectives des travaux futurs.

General introduction

Nuclear medicine is a medical specialty whose applications, essentially diagnostic allow the study of organ physiology and the metabolism of various types of tumours. Targeted radionuclide therapies (TRT) is a therapeutic approach to nuclear medicine. The purpose of TRT is to transport the radionuclide to the tumor. It will therefore be necessary to consider different types of carrier molecules, their affinity for tumours, different radioactive isotopes and binding of the isotope to the carrier molecule. The TRT can be categorized in many ways, for example, according to the type of carrier molecules used (radioimmunotherapy, radiopeptidetherapy), or according to the selected isotope.

The response to treatment depends on many factors, one of them being the type of radiation. The radionuclides selection is based on the type of emission- alpha or beta particles, or Auger having a reduced path in the material and allowing localized irradiation to be delivered around the emission point. Depending on the penetration of these particles into the material, a crossfire effect can be expected (depending on the radiation range and tumour size), which theoretically increases the effectiveness of the therapy. For alpha particle emitters, it is also possible to benefit from the high linear energy transfer (LET) of this type of particle thus leading to an increase in irradiation efficiency for the same delivered energy. In addition, if the isotopes have gamma emission, it will be possible to generate images to monitor the fate of the radioactive vector in the patient.

The place of dosimetry in TRT is a debated issue (Chiesa et al., 2017; Flux et al., 2017; Giammarile et al., 2017). Between the need to document the delivered irradiation and the possibility to optimize the treatment, the development of clinical dosimetry is contrasted but undeniable. Article 56 (Optimization) of Council Directive 2013/59/Euratom (Council of the European Union 2014) explicitly states that "For all medical exposures of patients for radiotherapeutic purposes, exposures of target volumes shall be planned individually and their delivery duly verified taking into account that doses to non-target volumes and tissues shall be as low as reasonably achievable and consistent with the radiotherapeutic objective of exposure".

The methodology is available - but implemented very differently in clinics depending on the countries and clinical centers. Indeed, a good indicator of the clinical dosimetry development is availability of commercial solutions in the market that has seen spectacular recent developments. It is now possible to perform personalized dosimetries, considering the pharmacokinetics of radiopharmaceuticals and the morphology of each patient.

As far as dosimetry in a diagnostic context is concerned, it is mainly carried out during the development of new tracers, in order to determine orders of magnitude of the (low) irradiation delivered. This is referred to as reference dosimetry.

This doctoral project focuses on clinical dosimetry of radiopharmaceuticals:

- We first established the reference absorbed doses for three new diagnostic radiopharmaceuticals by extrapolating the preclinical data to humans using the three software packages and comparing the results.
- Subsequently, we studied four commercial dosimetry solutions, using phantom experiments and clinical data processing. For the 4 commercial solutions studied, similarities and differences are presented. The comparison proved difficult as the different commercial solutions offer different implementations of clinical dosimetry, which sometimes limits the evaluation or comparison of performance.

In the first chapter of this work, different approaches to vectorized internal radiotherapy are mentioned. Depending on the type of carrier molecule, they can be divided into different groups:

- The case where the isotope is also the carrier/vector (^{131}I, ^{223}Ra),
- The case where the vector participates in tumour metabolism (mIBG),
- Peptide-based therapies (peptide receptor radionuclide therapy or PRRT),
- Antibody therapies (radioimmunotherapy),
- Selective internal radiotherapy (STIR): It uses radioactive microspheres (^{90}Y or ^{166}Ho) placed in contact with tumor targets. This technique is increasingly used for the therapy of hepatic tumours. This is a special group of therapies that uses medical devices instead of radiopharmaceuticals. Interventional radiologists perform an angiographic evaluation in search of the vessel that feeds the tumors, and then places the microspheres in contact with the areas to be treated.

In case of PRRT, the most commonly used radionuclides are 111-Indium (^{111}In), 90-Yttrium (^{90}Y) and 177-Lutetium (^{177}Lu). They are linked to a peptide, for example DOTATATE and DOTATOC (frequently used). ^{111}In was initially used because images could be generated and, at the same time, the tumor could be treated. However, because of its low efficacy compared to that of therapies using other isotopes, it is not in use nowadays. ^{90}Y has had successful start, however significant toxicities have been reported. In addition, the images generated by bremsstrahlung are of reduced quality. Therefore, quantification is not easy to achieve. In the case of ^{177}Lu, the therapeutic response is very good and images can be taken with sufficient quality to allow a good estimate of the absorbed doses.

In the case of radioimmunotherapy, anti-CD20 has been used for many years (but not in Europe) with the commercial product Bexxar (^{131}I-tositumomab) and has been discontinued. Zevalin (^{90}Y-ibritumomab tiuxetan) has been introduced in the market (Europe and USA). Both drugs have been used to treat lymphoma. In the case of non-Hodgkin's lymphoma, ^{131}I-rituximab in conjunction with rituximab is one of the most commonly used antibodies today (Gill et al., 2017; McQuillan et al., 2015).

An introduction of the different dosimetric concepts that are used in following chapters of this work is presented. Particular attention is paid to planar and SPECT quantification techniques used in clinical dosimetry, as well as to techniques related to correction effects degrading the image quality and limiting the quantification of activity.

In the second chapter of this work, the study of three new diagnostic radiopharmaceuticals is presented. The introduction of radiopharmaceuticals into the clinical environment requires pre-clinical studies (cellular and small animal). In the latter case, different animals are used to establish biodistribution and biokinetics: rodents, different types of monkeys, dogs and even pigs can be used. The idea is to search for the animal that has the greatest similarity with the human being, from the point of view of the physiology of the organ being studied. In the case of diagnostic radiopharmaceuticals, the irradiation delivered is low. However, it must be evaluated before the product is granted a marketing authorisation (MA). Extrapolation of pharmacokinetic results from animal to human allows to estimate the irradiation delivered in clinics.

The first radiopharmaceutical was developed in France (CHU-Hôpital Purpan) and the other two in Uruguay (CUDIM). Two of them are used to study brain diseases and the last one for diagnosing prostate cancer. A dosimetric study based on preclinical studies was performed for these three radiopharmaceuticals.

The dosimetric study of the radiopharmaceutical developed in France was based on PET/CT images of rats, determining the biodistribution and biokinetics of the product. A biokinetic model was determined that accurately represents the activity curves over time for various organs. This biokinetic model was used to determine residence times. For organs in which this model was not suitable, the integration of activity over time was performed by the trapezoidal method.

In the case of the two radiopharmaceuticals developed in Uruguay, the dosimetric study was carried out by quantifying the activity directly from the counts of radioactivity present in samples (organs, tissues) taken after dissection. In both cases, the integration of the activity over time was carried out by the trapezoid method in order to determine the residence times.

Extrapolation of preclinical results to humans was performed by weighing organ masses between the two species. One of the radiopharmaceuticals was used to study prostate cancer. For this product, it was possible to determine that the excretion route is through urine. Extrapolation of pharmacokinetic data was performed with or without consideration of emptying bladder at different times after injection. For radiopharmaceuticals used to study brain diseases, in one case the excretion pathway is faecal, and in the other the quantification of dynamic bladder emptying has not been performed.

The reference dosimetric models proposed by the International Commission on Radiological Protection (ICRP) have been used to determine the masses of organs in humans. Absorbed and effective doses were estimated using the three OLINDA/EXM programs V1.0, V2.0 and IDAC2.1, and it is possible to explain the differences between the results obtained by differences between the dosimetric models used, the way in which the calculation of absorbed and effective doses is implemented, and the different codes used for the calculation of S-values.

In the third chapter, clinical dosimetry in TRT was studied. The different steps of clinical dosimetry in this context includes the determination of the calibration factor of imaging systems, image acquisition and reconstruction, segmentation of volumes of interest and their repositioning on different images acquired at different times, adjustment of time-activity curves, determination of residence times and calculation of absorbed dose. However, each of these steps can be addressed in several ways.

Generally, clinical dosimetry protocols are implemented in institutions that have resources, including specialized personnel, the necessary infrastructure and calculation programs to determine the dose absorbed by a particular organ or tumour. Unfortunately, since clinical dosimetry software solutions are most often developed locally, they are generally not accessible to the international community.

In addition to academic solutions, there are now commercial programs in which various dosimetric protocols are available. For example, the choice of planar, SPECT/CT or hybrid protocols, which require a minimum (but variable!) number of measurement points for each patient to determine time-activity curves. Some of them have tools to perform image reconstruction using different effect correction methods thus limiting the quantification of activity while some have their main objective to determine the absorbed dose from reconstructed images. To perform these tasks, each program determines how to enter a calibration factor (counts/Bq or equivalent). Different tools for image registration and segmentation are generally available. However, some codes only estimate residence time. The calculation of the absorbed dose is then performed on another specific code whether or not provided in the dosimetry solution. Others, in addition to estimating residence times, can calculate the absorbed dose directly in different ways.

The calibration factor is a parameter that must be entered in order to estimate the activity at a certain measurement point. Many research groups have studied the use of different geometries of the sources and the phantoms and this can be found in the literature. There is a relationship between the form of image acquisition, reconstruction and correction, both for the estimation of the calibration factor and for the determination of activity in patients.

In sequential studies, patient positioning is an important factor when relocating different structures. But in clinical practice, it is possible that the patient's positioning may not be 100% identical for all acquired studies. Organ movements between two images acquired at different times can occur due to breathing, change of position or even during image acquisition by patient movements. All these aspects affect the quantification of the studied structures. The segmentation and image registration techniques available today makes it possible to reduce the errors introduced in sequential clinical studies.

Determining the pharmacokinetics of a radiopharmaceutical can be difficult because the available measurement points (time) are generally few, partly because of the patient's clinical condition, which does not always allow images to be acquired as often as desired. The adjustment of the time-activity curve is also dependent on the algorithm selected and the ability to assess the uncertainty associated with the calculation of pharmacokinetic parameters.

Finally, the different algorithms for calculating the absorbed dose may generate different results depending on the type of approach considered in the calculation.

The results are presented for a planar calibration recommended by GE for the implementation of its dosimetry program. A SPECT/CT calibration is also performed thereafter for all software solutions. In addition, SPECT/CT calibration is presented where different calibration sources, geometries and different aspects related to the reconstruction method were considered, for example: the number of iterations, subsets and correction methods that can be implemented. A variation in the calibration factor can be established by changing each of them.

In this work, ^{177}Lu PRRT was used to evaluate commercial clinical dosimetry software solutions: Dosimetry Toolkit (DTK), an application of GE's Xeleris®; Hybrid Dosimetry Module™ (HDM) from HERMES; STRATOS, which is part of IMALYTICS; the Phillips Research Workstation and PLANET® Onco Dose (PDOSE) from Dosisoft.

In order to validate the calibration factor for HDM, STRATOS and PDOSE, an experiment was developed for a specific geometry (phantom) in which the ability of each software to determine residence time was evaluated. This criterion was being selected for comparison purposes. Another evaluation criterion was the determination of activity at each measurement point. For the phantom, a bottle was filled with water with a ^{177}Lu solution. The bottle was placed inside another phantom the NEMA 2012/IEC 2008 PET. Five measurement points were obtained to generate a radioactive decay curve representative of ^{177}Lu. The position of the phantom was not always the same, which made it possible to study the influence of rigid registration of sequential images on the determination of residence time (in a favorable case), for each software and different calibration factors. The images were reconstructed in HERMES, then uploaded and analyzed in the HDM, STRATOS and PDOSE workflows. In this sense, the workflows of each solution have been studied to understand their strengths and weaknesses. Based on the results obtained from residence times and activity for each measurement point, two calibration factors were selected for use in dosimetries with patient data sets.

In the fourth chapter, clinical data from two patients (one male and one female) with neuroendocrine gastroenteropancreatic tumours treated with ^{177}Lu-DOTATATE were used. For each patient, two treatment cycles were used to estimate residence times and absorbed doses in the kidneys, liver, spleen, bone marrow and whole body using the different dosimetric workstations/commercial software solutions. The administered activity was approximately 7.2 GBq per cycle for each patient.

Dosimetries were performed on the basis of SPECT/CT acquisitions. Only Xeleris® and HERMES can reconstruct images. Patient images were reconstructed independently and by different users with Xeleris® and HERMES. Images reconstructed with Xeleris® were only analyzed with DTK, but images reconstructed with HERMES were loaded and analyzed with HDM, STRATOS and PDOSE.

In all workstations, the same method of image registration and segmentation was used. In the case of image registration, for DTK, HDM and STRATOS the method was applied using the entire image of the field of view. In the case of PDOSE, the method applied was optimized for each organ. In the case of DTK the segmentation was automatic and for HDM, STRATOS and PDOSE, the manual segmentation was used.

The methods of fitting time-activity curves implemented in the software differ which makes it impossible to apply the same method to all. We therefore used the best possible method available in each software. Only one workstation has a method to objectively validate the selected adjustment method.

Regarding the dosimetric calculation method, it can be seen that for ^{177}Lu, the greatest contribution to the local absorbed dose is due to beta emission and that for all organs, the gamma contribution is generally lower by two orders of magnitude.

The absorbed doses were estimated using the tools available in each software package. This calculation is performed for the liver, spleen and kidneys. In the case of DTK and HDM, a calculation is performed using OLINDA/EXM V1.0 and V2.0 respectively, since both software packages export their results to them. In addition, doses are adjusted according to the mass of each organ. In the case of PDOSE, the local energy deposition method is used and in the case of STRATOS a convolution calculation is performed. In addition, all software can estimate residence times.

The comparison of workstations is made using the results of segmentation (mass of organs), residence times and absorbed doses. Even considering the mass adjustment of organs/tissues, absorbed dose calculations directly followed the residence time calculations.

We can therefore see that the masses are variable from one patient to another, but less variable from one cycle to another and they depend little on the workstation used for segmentation (low relative standard deviation).

It can be seen that residence times vary greatly from one patient to another (factor greater than 10 for example between men and women for the liver). Also, it varies from one cycle to another for the same patient (example: residence time in the liver for the patient) but overall slightly variable from one workstation to another.

For the female patient, the average absorbed dose to the liver decreased by nearly 50% between the 2 cycles. For this organ, multiple metastases are visible. It is likely that these lesions capture less radiopharmaceutical, resulting in a decrease in the absorbed dose. The average absorbed doses for the spleen are higher than for the kidneys due to the S-value associated with this organ for ^{177}Lu. The mean absorbed dose results for the kidneys are of the same order of magnitude as those reported by Sundlöv et al. (Sundlöv et al. 2017), for the median absorbed renal dose = 4.5 Gy/fraction, for 51 patients (199 treatment cycles).

Dosimetry was performed on the basis of SPECT/CT acquisitions. Only Xeleris® and HERMES can rebuild images. All programs calculate residence times and DTK exports its results to OLINDA/EXM V1.0.

The results are first presented for a planar calibration, recommended by GE for the implementation of its dosimetry program. A SPECT/CT calibration is also performed thereafter for all software solutions.

Patient images were reconstructed independently and by different users with Xeleris® and HERMES. Images reconstructed with Xeleris® are only analyzed with DTK, but images reconstructed with HERMES are analyzed with HDM, STRATOS and PDOSE.

In addition, SPECT/CT calibration is presented where different calibration sources and geometries are considered along with different aspects related to the reconstruction method, for example: the number of iterations, subsets and correction methods. A variation in the calibration factor can be established by making changes to each of them.

In addition, the recovery factor curves were studied for a phantom of spheres with and without background activity.

An artifact known as "Gibbs-like" is represented in several geometries relating to corrections of collimator response and increasing number of updates (iterations - subsets).

In order to validate the calibration factor for different commercial software, an experiment was performed for a specific geometry (phantom) to assess the ability of each software to determine residence time and this criterion was therefore selected for comparison purposes. For the phantom, a bottle was filled with water with a ^{177}Lu solution. The bottle was placed inside another phantom - the NEMA 2012/IEC 2008 PET. Five measurement points were obtained to generate a radioactive decay curve representing the decay of ^{177}Lu. The position of the phantom was not always the same, which made it possible to study the influence of rigid registration of sequential images on the determination of residence time (in a favorable case) for each software and different calibration factors.

The workflows of each solution were studied to understand their strengths and weaknesses.

Clinical data from two patients (one male and one female) with neuroendocrine gastroenteropancreatic tumours (NETs) treated with ^{177}Lu-DOTATATE were used. For each patient, two treatment cycles were used to estimate residence times and absorbed doses in the kidneys, liver, spleen, bone marrow and whole body with different dosimetric workstations/commercial software solutions. The administered activity was approximately 7.4 GBq per cycle for each patient.

In all workstations, the same method of image registration and segmentation was used. In the case of image registration, for DTK, HDM and STRATOS, the method was applied using the entire image of the field of view. In the case of PDOSE, the method applied was optimized for each organ. In all cases, manual segmentation was used.

The methods of fitting time-activity curves implemented in the software were different thus making it impossible to apply the same method to all. We therefore used the best possible method available in each IT solution. Only one workstation has a method to objectively validate the selected adjustment method.

Absorbed doses were estimated using OLINDA/EXM V1.0 and OLINDA/EXM V2.0 software. All results were adjusted according to the masses of each organ/tissue.

Comparison parameters were mass of segmented organs, residence time and absorbed dose results. Table I.1 shows the performance results for all software.

In the case of the estimation of absorbed dose in bone marrow and in accordance with the MIRD scheme, both the contribution of self-absorption and cross-reactivity should be considered. In the case of self-absorption, the estimate of the absorbed dose can be given by means of blood measurements or images of the vertebrae L_2 to L_4. In principle, the two methods should be comparable, although some authors have recently mentioned (Beykan et al., 2018) that this may not be the case for the studied peptide. In the case of cross radiation (gamma contribution), the contribution of the different source organs and the whole body must be estimated. For these patients, it was not possible to rely on whole body measurements so a new approach is presented to estimate the absorbed dose without the need to use whole body measurements. The results obtained were comparable to other results in the literature (Forrer et al., 2009).

The last section of this work is devoted to the general conclusion, questions that are still pending and the perspectives for future work.

References of the introduction

Beykan, S., et al. (2018). Patient-specific dosimetry of 177Lu-DOTATATE peptide receptor therapy with high activities. *Eur J Nucl Med Mol Imaging*, *45*(Suppl 1), S33.

Chiesa, C., et al. (2017). The conflict between treatment optimization and registration of radiopharmaceuticals with fixed activity posology in oncological nuclear medicine therapy Formalization of the optimization principle in the new European Council Directive 2013/59. *Eur J Nucl Med Mol Imaging*, 44(11), 1783-1786

Flux, G. D., et al. (2017). From fixed activities to personalized treatments in radionuclide therapy: lost in translation? *Eur J Nucl Med Mol Imaging*, 12–14.

Forrer, F., et al. (2009). Bone marrow dosimetry in peptide receptor radionuclide therapy with [177Lu-DOTA0,Tyr3]octreotate. *Eur J Nucl Med Mol Imaging*, *36*(7), 1138–1146.

Giammarile, F., et al. (2017). Dosimetry in clinical radionuclide therapy: the devil is in the detail. *Eur J Nucl Med Mol Imaging*, 3–5.

Gill, M. R., Falzone, N., Du, Y., & Vallis, K. A. (2017). Targeted radionuclide therapy in combined-modality regimens. *The Lancet Oncology*, *18*(7), e414–e423. https://doi.org/10.1016/S1470-2045(17)30379-0

Hänscheid, H., et al. (2018). Dose Mapping after Endoradiotherapy with 177 Lu-DOTATATE/-TOC by One Single Measurement after Four Days. *J Nucl Med*, *59*, 75–81.

McQuillan, A. D., et al. (2015). Phase II study of first-line 131I-rituximab radioimmunotherapy in follicular non-Hodgkin lymphoma and prognostic 18F-fluorodeoxyglucose positron emission tomography. *Leukemia and Lymphoma*, *56*(5), 1271–1277.

1. Therapeutic Nuclear Medicine

Treatment of cancer can occur by surgical resection and/or using chemotherapy and/or external beam radiotherapy (EBRT). In addition, the use of radiopharmaceuticals for cancer therapy (targeted radionuclide therapy - TRT) exists, albeit restricted to some tumours. Nowadays therapies provided by nuclear medicine can be incorporated as regular methods to treat certain types of tumours (therapeutic radiopharmaceutical have FDA or EMA approval). The timeline to use either alone or a combination of these tools is decided by the group of physicians in charge of a given patient treatment. In the case of locoregional tumours, EBRT and/or surgery are often used, but in the case of spread disease chemotherapy and TRT can be chosen. The goal TRT is to irradiate cancer cells (localized or metastatic tumours) while causing minimal toxicity to surrounding normal tissues.

1.1. Targeted radionuclide radiotherapy (TRT)

This type of therapy is also called Molecular Radiotherapy (MRT) and is based on the use of high-affinity molecules as carriers of radionuclides to tumour cells. Radiopharmaceuticals used in this type of therapy are often injected intravenously or intracavitary (Gudkov et al., 2015). Following the injection, such drugs go into to blood stream, reach the target thanks to the carrier, then damage the tumour thanks to the ionizing radiations emitted by the radionuclide. The basis of its success is related to the concentration and prolonged retention of the radiopharmaceutical within the tumour. Tumour response depends on several factors. Dosimetric factors such as radiation range, cumulated absorbed dose, (maximum) absorbed dose rate may impact the treatment. Tumour radiosensitivity – considering also bystander effect (Ersahin et al., 2011; Gill et al., 2017) is also a parameter that influences the success of the therapy.

In order to choose a radiopharmaceutical product that can be used in TRT, at least two different components need to be considered, the radionuclide and the targeting vector. The choice of these two components sometimes can be unique due to physicochemical properties, pairing this combination to be tailored precisely to specific clinical scenario. In terms of the latest aspect, antibodies, antibodies fragments and platforms, proteins, peptides and small molecules have been used, having great affinity and specificity for the target (Gill et al., 2017; Gudkov et al., 2015).

In terms of radionuclides several aspects can be considered, for instance, their radioactive decay properties, and how are produced (Gill et al., 2017; Gudkov et al., 2015). Three types of emissions are preferred, $\beta-$particles that can be used for irradiation of volumes with multicellular dimensions; $\alpha-$particles, that are used to irradiate volumes with cellular dimensions; and Auger electrons that can irradiate volumes with subcellular dimensions. Moreover, if the radionuclides have $\gamma-$rays' emissions or annihilation photons, those can be used for dual therapeutic and diagnostic applications (so-called theragnostic). Considering each type of emission important aspects are the linear transfer energy (LET), their range in tissue and their physical half-life.

For instance, the LET of α-particles varies between 50 – 230 keV/μm, with a range in tissue varying between 20 -100 μm. For β-particles the LET is between 0.2 – 4 keV/μm, with a range in tissue varying between 0.05 – 12 mm. For Auger electrons the LET varies between 4 – 26 keV/μm and the range in tissue is less than 20 μm (Gill et al., 2017). An illustration of previous characteristics is shown in figure 1.1.

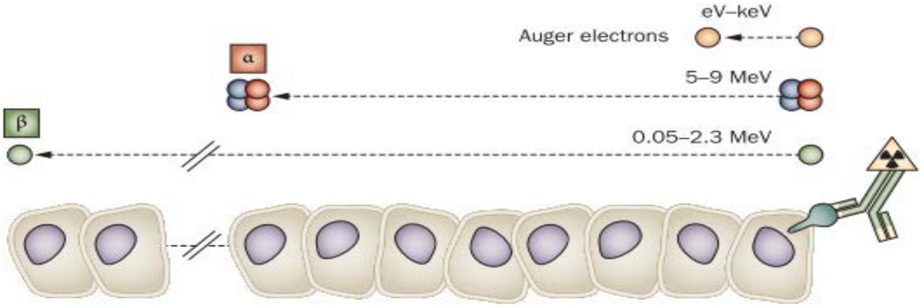

Figure 1.1: Schematic illustration of the range in tissue, at cellular level for α- and β- particles, and Auger electrons. Image taken from (Pouget et al., 2011).

Pouget et al. presents information regarding half-life, type of emission, maximum energy range and maximum range in tissue for several radionuclides (Pouget et al., 2011). On the other hand, Gudkov et al. shows the method of production for other radionuclides (Gudkov et al., 2015). According to the size of the tumour, Auger electrons are suitable to target single cells, α-particles are ideal for treating small or micro-metastases and blood or bone marrow diseases (short range and high energy); finally β-particles are superior for targeting large tumours (long range) and even cells without expression of the molecular target will be irradiated due to the so-called cross-fire effect (Gill et al., 2017).

1.1.1. Peptide receptor radionuclide therapy (PRRT) for neuroendocrine tumours (NET’s)

This type of therapy is mostly used in gastroenteropancreatic neuroendocrine tumours (GEP-NET) and neuroendocrine tumours (NET’s), also located in the lung, where somatostatin (SS) receptor expression is over-expressed (Ersahin et al., 2011). Generally, these are slow-growing tumours, but in some instances may become very aggressive; additionally, they may be identified when the metastatic spread is important. Metastasis can be local or may be located in diverse sites such as bone, brain and liver (Bodei et al., 2014). Moreover, PRRT has been suggested as a therapy in the management of pheochromocytoma, paraganglioma, neuroblastoma, meningioma, medullary thyroid carcinoma and even in non-iodine avid differentiated thyroid cancer (Baum R. P., 2014).

Inoperable or metastasized progressive well-differentiated NET’s patient are candidates to highly effective PRRT treatments, and also the determination of the Ki-67 tumour proliferation index is essential for patient selection. Moreover, high SS receptor expression of the tumours has to be assured previously to the therapy (Baum R. P., 2014; Ezziddin et al., 2011). Initially diagnostic occurred using SPECT/CT images after administration of ^{111}In-Octreotide, but PET/CT imaging using ^{68}Ga-DOTA-peptides is becoming available.

As previously mentioned in TRT the radiopharmaceutical is a combination of two components, the pharmaceutical product and the radionuclide. A general configuration of this combination can be seen in figure 1.2.

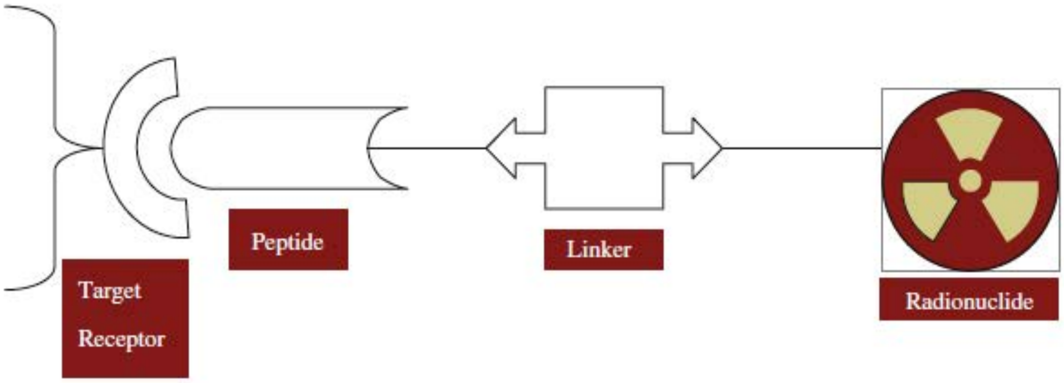

Figure 1.2: Illustration of a radiolabeled peptide radiopharmaceutical for tumour receptor targeting. Image taken from (Baum R. P., 2014).

Normally a chelator agent is used as a linker for successful radiolabelling of the SS analogues, such is the case of the DOTA, that can be used for diagnosis or therapy of NETs: DOTATOC ([DOTA^0, Tyr^3]-octreotide) for diagnosis. For therapy DOTATATE ([DOTA^0, Tyr^3]-octreotate), that presents higher affinity to SS target receptor 2 (Baum R. P., 2014).

The radionuclides used with these chelators have been changing during the last two decades; the PRRT was introduced into clinical practice by the group of (Krenning et al., 1994) in 1994 using [^{111}In-DTPA^0]-octreotide, initially for diagnosis and then, by incrementing the injected activity, to treat NET's. However, 111-Indium (^{111}In) is no longer used in practice (Valkema et al., 2002), because therapies using other isotopes such as 90-Ytrium (^{90}Y) and later 177-Lutetium (^{177}Lu) have shown better outcomes.

In the case of ^{90}Y, this radionuclide was attractive due to its high energy β emissions (maximum energy = 2.28 MeV), with a range penetration in tissue of 11.3 mm, with a half-life of 64.1 h (Eckerman & Endo, 2008), therefore suitable for large tumours. Nonetheless, a drawback of using this radionuclide is associated with the lack of gamma emission, and activity quantification by bremsstrahlung imaging is very complex (Baum R. P., 2014).

^{177}Lu is used since 2000 the chelated analogue DOTATATE (Bodei et al., 2014). Some characteristics of this radionuclide are presented in table 1.1.

Table 1.1. Physical characteristics of ^{177}Lu (Eckerman & Endo, 2008; Garkavij et al., 2010; Ljungberg et al., 2016).

Emissions	Energy (keV)	% β	% γ
β- (therapy)	47.5	12.2	
	111.5	9.1	
	149.1	78.6	
γ (imaging and dosimetry)	112.9		6.17
	208.4		10.36
	249.7		0.21
	321.3		0.22
$E_{\beta max}$: 498.3 keV	Range in tissue ($E_{\beta max}$): 2.0 mm	Physical half-life: 6.7 days	

Kidneys have been identified such a limiting organ in PRRT. This is due to the small size of the peptides, that are going to be filtered through glomerular capillaries in the kidneys and then reabsorbed and kept in the proximal tubular. Maximum tolerable absorbed doses, extrapolated from EBRT are between 23-27 Gy (Baum R. P., 2014; Bodei et al., 2014).

Haematological toxicity can be associated to bone marrow uptake in PRRT. However, poor correlation between the development of haematological toxicity and mean absorbed dose to bone marrow (Bodei et al., 2008; Forrer et al., 2009) has been shown. Moreover, it has been shown that blood-based dosimetry cannot be compared with image-based dosimetry approaches (Beykan et al., 2018), due the difference in the results obtained from both techniques. Thus, in principle a clear absorbed dose-response relationship cannot be based on blood measurements and further investigations have to be performed to evaluate patient toxicity using image-based approaches. On the other hand, haematological toxicity could be associated to exposure of the spleen, because the uptake for this organ could be important, nevertheless further studies have to be performed to confirm or dismiss this hypothesis (Svensson et al., 2016).

1.1.2. Molecular radionuclide therapy (using ^{131}I)

One of the oldest therapy treatments can be related to the use of ^{131}I for patient with differentiated thyroid cancer (papillary and follicular thyroid cancer) and also for benign thyroid pathology such as toxic and non-toxic goitre, hyperfunctioning nodules and Graves' disease.

Some physical properties of 131-Iodine (^{131}I) (half-life of 8.1 days, maximum electron energy of 606 keV with tissue range penetration around 2.3 mm) make it suitable as a treatment agent. Also with its four gamma emissions 284 keV (5.8%), 364 keV (82%), 637 keV (6.5%) and 723 keV(1.7%) images can be created to quantify activity using a SPECT/CT (Dewaraja et al., 1998; Pouget et al., 2011).

Probably the first dosimetric results using this therapy in thyroid cancer treatment were reported from Benua et al. in 1962 (Benua et al., 1962). Since then a lot of experience has been created around the nuclear medicine societies producing several guidelines to treat patients at different clinical stages for both types of thyroid diseases (Cooper et al., 2009; Haugen et al., 2016; Luster et al., 2008; Stokkel et al., 2010).

In the case of thyroid cancer, these guidelines take into account multiple aspects, since the proper identification of the thyroid cancer, the stage of disease, placement of a patient in a particular thyroid treatment scheme; this mean surgery, time of activity administration after surgery, their follow-up and further actions in the case of disease resistance. Moreover, EBRT can also be considered in some cases.

These guidelines also consider the preparation of the patient before the treatment, for instance, when rhTSH stimulation is used or not, the time of low iodine diet and the time avoiding TSH drug. Additionally, these guidelines consider how to proceed with patients at different ages, for instance, in the case of children or elderly people. However, most of the time the prescribing procedure using ^{131}I is referring to administrated activity instead of absorbed dose. Therefore, more efforts must be undertaken to provide evidence to the physicians of a relevance of dosimetry for this treatment.

In the case of hyperthyroidism, the case of the European Association of Nuclear Medicine (EANM) guidelines recommend prescribing different absorbed doses depending on the type of disease. Moreover, the EANM has dosimetry guidelines for both diseases targeting organs such as the thyroid itself and the bone marrow (Hänscheid et al., 2013; Hindorf et al., 2010; Lassmann et al., 2008). In these guidelines, how to calibrate the equipment, analyse patient data and how to estimate absorbed dose is described. Moreover, the International Atomic Energy Agency (IAEA) has created a report in which radiological protection recommendations are given to patients who are receiving these treatments (IAEA, 2009). To generate these recommendations, the administrated activity was the criteria used. Hence, isolation periods from relatives, co-workers, time to sleep alone and visits from children are defined for patients who underwent thyroid cancer (for ablation or recurrence) and hyperthyroidism treatments. This comprehensive report also considers how to proceed with pregnant patients (or potentially pregnant), under breast-feeding and even patient death, thus, how to manage radioactive bodies and how-to carry-on an autopsy, are topics also considered. On the other hand, the United States Nuclear Regulatory Commission (USNRC) (Howe et al., 2008), in the appendix U, considering biokinetics of the ^{131}I into the patient and try to personalize these recommendations, created a mathematical model for ^{131}I, that can be implemented in a nuclear medicine department.

In recurrent medullary thyroid carcinoma, radiolabelled somatostatin analogues could be used, even though they are less sensitive for diagnosis of distant metastases and progressive disease, even comparing ^{68}Ga-DOTATATE with ^{18}F-Fluorodeoxyglucose (FDG) outcomes (Baum R. P., 2014; Conry et al., 2010).

In the case of neuroendocrine tumours, ^{131}I-Meta Iodobenzylguanidine (MIBG) has been used for the treatment of neuroblastoma, pheochromocytoma, extra cranial paraganglioma and gastroenteric neuroendocrine tumours (Ersahin et al., 2011), as these tumours arise from the primitive neural crest that express the noradrenaline (NA) transporter. The use of this radiopharmaceutical has diminished due to emergence of radiolabelled peptides and non-radioactive targeted therapies, but in the case of inoperable tumours it is still an option (Baum R. P., 2014). In neuroblastoma, that is mostly a child disease, in most of stage I and II patients the best treatment is surgery alone. For stages III and IV the treatment using ^{131}I-MIBG can be considered and depending on the case, in stage III chemotherapy is used as neoadjuvant prior surgery (Ersahin et al., 2011). Patients eligible for this treatment have stable bone marrow reserve and renal function, respectively (Baum R. P., 2014). Patients treated are normally isolated; receiving the radiopharmaceutical product using an infusion pump for 1 to 2 h. Patients should avoid sunlight exposure and remain well hydrated. More than 50% of the given activity will be excreted within urine during the first 48 h (Ersahin et al., 2011).

1.1.3. Radioimmunotherapy for antibody-targeted tumours (e.g. non-Hodgkin lymphomas)

Lymphomas are among the most radiosensitive tumours. When they are well localized EBRT can be a curative method. However, in the case of non-Hodgkin lymphoma (NHL) the disease is normally disseminated throughout the body. One possible solution to treat the NHL is to use total body irradiation but the major drawback is bone marrow aplasia (Baum R. P., 2014). Then the use of radiolabelled monoclonal antibodies has been used as another line of treatment of this disease.

Antibodies are immunoglobulins that can be found in the serum of vertebrates, the IgG (immunoglobulin G) is the most common used in clinical practice. This large protein is composed of pairs of heavy and light polypeptide chains, showing a “Y”-shaped structure after they are assembled (Baum R. P., 2014). Illustration of antibodies being coupled to different types of drugs or radionuclides can be observed in figure 1.3.

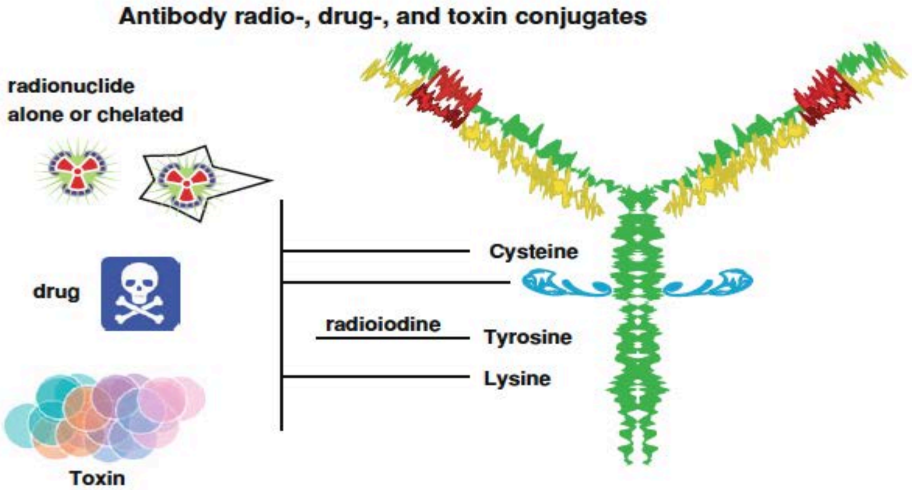

Figure 1.3: Illustration of antibody conjugates, in which radio- or drug- conjugates are chemically associated by linking them to lysine or by sulfhydryl-linkage chemistry. Image taken from (Baum R. P., 2014).

The antibody-radioconjugate, so called-radioimmunotherapeutic agent, combine the specificity of antibody affinity for cell-surface proteins with a cytotoxic effect. The advantage of antibody-radioconjugate agents over non-radionuclide antibody-drugs is the lack of internalization into cancer cells (Gill et al., 2017).

Two radiolabelled anti-CD20 murine monoclonal antibodies have been used to treat lymphomas, the ^{131}I-tositumomab (Bexxar) and ^{90}Y-ibritumomab tiuxetan (Zevalin) (Ersahin et al., 2011). Both differs from ^{131}I-rituximab, which has been used as a first-line treatment for patients with NHL in conjunction with rituximab (McQuillan et al., 2015). Bexxar was withdrawn from the market in 2014. On the other hand, Zevalin has been used in combination with chemotherapy in both indolent and aggressive NHL (Gill et al., 2017). Rizzieri (Rizzieri, 2016) discuss the continuing clinical research in NHL patients using Zevalin.

Gill et al. (Gill et al., 2017) mentioned that α-particles are starting to be used to treat leukaemia in combination with the humanized anti-CD33, using 213-Bismuth (^{213}Bi)- and 225-Actinium (^{225}Ac)-lintuzumab; however, clinical trials are still on-going (Finn et al., 2017; Jurcic et al., 2016; Rosenblat et al., 2010). On the other hand, β-particles (^{177}Lu and ^{90}Y) have been used with J591 to treat prostate cancer. In *part IX of* Baum's *book* (Baum R.P., 2014) there are several sections dedicated to the use of antibodies to treat different types of cancer.

1.1.4. Others

Refractory metastatic bone pain is caused by skeletal metastases from advanced cancers such as prostate, breast, lung, thyroid and kidney cancer. The first two types of cancers can be associated with more than 80% of bone metastases (Ersahin et al., 2011). Treatments using ^{89}Sr, ^{153}Sm and ^{186}Re have been addressed by the EANM which has proposed a specific guideline (Bodei, Lam, et al., 2008).

^{177}Lu-labelled prostate-specific membrane antigen (PSMA) has been used for metastatic castrate-resistant prostate cancer treatment (Baum R. P., 2014; Gill et al., 2017). Using α-emitters such as ^{213}Bi (Wild et al., 2011) and ^{225}Ac (Kratochwil et al., 2016) labelled to PSMA has also been proposed to be used with patients not responding to the therapy using ^{177}Lu. Also for the same type of disease ^{223}Ra (radium-223 dichloride) has been used (Hoskin et al., 2014; Nilsson, 2016) and got the EMA and FDA approval.

Selective internal radiation therapy (SIRT) groups special therapies that do not use radiopharmaceuticals but radioactive medical devices (like brachytherapy), placed near tumours (usually in the liver) by the physician, by intra-arterial administration. Two types of products can be found in the market made of resin (SIR-Spheres®, Sirtex Medical Europe, Bonn, Germany) and made of glass (TheraSphere®, MDS Nordion, Toronto, Canada) (Baum R. P., 2014), both products use ^{90}Y as radionuclide to treat the lesions and images can be generate using the bremsstrahlung emission using PET/CT systems (Giammarile et al., 2011; Carlier et al., 2013; Lhommel et al., 2010).

Microspheres of ^{166}Ho are also been studied (Seppenwoolde et al., 2005).

Dosimetry studies can be performed for radiopharmaceutical products, used either for diagnostic or therapeutic purposes.

2. Radiopharmaceutical dosimetry in diagnostic and therapy

The medical decision in order to treat a patient will depend on many aspects, such tumours and the organs at risk.

According to the article 56.1, of the Council Directive 2013/59/Euratom (The Council of the European Union, 2014), *"For all medical exposure of patients for radiotherapeutic purposes, exposures of target volumes shall be individually planned and their delivery appropriately verified taking into account that doses to non-target volumes and tissues shall be as low as reasonably achievable and consistent with the intended radiotherapeutic purpose of the exposure"*. In the article 56.6, the same document mentioned *"Member States shall ensure that in the case of a patient undergoing treatment or diagnosis with radionuclides, the practitioner or the undertaking, as specified by Member States, provides the patient or their representative with information on the risks of ionizing radiation and appropriate instructions with a view to restricting doses to persons in contact with the patient as far as reasonably achievable. For therapeutic procedures these shall be written instructions."* Moreover, in the definitions of Chapter 4 (81), the Directive explicitly mentions that "radiotherapeutic" means pertaining to radiotherapy, including nuclear medicine for therapeutic purposes.

From these articles, one can contend that patient-specific dosimetry is a right when a patient is benefiting from a therapeutic treatment involving ionising radiations. Therefore, all possible efforts should be done in order to implement dosimetry and provide accurate results.

In the case of fixed activity administration, dosimetry can be used to document the therapeutic procedure, in order to generate an objective index (efficacy or toxicity) to relate to the outcome. For example it may be necessary to give a therapeutic activity to a patient that afterwards will receive an external radiation therapy treatment as is described by Hobbs et al. (Hobbs et al., 2011). Therefore as suggested by the SNMMI (Silberstein et al., 2012) the dosimetry calculation are especially important to avoid potential damage to certain organs/tissues. Dosimetry will not impact the nuclear medicine therapeutic procedure itself (i.e. activity will not be modulated) but will participate to the planning of subsequent external beam radiotherapy.

Dosimetry may also help to modulate the therapeutic activity, which means that depending on the dosimetric results the physician will prescribe more or less activity. This participates to "personalized medicine", where every patient is given what he or she needs. This can be implemented depending on the needs, in two particular time-scenarios:

a) when the therapy consists in only *one* cycle of treatment (or for repeated cycles that are separated in time so that they can be considered as single treatment)

b) when cycles of treatment are repeated and close enough so that the results obtained on one cycle can be used to plan subsequent cycles.

For the first scenario, patient may follow a preparation process (indicated by the medical staff). Then, a tracer amount of activity will be administered to the patient to proceed with the dosimetry measurements. In the case of thyroid cancer cell, a saturation effect, called stunning is well known (Coakley, 1998; Lees et al., 2002; Sisson et al., 2006), then tracer activities as low as 30 MBq can be used to perform a pretherapeutic dosimetric study. In the case of benign thyroid diseases the EANM has proposed this method (Hänscheid et al., 2013) using a tracer activity about 2 MBq. The therapeutic activity will be therefore administrated after the dosimetric procedure. The second scenario will estimate absorbed doses to certain organ at risk for the first therapy cycle. Under the assumption that organs at risk will have same biokinetics among all treatment cycles, a dosimetric extrapolation can be done in order to calculate the activity that can safely be administered for subsequent cycles.

This administration scheme could be implemented for PRRT patients. However nowadays patients receive the same therapeutic administration (constant activity) for each cycle of treatment (7.4 GBq per cycle, four cycles of treatment maximum).

Yet, Beykan et al. (Beykan et al., 2018) shown that the adjustment of the therapeutic activity between cycles can be done for PRRT patients treated with Lutathera using high administrated activities. Sundlöv et al. demonstrated that, due to inter-patient variability, most patients may benefit of more cycles of treatment (under the fixed activity/cycle paradigm) because one of the main organs at risk (the kidneys) was not reaching the maximum tolerable absorbed dose after four cycles. For most patients, the absorbed dose to the kidneys was more or less the same for each cycle of treatment. Conversely, for some other patients, due to intra-patient variability, the absorbed dose for each cycle of treatment was very different. While variable, these results all conclude to the relevance of patient-specific dosimetry in a context of therapeutic optimisation (Sundlöv et al., 2017).

Clinical dosimetry is an evolving area in which different patient pathologies are addressed and the treatment is optimized during the time due to new equipment, new radiopharmaceuticals, more professional staff, software availability (to acquire, to reconstruct, to correct images), new regulations, etc.

Probably these are the reasons to find in the literature several acquisition protocols, from whole-body planar images (Cremonesi et al., 2006; Mirzaei et al., 2013; Schuchardt et al., 2013; Svensson et al., 2016) to SPECT/CT images (Beauregard et al., 2011; Hänscheid et al., 2018; Ilan et al., 2015; Sanders et al., 2015) and passing by a combination of them, called the hybrid method (using one or two SPECT/CT) (Bailey et al., 2015; Brolin et al., 2015; Garkavij et al., 2010; Guerriero et al., 2013; Sandström et al., 2010).

In fact, implementing clinical dosimetry in practice is quite a demanding task. This is why different dosimetric approaches have been proposed, using mostly academic software as research tools, even though commercial software is becoming increasingly available.

The most famous radiopharmaceutical calculation scheme was proposed by the MIRD committee.

3. MIRD schema for absorbed dose determination

This committee is part of the Society of Nuclear Medicine & Molecular Imaging (SNMMI). It develops standard methods, models, assumptions, and mathematical schemas for assessing internal dosimetry from administrated radiopharmaceuticals.

By checking their web site, one can verify that The Medical Internal Radiation Dose (MIRD) Committee started its publications in 1968 with the MIRD Pamphlet No. 1: *Schema for absorbed-dose calculation for biologically distributed radionuclides*. This first document was revised in 1975 and further publications in 1988 and 1991 containing examples. In 2009, the MIRD Pamphlet No. 21 (Bolch et al., 2009) proposed a new nomenclature, intended to conciliate MIRD and ICRP terminology. Even though the initial objective of the MIRD committee was to propose means to compute absorbed doses, several publications are intended to address the complexity of nuclear medicine imaging quantification. In 1999 the MIRD Pamphlet No. 16 (Siegel et al., 1999) showed how to proceed with quantification using planar images. In the same year the MIRD No. 17 (Bolch et al., 1999) showed how to perform dosimetric calculation for non-uniform activity distributions at voxel level. In 2012 the MIRD Pamphlet No. 23 (Dewaraja et al., 2012) addressed the quantification of SPECT images aiming for patient-specific 3D-dosimetry. In 2016 the MIRD Pamphlet No. 26 (Ljungberg et al., 2016) was a joint document between the EANM and MIRD Committee and addressed SPECT quantification for ^{177}Lu.

3.1. Absorbed dose definition

Taking into consideration information from *MIRD Pamphlet 21*, the absorbed dose rate (J kg^{-1} s^{-1}) for a target tissue r_T can be expressed as in equation 1.1

$$\dot{D}(r_T, t) = \sum_{r_S} A(r_S, t)\, S(r_T \leftarrow r_S, t) \tag{1.1}$$

Where $A(r_S, t)$ is the time-dependent activity of the radiopharmaceutical product in the source tissue r_S, and $S(r_T \leftarrow r_S, t)$ in known as the S-value which is a quantity representing the mean absorbed dose rate to a target tissue r_T at time t after administration per unit activity present in source tissue r_S. The S-values are estimated using computational models considering age, sex, organs mass (and composition), total-body mass and height (Menzel et al., 2009).

The mean absorbed dose for target tissue r_T can be estimated by integration of equation 1.1 over a period of time T_D (which normaly is defined as infinity), as is expressed in equation 1.2

$$D(r_T, T_D) = \int_0^{T_D} \dot{D}(r_T, t)\, dt = \sum_{r_S} \int_0^{T_D} A(r_S, t)\, S(r_T \leftarrow r_S, t)\, dt \tag{1.2}$$

Two additional quantities are used for radiation protection purposes in diagnostic procedures in nuclear medicine. These are the equivalent dose, H_T, and the effective dose, E. These parameters are mandatory when a new diagnostic radiopharmaceutical is incorporated in the market. It is therefore required to determine reference dosimetric values for each new diagnostic radiopharmaceutical. These dosimetric quantities are intended to give account of the detriment induced by stochastic effects of radiations only. Therefore, they cannot be used in the context of therapeutic nuclear medicine procedures where deterministic effects are preponderant.

According to *MIRD Pamphlet 21*, the equivalent dose, in units of sievert (Sv = J*kg^{-1}), can be defined as in equation 1.3:

$$\mathrm{H}_T(r_T, T_D) = \sum_R w_R D_R(r_T, T_D) \quad 1.3$$

Where w_R is the radiation-weighting factor for radiation type R, and $D_R(r_T, T_D)$ is the contribution of radiation type R to the mean absorbed dose in target tissue r_T. Table 1.2 provides radiation-weighting factors according to ICRP-103 recommendations.

Table 1.2. Radiation-weighting factors from ICRP-103 (ICRP, 2007).

Radiation type	W_R
Photons, electrons and muons	1
Protons and charged pions	2
Alpha particules, fission fragments, heavy ions	20
Neutrons	A continuous curve as a function of neutron energy

The effective dose, also in units of sievert, considers the tissue-weighting factor, w_T, for a target tissue r_T. Moreover, the condition $\sum_T w_T = 1$ has to be fulfilled. According to ICRP 103, this quantity can be defined as in equation 1.4:

$$\mathrm{E} = \sum_T w_T \left[\frac{H(r_T, T_D)^{male} + H(r_T, T_D)^{female}}{2}\right] \quad 1.4$$

The previous equation gives the effective dose to a reference person. Table 1.3 shows tissue weighting factor according ICRP-103.

Table 1.3. Tissue weighting factors (w_T) from ICRP-103 (ICRP, 2007).

Tissue	w_T	$\sum_T w_T$
Red bone-marrow, colon, lung, stomach, breast, remainder tissues£	0.12	0.72
Gonads	0.08	0.08
Bladder, oesophagus, liver, thyroid	0.04	0.16
Bone surface, brain, salivary glands, skin	0.01	0.04

£Remainder tissues (14 in total): adrenals, extra-thoracic region, gall bladder, heart, kidneys, lymphatic nodes, muscle, oral mucosa, pancreas, prostate, small intestine, thymus, uterus/cervix.

Figure 1.4 shows a schematic representation of the effective dose determination for a reference person.

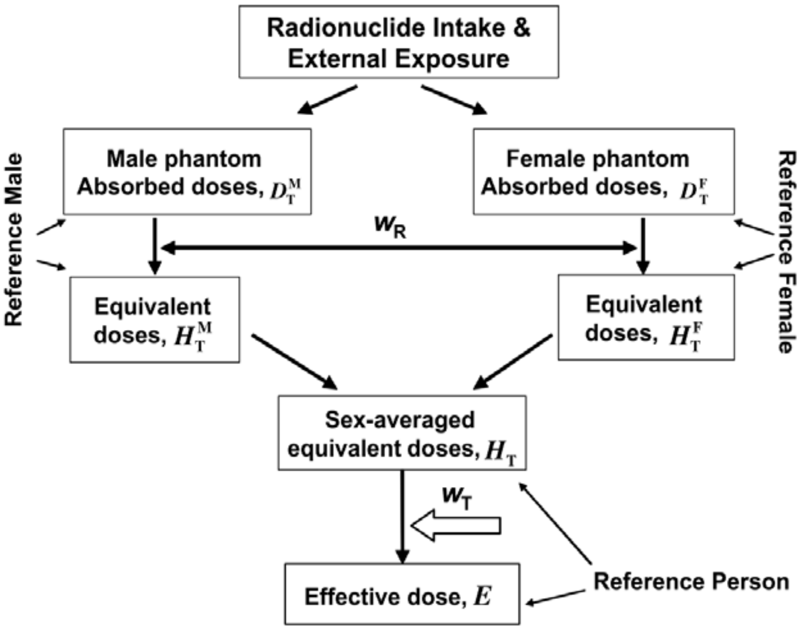

Figure 1.4: Estimation of effective dose by sex averaging. Image taken from (Menzel et al., 2009).

3.2. Biokinetics assessment

3.2.1. Time-integrated activity and residence time

The bio-kinetics of a radiopharmaceutical can be described knowing the relationship of the activity (or number of counts) per time point. By plotting this relationship among all pairs (time, activity) a time activity curve (TAC) can be generated. Figure 1.5 shows a theoretical representation of a TAC. Estimating the area under the TAC will produce the time-integrated activity (TIA), which was also known as cumulated activity, in units (Bq.s). *Essentially this is a measure of the total number of disintegrations occurring in an organ source containing the radiopharmaceutical* (Cherry et al., 2012).

Looking at first coefficient of equation 1.1, the TIA can be expressed as follows:

$$\tilde{A}(r_s, T_D) = \int_0^{T_D} A(r_s, t)\, dt \tag{1.5}$$

Where T_D is defined as the dose-integration period.

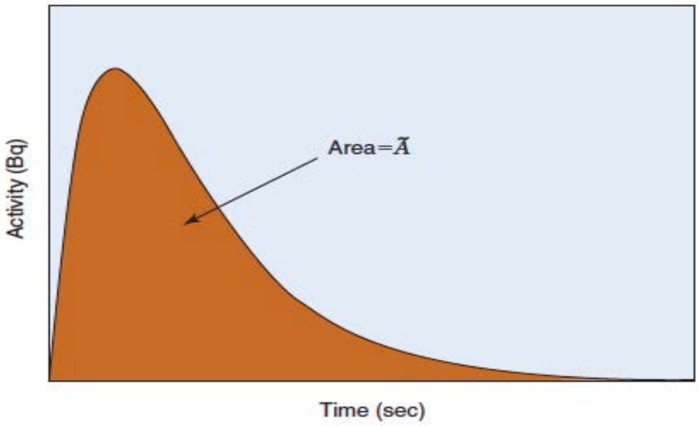

Figure 1.5: hypothetical description of time-activity curve for radioactivity in a source organ, also showing that the area under the curve is the time-integrated activity. Image taken from (Cherry et al., 2012).

Normally, the TAC can be mathematically described as the sum of exponential functions, as it is shown in equation 1.6:

$$\tilde{A}(r_s, T_D) = \sum_{i=1}^{n} A_i e^{-\lambda_i t} \tag{1.6}$$

As equation 1.5 shown, TIA will be generated as the integration of equation 1.6, in a general scenario

$$\tilde{A}(r_s, T_D) = \sum_{i=1}^{n} \frac{A_i}{\lambda_i} \tag{1.7}$$

Some organs sources will express a mono-exponential behaviour; other may express bi- or tri-exponential behaviour.

For mono-exponential behaviour, $\tilde{A}(r_s, T_D) = \frac{A_1}{\lambda_1}$ 1.8

For bi-exponential behaviour, $\tilde{A}(r_s, T_D) = \frac{A_1}{\lambda_1} + \frac{A_2}{\lambda_2}$ 1.9

The A_i term is associated with the initial injected to a patient, and λ_i is known as the decay constant, which considers the biological and physical decay of the product in the organ source. Hence, the effective decay constant λ_{eff} can be expressed as:

$$\lambda_{eff} = \frac{ln(2)}{T_{\frac{1}{2}eff}} = ln(2) * \left(\frac{1}{T_{\frac{1}{2}biol} + T_{\frac{1}{2}phys}}\right) \qquad 1.10$$

The term $T_{\frac{1}{2}eff}$ is the effective half-life and $T_{\frac{1}{2}biol}$, $T_{\frac{1}{2}phys}$ are the biological and physical half-lives, respectively.

The time-integrated activity coefficient (TIAC) $\tilde{a}(r_s, T_D)$, given in units of time (i.e. seconds) can be obtained dividing equation 1.5 by the administrated activity A_o (IAEA, 2014). These coefficients were named as residence times, τ, in MIRD Primer (Loevinger et al., 1991).

3.3. S-Values

The S-value is associated to the radionuclide and the model used, which means that they take into account the geometry and composition of both the source and the target. Therefore, this quantity can be expressed as in equation 1.11

$$\begin{aligned} S(r_T \leftarrow r_s, t) &= \frac{1}{M(r_T, t)} \sum_i E_i Y_i \phi(r_T \leftarrow r_s, E_i, t) \\ &= \frac{1}{M(r_T, t)} \sum_i \Delta_i \phi(r_T \leftarrow r_s, E_i, t) \end{aligned} \qquad 1.11$$

Where E_i is the mean energy of the ith nuclear transition, Y_i is the number of ith nuclear transition per nuclear transformation. $\phi(r_T \leftarrow r_s, E_i, t)$ is the absorbed fraction, which is the fraction of radiation energy emitted E_i within the source tissue r_s that is absorbed in the target tissue r_T , at the time t.

From equation 1.11 it is important to highlight that the term associated to the organ mass is dependent on time. This is a concept that normally is not considered for the TIAC estimations, because normally organ mass is seen as a constant value among all time point measurements, however, this quantity may change due to organ movements, patient respiration movement and patient movement.

On the other hand, in the same equation, the absorbed fraction is a quantity depending on energy and organ mass. This is especially important at small scale (cell or small animal dosimetry).

From the absorbed fraction, the specific absorbed fraction can be defined in equation 1.12 as follows:

$$\Phi(r_T \leftarrow r_s, t) = \frac{\phi(r_T \leftarrow r_s, E_i, t)}{M(r_T, t)} \qquad 1.12$$

The first step in direction of patient-specific dosimetry is the accurate determination of patient-specific pharmacokinetics. Then, assuming that part is dealt correctly, the absorbed dose calculation itself is not trivial. There are two possibilities to address that aspect for clinical dosimetry purposes.

4. Types of dosimetry

4.1. Reference dosimetry (Model-based dosimetry)

This type of dosimetry is implemented for new radiopharmaceutical during the course of their development. Reference dosimetry is meant to document the irradiation delivered by standard diagnostic procedures. Reference models are used to allow the comparison between different diagnostic radiopharmaceuticals. Keeping the dosimetric model constant allows for a fair comparison of the dosimetric properties of different radiopharmaceuticals. In that context, and for the production of reference dosimetric data such as presented in ICRP-128 reports (ICRP, 2015), averaged pharmacokinetics obtained on groups of healthy volunteers, patients or even sometime extrapolated from animals are entered in reference dosimetric models to provide an order of magnitude of the (low) irradiation delivered during diagnostic procedures.

Reference dosimetry is opposed to patient-specific dosimetry.

4.1.1. Computational reference models for organ/structures-based dosimetry

The *MIRD Pamphlet 21* was proposed for the standardization of the nomenclature used in dosimetric calculations was considered between MIRD and ICRP.

The historical development of both institutions was trying to address most of the time the same problems from different point of views. In the case of ICRP, since 1928 their goal was to create publications and recommendations that nowadays became the basis of world´s regulatory codes and regulations on radiological safety. As a summary, from the nuclear medicine point of view, the ICRP has been generating recommendations.

The first recommendation is related to digital models and dosimetric models of biological systems in order to have a human representation (from babies to adults). The latest ICRP publication regarding digital model dosimetric results is the ICRP-133 (ICRP, 2016). *This document replaces publications 30 and 68 (ICRP, 1979, 1980, 1981, 1988, 1994b). This publication provides the technical basis for SAFs relevant to internalized radionuclide activity in the organs of Reference Adult Male and Reference Adult Female as defined in Publications 89 and 110 (ICRP, 2002, 2009). SAFs are given for uniform distributions of mono-energetic photons, electrons, alpha particles, and fission-spectrum neutrons over a range of relevant energies. Electron SAFs include both collision and radioactive components of energy deposition*.

In terms of dosimetric models of biological systems, this document considers the bone and bone marrow, gastrointestinal tract, respiratory system, skeletal model and the alimentary tract model. McParland (McParland, 2010) shows an overview of several of these biological systems. For instance, the respiratory system according to ICRP (30 and 66) and MIRD Report 18, gastrointestinal tract according to ICRP (30 and 100), the kidney according to *MIRD Pamphlet 19*, urinary bladder considering a dynamic urinary model, head and brain according to *MIRD Pamphlet 15*, cardiac wall and contents according to *MIRD Pamphlet 13*, bone and red bone marrow, peritoneal cavity, tumours, prostate and rectum.

Second recommendation, the ICRP-128 (ICRP, 2015), *provides a compendium of current information relating to irradiation of patients, including biokinetic models, biokinetic data, dose coefficients for organ and tissue absorbed doses, and effective dose for major radiopharmaceuticals based on the radiation protection guidance given in Publication 60 (ICRP, 1991). These data were mainly compiled from Publications 53, 80, and 106 (ICRP, 1987, 1998, 2008), and related amendments and corrections. This report also includes new information for* ^{82}*Rb-chloride, iodide (*^{123}*I,* ^{124}*I,* ^{125}*I, and* ^{131}*I) and* ^{123}*I labelled 2-carbomethoxy 3-(4-iodophenyl)-N-(3-fluoropropyl) nortropane (FPCIT).*

Third recommendation, to define quantities that are going to be associated to stochastic effects, and could be used for diagnostic purposes and never be applied in a therapeutic context. In the ICRP-103 (2007), several recommendations were updated such as the radiation and tissue weighting factors, in the quantities equivalent and effective dose and update the radiation detriment. Also, some recommendations were maintained for instance, the current individual dose limits for effective dose and equivalent dose from all regulated sources in planned exposure situations.

Finally, the ICRP also referenced nuclear decay data (available in ICRP-107 (2008)).

Regarding the MIRD committee, several publications are available, the MIRD Pamphlet´s *provide the scientific overview of a particular nuclear medicine application whereas the MIRD dose estimate, provides dosimetric data specific for a given radiopharmaceutical* (McParland, 2010).

4.1.2. Anthropomorphic models

The use of digital models that can represent the human body or organs has been subject of development for several decades by different research groups. These representations are created because it is not practical perform direct measurements of radiation inside the human body using detectors.

The reference man concept was introduced by the ICRP-23 (ICRP, 1975), representing in detail the anatomy, composition and physiology of a “Caucasian male” between 20 and 30 years old, with 70kg body mass and 1.7 m. Nowadays, the reference man and woman are available in the ICRP-110 with 73 kg body mass and 1.76 m height. For the woman 60 kg body mass and 1.63 m height. The reference man and woman were created using digital models, also named computational anthropomorphic models.

Using Monte Carlo simulations, or other calculation means and digital models, the S-value (previously defined) can be calculated for a specific isotope, source-target relation and digital model. One example in nuclear medicine is to estimate the absorbed dose from one organ “source” to other organs “targets”. By grouping the S-values, databases can be created to easy estimate the mean absorbed dose from the TIAC. There are software available in the market that include these data bases, for instance OLINDA/EXM (Stabin et al., 2005) and IDAC (Andersson et al., 2017).

Digital models can be grouped in three: the stylized, the tomographic or voxelized and hybrid (for instance BREP models); the last combines features from the stylized and voxelized models. This division is based on their topological characteristics and mathematical approach to represent a structure.

4.1.2.1. Stylized (mathematical) models

These phantoms represent the morphology of the organ by using simple geometrical structures also called primitives, for example; cuboids, prims, pyramids, cones, cylinders, ellipsoids and spheres (McParland, 2010). Advance primitives can be B-splines lines or non-uniform rational B-splines (NURBS) or polygon mesh (Xu & Eckerman, 2009). To create these geometrical structures a solid-geometry modelling method called constructive solid geometry (CSG) is used. With CSG a solid object can be created using Boolean operators combining the primitives, which are easily described by quadric equations (Xu & Eckerman, 2009). As an example, a lung in which one section has been removed can be defined using a Boolean operation by subtracting one ellipsoid from the other. The quadric equations that may represent this example are presented in equation 1.13.

$$\begin{aligned} &Ellipsoid\ A\colon \left(\frac{x-8.5}{5}\right)^2+\left(\frac{y}{7.5}\right)^2+\left(\frac{z-43.5}{24}\right)^2 \le 1, z \ge 43.5 \\ &Ellipsoid\ B\colon \left(\frac{x-2.5}{5}\right)^2+\left(\frac{y}{7.5}\right)^2+\left(\frac{z-43.5}{24}\right)^2 \ge 1, if\ y < 0 \end{aligned} \qquad 1.13$$

An illustration of the previous operation can be seen in figure 1.6A, where the lung is presented before and after the Boolean operation. These types of surface equations are accepted by Monte Carlo Codes. However, looking at these images, they are not very realistic in terms of geometry. These types of phantoms are also called “mathematical” phantoms. The same lung can be represented using the CSG modelling technique as an assembly of 3D cuboids, as it can be seen in figure 1.6B. Looking at this image, the boundary of the lung in a voxel phantom is defined by uneven steps instead of smooth surface, therefore the anatomical fidelity depends on the voxel size and this can be an issue for small organ/tissues such as eye lens and bone marrow (Xu & Eckerman, 2009).

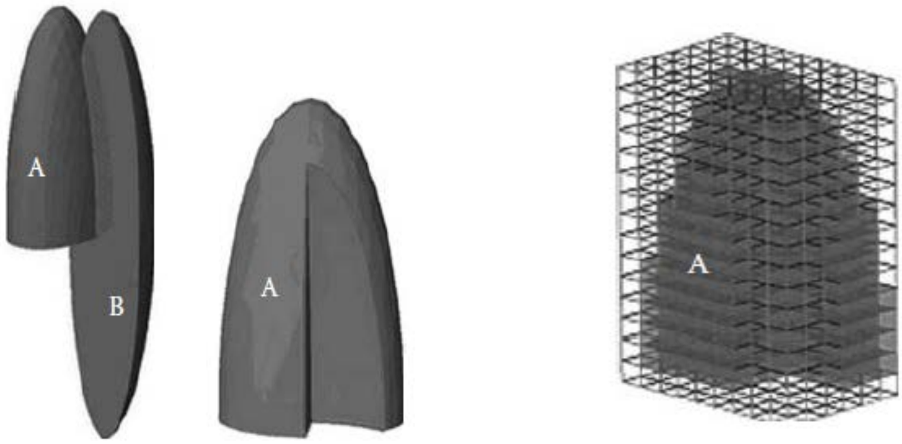

Figure 1.6: A) A stylized lung model using the CSG-type method before and after Boolean operation is performed. B) A CSG-type method including rigid voxels with an anatomical detail dependent on the voxel size. Images from (Xu & Eckerman, 2009).

The first digital models were created by *Fisher–Snyder* (Fisher & Snyder, 1966) in the 1960s. They were designed using CSG modelling techniques using elliptical cylinders and cones. In 1969, Snyder et al. created the first heterogeneous model, this model was composed of a skeleton, a pair of lungs; and the remainder (soft tissue) (Snyder et al., 1969). The representation of the organs was crude, as the simple equations captured only the most general description of the position and geometry of each organ (Xu & Eckerman, 2009). In 1978, Snyder et al. published an improved version of the heterogeneous model, including spheres; ellipsoids; cones, tori, and subsections of such objects (Snyder et al., 1978). It was described in three sections; an elliptical cylinder, containing arms, torso and hips, then, a truncated elliptical cone representing the legs and feet, and finally, an elliptical cylinder to represent the head and neck (Zaidi & Xu, 2007). In figure 1.7 representation of the Snyder et al. digital model can be seen (Snyder et al., 1978).

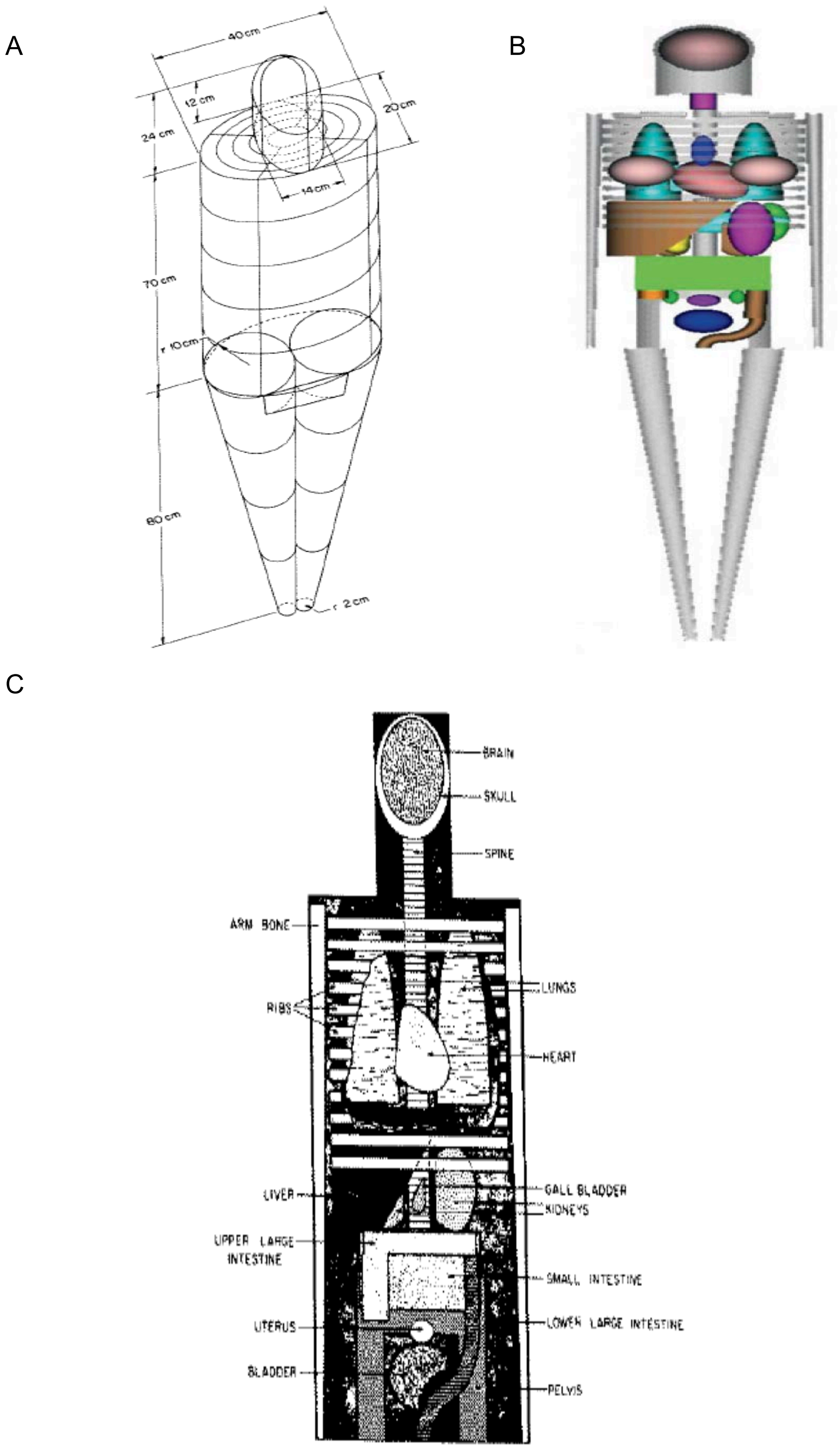

Figure 1.7: Stylized models. A) Exterior view of the adult male. B) Skeleton and internal organs. C) Anterior view of the principal organs. Image A and C from (Snyder et al., 1978). Image C) from (Zaidi & Xu, 2007)

4.1.2.2. Voxel (digital) models

Anatomical realistic representation of the human body was possible until tomographic images and computer capacity became available in the 80's. CT and MRI allow visualizing the internal structures of the body in three dimensions. Due to powerful computers, both types of images could be stored in versatile digital formats. These characteristics helped to create the so-called voxel- or tomographic phantoms. In terms of solid-geometry modelling techniques, a voxel is a basic CSG primitive.

The creation of these models where very challenging for several reasons: images from the whole-body were necessary from live subjects or cadavers, then, the identification of organs and tissues had to be made, which is really important for dosimetric calculations. The amount of data was potentially too big for a computer's memory to handle and finally, having created the model, radiation transport had to be done for various types of radiation, however at the time computing capabilities were limited (Zaidi & Xu, 2007).

On the other hand, tomographic models are fundamentally different from the stylized ones, because the 3D tomographic representation is the displaying of multiple two-dimensional pixel maps. This type of models contains a huge amount of voxels grouped to represent different tissues or organs (Xu & Eckerman, 2009). One limiting factor using this type of models is the size of the voxel, as was shown in figure 1.6B. Depending on the tissue or structure the voxel size is important; for instance, in the case of defining the bladder walls, or the inner parts of the kidneys, voxels have to be sufficiently small to give account of the geometry (Marcatili et al., 2014), otherwise a hybrid calculation scheme must be implemented. In order to gain the battle to the limited spatial sampling, the Visible Human Project (VHP) (Spitzer & Whitlock, 1998) produced anatomically similar CT, MRI and cross-sectional colour photographs, creating voxel sizes of 0.33x0.33x1 mm^3 for the male and 0.33x0.33x0.33 mm^3 for the female.

One of the first groups developing these models, in the early 80's, was at the GSF (*German National Research Centre for Environment and Health, Gesellschaft für Strahlenforschung*) creating a model series with a range of anatomical characteristic (Becker et al., 2007; Fill et al., 2004; Petoussi-Henss et al., 2001; Williams et al., 1986; Zankl et al., 1988; Zankl et al., 2005; Zankl et al., 2002) trying to cover the majority of man and woman anatomies. Figure 1.8 shows one set of women models created by this group.

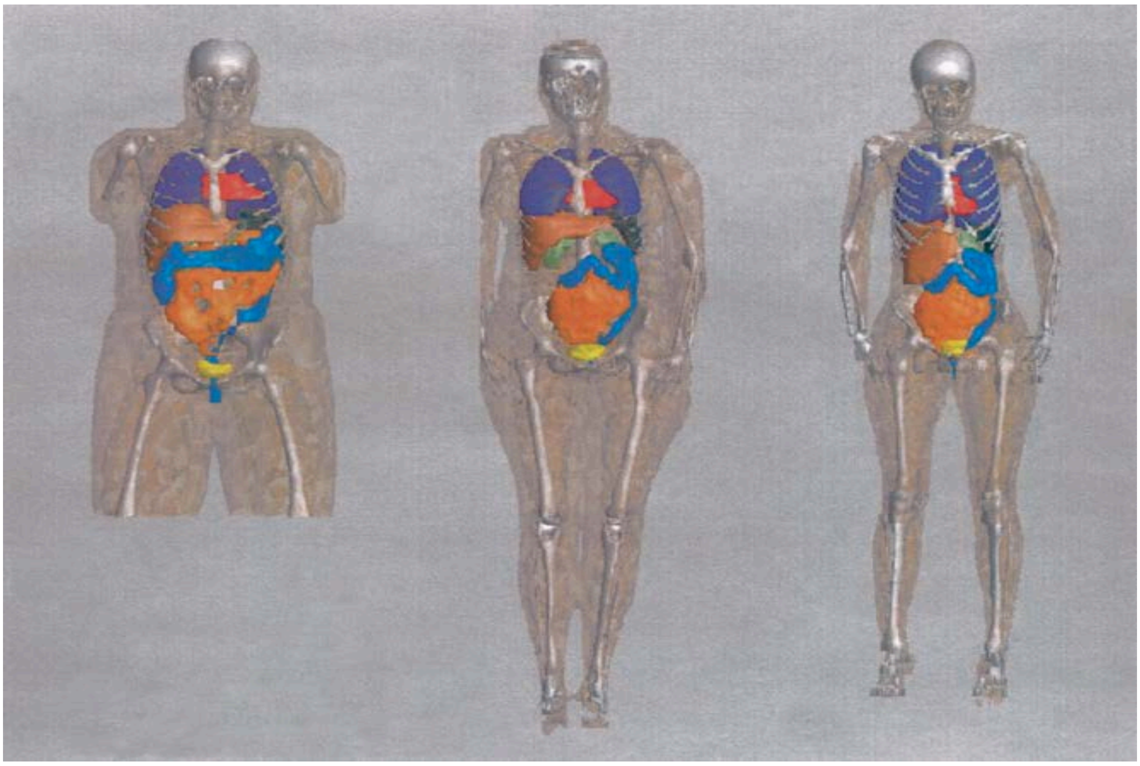

Figure 1.8: Images from Helga, Donna and Irene, from (Fill et al., 2004).

Efforts in this way were developed by Zubal et al. creating the VoxelMan (Zubal et al., 1994). Moreover, *Kramer et al.* developed the models called, Male Adult voXel (MAX) (Kramer et al., 2003) and the Female Adult voXel (FAX) (Kramer et al., 2004) which were adjusted according to the ICRP-89 body heights and organ masses and trying to be compatible with the ICRP-89 voxel models. Finally, the ICRP modified the voxel models (Golem and Laura) to create their own voxel models in the ICRP-110 and these are consistent with reference anatomical physiological parameters defined in the ICRP-89. In table 1.4 some characteristics of the adult male and female reference computational phantoms can be seen. In figures 1.9 and 1.10 illustrations from ICRP computational adult models can be seen.

Table 1.4. Main characteristic of the adult male and female reference computational models from ICRP-110 (ICRP, 2008).

Characteristics	Male	Female
Height (m)	1.76	1.63
Mass (kg)	73.0	60.0
Number of tissue voxels	1,946,375	3,866,020
Slice thickness (voxel height, mm)	8.0	4.84
Voxel in-plane resolution (mm)	2.137	1.775
Voxel volume (mm3)	36.54	15.25
Number of columns	254	299
Number of rows	127	137
Number of slices	220(+2)*	346(+2)*

***Additional slices of skin at the top and bottom**

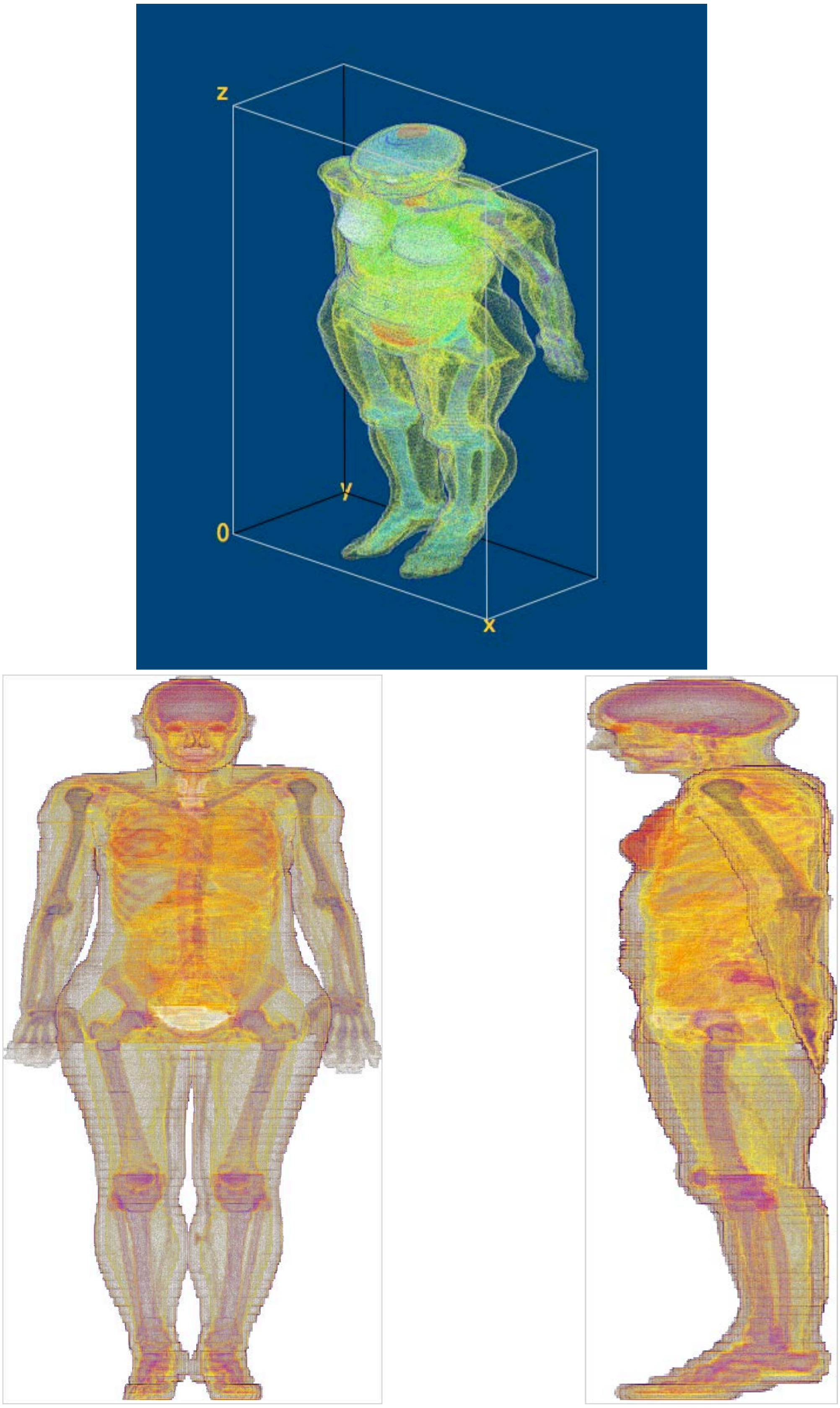

Figure 1.9: Different views of the adult female (AF) model from ICRP-110 (ICRP, 2008). Images created at CRCT using ImageJ.

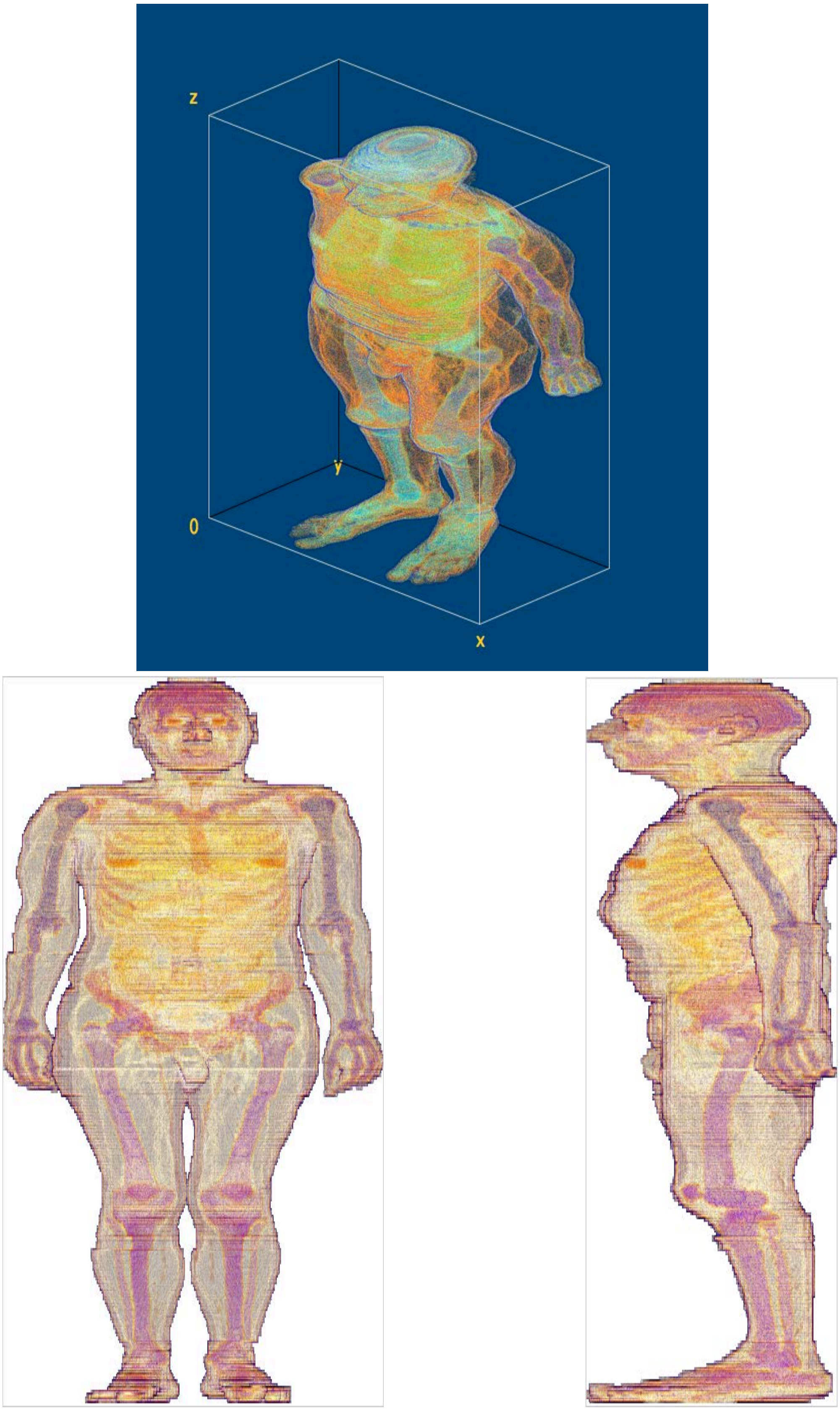

Figure 1.10: Different views of the adult male (AM) model from ICRP-110 (ICRP, 2008). Images created at CRCT using ImageJ.

4.1.2.3. BREP (hybrid) models

The boundary representation (BREP) is other general method of solid-geometry modelling, including two types of information: the topological and the geometric. Topological information provides relationships among vertices, edges, faces and also its orientations. With NURBS very smoothed surfaces can be generated; then exterior part of an object can be created. For example, the faces can be represented as polygons defined using coordinates values. BREP is much flexible because a richer set of operations tools are available (e.g. extrusion, chamfering, blending, drafting, shelling, and tweaking) (Xu & Eckerman, 2009). Also, BREP is ideal for surface deformation, which might be necessary for organ size adjustment and for organ motion correction, then comparing to voxel-based models, BREP allow the construction of models close to the real patient anatomy. One of the first implementation of BREP-based models was the Cardiac-Torso (NCAT) model, create by Segars et al. (Segars et al., 2001; Segars & Tsui, 2002) using NURBS using information from the Visible Human Project taking into account CT image data sets. The NCAT was created to replace the stylized mathematical cardiac torso model (MCAT) developed by Snyder et al. taking information from the MIRD-5 (Snyder et al., 1969). Organ shapes in the NCAT model are more realistic than those from the MCAT model, also the NCAT is more flexible because it considers the cardiac and the respiratory motion (Lee et al., 2007).

Other example from BREP-models is the series of model representing a pregnant woman and her foetus at different stages of gestations, this work was developed by Xu et al. at the Rensselaer Polytechnic Institute (RPI) in the United States (Xu et al., 2007). In this work pregnant women were defined by polygonal meshes from three sets of data: a nonpregnant female, a 7-month pregnant woman, and a mesh model of the foetus. The organs were adjusted in mesh format. Figure 1.11 shows the finalized models that were created by this group and were exported to the Monte Carlo code MCNPX.

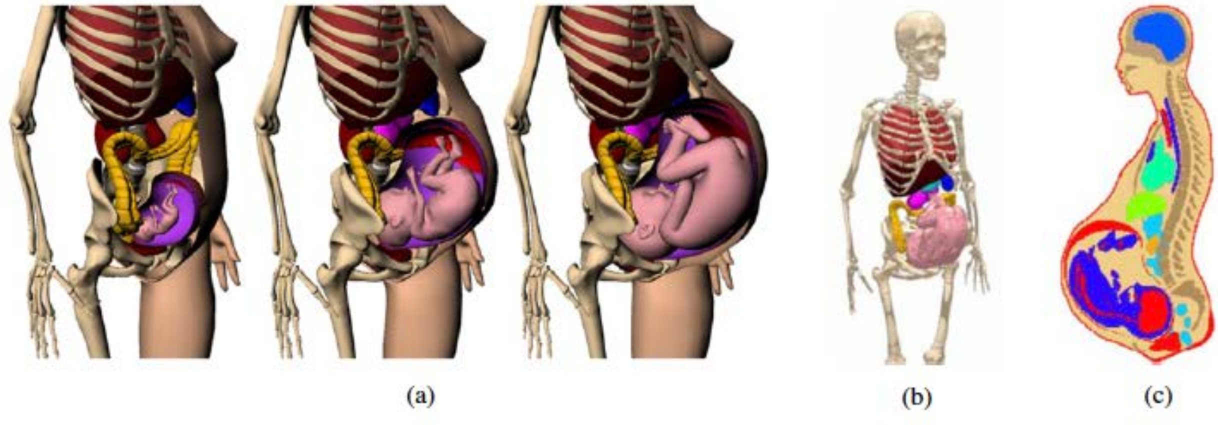

Figure 1.11: Finalized RPI-P models. (a) rendering of 3D models of pregnant female RPI-P3, -P6 and –P9. (b) rendering of the voxelized RPI-P9 model before translated into the MCNPX, (c) a direct MNCPX geometry plot showing a cross-section view of the 3 mm voxel model of the RPI-P9 implemented for MC radiation transport calculations. Images from (Xu et al., 2007).

As it was shown in figure 1.11, these models were voxelized to be implemented in Monte Carlo simulation codes. Therefore, in order to voxelize the NURBS smooth models, the surfaces have to be transferred back to polygonal meshes (see figure 1.12).

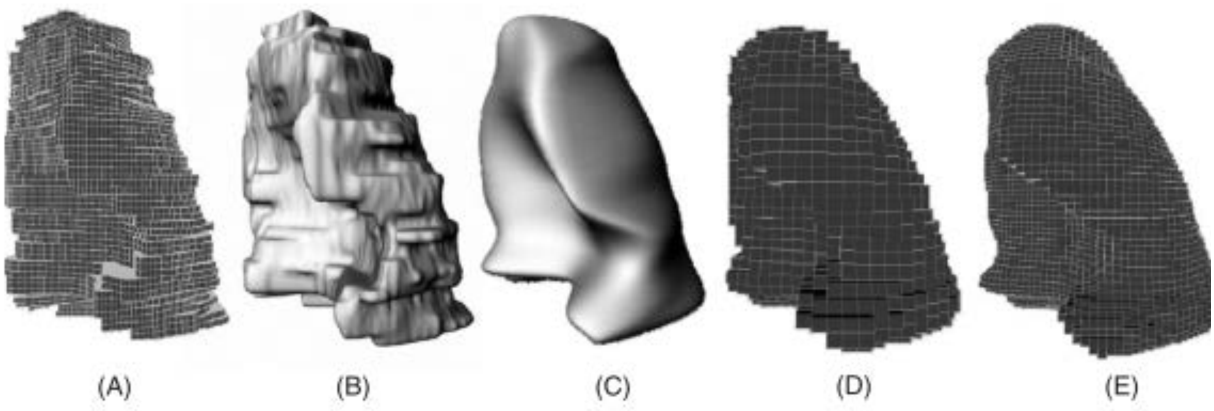

Figure 1.12: Example of voxelization process starting with (A) the original voxel model of the left lung, (B) its polygon mesh model, (C) its NURBS surface model and (D) and (E) voxelized models of the left lung at two different isotropic voxel resolutions (2 mm and 1 mm, respectively). Image from (Lee et al., 2007).

Moreover, using a triangular mesh approach a pair of adult male and female models were created, called RPI adult male and female (Hegenbart et al., 2008; Xu et al., 2008), which were carefully adjusted to match the ICRP-89 reference values for more than 70 organs, 45 bones and muscles.

For dosimetric purposes, small animal models have also been developed.

4.1.3. Small animal models

Nowadays the increasing number of radiopharmaceuticals in the market has developed technological platforms to acquire animal images of different sizes. For example, looking at Mediso Medical Imaging Systems website (http://www.mediso.com), the image modalities available, for pre-clinical studies, are hybrid including SPECT/CT/PET, SPECT/CT, PET/CT, SPECT/MRI, PET/MRI. Then, animal dosimetry may have two different global objectives, one is related to the absorbed dose estimations to animal tissues and, second the extrapolation of bio-kinetics results to humans. In case of the first objective, using images can be very challenging, due to logistics, setting the equipment, animal conditions, etc.

In order to help with the dosimetric estimations animal models can be an option. As was presented for anthropomorphic models, the development started with stylized models, then, passing to voxelized models and, finally, today hybrid (NURBS) models such as ROBY and MOBY are available. Figure 1.13 shows real size images from these two models.

The development of small animal models started years later comparing with the anthropomorphic models. One of the first studies was from Hui (Hui et al., 1994) which developed a stylized model, based-on athymic nude mice for radioimmunotherapy calculating organ self-doses for ^{90}Y. This was the first murine phantom used exclusively for internal absorbed dose using antibodies labelled with this isotope. Most of the organs were modelled such as ellipsoids, the skeleton was modelled by the femur, the bone and marrow were represented by concentric cylinders and a spherical tumour was also included (McParland, 2010).

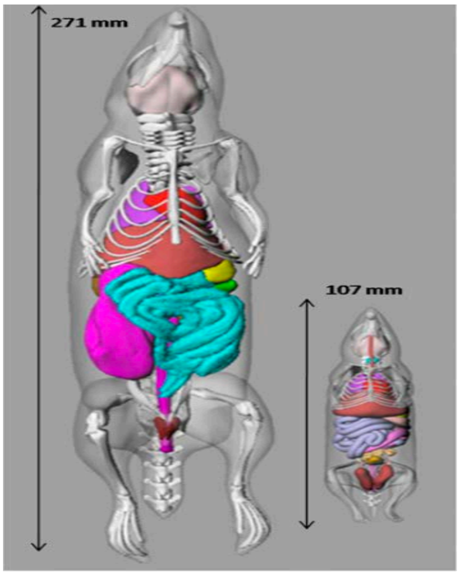

Figure 1.13: Unmodified images from ROBY and MOBY, showing their real size. (Keenan et al., 2010; Segars & Tsui, 2007)

Muthuswamy et al. complemented the model developed by Hui et al. developing a model of marrow applied for ^{131}I, ^{186}Re and ^{90}Y (Muthuswamy et al., 1998). Some other authors have created more stylized models, for instance, mouse models were created by Flynn et al. (Flynn et al., 2001), Hindorf et al. (Hindorf et al., 2004) and a model of Wistar rat was created by Konijnenberg et al. (Konijnenberg et al., 2004). In the case of Hindorf et al. (Hindorf et al., 2004) they treated the model in a voxel format. In figure 1.14 images from Konijnenberg et al. and Hindorf et al. models can be seen.

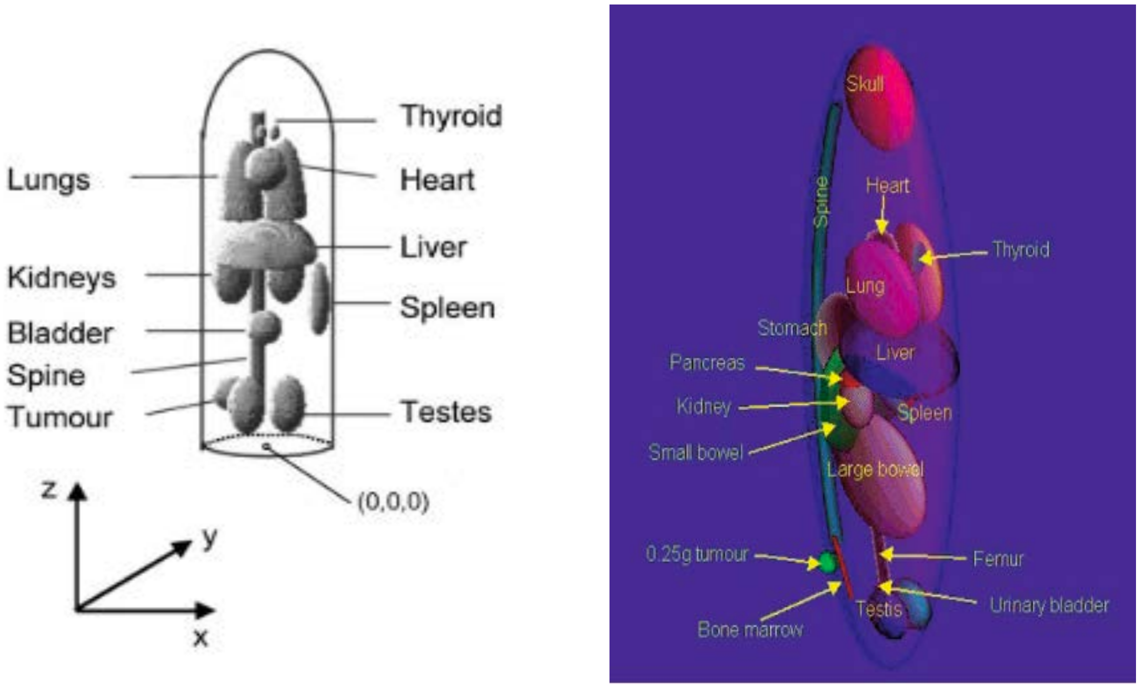

Figure 1.14: Stylized models examples of two different rodents: A) Hindorf et al. (Hindorf et al., 2004), B) Konijnenberg et al. (Konijnenberg et al., 2004).

Other voxelized models have been created using high-spatial resolution MRI and CT studies (Bitar et al., 2007; Dogdas et al., 2007). For example, Kolbert et al. used MRI of a female athymic mouse representing realistic models of the kidneys, spleen and liver (Kolbert et al., 2003). Stabin et al. used micro-CT images of a mouse and rat to estimated SAFs for photon and electron sources (Stabin et al., 2006).

In the case of hybrid models, Segars et al. implement NURBS using MRM create a murine model including respiratory and cardiac motion (Segars et al., 2004). From this initial work, Segars et al. manage to develop more the models as they are presented in figure 1.13 (Segars & Tsui, 2007).

4.2. Adjusted model-based dosimetry

Since not every centre has the possibility to compute the absorbed dose specifically for a given patient morphology, a workaround consists in adjusting reference dosimetric data to give account the morphology of the patient.

A first order correction consists in adjusting S values by the mass ratio between patient and reference model source organ mass (or volume). This in strictly true only for non-penetrating radiations (i.e. alpha and beta emissions at the scale of human organs/tissues), but provides reasonable results in most situations (Divoli et al., 2009).

When the organ mass is adjusted, the S-value is modified according to the radionuclide emission (Divoli et al., 2009; Grimes et al., 2012; HERMES Medical Solutions, 2016; Petoussi-Henss et al., 2007). Equation 1.14 shows the linear-scaling applied to organ mass for non-penetrating radiation

$$S(r_s \leftarrow r_s)^{patient} = S(r_s \leftarrow r_s)^{reference} \left(\frac{m_s^{reference}}{m_s^{patient}}\right) \qquad 1.14$$

A correction for the gamma contribution to self-irradiation according to equation 1.15 is integrated in OLINDA, but most often can be considered as a second order correction

$$S(r_s \leftarrow r_s)^{patient} = S(r_s \leftarrow r_s)^{reference} \left(\frac{m_s^{reference}}{m_s^{patient}}\right)^{2/3} \qquad 1.15$$

The correction for cross irradiation is usually considered as not necessary – and by all means would be difficult to implement. Petoussi-Henss (Petoussi-Henss et al., 2007) mentioned that correction by mass is unnecessary even when the source and target are close to each other. Moreover, they concluded that another descriptor (related to geometry) for patient-specific scaling of reference S-values should be found.

As a conclusion, adjusting S values from a reference model to a given patient geometry is a fast way to personalise dosimetry.

4.3. Full patient-specific dosimetry

In the case of fully-specific patient dosimetry all aspects related to clinical dosimetry have to be patient specific, not only pharmacokinetics determination but also absorbed dose calculation. This will necessitate computing capabilities from the nuclear medicine centre. However, academic and commercial solutions are increasingly available to deal with the many aspects making available dosimetric workflows.

5. Implementing clinical dosimetry

5.1. Dosimetric workflow/chain

The dosimetric workflow or dosimetric chain is related with the phases that are associated to treat all images and data in a multi-SPECT/CT or PET/CT scenario, in which the aim is to calculate the absorbed dose for a specific organ/tissue. Usually this workflow is associated to a particular philosophy in which data are acquired and treated. There is software that has been created for this purpose, some from academic or hospital institutions, other from commercial companies. In figure 1.15 an illustration of the clinical dosimetric workflow is presented.

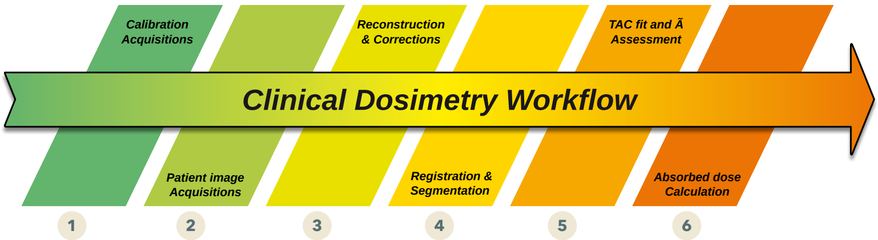

Figure 1.15: Clinical dosimetric workflow scheme. Created by Manuel Bardiès. Used with his permission.

Depending on the available software, there are several steps to treat patient data. Hence, six different phases are considered as follows:

1. Image acquisition for calibration: In principle this acquisition should be done using the same protocol used for patient imaging. Normally a test-object (also called phantom) is used for that purpose. In the literature there are different investigations to address this problem for different radionuclides. The objective is to calculate the calibration factor, which is going to relate the number of counts within the image per voxel with the quantified activity per voxel.
2. Patient image acquisition: This image covers one section of the patient body, where critical organs and/or tumours are present. Depending on the dosimetric protocol, several sections can be obtained for the same time point measurement. Normally several times point measurements are needed.
3. Reconstructions and corrections: In a 3D scenario when reconstructions are performed corrections are also implemented; hence, counts per voxel are going to be generated. Using the calibration factor, activity per voxel can be determined instead of counts per voxel, if is necessary.
4. Registration and segmentation: Due to several patient images acquisition, a registration process is necessary to create a reference space among all data sets, some software use Whole-FOV registration; few use organ-based registration. Normally one data set is used to be the reference against the other data sets, to match/fit two images. Segmentation is a procedure in which a ROI or VOI is generated with the aim to be characterize the biokinetics within.
5. TAC and TIA assessment: Having the same reference for all time points and ROI/VOI segmented, generating time-activity curves for each structure occurs to calculate the TIA as it is expressed in equation 1.5. There are several options to integrate these curves.
6. Absorbed dose calculation: There are several ways to calculate absorbed dose, at the end of this chapter some approaches are addressed, for instance, the analytical, local energy deposition, dose point kernel, dose voxel kernels, Monte Carlo and tabular approaches. All these possibilities will produce different types of outputs, average absorbed dose, absorbed dose maps and voxel-based absorbed dose in which absorbed dose volume histogram can be generated. Knowing radiobiological information, some other parameters can be estimated.

5.2. Activity quantification

Before TIA estimations can occur, activity quantification has to be determined for a particular ROI/VOI/structure. As previously mentioned in section 2, there are three possibilities to acquire patient data images, using gamma-cameras. The three of them are going to be implemented depending on the clinical requirements and the techno/methodological capabilities of each nuclear medicine department. Evidently there are negatives and positives aspects in each quantification approach.

5.2.1. Patient planar imaging

Nowadays, most nuclear medicine department have a single- or dual-head imaging system. These systems can be used to image one section of the patient-body or the patient whole-body. Static, dynamic images or whole-body images can be acquired with these systems. Also, in the case of whole-body images an auto-contour can be activated to generate images as close as possible of the patient.

According to *MIRD Pamphlet 16*, *“this method will be greatest for radiopharmaceuticals distributed in a single region or isolated regions that do not overlap (non superimposed) in the planar projection”.* Figure 1.16 shows an illustration to introduce the quantification scenario.

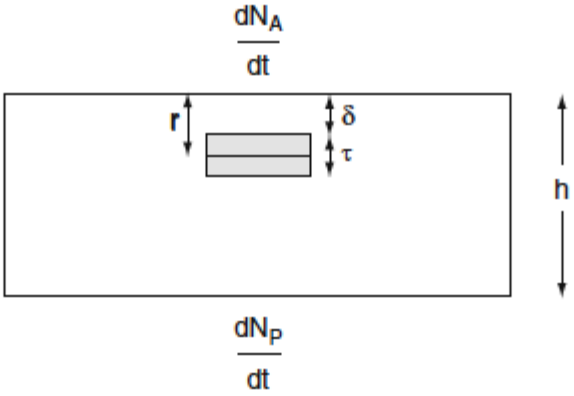

Figure 1.16: A source region containing activity “A”, which is embedded in a medium of overall thickness “h” and which contains no activity. Image taken from (McParland, 2010).

In McParland (McParland, 2010), the conjugate view approach is explained more in-depth. In this example, an object with thickness τ is placed at depth δ. Here assumption of no activity in the medium surrounding the object is considered, and also the medium and the object have same physical properties and no scatter is presented. A differential slice of activity dA, with thickness dr is placed at distance r. Then, this differential of activity is expressed as:

$$dA = C_A dt \tag{1.16}$$

The amount of activity per unit thickness in the object is:

$$C_A = \frac{A}{\tau} \qquad 1.17$$

The rate of photons detected from this differential thickness in the anterior and posterior views are:

Anterior
$$\frac{d^2 N_A}{dt\, dr} = \kappa\, C_A e^{-ur} \Rightarrow \frac{dN_A}{dt} = \kappa\, C_A \int_{\delta}^{\delta+\tau} e^{-ur} dr \qquad 1.18$$

Posterior
$$\frac{d^2 N_P}{dt\, dr} = \kappa\, C_A e^{-ur} \Rightarrow \frac{dN_P}{dt} = \kappa\, C_A \int_{h-\tau-\delta}^{h-\delta} e^{-ur} dr \qquad 1.19$$

Where κ is the planar calibration factor of the gamma-camera system, μ is the linear attenuation coefficient. Then the geometric mean of the two count rates is:

$$\left(\frac{dN}{dt}\right)_{geom} = \sqrt{\frac{dN_A}{dt}\frac{dN_P}{dt}} = \kappa\, A\, \frac{\sinh\left({}^{\mu\tau}/_{2}\right)}{\left({}^{\mu\tau}/_{2}\right)} \sqrt{\mathfrak{H}} \qquad 1.20$$

The attenuation of the emitted photons ($\mathfrak{H}$) through the entire thickness of the medium is given by:

$$\mathfrak{H} = e^{-\mu h} \qquad 1.21$$

Finally, for the object, the activity can be expressed as follows:

$$A = \frac{1}{\kappa\sqrt{\mathfrak{H}}}\left(\frac{dN}{dt}\right)_{geom} \left(\frac{\left({}^{\mu\tau}/_{2}\right)}{\sinh\left({}^{\mu\tau}/_{2}\right)}\right) = \frac{1}{\kappa\sqrt{\mathfrak{H}}}\left(\frac{dN}{dt}\right)_{geom} \xi \qquad 1.22$$

Where ξ is called the self-attenuation factor of the activity contained in the object.

Now, considering a scenario in which many overlaying source regions are presented, such as the case illustrated in figure 1.17, the activity for a source region jth A_j, is given by the general expression:

$$A_j = \frac{1}{\kappa\sqrt{\mathfrak{H}}}\left(\frac{dN}{dt}\right)_{geom} \left(\frac{\left({}^{\mu_j\tau_j}/_{2}\right)}{\sinh\left({}^{\mu_j\tau_j}/_{2}\right)}\right) \qquad 1.23$$

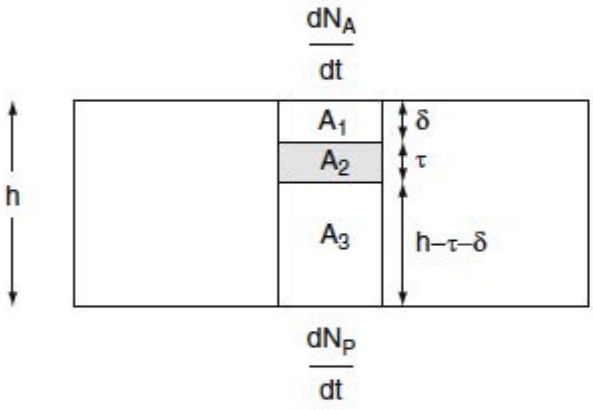

Figure 1.17: Illustration of surrounding medium containing two different activities A1 and A3. Image taken from (McParland, 2010).

The cases showed in the figures 1.16 and 1.17 are ideal, most of the time patient images are degraded by different physical effects, for example, dead time, background, organ overlapping, scatter and attenuation.

5.2.1.1. Dead time correction

This correction must be done when high-count rates are present. This phenomenon can be easily seen when scanning a patient after few hours of administration of a high amount the radiopharmaceutical (A_0 > 3700 MBq, i.e. for ^{131}I). Figure 1.18 illustrates the effect of counting losses from a high activity source placed in air and placed behind 10 cm of water, also in the same figure shows the “ideal” performance of a gamma camera. In the case of the scatter medium, less count are observed within the energy window used to perform the measurement. This is due to the scatter photons associated with the Compton effect that occurred and then, with the corresponding lost of energy for those photons.

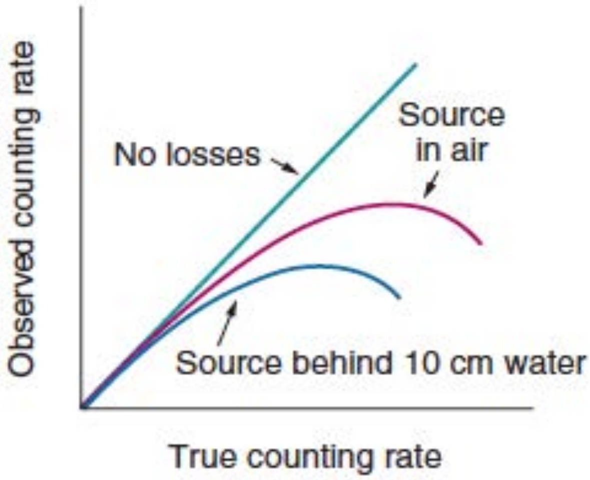

Figure 1.18: Effect on counting losses in the presence of a high activity source. Counting losses effect when the source is in air and the source is behind 10 cm of water. Image taken from (Cherry et al., 2012).

According to Sharp et al. *because the gamma camera is a paralyzable system, a second event occurring within the dead time due to the first event will not be recorded but will also initiate a pile-up effect. This means that not only will be recorded counting rate be less than the true counting rate but that, at high sample activities, the recorded counting rate will begin to decrease* (Sharp et al., 2005).

If τ is the system dead time, the observed counting rate R_o is related to the true counting rate R_t, in a paralyzable system is as follows:

$$R_o = R_t e^{-R_t \tau} \qquad 1.24$$

According to Cherry (Cherry et al., 2012) the observed counting rate rises to a maximum value given by:

$$R_o = \frac{1}{(e \cdot \tau)} \qquad 1.25$$

Moreover, Cherry et al. proposed a method to determine the dead time τ, called *"the two-source method"* (Cherry et al., 2012), in which two sources with similar activities are used, for which the dead time losses are expected between 10% and 20%. First step is to place source 1 to establish its the count rate R_1. Then without moving source 1, source 2 is place at certain distance from source 1, then establishing the count rate of the two sources together R_{12}. Then source 1 is removed without disturbing source 2 and recording the count rate of source 2, R_2.

Figure 1.19 illustrates the followed steps to carry-on with this procedure. For a paralyzable system, the dead time τ is given in seconds by:

$$\tau \approx \left[\frac{2R_{12}}{(R_1 + R_2)^2}\right] ln \left[\frac{(R_1 + R_2)}{R_{12}}\right] \qquad 1.26$$

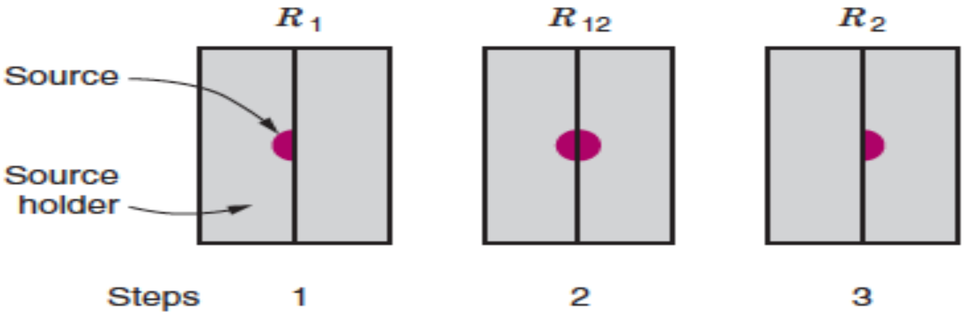

Figure 1.19: Illustration of the steps followed to determining dead time losses by the two sources method. Image taken from (Cherry et al., 2012).

5.2.1.2. Background correction

Considering figure 1.17 but now assuming an homogeneous background source activity surrounding the source object, the background contribution in each view (detector) can be corrected.

The conventional background correction would be to generated a VOI close to A_2 and subtract the counts in this VOI to A_2 counts, the definition of this VOI is very difficult because care must be taken to avoid hot or cold areas, moreover, according to MIRD Pamphlet 16, this VOI *does not consider the portion of the background equivalent to the source region volume and may underestimate the source region activity due to oversubtraction of background*.

Therefore, the fraction "F" of geometric mean counts that originates from A_2 alone is:

$$F = \left\{ \left[1 - \left(\frac{dN_x}{dt} \Big/ \frac{dN_A}{dt} \right) \left(1 - \frac{\tau}{h} \right) \right] \left[\left(\frac{dN_x}{dt} \Big/ \frac{dN_P}{dt} \right) \left(1 - \frac{\tau}{h} \right) \right] \right\}^{1/2} \qquad 1.27$$

Where $\frac{dN_x}{dt}$ is the count rate through the patient from a region adjacent to the object with equal area. Considering one patient τ and h thickness could be measured from NM lateral views or using CT information.

5.2.1.3. Organ overlapping correction

Organ overlapping can occurs for some organs or tumours, and this is the major drawback for planar quantification. For instance, right kidney and liver are frequently partially superimposed on planar images. Stabin et al. suggested two methods to solve this problem (Stabin, 2008). One option for pairs organs, such as kidneys and lungs, is to quantify the activity in one of the organs in which there is no overlap, then double the number of counts obtained in this organ to estimate the counts in the two organs.

The second approximation: is to draw an ROI over the organ region in scans where there is overlap, count the number of pixels and record the count per pixel, then use a ROI from another image in which there is no overlap; record the number of pixel from this new image, then multiply the count rate per pixel from the first image by the number of pixels in the second image.

5.2.1.4. Scatter correction

This correction can be implemented mostly considering two different factors, first the image acquisition itself, depending on the number of energy windows used to generate the images, and second, the processing software used to perform the correction.

This correction must be applied to determine the amount of scatter photons included into the main energy window at its contribution to the total amount of counts within this energy window. The scatter counts will degrade the quality of the acquired image and it will affect the quantification. In figure 1.20 an example of the scatter photons within the photo-peak and the additional energy window. The multiple order of scatter photons can be seen in this figure due to the Monte Carlo simulation.

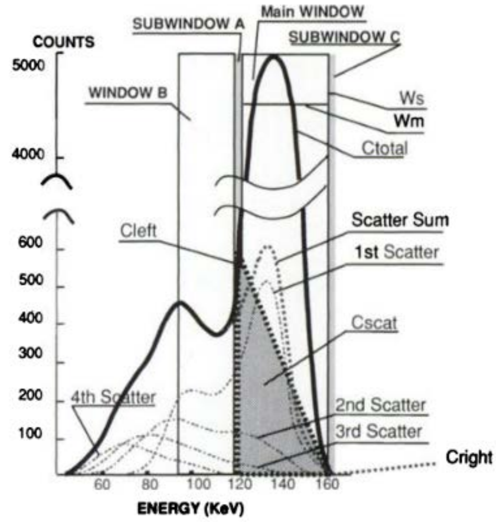

Figure 1.20: Total energy spectrum of a ^{99m}Tc and its Monte Carlo simulation. Energy window positioning and multiple order of scattering. Image taken from (Ichihara et al., 1993).

Chapter 7 from Zaidi (Zaidi, 2006) addressed implicit and explicit scatter corrections methods, few of these methods are mentioned in the MIRD Pamphlet 16. According to McParland (McParland, 2010) scatter correction can be divided into four categories, an explanation of the first two is going to be addressed due to their implementation in clinical practice:

- Photon energy discrimination or analysis (Buvat et al., 1994; Buvat et al.,1995; Ichihara et al., 1993; Ogawa et al., 1991)
- The build-up factor (Raymond & Siegel, 1984)
- Factor analysis (Mas et al., 1990)
- Convolution/subtraction methods analysis (Axelsson et al., 1984; Willowson et al., 2008)

- **Photon energy discrimination or analysis**

In the case of the photon energy discrimination or analysis, corrections can be implemented by using one, two or more energy windows additionally to the main photo-peak energy window. Hence, *one can estimate either the complete energy spectrum of scatter counts, or at least the integral of that spectrum from the lower-energy cut-off of the photo-peak window to the upper-energy cut-off of that window, subtraction of the scattered counts, pixel by pixel, is still the goal* (Zaidi, 2006).

The dual-energy window (DEW), using just one energy window below the main, both with the same width. An assumption is made, considering that the number of scattered photons in the “low energy” window is proportional to the number of scattered photons in the main energy window. The number of primary photons is given by:

$$C_{primary} = C_{Total} - \kappa \cdot C_{scatter} \qquad 1.28$$

Where κ is a constant value, found to be 0.5 for ^{99mT}c (Koral et al., 1988; Oppenheim, 1984).

The Triple Energy Window (TEW) method employs two energy windows close to the main energy window. One of the first articles showing its applicability in nuclear medicine was from Ogawa et al. in which they were performing scatter correction under different phantom-objects configurations and using Monte Carlo simulations (Ogawa et al., 1991). The number of scattered photons can be determined as follows:

$$C_{scatter} \cong \left(\frac{C_{left}}{W_s} + \frac{C_{Right}}{W_s}\right) \cdot \frac{W_m}{2} \qquad 1.29$$

Where C_{left} and C_{Right} are the acquired count from the two energy windows W_s placed above and under the main energy window W_m. Then the amount of scatter counts can be estimated from the trapezoidal region having a left height of $\frac{C_{left}}{W_s}$, a right height of $\frac{C_{Right}}{W_s}$, and a base of W_m. Figure 1.21 also shows an illustration of this trapezoidal correction.

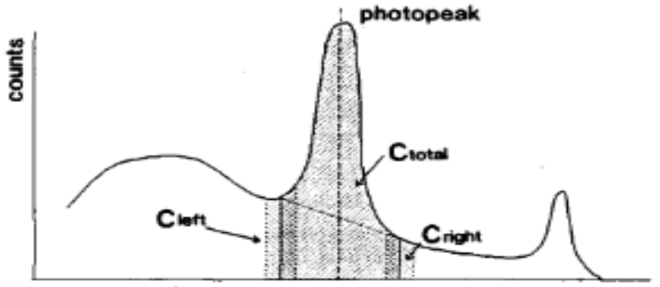

Figure 1.21: Location and width of the energy windows. The counts of primary photons in the main energy window are estimated as a trapezoidal using the photons of the other two energy windows. Image taken from (Ogawa et al., 1991).

Therefore, using the result from 1.31, the count of primary photons is given by:

$$C_{primary} = C_{Total} - C_{scatter} \qquad 1.30$$

- **The build-up factor**

This method considers no activity in a scatter medium, as can be seen in figure 1.22. To introduce to this method, first the pseudo-extrapolation number method (PNM), mentioned at *MIRD Pamphlet 16*, is considered. The PNM take into account the effect of the scatter radiation with a scatter medium as a function of depth. Initially a straight line is expected from the simple narrow beam geometry ($\mathcal{T} = {}^{I}/_{I_0} = e^{-\mu t}$), but because scatter is present in the transmission measurements, a "shoulder" on the semi log plot can be seen, therefore the straight line in the semi log plot can be expressed as follows:

$$\mathcal{T} = ne^{-\mu t} \tag{1.31}$$

The shoulder is a manifestation of the increased scatter photons from the activity close to the collimator, n is the pseudo-extrapolation number.

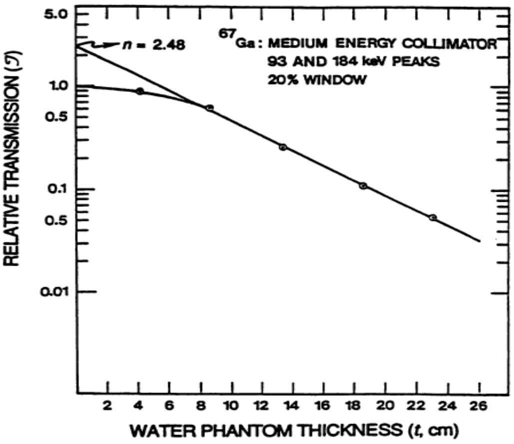

Figure 1.22: Experimental measured transmission curve in a tissue equivalent medium using a ^{67}Ga source with a medium-energy collimator, showing pseudo-extrapolation number n. Image taken from (Siegel et al., 1999).

The build-up factor method depends on the radionuclide, collimator type, energy window, measurement geometry, source size, and it may depend also on the source depth and source thickness. The build-up factor can be depth-dependent (DDBF) or depth-independent (DIBF).

According to *MIRD Pamphlet 16*, *the DDBF is defined as the factor by which the transmission measurement is made across the patient. Then, an iterative calculation procedure is used involving the solution of the set of simultaneous equations representing the conjugate-view count rate pairs*. Assuming initially source thickness $\tau = 0$. The conjugate-view count rate can be expressed as follows:

Anterior
$$\frac{dN_A}{dt} = \frac{dN_0^{SCD}}{dt} B_{\delta}^{SCD} e^{-u\delta} \tag{1.32}$$

Posterior
$$\frac{dN_P}{dt} = \frac{dN_0^{SCD}}{dt} B_{h-\delta}^{SCD} e^{-u(h-\delta)} \tag{1.33}$$

Where $\frac{dN_0^{SCD}}{dt}$ is the count rate measured in air at the source-collimator distance (SCD); B_d^{SCD} is the measured buildup factor for a SCD and for the source at a depth "d" in a scattering and attenuation medium, u is the narrow-beam linear attenuation coefficient. Considering $\tau \neq 0$, the previous equation can be expressed as follows:

$$\text{Anterior} \qquad \frac{dN_A}{dt} = \frac{dN_0^{SCD}}{dt} B_\delta^{SCD} e^{-u\delta} \tag{1.34}$$

$$\text{Posterior} \qquad \frac{dN_P}{dt} = \frac{dN_0^{SCD}}{dt} B_{h-\delta}^{SCD} e^{-u(h-\delta)} e^{-\mu\tau} \left(\frac{\sinh\left({}^{\mu\tau}/_{2}\right)}{\mu\tau} \right) \tag{1.35}$$

Because of the contribution of scatter to the broad geometry is inherent to NM images, photon attenuation is not purely exponential, as shown in 1.31. This was considered by Siegel et al. presenting equation 1.31 (Siegel et al., 1985), parameterized the transmission as a function of depth δ as:

$$\mathcal{T} = 1 - \left(1 - e^{-\mu\delta}\right)^n \tag{1.36}$$

Then, the build-up factor for an infinite depth (which means, large δ), is equal to B^∞. Therefore equation 1.36 can be written as follows:

$$\mathcal{T} = 1 - \left(1 - e^{-\mu\delta}\right)^{B^\infty} \tag{1.37}$$

Then, equations 1.34 and 1.35 can be written as follows:

$$\text{Anterior} \qquad \frac{dN_A}{dt} = \frac{dN_0^{SCD}}{dt} \left(1 - \left(1 - e^{-\mu\delta}\right)^{B^\infty}\right) e^{-\mu\tau} \left(\frac{\sinh\left({}^{\mu\tau}/_{2}\right)}{\mu\tau} \right) \tag{1.38}$$

$$\text{Posterior} \qquad \frac{dN_P}{dt} = \frac{dN_0^{SCD}}{dt} \left(1 - \left(1 - e^{-\mu(h-\delta)}\right)^{B^\infty}\right) e^{-\mu\tau} \left(\frac{\sinh\left({}^{\mu\tau}/_{2}\right)}{\mu\tau} \right) \tag{1.39}$$

The depth-independent build-up factor, is independent of source size and depth for a given settings, an in this case is associate to B^∞.

5.2.1.5. Attenuation correction (Transmission method)

In this conjugate view scenario, the attenuation correction can be done by using a transmission factor, similar to the one presented in equation 1.21. In order to generate this factor, a transmission scan is required, sometimes using a ^{57}Co sheet source, or flood phantoms (using ^{99m}Tc or ideally the isotope used for emission image acquisitions). Specific devices have also been presented (Lenta et al., 2000), but not integrated in commercial systems. The CT scout can also be used (Minarik et al., 2005).

For a given ROI (or Whole-Body) the transmission factor $\mathfrak{H}$ can be expressed as follows:

$$\mathfrak{H} = \frac{\left[\frac{dN}{dt}\right]_{ROI,\ object}}{\left[\frac{dN}{dt}\right]_{ROI, no-object}} \tag{1.40}$$

In a whole-body scan, same bed speed must be applied for both scans.

When using a different isotope for transmission than for emission images, a correction must be applied due to differences in linear attenuation coefficients between radionuclides. In this case, the transmission factor can be scaled, as presented in equation 1.41:

$$\mathfrak{H} = e^{\left(\frac{\mu}{\mu_{Measured}} ln(\mathfrak{H}_{Measured})\right)} \tag{1.41}$$

Where μ is the linear attenuation coefficient associated to the injected radionuclide (considering broad beam geometry), $\mu_{Measured}$ and $\mathfrak{H}_{Measured}$ are the attenuation coefficient and the transmission factor of the radionuclide used for the transmission scan, respectively. Hence, these two parameters have to be known and measured in advance.

5.2.2. Patient SPECT/CT imaging

Tomoscintigraphic imaging avoids the overlap between different organs or structures. SPECT/CT imaging is a complex and non-standardized image acquisition technique and in this section some of the aspects involving image generation are covered. Depending on the administrated activity, dead time effect can be also present even before the image reconstruction process.

5.2.2.1. Dead time correction

In the case of SPECT acquisitions, dead time effects have been studied for several radionuclides. According to *MIRD Pamphlet 26*, in the case of ^{177}Lu because of the low yield of γ-photons emitted the impact of dead time on SPECT images is limited, even for high activities. However, it may be present when scans are obtained shortly after the therapeutic injection. This effect also is related to the number of energy windows used (which means more photons are detected), the collimator type and the amount of administrated activity to the patient.

5.2.2.2. Image reconstruction

Projections are generated from images acquired at different angles, when the gamma camera is in rotation around one source or a patient. The reconstruction is the process in which 2D projections are converted in a 3D source distribution. Using this technique overlapping structures in planar images can be seen properly distributed in 3D image.

From the IAEA book (IAEA, 2014) (chapter 13) and Zaidi (Zaidi, 2006) (chapters 3 and 4) the reconstruction techniques are presented in more details.

Generally, each projection is associated to one angle, its signal information is recorded in a form of a 2D matrix. In cartesian coordinates data can be converted to polar coordinates, generating a new representation of the data called sinogram. A representation of an object source can be seen from the projections (cartesian coordinates) and from the sinogram (polar coordinates) points of view can be observed in figure 1.23.

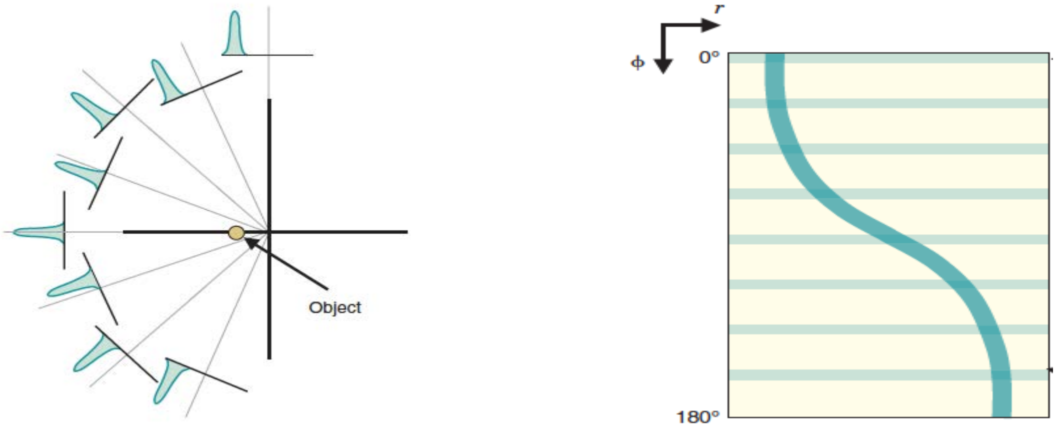

Figure 1.23: Illustration of an object representation in A: cartesian coordinates, B: Polar coordinates. Images taken from (Cherry et al., 2012).

Therefore, the position of the object (the projection profile) in figure 1.23 can be mathematically described as:

$$\begin{aligned} r &= x\cos\phi + y\sin\phi && \text{Cartesian coordinates} \\ s &= x\cos\phi - y\sin\phi && \text{Polar coordinates} \end{aligned} \tag{1.42}$$

From this example the generation of a reconstructed image can occurred, because the projection profile can be back projected, and recorded in an image matrix (from 64x64 to 1024x1024 pixels), as can be observed in figure 1.24A where only one projection profiles was back projected.

In figure 1.24B the effect of adding projection profiles and back projected can be noticed. Increasing the number of projection profiles that are back projected, the approximation to the real object is improved.

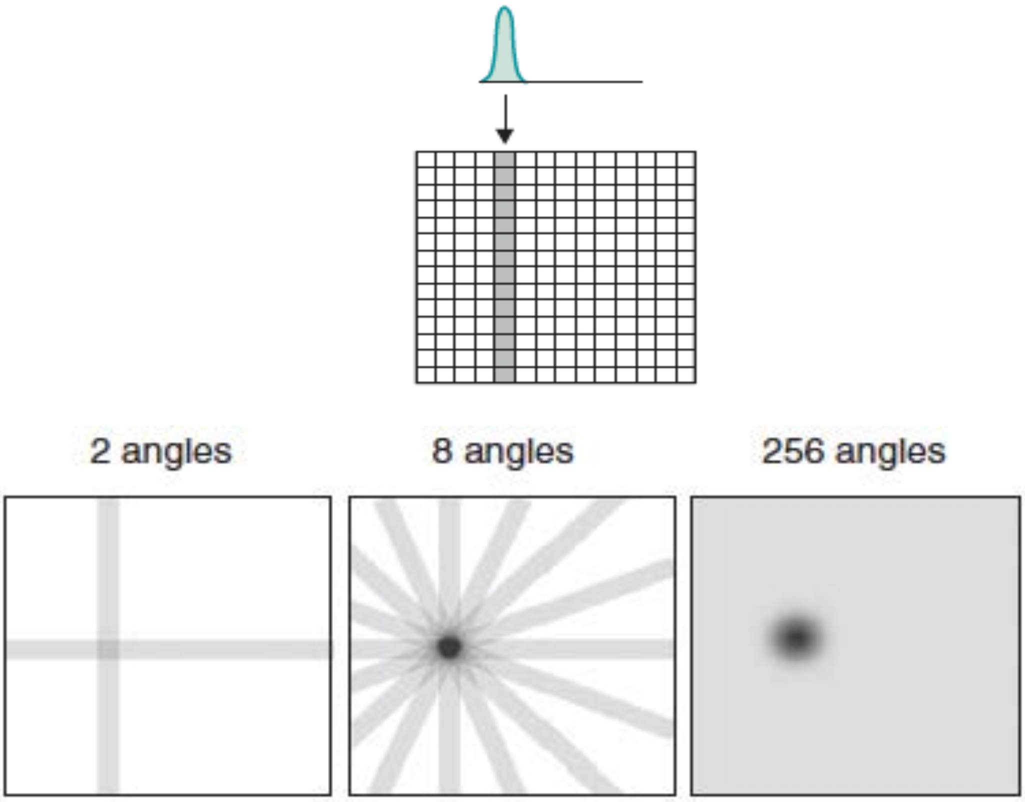

Figure 1.24: Illustration of back projection process. A: One projection profile is back projected. B: the effect of increasing projection profiles. Images taken from (Cherry et al., 2012).

Mathematically, the back projection of N profiles can be described as follows:

$$f'(x,y) = \frac{1}{N}\sum_{i=1}^{N} p(x\,cos\phi_i + y\sin\phi_i\,,\phi_i) \qquad 1.43$$

Where $f'(x,y)$ denotes an approximation to the true activity distribution, $f(x,y)$, ϕ_i is the ith projection angle and $p(r,\phi_i)$ is the projection profile. In figure 1.24B, an artefact is created increasing the number projection profiles that are back projected, the object cannot be seen clearly, it is blurred. To correct this blur artefact, the filtered back projection process has been developed.

5.2.2.2.1. Filtered back projection (FBP)

The filtered back projection implies the use of a filter in order to decrease the blurring artefact. One simple approximation that can be applied to the source activity in figure 1.24, is to use a profile from a reconstructed image of a point-source, that is taken from finely sampled data decreasing in proportion to “1/r”, where “r” is the distance from the centre of the point-source location.

Mathematically, this process can be expressed as follows:

$$f'(x,y) = f(x,y) * \frac{1}{r} \qquad 1.44$$

Where "$*$" denotes a convolution process. This process is easily processed expressing all functions in Fourier transforms. Cherry et al. provides the basis on how to perform this process under the spatial frequencies space (Cherry et al., 2012). The approximation "1/r" in the spatial frequencies space is known as "ramp filter". Then, after performing the convolution, equation 1.44 can be expressed as follows:

$$f(x,y) = \frac{1}{N}\sum_{i=1}^{N} p'(x\,cos\phi_i + y\sin\phi_i\,, \phi_i) \qquad 1.45$$

Where $f(x,y)$ is the true source object activity distribution corrected by the convolution process and $p'(r,\phi_i)$ is the projection profile considering the ramp filter, which provides the filtered back projected profile. Figure 1.25 shows the effect of the filtered back projection process using a similar example that it was used in figure 1.24B.

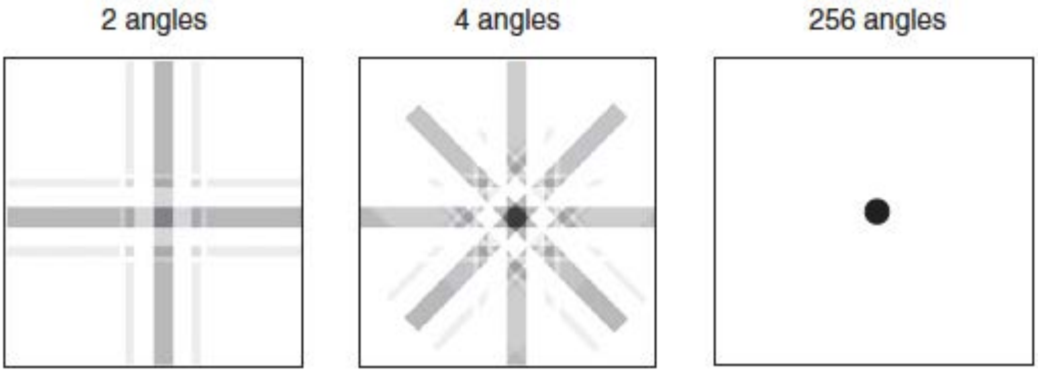

Figure 1.25: Illustration of filtered back projection process implemented with data from figure 1.25B. Images taken from (Cherry et al., 2012).

5.2.2.2.2. Iterative reconstruction

As an improvement of the FBP reconstruction technique, the iterative algorithm was developed to deal with the streak artefacts created in the back projection process. These artefacts are present specially when many "hot" sources are in the image.

Using this reconstruction technique, the "best" estimation of the activity distribution can be found, using some criterion that measures the goodness of the fit between two images: the reconstructed image and the measured image; thus, the reconstruction technique use a mathematical algorithms to find the optimal solution, minimizing differences between these two images, in successive approximations.

According to Zaidi (Zaidi, 2006) *the iterative process begins with an initial estimate of the object count distribution. Provided a suitable model of the emission and detection physics is incorporated, the projections that would arise from this initial object can be estimated (by forward projection): this effectively an estimate of what* *the detector would measure given the initial object; normally this estimate of projections will differ from the actual measured projections, then, the difference between estimated and measured projection can be seed to modify the original estimate of the object by use of suitable additive of multiplicative corrections at each point (usually via back projection). Thus, the adjusted object becomes the starting point for a second iteration.* The process will continuous in a feedback loop until a final solution is reached. This process previously described can be seen in figure 1.26.

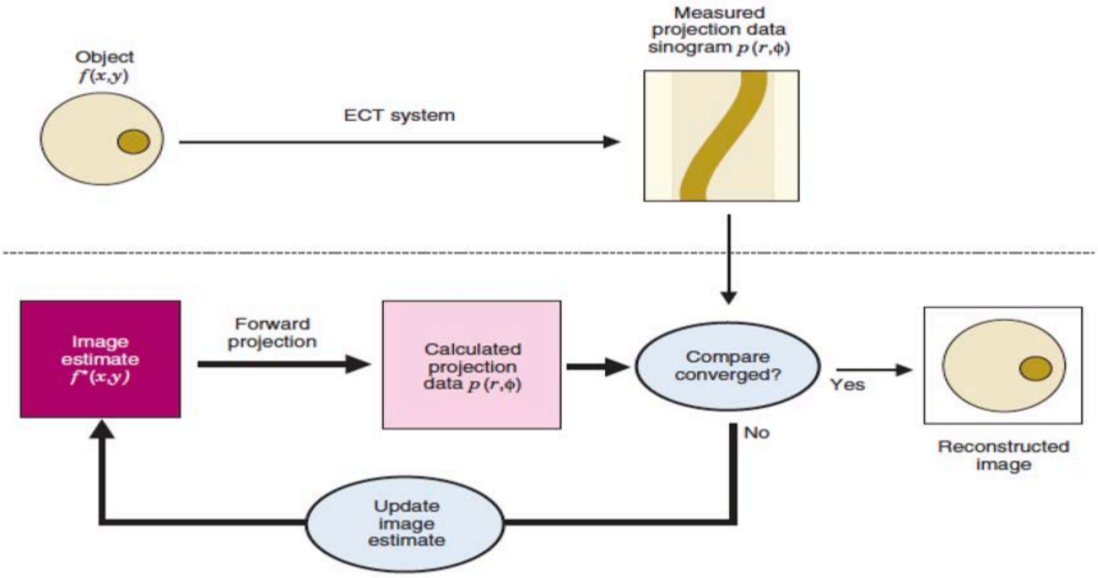

Figure 1. 26: Illustration of iterative reconstruction procedure. Images taken from (Cherry et al., 2012).

According to Cherry et al. (Cherry et al., 2012) the two basic components of iterative reconstruction algorithms are: the method for comparing the estimated and the actual images and the method by which the image is updated on the basis of this comparison. Then, the goal of the iterative reconstruction is to produce convergence of the estimated image towards the true image as rapidly and accurate as possible.

The iterative algorithm normally takes into account factor for specific characteristics of the gamma camera, for instance, the collimator, its system geometry, system spatial resolution, noise characteristics, attenuation and object scatter.

Mathematically, the iterative reconstruction algorithm can be expressed as follows:

$$p_i = \sum_j a_{ij} f_j \tag{1.46}$$

Where p_i is the equivalent discrete set of projection pixel values, for counts originating from the object voxel activiy concentration f_j. This essentially defines the probability of detecting an emitted photon, originating from location j, at any particular position, I, on the detector. a_{ij} is the transition or system matrix.

As it is mentioned *in chapter 4 from* Zaidi (Zaidi, 2006), one reconstruction algorithms used is the Maximum Likelihood-Expectation Maximization (ML-EM), which involves two steps: first the expected projections are calculated by forward projection using the appropriate system matrix, based on the estimate of the activity distribution from the previous iteration. Second, the current estimate is updated so as to maximise the likelihood, achieved by multiplication of the previous estimate by the back projection of the ratio of measured over estimated projections. Mathematically this is described as follows:

$$f_j^{new} = \frac{f_j^{old}}{\sum_l a_{lj}} \sum_i a_{ij} \frac{p_i}{\sum_k a_{ik} f_k^{old}} \qquad 1.47$$

To ordered subsets expectation maximization (OS-EM) method use a subset of projections for updating rather than comparison of all estimated and measured projections. For OS-EM one iteration is normally considered the use of all data one; consequently, use of only part of the data during the update process is termed a sub-iteration. The process is very similar to that presented in equation 1.47, the only difference being the use of subsets, S_n, where $n \in N$, the total number of projections divided by the total number of projections per subset, mathematically expressed as:

$$f_j^{new} = \frac{f_j^{old}}{\sum_{i \in S_n} a_{ij}} \sum_{i \in S_n} a_{ij} \frac{p_i}{\sum_k a_{ik} f_k^{old}} \qquad 1.48$$

5.2.2.3. Collimator detector response correction

This is a really complex topic, fortunately most of the reconstruction algorithms include this correction. *The collimator-detector response (CDR) in a nuclear medicine image system refers to the image generated from a point source of activity. The shape of the CDR is the primary factor determining the image resolution in SPECT* (Zaidi, 2006).

According *to the MIRD Pamphlet 23*, the CDR has four components: the intrinsic response of the detector and three related to the collimator response (geometric, septal penetration and scatter). *The intrinsic response is well modelled as a Gaussian function. The geometric response of the collimator can be calculated theoretically and is also often approximated as a Gaussian function as well, with a FWHM that is linear function of source-to-collimator distance.* The last two components of the collimator response cannot be determined as the geometric response and both have to be determined by Monte Carlo simulations (which are normally performed to fully determine the CDR). The use of this correction method helps to reduce the partial volume effect, but is not full compensated.

In fact, *chapter 5 from* Zaidi (Zaidi, 2006) explains in detail all these different components and how to compensate them. According *to MIRD Pamphlet 26*, the reconstruction algorithms, which include this correction, *will modify the distribution of* *counts in the image but do not change their total number. Also, this correction will generate changes in noise texture, so image will appear smoother; moreover, it decreases the resolution-induced spill-out of counts from hot regions. This correction depends on the signal-to-n ratio, noise levels in the data, camera orbit, and the number of iterations*. The drawback on this compensation is the generation of Gibss-like artefacts.

5.2.2.4. Scatter correction

Scatter corrections mentioned in section 5.2.1.4 can also be applied in SPECT images, this correction can be considered in some cases into the iterative reconstruction algorithm.

5.2.2.5. Attenuation correction

To address this problem in SPECT, Chang (Chang, 1978) proposed an analytical method assuming homogeneous density and using a fixed linear attenuation coefficient to correct it; this method is applied after reconstruction, taking into account each pixel of the image, however, this technique is assuming a constant attenuation coefficient. The attenuation coefficient can be derived from narrow- or broad-beam geometries. This method is not used nowadays, because of the hybrid SPECT/CT technology available in the nuclear medicine departments. Nonetheless, this method can be used with this hybrid system is not available.

The impact of this attenuation correction method can be seen in figure 1.23.

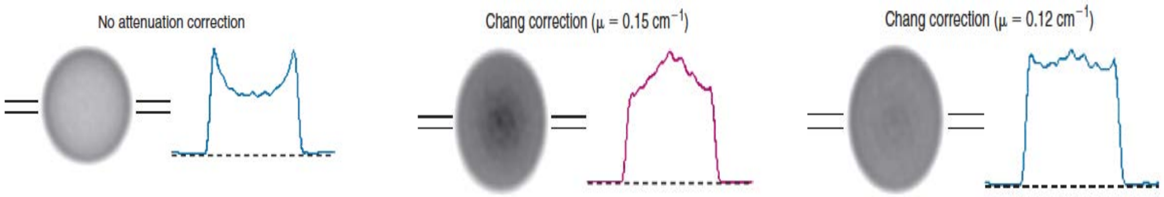

Figure 1.27: Effect of Chang attenuation correction on SPECT images of a 20-cm diameter cylinder containing a uniform concentration of ^{99m}Tc. No attenuation correction effect, narrow-beam geometry coefficient and broad-beam geometry coefficient can be seen. Images taken from (Cherry et al., 2012).

Due to the heterogeneity in tissue composition in the human body, the estimation of an accurate and patient-specific attenuation map for nonuniform attenuation compensation is necessary. This map is a voxel-by-voxel representation of the linear attenuation coefficients at the SPECT photon energy. Generally these maps have lower noise, better spatial resolution, better contrast and are faster and easier to acquire (Dewaraja et al., 2012; IAEA, 2014).

The attenuation map is described by the matrix of CT numbers associated with each pixel in a tomographic slice, generated by a CT scanner. The CT number can be defined as it is shown in equation 1.49:

$$CT\# = \left(\frac{\mu}{\mu_{H_2O}} - 1\right)\cdot 1000 \qquad 1.49$$

Where μ is the linear attenuation coefficient of the medium and μ_{H_2O} is the linear attenuation coefficient of water. CT number units are Hounsfield Units (HU).

Because linear attenuation coefficients are energy-dependent, the CT numbers at the x-ray energy must be scaled to the energy of the SPECT isotope. In the case of low-Z materials, a single scaling factor can be used to convert from x-ray energies to SPECT photon energies. For high-Z materials a bilinear scaling is more convenient. According to the American Association of Physicists in Medicine (AAPM) (Mutic et al., 2003) these relationships are typically scanner dependent.

Brown et al. derived bilinear functions, using emission sources of different radionuclides and trying to perform narrow-beam geometry to find the linear attenuation coefficients for several materials (Brown et al., 2008). The International Atomic Energy Agency (IAEA) in their book dedicated to Nuclear Medicine teachers and students (IAEA, 2014) proposed to generated the attenuation map $\mu(h)$ taking into account the attenuation coefficients for water and bone as follows (h = Hounsfield units):

$$\mu(h) = \frac{1000+h}{1000}\mu_{water} \qquad \mathbf{for\ h \leq 0}$$

$$\mu(h) = \mu_{water} + \frac{h}{h_{bone}}(\mu_{bone} - \mu_{water}) \qquad \mathbf{for\ 0 < h < h_{bone}} \qquad 1.50$$

$$\mu(h) = \frac{h}{h_{bone}}\mu_{bone} \qquad \mathbf{for\ h > h_{bone}}$$

Another approach in similar terms is proposed by McParland (McParland, 2010), knowing linear attenuation coefficients for a particular energy emission and kVp, for particular tissue (bone, water):

$$\mu_{tisue,em} = \frac{\mu_{water}}{1000}\cdot CT\# \qquad \mathbf{for\ CT\# \leq 0}$$

$$\mu_{tisue,em} = \mu_{H_2O,Em} + \mu_{H_2O,kVp}\left(\frac{\mu_{Bone,Em} - \mu_{H_2O,Em}}{\mu_{Bone,kVp} - \mu_{H_2O,kVp}}\right)\cdot CT\# \qquad \mathbf{for\ 0 < CT\# < h_{bone}} \qquad 1.51$$

5.2.2.5.1. CT calibration curve

According to the AAPM, *this is a curve in which the CT numbers are corresponding to the mean linear attenuation coefficients of the material in each voxel. These calculations rely on relative physical or electron density, information contained in the CT images.* For a hybrid SPECT/CT system, the CT part of the software has tools to report the mean CT numbers for the region of interest in a CT image. To generate this curve an electron density phantom is used, which normally consists of a water-equivalent material with holes, in order to hold interchangeable rods made of various tissue and water simulating materials. The sizes of the density phantom vary depending on the manufacturer, but normally are available with Head and Body inserts, the number of rods varies, also depending company.

5.2.2.6. Partial volume effect correction

According *to the MIRD Pamphlet 23* this effect starts to appear in small structures with dimensions less than 3 x FWHM of the reconstructed image. The objects show smaller concentration of activity than they actually do. Nonetheless, it can also affect the activity determination at the edge of larger objects because of count spill-on and spill-out. The same MIRD Pamphlet mentioned different forms to reduce or try to correct for this effect:

- To determine the ratio of the apparent concentration to true concentration; this ratio is called the recovery coefficient factor (RCF). Then applying this factor to correct for the partial-volume underestimation of the activity concentration in small objects. To estimate the RCF, phantom measurements of simple geometric structures are ideal. For instance, using spheres varying in size. However, this method depends on several aspects such as, shape of the object, its position in the image, and object-to-background contrast.
- Applying the collimator response correction function in the iterative reconstruction model. Nevertheless, this does not produce a full recovery of the activity concentration.
- Using Monte Carlo simulations that generate an accurate characterization of the imaging system.

5.2.2.7. Calibration factor

This factor is a key aspect that needs to be considered for absolute quantification. The calibration factor can be derived from the sensitivity of the SPECT/CT system. Normally the sensitivity is given in units of cps/MBq and it is obtained by imaging a known activity for a certain period of time.

According to *MIRD Pamphlet 23, the more reliable calibration measurement is a SPECT acquisition with a source geometry that better approximates the scatter and attenuation properties in patient imaging, such as a tank of uniform activity or hot spheres in uniform background activity, thereby reducing the effects of imperfect compensation"*. Moreover, *acquisition, reconstruction and target definition in the calibration study should be performed in the same manner as in the patient study.*

Generally, the calibration factor can be obtained from planar and SPECT/CT acquisitions. According to Zhao et al. the variation in calibration factor results obtained by different experimental geometries (including planar acquisitions) is less than 10% in the case of ^{177}Lu (Zhao et al., 2018). Thus, a SPECT/CT calibration factor may be obtained from SPECT/CT acquisitions and planar sensitivity verification can be obtained to verify system stability before patient image acquisition.

5.2.3. Patient planar imaging + patient SPECT/CT imaging (hybrid method)

Planar quantification can be considered as less accurate than SPECT, but combining it with SPECT/CT information it can overcome this lack of accuracy. This technique implements the whole-body acquisition and the adjustment of the activity (or TIA) using one or two SPECT/CT. The SPECT/CT will adjust the planar results. The adjustment considers the ratio of the activity measurements from the same organ of interest. This technique assumes same biokinetics behaviour between the 2D and 3D data for the same organ.

In clinical practice this methodology can be implemented to reduce the time of the patient in the nuclear medicine department, because planar whole-body acquisitions are less time consuming than SPECT/CT acquisitions.

5.3. Segmentation

In order to identify and quantify the information gathered from the images, regions of interest must be precisely delineated and separated out for further processing. Segmentation is the name of this process (Zaidi, 2006). Then, all subsequent interpretation tasks like feature extraction, object recognition, and classification depend largely on the quality of the segmentation output. The level to which the segmentation is carried out depends on the problem to solve. Segmentation should stop when the regions of interest are generated. Thus, one of the main challenges of segmentation is to accurately delineate the organ or structure and separate it out from the rest of the data sets.

According to Zaidi (Zaidi, 2006), the segmentation process can be defined as follows:

a) $$\bigcup_{i=1}^{C} R_i = I$$

b) R_i is the connected region, $i = 1, 2, \dots, C$

c) $$R_i \bigcap R_j = \emptyset \ \forall i, j, i \neq j \qquad 1.52$$

d) $P\ (R_i)$ = true for $i = 1, 2, \dots, C$

e) $P\ (R_i \cup R_j)$ = false for $i \neq j$

Where P () is a uniform (homogeneity) predicate, C is the number of regions "R". Each region is homogeneous and the union of two non-adjacent regions is homogeneous. The conditions defined in 1.55 are explained as follows:

a) indicates that the segmentation must be complete, then every pixel must be in the region
b) requires that points in a region must be connected
c) indicates that the regions must be disjoint
d) deals with the properties that must be satisfied by the pixels in a segmented region
e) indicates that regions R_i and R_j are different in the sense of predicate P().

Removing the constraint that regions must be connected, then the regions are called *pixel classification* and the regions themselves are named *classes*, this is important when disconnected regions belonging to the same tissue class need to be identified. Labelling is the process of assigning identification to each region or class and can be performed separately from segmentation (Pham et al., 1998). There are several segmentation approaches that can be implemented:

5.3.1. Thresholding

With this approach a scalar image is generated by binary partitioning of the image intensities. The aim of the thresholding is to determine an intensity value in order to separate the desired regions. Then by grouping all pixels with intensity greater than the threshold, one region is created and the rest of pixels will be associated to other regions (Pham et al., 1998). If only one threshold is used, the process is called global thresholding. If there are several thresholds partitioning the image in multiple sub-regions, then the process is called local thresholding (Zaidi, 2006). One limitation of this process is that typically does not consider the spatial characteristics of an image, and is sensitive to noise and inhomogeneities.

5.3.2. Region growing

The goal is to connect regions of pixels with similar grey values, growing uniformly using a seed point that is manually selected by the operator. Disadvantages of this approach are related to the manual interaction to obtain the seed point, also it can be sensitive to noise (Pham et al., 1998).

5.3.3. Classifiers

Classifier methods are pattern recognition that deals with association of regions linked to several tissues, thus called labelling (Zaidi, 2006). A feature space is the range space of any function of the image that can be related to the image intensities themselves or a gradient at a given pixel. This approach is also known as supervised methods because requires training data that are manually segmented and the used as references for automatically segmenting new data. Standard classifiers require that the structures to be segmented possess distinct quantifiable features. Disadvantages to this approach is that they generally do not perform any spatial modelling, and also require manual interaction for obtaining training data (Pham et al., 1998).

5.3.4. Clustering

These algorithms essentially perform the same function as classifiers but avoid the training phase, and therefore are known as unsupervised methods. These methods iterate between segmenting the image and characterizing the properties of each region. However, they do require an initial segmentation. As the classifier methods, there are no incorporation of spatial modelling and then are sensitive to noise and intensity inhomogeneities (Pham et al., 1998).

5.3.5. Edge detection

The edge of a region is characterized by the abrupt change in grey level of intensity values when there is an intersection with another region. This approach has more advantages with images with good contrast. Since edges are local features, they are determined based on local information (Zaidi, 2006).

5.3.6. Markov random field model

Thresholding and clustering showed disadvantages regarding noise and intensity inhomogeneities, the Markov random field model (MRF) is not a segmentation method but a statistical model that considers spatial interactions between neighbouring and nearby pixels. Thus, the random nature of the noise and any texture in the image are taking into account by the MRF (Zaidi, 2006). This type of models can be incorporated into clustering segmentation algorithms; *hence the segmented region is obtained by maximizing a posteriori probability of the segmentation given the image data using iterative methods. The disadvantage of this method is linked to the selection of the parameters to control the strength of the spatial interactions* (Pham et al., 1998).

5.3.7. Artificial neural networks

The goal of this method is to emulate some aspects of the human information processing and to have the output in real time (Zaidi, 2006). The artificial neural networks (ANN) are massively networks of processing elements or nodes simulating biological learning. Each node is capable of performing elementary processors. To learn the ANN adapts weights assigned to the connections between nodes (Pham et al., 1998). *The massive connectionist architecture usually makes the system robust while the parallel processing enables the system to produce output in real time* (Zaidi, 2006). They are used as classifiers, where the weights are determined using training data, also it can be used as unsupervised clustering method as well as deformable models. Spatial information can be incorporated into its classification procedures.

5.3.8. Deformable models

These models are curves, surfaces or solids defined with an image, also they deform under the influence of internal and external forces. Delineation of an object boundary can be generated using a closed curve or surface placed near the desired boundary and then allowed to undergo an iterative relaxation process. External forces are usually derived from the image to drive the curve towards the desired feature of interest. Internal forces are calculated from within the curve to keep it smooth throughout the deformation (Zaidi, 2006).

5.4. Registration

Registration consist in geometric transformations assessment in order to relate two image series, one is a moving dataset and one stationary dataset (Brock et al., 2017). This process can be associated to the nature of the registration or the nature of the transformation. The nature of the registration can be based on extrinsic or intrinsic methods. The first ones use foreign objects into the image space, and the latest are based on information extracted from the patient (Maintz & Viergever, 1998). In the case of intrinsic methods, the registration can be based on a limited set of identified salient points (landmarks), on the alignment of segmented binary structures, or directly on measures computed from the image grey values, called voxel-property based (without prior data reduction by the segmentation). Landmarks can be points located in the patient anatomy, that can be identified interactively by the user, or points that can be associated with a geometric property of the anatomy. In principle this registration is versatile because it can be applied to any image, also these methods are mostly used to find rigid or affine transformations (Maintz & Viergever, 1998).

Segmentation-based methods, these can be rigid-model based, where anatomically the same structures are extracted from both images to be registered and used as sole input for the alignment procedure. When the extracted structures from one image is elastically deformed to fit the second image, this method can be deformable-model based (Maintz & Viergever, 1998).

Finally, the voxel-property based methods, two approaches can be used: to reduce the image grey content to a representative set of scalars and orientation and to use the full image content throughout the registration process (Maintz & Viergever, 1998). Regarding the nature of the transformation, there are four possibilities, rigid, affine, projective and curved (elastic). The transformation is called rigid, when only translations and rotations are allowed. If the transformation maps parallel lines onto parallel lines it is called affined. If it maps lines onto lines, then is called projective. If it maps lines onto curves, it is called elastic.

A composition of more than one transformation can be categorized as a single transformation of more complex ones. Zaidi (Zaidi, 2006) and Maintz (Maintz & Viergever, 1998) expressed the transformed coordinates as follows:

$$\begin{bmatrix} x' \\ y' \\ z' \\ 1 \end{bmatrix} = \begin{bmatrix} a_{11} & a_{12} & a_{13} & \Delta x \\ a_{21} & a_{22} & a_{23} & \Delta y \\ a_{31} & a_{32} & a_{33} & \Delta z \\ 0 & 0 & 0 & 1 \end{bmatrix} \begin{bmatrix} x_1 \\ y_2 \\ z_3 \\ 1 \end{bmatrix} \tag{1.53}$$

Where $\Delta t = [\Delta x, \Delta y, \Delta z]^T$ is an arbitrary translation vector, a_{ij} is the rotation matrix defined as follows:

$$a_{ij} = a^1_{ik}\, a^2_{kl}\, a^3_{lj}$$

$$a^1 = \begin{bmatrix} 1 & 0 & 0 \\ 0 & \cos\theta_1 & -\sin\theta_1 \\ 0 & \sin\theta_1 & \cos\theta_1 \end{bmatrix}$$

$$a^2 = \begin{bmatrix} \cos\theta_2 & 0 & \sin\theta_2 \\ 0 & 1 & 0 \\ -\sin\theta_2 & 0 & \cos\theta_2 \end{bmatrix} \tag{1.54}$$

$$a^3 = \begin{bmatrix} \cos\theta_3 & -\sin\theta_3 & 0 \\ \sin\theta_3 & \cos\theta_3 & 0 \\ 0 & 0 & 1 \end{bmatrix}$$

Where a^i rotates the image around the axis “i” by an angle θ_i.

5.4.1. Rigid

A rigid or affine 3-D transformation can be described as a single constant matrix equation as follows:

$$x'_i = a_{ij} x_j \tag{1.55}$$

Where x_j and x'_i are the old and new coordinate vectors respectively. In the case of affine transformation, a_{ij} is unrestricted.

5.4.2. Elastic

In the case of elastic transformations these constant matrices cannot be used. Generally, in these cases, the transformation is represented in terms of a local vector displacement (disparity) field, or as a polynomial transformation in terms of the old coordinates. Until this point all different steps associate to the dosimetric workflow have been covered. Last step of this chain is the absorbed-dose calculation.

5.5. Absorbed-dose calculation approaches

In reference dosimetry, the absorbed dose can be calculated using S-values from a reference model.

In TRT, the objective is to assess patient-specific dosimetry. Patients are different from reference models in terms of total-body weight and size, organs masses, etc. Also, depending on the emission that is within the source, the radiation transport algorithm implemented for absorbed dose calculation may differ. Therefore, considerations regarding the size of the source and targets vs. radiation range are key aspects for the selection of absorbed dose calculation algorithms.

TRT patient data sets are represented in 2D (pixel maps) or 3D (voxel maps) images in which the provided information will vary according to the biokinetics of the radiopharmaceutical product inside an organ.

Such a general case, one can considers of homogenous medium with a volume V, also for simplicity only γ-emissions uniformly distributed in V are taken into account. The absorbed dose a given point will depends on its the distance. Figure 1.28 illustrated the case in these conditions are presented.

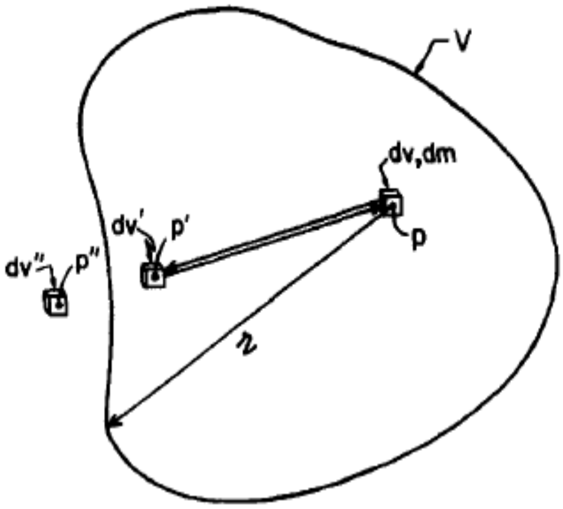

Figure 1.28: Illustration to show how to estimate the absorbed dose due to γ-emissions at point P within a homogeneous, uniformly radioactive object V. Image from (Attix, 2004).

In this case two hypothesis can be made, one, the volume V is surrounded by an identical medium, infinite, homogeneous and non-radioactive. Two, volume V is surrounding by air (which is not going to be considered). The three points, p, p' and p'' are points of interests considering volumes dv, dv' and dv''. If the volume has a mean effective attenuation coefficient μ and considering $e^{-\mu r}$ as the fraction of γ-emissions escaping from V in the direction "r" from p, the value of absorbed fraction in polar coordinates can be expressed as in (Attix, 2004):

$$\phi(p' \leftarrow p) = \frac{1}{4\pi}\int_{\theta=0}^{\pi}\int_{\beta=0}^{2\pi}(1 - e^{-\mu r})\ sin\theta\ d\theta d\beta \qquad 1.56$$

One case, in which photons might not have an influence in the absorbed dose result, is when the size of the volume is reduced, for instance, at cellular level. In this case the absorbed dose is going to be related to the integration of particle stopping powers. Then, the absorbed fraction in this case can be expressed as follows:

$$\phi(p' \leftarrow p, E_i) = \int_0^\infty \psi_{p' \leftarrow p}(x) \frac{1}{E_i} \frac{dE}{dX}\bigg|_{X(E_i)-x} dx \qquad 1.57$$

Where $\psi_{p' \leftarrow p}(x)$ is the geometric reduction factor, E_i is the initial energy of the ith particle, $\frac{dE}{dX}\Big|_{X(E_i)-x}$ is the stopping power evaluated at $X(E_i) - x$, $X(E_i)$ is the range of a particle of energy E_i , after passing a distance x through the medium. The geometric factor is the mean probability that a randomly directed vector of length x starting from a random point within p ends within p'. Its value depends on source and target geometries (Goddu et al., 1994).

The calculation of absorbed doses in a patient data set can done using different approaches.

5.5.1. Local energy deposition approach

This method allows calculating the beta contribution to the 3D dose distribution by multiplying the time-integrated activity in the voxel for a unique dosimetric factor. Here, all kinetic energy released from β-particles are considered as non-penetrating radiation; hence, all energy deposition is within the voxel. The dosimetric factor, for a continuous beta spectrum, is calculated as the coefficient of the mean beta energy emitted per decay and the voxel mass, as follows (Pacilio et al., 2015):

$$S_{LED} = \frac{E_\beta^{mean}}{mass_{voxel}} \qquad 1.58$$

An application of this method was proposed by Pasciak et al. for selective internal radiation therapy (SIRT) (Pasciak et al., 2014). Here, the absorbed dose at organ-level $D_{abs}(Gy)$ can be estimated as follows:

$$D_{abs}(Gy) = \frac{E_{abs}(J)}{m(kg)} = \frac{E_{com}\left(\frac{J}{ml}\right)}{\rho_{organ}\left(\frac{kg}{ml}\right)} \qquad 1.59$$

Where E_{com} is the committed total energy released per unit volume, E_{abs} is the energy absorbed, ρ is the density and "m" is the mass of the segmented volume. Then, E_{com} can be estimated as follows:

$$E_{com}\left(\frac{J}{ml}\right) = A_0\left(\frac{Bq}{ml}\right) * E_{avg} * \int_0^\infty e^{-\lambda t} dt = \frac{A_0}{\lambda} * E_{avg} \qquad 1.60$$

Where E_{avg} and λ are the average energy release per decay and the decay constant for the radionuclide, respectively.

5.5.2. Dose point kernel (DPK) approach

According to Bardiès et al. DPK can be defined as the radial distribution of absorbed dose around an isotropic point source in an infinite homogeneous propagation medium (Bardiès et al., 2003). *The superposition concept is implicit in this approach. Any source volume can be broken down into a set of point sources, and the determination of dose distribution around point sources allows non-point sources to be treated by suitable summation* (Bardiès et al., 2003).

In an analytic way to express the dose point kernel, Giap et al. show for ^{131}I its two contributions (Giap et al., 1995), from penetrating and non-penetration emissions as follows:

$$k(r) = k_\gamma(r) + k_\beta(r) \qquad 1.61$$

In the case of $k_\gamma(r)$, considering the inverse square, attenuation, and scatter build-up effects, the same authors expressed $k_\gamma(r)$ as shown in equation 1.62:

$$k_\gamma(r) = c\sum_{i}^{N_\gamma} n_i E_i \left[\left({}^{\mu_{en}}/_{\rho}\right)\frac{1}{4\pi r^2}e^{-\mu r}B_{en}(\mu r)\right] \qquad 1.62$$

Where c = 1.60x10^{-8}g cGy MeV^{-1}, N_γ is the total number of photons emitted per disintegration, n_i is the number of the ith gamma radiation emitted per disintegration, E_i is the mean energy of the ith gamma radiation (MeV), μ_{en} is the linear photon energy-absorption coefficient (cm^{-1}) at energy E_i, $\mu$is the linear photon attenuation coefficient for the same energy, ρ is the density of the medium (g*cm^{-3}), and B_{en} is the energy absorption build-up factor at the distance μr.

Bardiès (Bardiès & Myers, 1990) expressed the $k_\beta(r)$, such as “scaled point kernel”, as it is presented in equation 1.63:

$$k_\beta(r) = F(x/r_0, E_0) = 4\pi\rho x^2 r_0 \Phi(x, E_0) \qquad 1.63$$

Where ρ is the density of the medium, r_0 is the continuous slowing down approximation (CSDA) range at energy E_0 and $\Phi(x, E_0)$ is the specific absorbed fraction. The CSDA is associated to the stopping power for the same energy range.

Using the DPK expressed in equation 1.61, the absorbed dose can be estimated, using the inverse Fourier transform of the convolution result from the TIA Fourier transform and the kernel Fourier transform, as follows:

$$D(r_T, T_D) = F^{-1}\left[\left(F\left(\tilde{A}(r_S, T_D)\right) * F(k)\right)\right] \qquad 1.64$$

A drawback using this approach is related to the homogeneous medium in which is used. To overcome this limitation the following approach can be used.

5.5.3. Dose voxel kernel approach

The methodology implemented for organ-based dosimetry, can be extrapolated to the voxel level, which are contained within the organ, then, explicitly non-uniform distribution of activity within target organs can be considered. From *MIRD Pamphlet 17*, the absorbed dose be applied in a three-dimensional array summation to assess the absorbed dose to a given target voxel k from N surrounding source voxels h (including absorbed dose contributions from the target voxel itself, h=0) (Bolch et al., 1999):

$$\bar{D}(voxel_k) = \sum_{h=0}^{N} \tilde{A}_{voxel_h} \cdot S(voxel_k \leftarrow voxel_h) \qquad 1.65$$

From equation 1.67, the Dose voxel kernel (DVK) can be generated using Monte Carlo simulation of voxel geometries; the radionuclide source will be placed at the centre of the voxel, and the absorbed dose will be estimated in surrounding voxels. The mathematical convolution of pre-calculated DVKs with TIA maps provides the absorbed dose distribution of the studied structure. The evaluation of equation 1.67 for all target voxels in the VOI can be made by the calculation of isodose contours and absorbed dose volume histograms (DVH) within the same region.

In order to perform the mathematical convolution, the DVK sampling must match image voxel size, otherwise resampling may be possible as published by Dieudonné et al. (Dieudonne et al., 2010) and Fernandez et al. (Fernández et al., 2013). Hence DVK must be generated for each radionuclide of interest and for any possible sampling. This is not an easy task, due to the variety of voxels size available for clinical and pre-clinical applications.

Aside of the work of Bolch in MIRD Pamphlet 17, Lanconelli et al. (Lanconelli et al., 2012) and Amato et al. (Amato et al., 2013) have published DVK or voxel S-value (VSV) for several radionuclides, for different voxel sizes.

DVK or VSV can be expressed as follows:

$$S(voxel_k \leftarrow voxel_h) = \sum_{i} \Delta_i \cdot \frac{\phi(voxel_k \leftarrow voxel_h)}{m_{voxel_k}} \qquad 1.66$$

Where Δ_i is the mean energy of the emission particle i per nuclear transition, $\phi(voxel_k \leftarrow voxel_h)$ is the absorbed fraction to target voxel k per emission of radiation particle i from within source voxel h, and m_{voxel_k} is the mass of tissue within target voxel k.

As was shown by Dieudonné et al. (Dieudonné et al., 2013), the dose voxel kernel in a certain group of voxels considering its density variation $\overline{D}(voxel_k, \rho_k)$ can be expressed as in equation 1.67:

$$\overline{D}(voxel_k, \rho_k) = \overline{D}(voxel_k) \times \frac{\rho}{\rho_k} \qquad 1.67$$

Where ρ is the material density implemented in the Monte Carlo simulation of the non-corrected kernel. Also taking into account ideas from Schneider et al. (Schneider et al., 2000) information from CT images can be incorporated to correct for tissue density variation for this approach.

5.5.4. Monte Carlo Approach

This method is considered the most accurate to estimate absorbed doses at any scale. Monte Carlo simulation considers the explicit radiation transport within heterogeneous media using random numbers. The SPECT image will provides the radioactivity information and hence its heterogeneity distribution within a VOI. Still, the best scenario will provide activity in each voxel, assuming that activity (or TIA) is uniform in each voxel. This image represents an emission probability map for the definition of voxel sources in the Monte Carlo simulation. CT images contain the anatomical information and are going to be associated with density tissue characteristics for each voxel. The MC codes have available different physics list to consider all physical interactions of all emission within each voxel. For each simulated particle its movement and interactions within each voxel are going to be recorded and tracked, providing the absorbed dose deposited in each voxel.

These codes are used for the estimation of S-values in pre-clinical (cellular and small animal) or clinical dosimetry, or for patient-specific 3D dosimetry: Fluka (Botta et al., 2013), GATE (Mauxion et al., 2013; Sarrut et al., 2014), MINERVA (Lehmann et al., 2005), MCNP (Bitar et al., 2007; Boutaleb et al., 2009) can be cited. Some of them qualify as treatment planning systems, like the Dose-Planning method (Dewaraja et al., 2005), the 3D-RD (Hobbs et al., 2009), Raydose (Marcatili et al., 2013), and others. Another way to apply MC codes, is to estimate the energy rate deposited per voxel per time point and calculate the absorbed dose rate per voxel, by dividing it by the voxel mass. Finally, the absorbed dose rate per voxel can be integrated and DVH can be created if needed.

5.5.5. Tabular approach

Different platforms have databases containing S-values results, for a combination of source-target organs, for a different radionuclide, for a specific anthropomorphic model. These S values can in turn be calculated using local energy deposition, or convolution, or MC approaches. The first software containing such information was called MIRDOSE (M G Stabin, 1996), which was developed by the Radiation Internal Dose Information Center (RIDIC) at the Oak Ridge National

Laboratory in 1980s. Three versions were created, allowing more than 200 radionuclides and 10 anthropomorphic models in the latest version (McParland, 2010). The second software developed was OLINDA/EXM, this version included more than 800 radionuclides, more anthropomorphic models, for instance the pregnant women, spherical tumours and 4 specific organ/tissue models such as the prostate gland, the peritoneal cavity, the kidneys and a model of head and brain. This version also included a menu to perform curve fitting.

Nowadays the second version of OLINDA/EXM is distributed by HERMES Medical Solutions (https://www.hermesmedical.com/). In principle both versions of OLINDA can be used for model (reference) dosimetry. These two software fulfil most of the requirements of ICRP to perform reference dosimetry. They can also be used for patient-specific dosimetry (adjusted model-based dosimetry) because patient organ masses can be introduced to modify reference S values.

In 2017, the “Internal Dose Assessed by Computer (IDAC-Dose2.1) (Andersson et al., 2017) was released to the community, this software fulfil all ICRP requirements for reference dosimetry, but only considers the two adult models from ICRP 110.

Another code use in radiation safety is “Activity and internal dose estimates” (AIDE) (Bertelli et al., 2008), which incorporates both *in vivo* biodistribution and *in vitro* assay data. With this software the biokinetic models can be edited.

6. Discussion and position of the doctoral project

The objective of clinical dosimetry is the determination of the absorbed dose within the patient, both for tumours and normal (critical) organs/tissues. Several steps have to be considered to assess this quantity. The dosimetric workflow described in this chapter tries to summarize those steps; each of them has their own background, their own theory, and multiple possibilities have been considered in the literature to address them in an optimal way.

The absorbed dose is obtained for radiopharmaceutical that can be used for diagnostic or therapeutic purposes. The dosimetric workflow to implement will not be the same for these two types of clinical applications. Different studies have to be done in order to introduce a diagnostic radiopharmaceutical in clinical practice. These studies initially occur at cellular and/or preclinical level. In the case of preclinical studies, initial biokinetics is established. Then, extrapolating the results from the preclinical level to humans is necessary to estimate the absorbed dose that could be delivered to human subjects.

In this doctoral project three diagnostic radiopharmaceuticals were studied by determining the biokinetics for several organs, based on organ harvesting or using images, and extrapolating the animal results to the human, before proceeding to an absorbed dose calculation using reference dosimetric model data.

A possible marker of clinical dosimetry spread in nuclear medicine departments is the growing availability of dosimetric software. Few years ago, academic institutions and/or some hospitals were the only ones having the capabilities to perform clinical dosimetry. Unfortunately, the majority of academic software is not available to the community, and may suffer from lack of validation and continuous support. Nowadays, commercial workstations are becoming increasingly available to the Nuclear Medicine departments, allowing the possibility to perform dosimetric studies. However, the features and characteristics of these packages must be externally reviewed.

In this doctoral project four commercial solutions were compared using phantom experiments and clinical datasets. The way to perform this comparison was challenging because even though some commercial solutions proceed similarly in some steps of the dosimetric workflow, for other steps their approaches are different. For these four workstation similarities and differences are presented.

The dosimetric chain was first validated by performing phantom experiments and using the TIAC as a point of comparison. As a further step in the case of two patients treated with ^{177}Lu-DOTATATE, TIAC, organ masses and absorbed doses were used as indexes of comparison between the different software. Having these results and using references from the literature or other tools from the same workstations, absorbed dose comparisons were performed for a subset of tissues/organs. Recommendations were derived regarding how to perform the evaluation of a dosimetric workstation.

7. References of the chapter

Amato, E., et al. (2013). Use of the GEANT4 Monte Carlo to determine three-dimensional dose factors for radionuclide dosimetry. *Nuclear Instruments and Methods in Physics Research, Section A: Accelerators, Spectrometers, Detectors and Associated Equipment*, *708*, 15–18.

Andersson, M., et al. (2017). IDAC-Dose 2.1, an internal dosimetry program for diagnostic nuclear medicine based on the ICRP adult reference voxel phantoms. *EJNMMI Research*, *7*, 1–10.

Attix, F. (2004). *Introduction to radiological physics and radiation dosimetry*. Germany: Wiley-VCH.

Axelsson, B., et al. (1984). Subtraction of comptron-scattered photons in single-photon emission computed tomography. *J Nucl Med*, *25*, 490–494.

Bailey, D. L., et al. (2015). In vivo quantification of 177Lu with planar whole-body and SPECT/CT gamma camera imaging. *EJNMMI Physics*, *2*(1), 20.

Bardiès, M., et al. (2003). *Therapeutic applications of monte carlo calculations in nuclear medicine*. Bristol and Philadelphia: IOP publishing Ltd.

Bardiès, M., & Myers, M. J. (1990). A simplified approach to alpha dosimetry for small spheres labelled on the surface. *Phys Med Biol*, *35*(11), 1551–61.

Baum, R. P. (2014). *Therapeutic Nuclear Medicine*.

Beauregard, J. M., et al. (2011). Quantitative 177Lu SPECT (QSPECT) imaging using a commercially available SPECT/CT system. *Cancer Imaging*, *11*, 56–66.

Becker, J., et al. (2007). About Katja, a virtual human phantom of a 24 week pregnant woman. *J. Univ. Appl. Sci. Mittweide*, *3*, 5–7.

Benua, R. S., et al. (1962). The relation of radioiodine dosimetry to results and complications in the treatment of metastatic thyroid cancer. *The American Journal of Roentgenology, Radium Therapy, and Nuclear Medicine*, *87*, 171–182.

Bertelli, L., et al. (2008). AIDE: internal dosimetry software. *Radiation Protection Dosimetry*, *130*(3), 358–367.

Beykan, S., et al. (2018). Patient-specific dosimetry of 177Lu-DOTATATE peptide receptor therapy with high activities. *Eur J Nucl Med Mol Imaging*, *45*(Suppl 1), S33.

Bitar, A., et al. (2007). A voxel-based mouse for internal dose calculations using Monte Carlo simulations (MCNP). *Phys Med Biol*, *52*(4), 1013–1025.

Bodei, L., et al. (2008). Long-term evaluation of renal toxicity after peptide receptor radionuclide therapy with 90Y-DOTATOC and 177Lu-DOTATATE: The role of associated risk factors. *Eur J Nucl Med Mol Imaging*, *35*, 1847–1856.

Bodei, L., et al. (2014). Peptide Receptor Radionuclide Therapy for Advanced Neuroendocrine Tumors. *Thoracic Surgery Clinics*, *24*(3), 333–349.

Bodei, L., et al. (2008). EANM procedure guideline for treatment of refractory metastatic bone pain. *Eur J Nucl Med Mol Imaging*, *35*(10), 1934–1940.

Bolch, W. E., et al. (1999). MIRD pamphlet No. 17: the dosimetry of nonuniform activity distributions--radionuclide S values at the voxel level. Medical Internal

Radiation Dose Committee. *J Nucl Med*, *40*(1), 11S–36S.

Bolch, W. E., et al. (2009). MIRD pamphlet No. 21: a generalized schema for radiopharmaceutical dosimetry--standardization of nomenclature. *J Nucl Med*, *50*(21), 477–484.

Botta, F., et al. (2013). Use of the FLUKA Monte Carlo code for 3D patient-specific dosimetry on PET-CT and SPECT-CT images. *Phys Med Biol*, *58*(22).

Boutaleb, S., et al. (2009). Impact of mouse model on pre-clinical dosimetry in targeted radionuclide therapy. *Proc. IEEE*, *97*, 2076–2085.

Brock, K. K., et al. (2017). Use of image registration and fusion algorithms and techniques in radiotherapy: Report of the AAPM Radiation Therapy Committee Task Group No. 132: Report. *Med Phys*, *44*(7), e43–e76.

Brolin, G., et al. (2015). Pharmacokinetic digital phantoms for accuracy assessment of image-based dosimetry in (177)Lu-DOTATATE peptide receptor radionuclide therapy. *Phys Med Biol*, *60*(15), 6131–49.

Brown, S., et al. (2008). Investigation of the relationship between linear attenuation coefficients and CT Hounsfield units using radionuclides for SPECT. *Applied Radiation and Isotopes*, *66*(9), 1206–1212.

Buvat, I., et al. (1994). Scatter correction in scintigraphy: the state of the art. *Eur J Nucl Med*, *21*(7), 675–694.

Buvat, I., et al. (1995). Comparative assessment of nine scatter correction methods based on spectral analysis using Monte Carlo simulations. *J Nucl Med*, *36*(8), 1476–88.

Carlier, T, et al. (2013). Assessment of acquisition protocols for routine imaging of Y-90 using PET/CT. *EJNMMI Research*, 3:11.

Chang, L. T. (1978). A method for attenuation correction in radionuclide computed tomography. *IEEE Transactions on Nuclear Science*, *25*(1), 638–643.

Cherry, S., Sorenson, J., & Phelps, M. (2012). *Phys Med Biol*. Philadelphia.

Coakley, A. J. (1998). Editorial Thyroid stunning. *Eur J Nucl Med*, *25*(3), 203–204.

Conry, B. G., et al. (2010). Comparison of68Ga-DOTATATE and18F-fluorodeoxyglucose PET/CT in the detection of recurrent medullary thyroid carcinoma. *Eur J Nucl Med Mol Imaging*, *37*(1), 49–57.

Cooper, D. S., et al. (2009). Revised American Thyroid Association Management Guidelines for Patients with Thyroid Nodules and Differentiated Thyroid Cancer. *Thyroid*, *19*(11), 1167–1214.

Cremonesi, M., et al. (2006). Dosimetry in Peptide radionuclide receptor therapy: a review. *J Nucl Med*, *47*(9), 1467–75.

Dewaraja, Y. K., et al. (2012). MIRD pamphlet No. 23: quantitative SPECT for patient-specific 3-dimensional dosimetry in internal radionuclide therapy. *J Nucl Med*, *53*(8), 1310–25.

Dewaraja, Y. K., et al. (2005). Accurate dosimetry in 131I radionuclide therapy using patient-specific, 3-dimensional methods for SPECT reconstruction and absorbed dose calculation. *J Nucl Med*, *46*(5), 840–9.

Dewaraja, Y., et al. (1998). Quantitative 131i SPECT with triple energy window compton scatter correction. *IEEE Transactions on Nuclear Science*, *45*(6), 3109–3114.

Dieudonne, A., et al. (2010). Fine-Resolution Voxel S Values for Constructing Absorbed Dose Distributions at Variable Voxel Size. *J Nucl Med*, *51*(10), 1600–1607.

Dieudonné, A., et al. (2013). Study of the impact of tissue density heterogeneities on 3-dimensional abdominal dosimetry: comparison between dose kernel convolution and direct Monte Carlo methods. *J Nucl Med*, *54*(2), 236–43.

Divoli, A., et al. (2009). Effect of Patient Morphology on Dosimetric Calculations for Internal Irradiation as Assessed by Comparisons of Monte Carlo Versus Conventional Methodologies. *J Nucl Med*, *50*(2), 316–323.

Dogdas, B., et al. (2007). Digimouse: A 3D whole body mouse atlas from CT and cryosection data. *Phys Med Biol*, *52*(3), 577–587.

Eckerman, K., & Endo, A. (2008). MIRD: radionuclide data and decay schemes 2nd edn (Reston, VA: Society for Nuclear Medicine).

Ersahin, D., et al. (2011). Targeted radionuclide therapy. *Cancers*, *3*(4), 3838–3855.

Ezziddin, S., et al. (2011). Impact of the Ki-67 proliferation index on response to peptide receptor radionuclide therapy. *Eur J of Nucl Med Mol Imaging*, *38*(3), 459–466.

Fernández, M., et al. (2013). A fast method for rescaling voxel S values for arbitrary voxel sizes in targeted radionuclide therapy from a single Monte Carlo calculation. *Medical Physics*, *40*(8), 082502.

Fill, U. A., et al. (2004). Adult female voxel models of different stature and photon conversion coefficients for radiation protection. *Health Physics*, *86*(3), 253–272.

Finn, L. E., et al. (2017). A Phase 2 Study of Actinium-225 (225Ac)-Lintuzumab in Older Patients with Previously Untreated Acute Myeloid Leukemia (AML) Unfit for Intensive Chemotherapy. *Blood*, *130*(Suppl 1), 2638 LP-2638.

Fisher, H. L., & Snyder, W. (1966). Variation of dose delivered by 137Cs as a function of body size from infancy to adulthood. *ORNL-4007, Oak Ridge, TN: Oak Ridge National Laboratory*, 221–228.

Flynn, A. A., et al. (2001). A mouse model for calculating the absorbed beta-particle dose from (131)I- and (90)Y-labeled immunoconjugates, including a method for dealing with heterogeneity in kidney and tumor. *Radiation Research*, *156*(1), 28–35.

Forrer, F., et al. (2009). Bone marrow dosimetry in peptide receptor radionuclide therapy with [177Lu-DOTA0,Tyr3]octreotate. *Eur J Nucl Med Mol Imaging*, *36*(7), 1138–1146.

Garkavij, M., et al. (2010). 177Lu-[DOTA0,Tyr3] Octreotate therapy in patients with disseminated neuroendocrine tumors: Analysis of dosimetry with impact on future therapeutic strategy. *Cancer*, *116*(Supple 4), 1084–1092.

Giammarile, F., et al. (2011). EANM procedure guidelines for the treatment of liver cancer and liver metastases with intra-arterial radioactive compounds. *Eur J Nucl Med Mol Imaging*,38,1393–1406.

Giap, H. B., et al. (1995). Validation of a dose-point kernel convolution technique for internal dosimetry. *Phys Med Biol*, *40*(3), 365–381.

Gill, M. R., et al. (2017). Targeted radionuclide therapy in combined-modality regimens. *The Lancet Oncology*, *18*(7), e414–e423.

Goddu, S. M., et al. (1994). Multicellular dosimetry for micrometastases: dependence of self-dose versus cross-dose to cell nuclei on type and energy of radiation and subcellular distribution of radionuclides. *J Nucl Med*, *35*(3), 521–30.

Grimes, J., et al. (2012). The accuracy and reproducibility of SPECT target volumes and activities estimated using an iterative adaptive thresholding technique. *Nucl Med Commun*, *33*(12), 1254–1266.

Gudkov, S. V., et al. (2015). Targeted radionuclide therapy of human tumors. *International Journal of Molecular Sciences*, *17*(1), 1–19.

Guerriero, F., et al. (2013). Kidney dosimetry in 177Lu and 90Y peptide receptor radionuclide therapy: Influence of image timing, time-activity integration method, and risk factors. *BioMed Res Int.*, *2013*, 1–12.

Hänscheid, H., et al. (2013). EANM dosimetry committee series on standard operational procedures for pre-therapeutic dosimetry II. Dosimetry prior to radioiodine therapy of benign thyroid diseases. *Eur J Nucl Med Mol Imaging*, *40*(7), 1126–1134.

Hänscheid, H., et al. (2018). Dose Mapping after Endoradiotherapy with 177 Lu-DOTATATE/-TOC by One Single Measurement after Four Days. *J Nucl Med*, *59*, 75–81.

Haugen, B. R., et al. (2016). 2015 American Thyroid Association Management Guidelines for Adult Patients with Thyroid Nodules and Differentiated Thyroid Cancer. In *Thyroid* (Vol. 26, pp. 1–133).

Hegenbart, L., et al. (2008). A Monte Carlo study of lung counting efficiency for female workers of different breast sizes using deformable phantoms. *Phys Med Biol*, *53*(19), 5527–5538.

HERMES Medical Solutions. (2016). *HERMES Data Analysis Applications-OLINDA Handbook*.

Hindorf, C., et al. (2010). EANM dosimetry committee guidelines for bone marrow and whole-body dosimetry. *Eur J Nucl Med Mol Imaging*, *37*(6), 1238–1250.

Hindorf, C., et al. (2004). Evaluation of parameters influencing S values in mouse dosimetry. *J Nucl Med*, *45*(11), 1960–5.

Hobbs, R. F., et al. (2011). A treatment planning method for sequentially combining radiopharmaceutical therapy and external radiation therapy. *Int. J. Radiation Oncology Biol. Phys.*, *80*(4), 1256–1262.

Hobbs, R. F., et al. (2009). 124I PET-Based 3D-RD Dosimetry for a Pediatric Thyroid Cancer Patient: Real-Time Treatment Planning and Methodologic Comparison. *J Nucl Med*, *50*(11), 1844–1847.

Hoskin, P., et al. (2014). Efficacy and safety of radium-223 dichloride in patients with castration-resistant prostate cancer and symptomatic bone metastases, with or without previous docetaxel use: A prespecified subgroup analysis from the randomised, double-blind, phase 3 ALSYMPC. *The Lancet Oncology*, *15*(12), 1397–1406.

Howe, D. B., et al. (2008). *Consolidated Guidance About Materials Licenses.*

Program-specific Guidance About Medical Use Licenses.

Hui, T., et al. (1994). A Mouse Model for Calculating Cross- Organ Beta Doses from Yttrium-90- Labeled Immunoconjugates. *Cancer*, *73*(S3), 951–957.

IAEA. (2009). *Release of patients after radionuclide therapy. SRS. No.63. International Atomic Energy Agency (IAEA)*. Vienna.

IAEA. (2014). Nuclear medicine physics: a handbook for students and teachers. Vienna.

Ichihara, T., et al. (1993). Compton Scatter Compensation the Triple-Energy Window Method for Single- and Dual-Isotope SPECT. *J Nucl Med*, *34*(12), 2216–2221.

ICRP. (1975). ICRP 23: Report of the task group on reference man. *Annals of the ICRP*, 0–480.

ICRP. (2007). ICRP-103. The 2007 recommendations of the International Commision on Radiological Protection. *Annals of the ICRP*, *2–4*, 1–334.

ICRP. (2008). ICRP Publication 110: Adult reference computational phantoms. *Annals of the ICRP*, *39*(2), 1–165.

ICRP. (2015). ICRP-128. Radiation Dose to Patients from Radiopharmaceuticals : a Compendium of Current Information Related to Frequently Used Substances. *Ann. ICRP*, *44*, 7–321.

ICRP. (2016). ICRP Publication 133: The ICRP computational framework for internal dose assessment for reference adults: specific absorbed fractions. *Ann. ICRP*, *45*(2), 1–74.

Ilan, E., et al. (2015). Dose response of pancreatic neuroendocrine tumors treated with peptide receptor radionuclide therapy using 177Lu-DOTATATE. *J Nucl Med*, *56*(2), 177–182.

Jurcic, J. G., et al. (2016). Phase I Trial of Targeted Alpha-Particle Therapy with Actinium-225 (225Ac)-Lintuzumab and Low-Dose Cytarabine (LDAC) in Patients Age 60 or Older with Untreated Acute Myeloid Leukemia (AML). *Blood*, *128*(22), 4050 LP-4050.

Keenan, M. A., et al. (2010). RADAR Realistic Animal Model Series for Dose Assessment. *J Nucl Med*, *51*(3), 471–476.

Kolbert, K. S., et al. (2003). Murine S factors for liver, spleen, and kidney. *J Nucl Med*, *44*(5), 784–91.

Konijnenberg, M. W., et al. (2004). A Stylized Computational Model of the Rat for Organ Dosimetry in Support of Preclinical Evaluations of Peptide Receptor Radionuclide Therapy with 90 Y, 111 In, or 177 Lu. *J Nucl Med*, *45*(7), 1260–1269.

Koral, K. F., et al. (1988). SPECT Compton-scattering correction by analysis of energy spectra. *J Nucl Med*, *29*(2), 195–202.

Kramer, R., et al. (2004). All about FAX: A Female Adult voXel phantom for Monte Carlo calculation in radiation protection dosimetry. *Phys Med Biol*, *49*(23), 5203–5216.

Kramer, R., et al. (2003). All about Max: a male adult voxel phantom for Monte Carlo calculations in radiation protection dosimetry. *Phys. Med. Biol.*, *48*, 1239–1261.

Kratochwil, C., et al. (2016). 225Ac-PSMA-617 for PSMA-Targeted -Radiation

Therapy of Metastatic Castration-Resistant Prostate Cancer. *J Nucl Med*, *57*(12), 1941–1944.

Krenning, E. P., et al. (1994). Radiotherapy with a Radiolabeled Somatostatin Analogue, [111In-DTPA-d-Phe1]-Octreotide: A Case History. *Annals of the New York Academy of Sciences*, *733*(1), 496–506.

Lanconelli, N., et al. (2012). A free database of radionuclide voxel S values for the dosimetry of nonuniform activity distributions. *Phys Med Biol*, *57*(2), 517–533.

Lassmann, M., et al. (2008). EANM Dosimetry Committee series on standard operational procedures for pre-therapeutic dosimetry I : blood and bone marrow dosimetry in differentiated thyroid cancer therapy, Eur J Nucl Med Mol Imaging,35(7),1405–1412.

Lee, C., et al. (2007). Hybrid computational phantoms of the male and female newborn patient: NURBS-based whole-body models. *Phys Med Biol*, *52*(12), 3309–3333.

Lees, W., et al. (2002). The clinical effects of thyroid stunning after diagnostic whole-body scanning with 185 MBq 131I. *Eur J Nucl Med*, *29*(11), 1421–1427.

Lehmann, J., et al. (2005). Monte Carlo treatment planning for molecular targeted radiotherapy within the MINERVA system. *Phys Med Biol*, *50*(5), 947–958.

Lenta, C., et al. (2000). Validation of an attenuation correction system for quantification of iodine-131 images. *Eur J Nucl Med*, *27*, 924.

Lhommel, R., et al. (2010). Feasibility of ^{90}Y TOF PET-based dosimetry in liver metastasis therapy using SIR-Spheres. *Eur J Nucl Med Mol Imaging*,37,1654–1662.

Ljungberg, M., et al. (2016). MIRD Pamphlet No. 26: Joint EANM/MIRD Guidelines for Quantitative 177Lu SPECT Applied for Dosimetry of Radiopharmaceutical Therapy. *J Nucl Med*, *57*, 151–162.

Loevinger, R., et al. (1991). *MIRD Primer for absorbed dose calculations, revised*. New York: The Society of Nuclear Medicine.

Luster, M., et al. (2008). Guidelines for radioiodine therapy of differentiated thyroid cancer. *Eur J Nucl Med Mol Imaging*, *35*(10), 1941–1959.

Maintz, J. B. A., & Viergever, M. A. (1998). A survey of medical image registration. *Medical Image Analysis*, *2*(1), 1–36.

Marcatili, S., et al. (2013). Development and validation of RAYDOSE: A Geant4-based application for molecular radiotherapy. *Phys Med Biol*, *58*(8), 2491–2508.

Marcatili, S., et al. (2014). Multi-scale hybrid models for radiopharmaceutical dosimetry with Geant4. *Phys Med Biol*, *59*(24), 7625.

Mas, J., et al. (1990). Scatter correction in planar imaging and SPECT by constrained factor analysis of dynamic structures (FADS). *Phys Med Biol*, *35*(11), 1451–1465.

Mauxion, T., et al. (2013). Improved realism of hybrid mouse models may not be sufficient to generate reference dosimetric data. *Med Phys*, *40*(5), 52501.

McParland, B. J. (2010). *Nuclear Medicine Radiation Dosimetry: Advanced Theoretical Principles*. Springer Science & Business Media.

McQuillan, A. D., et al. (2015). Phase II study of first-line 131I-rituximab radioimmunotherapy in follicular non-Hodgkin lymphoma and prognostic 18F-fluorodeoxyglucose positron emission tomography. *Leukemia and Lymphoma*, *56*(5), 1271–1277.

Menzel, H. G., et al. (2009). ICRP Publication 110. Realistic reference phantoms: an ICRP/ICRU joint effort. A report of adult reference computational phantoms. *Annals of the ICRP*, *39*(2), 1.

Minarik, D., et al. (2005). A New Method to Obtain Transmission Images for Planar Whole-Body Activity Quantification. *Cancer Biotherapy & Radiopharmaceuticals*, *20*(1), 72–76.

Mirzaei, S., et al. (2013). Easy-to-Use Online Software Package for Internal Dose Assessment After Radionuclide Treatment in Clinical Routine. *Clin Nucl Med*, *38*(9), 686–690.

Muthuswamy, M. S., et al. (1998). A mouse bone marrow dosimetry model. *J Nucl Med*, *39*(7), 1243–1247.

Mutic, S., et al. (2003). Quality assurance for computed-tomography simulators and the computed- tomography-simulation process: Report of the AAPM Radiation Therapy Committee Task Group No. 66. *Med Phys*, *30*(10), 2762–2792.

Nilsson, S. (2016). Radionuclide Therapies in Prostate Cancer: Integrating Radium-223 in the Treatment of Patients With Metastatic Castration-Resistant Prostate Cancer. *Current Oncology Reports*, *18*(2), 1–12.

Ogawa, K., et al. (1991). A Practical Method for Position-Dependent Compton-Scatter Correction in Single Photon Emission CT. *IEEE Transactions on Medical Imaging*, *10*(3), 408–412.

Oppenheim, B. E. (1984). ScatterCorrection for SPECT. *J Nucl Med*, *25*(8), 928–929.

Pacilio, M., et al. (2015). Differences in 3D dose distributions due to calculation method of voxel S-values and the influence of image blurring in SPECT. *Phys Med Biol*, *60*(5), 1945–64.

Pasciak, A. S., et al. (2014). A Comparison of Techniques for 90Y PET/CT Image-Based Dosimetry Following Radioembolization with Resin Microspheres. *Frontiers in Oncology*, *4*(May), 1–10.

Petoussi-Henss, N., et al. (2007). Patient-specific scaling of reference S-values for cross-organ radionuclide S-values: What is appropriate? *Radiation Protection Dosimetry*, *127*(1–4), 192–196.

Petoussi-Henss, N., et al. (2001). The GSF family of voxel phantoms. *Phys Med Biol*, *47*(1), 89.

Pham, D. L., et al. (1998). A Survey of current methods in medical image segmentation. *Annual Review of Biomedical Engineering*, 27.

Pouget, J. P., et al. (2011). Clinical radioimmunotherapy-the role of radiobiology. *Nature Reviews Clinical Oncology*, *8*(12), 720–734.

Raymond, K. W., & Siegel, J. A. (1984). Absolute quantitation of radioactivity using the buildup factor. *Med Phys*, *11*(2), 189–192.

Rizzieri, D. (2016). Zevalin®(ibritumomab tiuxetan): After more than a decade of treatment experience, what have we learned? *Critical Reviews in Oncology/Hematology*, 5-17.

Rosenblat, T. L., et al. (2010). Sequential cytarabine and α-particle immunotherapy with bismuth-213-lintuzumab (HuM195) for acute myeloid leukemia. *Clinical Cancer Research*, *16*(21), 5303–5311.

Sanders, J. C., et al. (2015). Quantitative SPECT/CT Imaging of 177Lu with In Vivo Validation in Patients Undergoing Peptide Receptor Radionuclide Therapy. *Mol Imaging Biol*, *17*(4), 585–593.

Sandström, M., et al. (2010). Individualized dosimetry in patients undergoing therapy with 177Lu-DOTA-D-Phe1-Tyr3-octreotate. *Eur J Nucl Med Mol Imaging*, *37*(2), 212–225.

Sarrut, D., et al. (2014). A review of the use and potential of the GATE Monte Carlo simulation code for radiation therapy and dosimetry applications. *Med Phys*, *41*(6).

Schneider, W., et al. (2000). Correlation between CT numbers and tissue parameters needed for Monte Carlo simulations of clinical dose distributions. *Phys Med Biol*, *45*, 459–78.

Schuchardt, C., et al. (2013). Dosimetry in Targeted Radionuclide Therapy : The Bad Berka Dose Protocol — Practical Experience. *Journal of Postgraduate Medicine, Education and Research*, *47*(March), 65–73.

Segars, W. P., et al. (2001). Modeling respiratory mechanics in the MCAT and spline-based MCAT phantoms. *IEEE Transactions on Nuclear Science*, *48*(1 I), 89–97.

Segars, W. P., & Tsui, B. M. W. (2002). Study of the Efficacy of Respiratory Gating in Myocardial SPECT Using the New 4D NCAT Phantom. *IEEE Transactions on Nuclear Science*, *49*(3), 675–679.

Segars, W. P., et al. (2004). Development of a 4-digital mouse phantom for molecular imaging research. *Mol Imaging Biol*, *6*(3), 149–159.

Segars, W., & Tsui, B. (2007). 4D MOBY and NCAT phantoms for medical imaging simulation of mice and men. *J Nucl Med*, *48*(supplement 2), 203P.

Seppenwoolde, J. H., et al. (2005). Internal radiation therapy of liver tumors: Qualitative and quantitative magnetic resonance imaging of the biodistribution of holmium-loaded microspheres in animal models. *Magnetic Resonance in Medicine*, *53*(1), 76–84.

Sharp, P. F., et al. (2005). *Practical nuclear medicine*. London: Springer.

Siegel, J. A, et al. (1999). MIRD pamphlet no. 16: Techniques for quantitative radiopharmaceutical biodistribution data acquisition and analysis for use in human radiation dose estimates. *J Nucl Med*, *40*(2), 37S–61S.

Siegel, J. A, et al. (1985). The buildup factor: effect of scatter on absolute volume determination. *J Nucl Med*, *26*(4), 390–394.

Silberstein, E. B., et al. (2012). The SNMMI Practice Guideline for Therapy of Thyroid Disease with 131I 3.0. *J Nucl Med*, *53*(10), 1633–1651.

Sisson, J. C., et al. (2006). The so-called stunning of thyroid tissue. *J Nucl Med*, *47*(9), 1406–1412.

Snyder, W., et al. MIRD Pamphlet No. 5: estimates of absorbed fractions for monoenergetic photon sources uniformly distributed in various organs of a heterogeneous phantom. *J Nucl Med*, *10*(Suppl. 3), 5–52.

Snyder, W. S., et al. (1978). MIRD pamphlet no. 5, revised: Estimates of specific absorbed fractions for photon sources uniformly distributed in various organs of a heterogeneous phantom. *New York, NY: Society of Nuclear Medicine*.

Snyder, W. S., et al. (1969). *Estimates of absorbed fractions for monoenergetic photon sources uniformly distributed in various organs of a heterogeneous phantom.* Oak Ridge National Lab., Tenn.

Spitzer, V. M., et al. (1998). The visible human dataset: The anatomical platform for human simulation. *Anatomical Record*, *253*(2), 49–57.

Stabin, M. G. (1996). MIRDOSE: personal computer software for internal dose assessment in nuclear medicine. *J Nucl Med*, *37*(3), 538–546.

Stabin, M. G. (2008). *Fundamentals of nuclear medicine dosimetry*. New York: Springer.

Stabin, M. G., et al. (2006). Voxel-based mouse and rat models for internal dose calculations. *J Nucl Med*, *47*(4), 655–9.

Stabin, M. G., et al. (2005). OLINDA/EXM: the second-generation personal computer software for internal dose assessment in nuclear medicine. *J Nucl Med*, *46*(6), 1023–1027.

Stokkel, M. P. M., et al. (2010). EANM procedure guidelines for therapy of benign thyroid disease. *Eur J Nucl Med Mol Imaging*, *37*(11), 2218–2228.

Sundlöv, A., et al. (2017). Individualised 177Lu-DOTATATE treatment of neuroendocrine tumours based on kidney dosimetry. *Eur J Nucl Med Mol Imaging*, *44*(9), 1480–1489.

Svensson, J., et al. (2016). Radiation exposure of the spleen during 177Lu-DOTATATE treatment and its correlation with haematological toxicity and spleen volume. *EJNMMI Physics*, *3*(1), 15.

Svensson, J., et al. (2016). A novel planar image-based method for bone marrow dosimetry in 177Lu-DOTATATE treatment correlates with haematological toxicity. *EJNMMI Physics*, *3*(1), 21.

The Council of the European Union. (2014). Directives - Council Directive 2013/59/Euratom. *Official Journal of the European Union*, 1–73.

Valkema, R., et al. (2002). Phase I study of peptide receptor radionuclide therapy with [111In-DTPA0]octreotide: The Rotterdam experience. *Sem Nucl Med*, *32*(2), 110–122.

Wild, D., et al. (2011). Alpha- versus beta-particle radiopeptide therapy in a human prostate cancer model (213Bi-DOTA-PESIN and 213Bi-AMBA versus 177Lu-DOTA-PESIN). *Cancer Research*, *71*(3), 1009–1018.

Williams, G., et al. (1986). The calculation of dose from external photon exposures using reference and realistic human phantoms and Monte Carlo methods. *Phys Med Biol*, *31*, 449–452.

Willowson, K., et al. (2008). Quantitative SPECT reconstruction using CT-derived corrections. *Phys Med Biol*, *53*(12), 3099–3112.

Xu, X. G., & Eckerman, K. F. (2009). *Handbook of anatomical models for radiation dosimetry*. CRC press.

Xu, X. G., et al. (2007). A boundary-representation method for designing whole-body radiation dosimetry models: Pregnant females at the ends of three gestational periods - RPI-P3, -P6 and -P9. *Phys Med Biol*, *52*(23), 7023–7044.

Xu, X. G., et al. (2008). Preliminary data for mesh-based deformable phantom development: is it possible to design person-specific phantoms on-demand. *ICRS-11 and RPSD*.

Zaidi, H. (2006). *Quantitative Analysis in Nuclear Medicine Imaging*. New York: Springer.

Zaidi, H., & Xu, X. G. (2007). Computational Anthropomorphic Models of the Human Anatomy: The Path to Realistic Monte Carlo Modeling in Radiological Sciences. *Annual Review of Biomedical Engineering*, *9*(1), 471–500.

Zankl, M., et al. (2005). GSF male and female adult voxel models representing ICRP Reference Man–the present status. *The Monte Carlo Method: Versatility Unbounded In A Dynamic Computing World*, 1–13.

Zankl, M., et al. (2002). Organ dose conversion coefficients for external photon irradiation of male and female voxel models. *Phys Med Biol*, *47*(14), 2367–85.

Zankl, M., et al, G. (1988). The construction of computer tomographic phantoms and their application in radiology and radiation protection. *Radiation and Environmental Biophysics*, *27*(2), 153–164.

Zhao, W., et al. (2018). Determination of gamma camera calibration factors for quantitation of therapeutic radioisotopes. *EJNMMI Physics*, *5*, 8.

Zubal, I. G., et al. (1994). Computerized three dimensional segmented human anatomy. *Med Phy, 299*.

1. Introduction

Regulations for new pharmaceuticals demand biodistribution and biokinetic studies in animal, prior evaluation in humans. Same pathway has to be followed by new radiopharmaceuticals (McParland, 2010). In that case, it is also required to provide an estimation of the irradiation potentially delivered in the human. This is obtained by extrapolation of pharmacokinetics data from the animal to the human. Hence, animals such as different types of monkeys, mice, rats, dogs or small pigs have been subject of investigation. Ideally the choice of the animal is based on a previous knowledge regarding the physiology of the animal compared to humans (the behavior of the radiopharmaceutical should be reasonably similar in the 2 species). However, this is not always the case, due to the financial cost associated to housing of the animals with respect to ethics requirements (McParland, 2010).

Depending on research laboratory facilities, biodistribution and biokinetics studies can be obtained from quantitative nuclear medicine (NM) imaging (SPECT, PET, or SPECT/CT or PET/CT or PET/MR), or by dissection of the small animal and counting of the radioactivity present in animal tissues. Both techniques have their own advantages/disadvantages, and require calibration of the equipment used to measure activity and different corrections factors.

For instance, in terms of advantages/disadvantages, in the case of the NM images less animals can be used, dynamic and/or many static acquisitions can be used to see the biokinetics followed by establishing the biodistribution of the radiopharmaceutical. Conversely, animals should be under anesthesia throughout, therefore depending on the organ studied, anesthesia could be an issue to consider. Other environmental aspects should also be considered such as the bed temperature. Also, animal movements can be an issue if the anesthesia does not work properly.

In the case of dissection, anesthesia is not an issue and normally animals are housed in special cages where environmental conditions are ideal. However, issues with this technique are related to the number of animals used per time point measurement (minimum 3) and the dissection technique that only provides for a time-point per animal: it is therefore not possible to perform longitudinal studies.

Three different radiopharmaceuticals were developed at two different research centers, at the "*Centre Hospitalier Universitaire (CHU) Hôpital Purpan"* in Toulouse, France and the "*Centro Uruguayo de Imagenología Molecular (CUDIM)*" in Montevideo, Uruguay. The aim of both centers was to assess the biodistribution of the products using small animals and then extrapolate the biokinetics results to humans. Finally, the "*Centre de Recherches en Cancerologie de Toulouse (CRCT)*" has collaboration agreements with both centers to do the absorbed and effective doses assessment.

At CHU-Hôpital Purpan [^{18}F]FNM (Fluoroethylnormemantine) was developed to better understand neurodegenerative diseases (Salabert et al., 2015). They explained *that this product is derived from memantine, which targets the open channel of the NMDA receptor (GluN)* (Salabert et al., 2018)*. These receptors are* *present in case of neurodegeneration, where neurotoxicity is induced by a massive influx of calcium following excessive activation of GluN. The [^{18}F]FNM crosses the blood-brain barrier and its distribution within the brain has been found to correlate well with the location of GluN. These receptors are also present in Alzheimer's disease; hence, in principle this radiopharmaceutical is a good candidate for human use in order to study neurological and psychiatric diseases*. This product was assessed in rats using PET/CT images (Salabert et al., 2018).

At CUDIM the first radiopharmaceutical developed was [^{11}C]SAM (S-adenosyl Methionine) which is a potential agent that can be used in the diagnosis of aggressive prostate cancer. Zoppolo et al. (Zoppolo et al., 2017) *explained that the overexpression of glycine N-methyltransferase (GNMT EC 2.1.1.20) could be present during prostate cancer progression. This enzyme is involved in the methylation catalysis of glycine to produce sarcosine using S-adenosyl methionine (SAM or AdoMet) as a substrate. As a result, the increased levels of GNMT cause an accumulation of sarcosine. It is important to note that this metabolite plays an intermediary role in cancer invasion and aggressiveness. The aim of CUDIM was to create a new PET tracer to improve sensitivity and specificity for primary prostate cancer detection in patients where biochemical failure is crucial.* The synthesis of this product was studied and reported (Zoppolo et al., 2017).

The second product successfully synthesized is the [^{18}F]SRF-101 (SR101 *N*-(3-[^{18}F]Fluoropropyl) sulphonamide) which is a Sulforhodamine 101 (SR101) derivative (Kreimerman et al., 2017). Kreimerman et al. *explained that this product has been reported as a specific marker of astroglia in the neocortex of rodents in vivo* (Kreimerman et al., 2018). *The astroglia is affected in the early stages of different neurologic diseases, and reactive astrocytes contribute to neuroinflammation at later stages. The CUDIM was focused on reactive astrocytosis in Alzheimer's disease*. Both products derived from CUDIM were assessed in mice using organ harvesting.

In this chapter, these three radiopharmaceuticals are addressed from the dosimetric point of view. In order to do so, biodistribution and biokinetics of the products have to be established and extrapolated from animal to human. Then, the Organ level internal dose assessment code (OLINDA) V1.0 (Stabin et al., 2005) is generally used for estimation of absorbed and effective doses, and can be considered as gold standard. Nowadays, OLINDA/EXM V2.0 (Stabin & Farmer, 2012; Stabin & Siegel, 2018) a new version is commercially available. A new software, based-on recent ICPR recommendations, called IDAC 2.1 (Andersson et al., 2017) can also be used for same purposes.

We estimated the absorbed and effective doses using the three software and compared the results. We tried to understand the differences between the results provided by the different codes, in regards of the reference models and the manner in which dosimetric quantities are estimated. Finally, the extrapolated results to humans can be compared with data using radiopharmaceutical products in voluntaries or patients. Chapter 3 addressed calibration process in a SPECT/CT system, this procedure is necessary previous the quantification of activity from patients and/or volunteers. An example of quantification process given dosimetric results is presented in chapter 4.

2. Material and Methods

2.1. Image data acquisition for [^{18}F]FNM based-on animal images and percentage of injected activity estimation

This study was conducted under protocols approved by French animal Ethics Committee (n°2016021711398144). Three Sprague Dawley female rats were anesthetized with 55 mg/kg of pentobarbital and a CT scan was performed. Intravenous injections of 67.8 ± 10 MBq of [^{18}F]FNM in the tail were performed at the beginning of PET acquisition. Acquisition was performed in list mode on PET/CT and lasted 70 min. PET list mode data were used to create 16 3D-sinograms such as dynamic histograms (3*10 s; 5*30 s; 4*105 s; 2*600 s; 2*1200 s). For reconstruction: the image size was 256*300, 6 iterations, 16 subsets were used and also 2 mm FWHM Gaussian filter. All dynamic images were automatically corrected for radioactive decay during acquisition following manufacturer software settings. Following the reconstruction, the CT images were spatially aligned to match the PET images. In addition to being reconstructed into a single image, the CT data was used for attenuation correction of PET images.

Processing of reconstructed images was performed with an in-house software (Tensaouti et al., 2008). Organs were identified and 3D volumes of interest (VOIs) were manually drawn on the CT in the center of each organ. This identification was carried out by an expert in animal image segmentation. All VOIs were transferred to dynamic PET images and the non-decay corrected mean time activity curves (TACs) were extracted for each target organ.

Eight VOIs were selected: brain, heart, lung, spleen, kidney, stomach, liver and whole body. For each rat, an average of three measurements of the same region of interest was done in order to obtain the values of activity as a function of time for each organ. In the case of the heart and the stomach, we assumed that VOI measurements were from the contents. After sacrificing the rats, the mass of the organs was obtained.

A mathematical model was used to fit time-activity data. Measured time points were t = 0.17, 0.33, 0.5, 1.0, 1.5, 2.0, 2.5, 3.0, 4.75, 6.5, 8.25, 10.0, 20.0, 30.0, 50.0 and 70.0 min corresponding to the 16 image datasets acquired. The mathematical model (Equation 2.1) takes into account the uptake and the clearance phases of the radiopharmaceutical for each organ (McParland, 2010).

$$f(t) = a * (e^{-bt} - e^{-ct}) \qquad 2.1$$

Integration of the fitting the model took place in order to estimate the cumulated activity, and hence, the residence time. For some organs, the fitting model did not match experimental data, especially for heart, lungs and brain. For these particular cases, fitting was carried out by segments, using two or three data points (and respectively a first or second-degree polynomial). From the last experimental data time point, mono-exponential decay (considering only physical decay) was assumed. To consider the contribution from the whole body, a remainder of the body was estimated. This means for each rat, all organs were summed and then subtracted from the whole body.

2.2. Percentage of injected activity for [^{11}C]SAM and [^{18}F]SFR101 based-on organ harvesting

The animal experimentation protocol for both radiopharmaceuticals was designed in accordance with institutional, national and international guidelines for the use of research animals. It was approved by the Ethical Committee of CUDIM (No. 14012202) in agreement with national regulations: national law on animal experimentation No. 18.611, Commission of Ethics for Animal Studies (CEUA) and National Commission of Experimentation with Animals (CNEA).

A solution of [^{11}C]SAM (7.7-36.0 MBq, 100-200 μL) was injected intravenously (IV) in male Swiss mice group (15-16 weeks old, 32.9-38.8 g) via the tail vein. Mice were sacrificed by cervical dislocation at 10, 30 and 70 min after injection (n=3 in the first two time points, and n=2 in the last one). Different organ and tissue samples were considered (blood, liver and gallbladder, heart, lungs, spleen, kidneys, muscles, bones, stomach, gastrointestinal tract, carcass, bladder+urine) because not all of them were "extracted".

In the case of [^{18}F]SRF101, male healthy black C57BL6J mice were injected IV with 1.5-35.5 MBq (100-250 μL) into the caudal tail vein and were sacrificed by cervical dislocation at 14, 33, 65 and 110 min after injection (n=3 in the first three time points, and n=2 in the last one). Organs removed were (lung, heart, spleen, liver, kidneys, muscle, bone, stomach, intestines, carcass, bladder and brain). Then these organs weighed (except stomach, intestines and bladder). Blood was also collected. Total urine volume was collected during the bio-distribution period and removed from the bladder after sacrifice, and its activity was measured. For the heart, we considered that measured activity came from the heart wall. In the case of the gastrointestinal tract and urinary bladder, we considered that measured activity came from their contents.

Using a gamma counter (3" x 3" well type NaI(Tl) solid scintillation detector coupled to a multichannel analyser ORTEC), the total number of counts per second (cps) were measured for each organ for both radiopharmaceuticals. To obtain the activity presented in each organ, a calibration factor is needed. This parameter is associated to the response of the detector for a known amount of activity. In our study this parameter was not available. However, we developed a methodology to establish it by knowing the total amount of counts per second (cps) and the total activity injected (MBq) to the small animal. This methodology is described as follows:

- Three different times were recorded: injection time (t_{inj}), sacrifice time (t_{sac}) and organ/tissue measuring time (t_{mes}).

- A geometric correction factor was applied to obtain the corrected counts per second for background and geometry $\left(cps_{bk,geo}\right)^{t=t_{mes}}$.
- Each organ measurement $\left(cps_{bk,geo}\right)^{t=t_{mes}}$ was decay corrected between the injection and the measured time to compare the injected activity (A_{inj}) to the sum of counts:

$$A_{inj} = \sum\nolimits_{organ} \left(cps_{bk,geo}\right)^{t=t_{mes}} * e^{\lambda \Delta t} = \sum\nolimits_{organ} \left(cps_{bk,geo}\right)^{t=t_{mes}} * e^{\lambda (t_{mes}-t_{inj})} \qquad 2.2$$

- In addition, each organ measurement $\left(cps_{bk,geo}\right)^{t=t_{mes}}$ was decay corrected between the sacrifice and measurement time:

$$cps_{sac}^{organ} = \left(cps_{bk,geo}\right)^{t=t_{mes}} * e^{\lambda \Delta t} = \left(cps_{bk,geo}\right)^{t=t_{mes}} * e^{\lambda (t_{mes}-t_{sac})} \qquad 2.3$$

- The percentage of injected activity $\left(\%A_{inj}\right)_{t_i}^{organ}$ for each organ/tissue at one particular time can therefore be expressed as shown in equation 2.4:

$$\left(\%A_{inj}\right)_{t_i}^{organ} = \frac{\left(cps_{bk,geo}\right)^{t=t_{mes}} * e^{\lambda (t_{mes}-t_{sac})}}{\sum_{organ}\left(cps_{bk,geo}\right)^{t=t_{mes}} * e^{\lambda (t_{mes}-t_{inj})}} * 100 \qquad 2.4$$

- The average percentage of injected activity for each organ $\overline{\left(\%A_{inj}\right)_{t_i}^{organ}}$ was also estimated for each mouse time group.
- To take into account the contribution from the whole body, a remainder of the body was estimated, that means summing all organs and subtracting them to the whole body for each rat.

Physical half-lives of 109.77 min for ^{18}F and 20.39 min for ^{11}C were used according to the MIRD Radionuclide Data and Decay Schemes (Eckerman & Endo, 2008).

2.3. Residence time calculation

As previously mentioned, in the case of [^{18}F]FNM bio-kinetics of some organs followed the fitting model. Then, integration took place to estimate the residence time. For some other organs, as well as in the case of [^{11}C]SAM and [^{18}F]SRF101, the procedure in order to estimate the residence times was as follows: an assumption of no activity at t=0 min was considered. Normalized non-decay corrected time activity curves were generated for each organ.

For the three radiopharmaceuticals normalized cumulated activity for humans was calculated using mass scaling between mice/rats and humans for the whole body and different organs. McParland (McParland, 2010) described the estimation of the normalised cumulated activity for humans. Based on this information, the normalized cumulated activity for humans can be re-written as shown in equation 2.5:

$$\tilde{A}_{Organ,Human} = \left(\frac{m_{Animal}}{m_{Human}}\right)_{WB} * \left(\frac{m_{Human}}{m_{Animal}}\right)_{Org} * \tilde{A}_{Organ,Animal} \qquad 2.5$$

To perform dosimetric extrapolations for humans, two versions of OLINDA are available. OLINDA/EXM V1.0 and OLINDA/EXM V2.0 provide information regarding human organ mass and consider different anthropomorphic dosimetric models: OLINDA/EXM V1.0 considers the Cristy and Eckerman mathematical models (Cristy & Eckerman, 1987) based on ICRP-23 recommendations (ICRP, 1975), whereas OLINDA/EXM V2.0 considers voxel-based models (Stabin et al., 2008) based on ICRP-89 recommendations.

The extrapolation of pharmaco-kinetic (PK) results from animal to human requires that for each source organ/tissue identified on the animal, an explicit counterpart exists in the human model. For example both OLINDA's versions provide information regarding human bladder content mass or human intestine content mass. This means that bladder, intestines and their contents can be dealt with as explicit sources.

In addition, current dosimetric codes explicitly separate male and female absorbed dose calculation by using reference human male and female models. This means that the extrapolation from animal to human (equation 2.5) must be done by considering the masses of organs/tissues of the different models, but from a unique rodent dataset.

Due to the bio-distribution of [^{11}C]SAM and [^{18}F]SRF101 radiopharmaceuticals in mice, three considerations were made:

a) For [^{11}C]SAM, it was assumed that no bladder voiding may lead to an overestimation of the irradiation delivered by the bladder content. Therefore, estimation of residence times was performed, by extrapolating data with and without bladder voiding. The remainder of the body residence time took into account blood, muscles, bones and carcass.

b) For [^{18}F]SRF101 and [^{11}C]SAM the residence time for each section of the intestines used in the models was estimated by assigning the residence time proportionally to the mass of each section;

c) In the case of [^{18}F]SRF101, the bladder voiding consideration was not addressed.

2.4. Absorbed dose estimations

Residence times obtained after mass scaling are used to calculate the absorbed doses using both versions of OLINDA/EXM. Since OLINDA/EXM V2.0 could be used for reference dosimetry of new radiopharmaceuticals (as it was used OLINDA/EXM V1.0 in the past), a decision was taken in order to compare it against IDAC 2.1. In order to carry-on this comparison, the residence times obtained after mass scaling using human models from OLINDA/EXM V2.0 are entered into IDAC 2.1 (for the same organ sources). In terms of human models IDAC 2.1 used reference from ICRP-110.

Since we had no specific assessment of male/female pharmacokinetics from animal experiments, the gender specific estimate was obtained during the extrapolation phase, by scaling differently the same animal pharmacokinetics.

As previously mentioned, OLINDA/EXM V1.0 and OLINDA/EXM V2.0 provide information regarding human organ mass and consider different anthropomorphic dosimetric models: OLINDA/EXM V1.0 considers the Cristy and Eckerman mathematical models (Cristy & Eckerman, 1987) based on ICRP-23 recommendations (ICRP, 1975), whereas OLINDA/EXM V2.0 considers voxel-based models (Stabin et al., 2008) based on ICRP-89 recommendations.

For absorbed dose estimation, the S-value is a key factor that is needed. As it was defined in chapter 1, S-value is obtained from the estimation of specific absorbed fractions (SAF). In the case of OLINDA/EXM V1.0 SAF were estimated using ALGAMP Monte Carlo code (Ryman et al., 1987). In the case of OLINDA/EXM V2.0 GEANT4 was used and in the case of IDAC 2.1 EGS4 was used. For effective dose calculation, OLINDA/EXM V1.0 and OLINDA/EXM V2.0 follow recommendations from ICRP-60 (ICRP, 1991) and ICRP-103 (ICRP, 2007), respectively. IDAC 2.1 fulfil with ICPR-133 recommendations and also provide results considering ICRP-60 recommendations.

3. Results

3.1. Residence times and absorbed dose estimations for [^{18}F]FNM

In figure 2.1 the same cross-sectional evolution of [^{18}F]FNM biodistribution (LUT is the same for all images) is appreciated. Also, uptake within the retina and pituitary Px (schiffer atlas) was also observed for all animals.

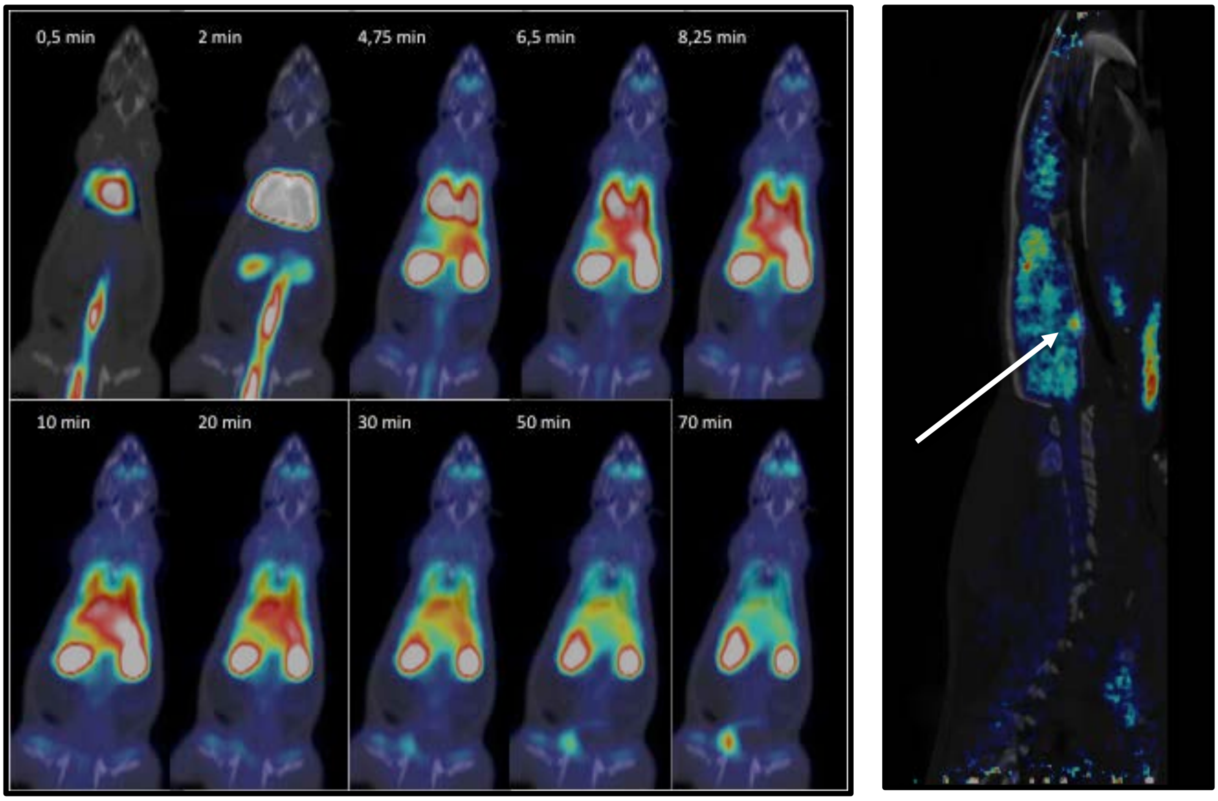

Figure 2.1: Left: Whole body biodistribution of [^{18}F]FNM after injection of 60 MBq in tail vein. Rigth: Arrow shows uptake in pituitary PX. Figure from Salabert et al. (Salabert et al., 2018), with permission from authors.

In table 2.1, results for cumulated activity and residence times for the three rats can be observed. In average, organs with highest residence times are kidneys, liver, lungs and whole body. In the case of Rat 3, measurement of the stomach contents was not available and therefore the average result considered 2 animals only.

Table 2.1. Summary of results for cumulative activity and residence times (T) for each rat.

Organ	Rat 1, A_o = 61.63 MBq		Rat 2, A_o = 18.00 MBq		Rat 3, A_o = 111.00 MBq		Average
	A (Bq.min)	T (h)	A (Bq.min)	T (h)	A (Bq.min)	T (h)	T (h)
Brain	2.09E+07	5.64E-03	4.01E+06	3.71E-03	6.30E+07	9.46E-03	6.27E-03
Heart	1.62E+07	4.37E-03	3.50E+06	3.24E-03	4.57E+07	6.87E-03	4.83E-03
Kidneys	1.67E+08	4.51E-02	4.54E+07	4.20E-02	3.02E+08	4.54E-02	4.42E-02
Liver	1.68E+08	4.55E-02	6.35E+07	5.88E-02	3.80E+08	5.71E-02	5.38E-02
Lungs	3.90E+07	1.06E-02	9.71E+06	8.99E-03	1.09E+08	1.64E-02	1.20E-02
Spleen	1.48E+07	3.99E-03	1.18E+06	1.09E-03	7.38E+07	1.11E-02	5.39E-03
Stomach	2.25E+07	6.09E-03	8.89E+06	8.23E-03	-	-	7.16E-03
Remainder	-	7.05E-01	-	2.81E-01	-	9.42E-01	6.43E-01
Whole body	3.05E+09	8.26E-01	4.40E+08	4.07E-01	7.25E+09	1.09E+00	7.74E-01

In table 2.2, organ masses for male and female dosimetric models and rats used for mass scaling can be seen. From this table it can be seen that differences in masses between human models and measured rat organs are between two or three orders of magnitude. The residence times used in OLINDA/EXM V2.0 after mass scaling are also exhibited. For both human models, the highest residence times are brain, kidneys, liver, lungs and spleen.

In the appendix, a table showing organ masses for different dosimetric human's and animal models can be seen. When OLINDA/EXM V1.0 is used similar results are observed.

Table 2.2. Organ masses for male/female dosimetric models and rats used for mass scaling. Moreover, residence times T used in OLINDA/EXM V2.0 after mass scaling.

Organ	M_{male} (g)	M_{female} (g)	M_{rat} (g)	T_{male} (h)	T_{female} (h)
Brain	1450	1300	1.99	2.07E-02	2.25E-02
Heart contents	510	370	1.22	9.12E-03	8.05E-03
Kidney	310	275.5	2.61	2.37E-02	2.56E-02
Liver	1800	1400	8.20	5.34E-02	5.05E-02
Lung	1200	950	1.65	3.94E-02	3.80E-02
Spleen	150	130	0.65	5.62E-03	5.93E-03
Stomach contents	250	230	1.34	6.04E-03	6.76E-03
Remainder	67330	55344.5	312.34	6.26E-01	6.26E-01
Whole body	73000	60000	330	-	-

In figure 2.2, looking at the right-up section of the figure, the uptake in the remainder is higher than other organs. Liver and kidneys also exhibit higher uptake. TACs show a rapid decrease in cardiac uptake, which could be due to a rapid blood clearance. Looking at the right-down section of the figure, uptake of different organs is observed without the remainder contribution, and the uptake in spleen, stomach, brain and lungs was weak. The kidney seems to be the significant clearance pathway. Uptake in the lung was very fast and remained high. Uptake in the liver, spleen and stomach seem to be more gradual. In the left section of the figure a sagittal whole-body PET-CT view of a sprague dawley rat can be seen.

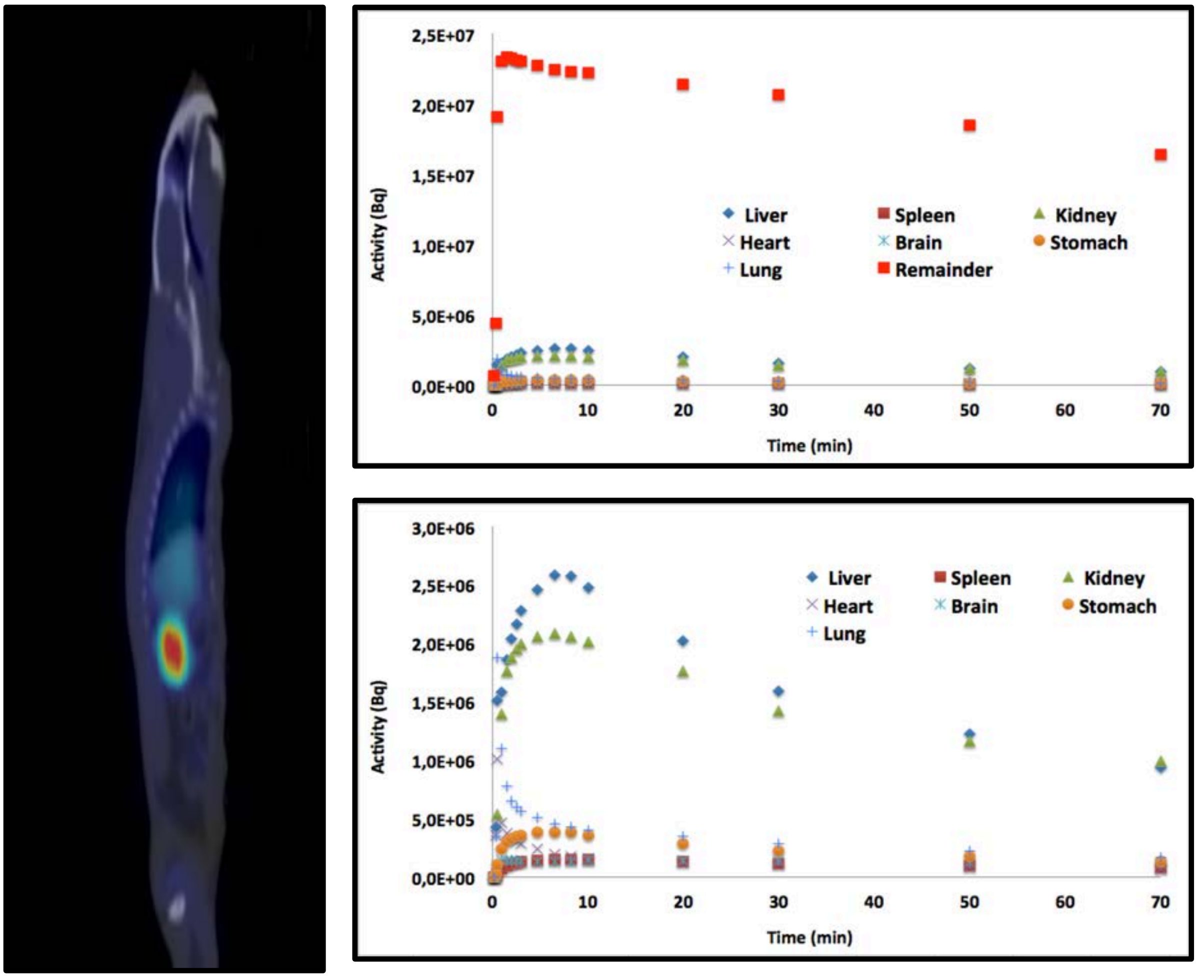

Figure 2.2: Left: Sagittal whole-body PET-CT of a sprague dawley rat. Right-up: Percentage of injected activity for each organ after an intravenous injection of [^{18}F]FNM, for rat 1 (A$_o$= 61.63 MBq), with the remainder. Right-down: Percentage of injected activity for each organ after an intravenous injection of [^{18}F]FNM, for rat 1, without the remainder. Figure from Salabert et al. (Salabert et al., 2018), with permission from authors.

Table 2.3 shows results for the absorbed dose coefficients (ADC) and the contribution to the effective dose factor (CEDF) per organ, for both adult models from OLINDA/EXM V2.0. As was expected, kidneys present the highest absorbed dose, probably because this organ can be associated with the clearance pathway of the radiopharmaceutical. Other organs showing high-absorbed dose for both adult models are adrenals, stomach wall, heart wall, liver, lungs and spleen.

Table 2.3. Absorbed dose coefficients (ADC) and contribution to the effective dose factor (CEDF) results for adult male and female models from OLINDA/EXM V2.0.

Organ	Male		Female	
	ADC (mGy/MBq)	**CEDF (mSv/MBq)**	**ADC (mGy/MBq)**	**CEDF (mSv/MBq)**
Adrenals	6.12E-03	5.65E-05	7.33E-03	6.77E-05
Brain	4.05E-03	4.05E-05	4.93E-03	4.93E-05
Breast	-	-	3.53E-03	4.24E-04
Esophagus	4.20E-03	1.68E-04	4.83E-03	1.93E-04
Eyes	2.91E-03	-	3.62E-03	-
Gallbladder Wall	5.35E-03	4.94E-05	5.78E-03	5.34E-05
Left colon	4.21E-03	2.04E-04	5.08E-03	2.47E-04
Small Intestine	4.08E-03	3.77E-05	4.65E-03	4.29E-05
Stomach Wall	6.51E-03	7.82E-04	7.84E-03	9.41E-04
Right colon	4.21E-03	2.04E-04	5.01E-03	2.43E-04
Rectum	3.75E-03	8.63E-05	4.57E-03	1.05E-04
Heart Wall	6.04E-03	5.57E-05	7.18E-03	6.62E-05
Kidneys	1.63E-02	1.51E-04	1.97E-02	1.81E-04
Liver	8.77E-03	3.51E-04	1.06E-02	4.22E-04
Lungs	7.55E-03	9.06E-04	9.14E-03	1.10E-03
Ovaries	-	-	4.66E-03	1.86E-04
Pancreas	4.73E-03	4.37E-05	5.97E-03	5.51E-05
Prostate	3.75E-03	1.73E-05	-	-
Salivary Glands	3.37E-03	3.37E-05	3.84E-03	3.84E-05
Red Marrow	3.36E-03	4.04E-04	4.09E-03	4.90E-04
Osteogenic Cells	2.96E-03	2.96E-05	3.49E-03	3.49E-05
Spleen	9.25E-03	8.54E-05	1.15E-02	1.06E-04
Testes	3.06E-03	1.22E-04	-	-
Thymus	3.90E-03	3.60E-05	4.94E-03	4.56E-05
Thyroid	3.62E-03	1.45E-04	4.08E-03	1.63E-04
Urinary Bladder Wall	3.68E-03	1.47E-04	3.78E-03	1.51E-04
Uterus	-	-	4.61E-03	2.13E-05
Total Body	3.52E-03	-	4.46E-03	-
Total effective dose (mSv/MBq)	-	4.16E-03	-	5.43E-03

Table 2.4 shows results of ADC and effective dose results, considering ICRP-60 and ICRP-103, for adult male and female models from IDAC 2.1. In both cases, organs exhibiting high-absorbed doses are adrenals, alveolar-interstitial, bronchioles, heart wall, kidneys, liver, lungs and spleen. The ADCs results for the female model are higher than the male model, which is due the difference in organ masses in each model.

To estimate the effective dose in OLINDA/EXM V2.0, all contributions from the organs were added. The results are 4.16×10^{-3} mSv/MBq and 5.43×10^{-3} mSv/MBq for male and female models, respectively. This would correspond to effective doses of 1.46 mSv (male) and 1.90 mSv (female) for a realistic administrated activity of 350 MBq.

On the other hand, for IDAC 2.1, effective doses are almost the same for both models, 5.03×10^{-3} mSv/MBq and 5.02×10^{-3} mSv/MBq for male and female model, respectively. This would correspond to effective doses of 1.76 mSv for both models, for the same administrative activity. In the case of ICRP-60 recommendations the effective dose for male model is 4.63×10^{-3} mSv/MBq and for the female model is 5.63×10^{-3} mSv/MBq.

Table 2.4. Absorbed dose coefficients (ADC) for adult male and female models from IDAC 2.1.

	From male bio-kinetics		From female bio-kinetics	
Target organ	**ADC male (mGy/MBq)**	**ADC female (mGy/MBq)**	**ADC male (mGy/MBq)**	**ADC female (mGy/MBq)**
Adipose/residual tissue	3.21E-03	3.68E-03	3.21E-03	3.68E-03
Adrenals	6.00E-03	6.92E-03	6.09E-03	6.94E-03
Alveolar-interstitial	8.63E-03	1.05E-02	8.40E-03	1.02E-02
Brain	3.88E-03	4.31E-03	4.15E-03	4.61E-03
Breast	3.13E-03	3.92E-03	3.11E-03	3.89E-03
Bronchi bound	5.15E-03	6.40E-03	5.05E-03	6.26E-03
Bronchi sequestered	5.14E-03	6.39E-03	5.04E-03	6.24E-03
Bronchioles	8.69E-03	1.05E-02	8.45E-03	1.02E-02
Colon Wall	3.42E-03	3.83E-03	3.43E-03	3.84E-03
Endosteum (bone surface)	3.53E-03	4.07E-03	3.54E-03	4.08E-03
ET región	2.26E-03	2.78E-03	2.29E-03	2.81E-03
ET1 basal cells	1.46E-03	2.08E-03	1.47E-03	2.09E-03
ET2 basal cells	2.26E-03	2.78E-03	2.29E-03	2.81E-03
Eye lenses	2.26E-03	2.67E-03	2.29E-03	2.69E-03
Gallbladder wall	5.65E-03	6.92E-03	5.53E-03	6.83E-03
Heart Wall	6.84E-03	8.54E-03	6.36E-03	7.91E-03
Kidneys	1.27E-02	1.50E-02	1.35E-02	1.59E-02
Left colon wall	3.37E-03	3.73E-03	3.39E-03	3.74E-03
Liver	7.22E-03	8.86E-03	6.95E-03	8.53E-03
Lung	7.49E-03	9.16E-03	7.30E-03	8.91E-03
Lymphatic nodes	3.90E-03	4.67E-03	3.89E-03	4.66E-03
Lymph nodes in ET region	3.34E-03	4.21E-03	3.34E-03	4.21E-03
Lymph nodes in sys	3.91E-03	4.66E-03	3.90E-03	4.65E-03
Lymph nodes in thoracic region	4.38E-03	5.24E-03	4.31E-03	5.16E-03
Muscle	3.22E-03	3.94E-03	3.22E-03	3.94E-03
Oesophagus	4.26E-03	4.98E-03	4.19E-03	4.90E-03
Oral mucosa	3.08E-03	3.61E-03	3.09E-03	3.62E-03
Ovaries	-	4.51E-03	-	4.51E-03
Pancreas	4.78E-03	5.70E-03	4.77E-03	5.74E-03
Pituitary gland	3.51E-03	4.16E-03	3.63E-03	4.28E-03
Prostate	3.71E-03	-	3.71E-03	-
Recto-sigmoid colon wall	3.15E-03	3.87E-03	3.15E-03	3.87E-03
Red (active) bone marrow	4.06E-03	4.68E-03	4.05E-03	4.66E-03
Right colon wall	3.61E-03	3.91E-03	3.60E-03	3.92E-03
Salivary glands	2.89E-03	3.59E-03	2.90E-03	3.60E-03
Skin	2.45E-03	2.92E-03	2.45E-03	2.91E-03
Small intestine wall	3.39E-03	4.10E-03	3.40E-03	4.12E-03
Spleen	7.11E-03	8.51E-03	7.37E-03	8.83E-03
Stomach wall	5.73E-03	6.59E-03	5.92E-03	6.80E-03
Testes	3.11E-03	-	3.11E-03	-
Thymus	3.86E-03	4.74E-03	3.81E-03	4.68E-03
Thyroid	3.33E-03	3.94E-03	3.31E-03	3.92E-03
Tongue	2.28E-03	2.49E-03	2.29E-03	2.50E-03
Tonsils	3.33E-03	3.73E-03	3.37E-03	3.76E-03
Ureters	4.19E-03	5.01E-03	4.21E-03	5.03E-03
Urinary bladder wall	3.46E-03	3.81E-03	3.46E-03	3.81E-03
Uterus/cervix	-	4.37E-03	-	4.37E-03
Effective dose 60 [mSv/MBq]	4.63E-03	5.63E-03	4.64E-03	5.63E-03
Effective dose 103 [mSv/MBq]	4.58E-03	-	-	5.07E-03

In table 2.5 a summary of the effective dose factor results can be seen for [^{18}F]FNM, considering the three software. For both models, results are in the same order of magnitude. In the case of female model, the effective dose factors are higher than the male model. For the female model, results from both versions of OLINDA are comparable to the results obtained using ICRP-60 (IDAC 2.1), but are higher comparing with ICRP-103 (IDAC 2.1). For male model, results from OLINDA/EXM V1.0 and ICRP-60 (IDAC 2.1) are almost the same and higher than OLINDA/EXM V2.0, and the values from ICRP-103 (IDAC 2.1) are similar to the others.

Table 2.5. Summary of effective dose factor results (mSv/MBq) for [^{18}F]FNM.

OLINDA/EXM V1.0		OLINDA/EXM V2.0		IDAC 2.1		
				ICRP-60		ICRP-103
Male	**Female**	**Male**	**Female**	**Male**	**Female**	**Reference person**
4.65E-03	5.73E-03	4.16E-03	5.43E-03	4.63E-03	5.63E-03	4.83E-03

3.2. Residence times and absorbed dose estimations for [^{11}C]SAM

The variations of the average of percentages of injected activity for all organs for each mice time group are shown in Figure 2.3.A. The difference between the organs with the highest average percentage of injected activity was approximately 12.44% at t=10 min (bladder+urine and carcass). The excretion of radioactive material was observed in the bladder+urine compartment. Depending on the transit of this radioactive material through the kidneys compartment, high-absorbed doses may be expected.

The average percentage of injected activity without the contribution of the bladder+urine is provided in Figure 2.3.B. From this figure at t=10 min kidneys are the organs with highest activity, which is in agreement with previous studies on rats (Ishiwata et al., 1986; Tolvanen et al., 2010). In another article, Ishiwata et al. described a high uptake in the kidneys and a rapid blood clearance for the same tracer in mice and rats bearing tumour cells (Ishiwata et al., 1988). Other organs with high activity uptakes were the liver-gallbladder, blood and intestines. The variations of the average percentages of injected activity in the bladder+urine compartment with and without bladder voiding are provided in Figure 2.3.C.

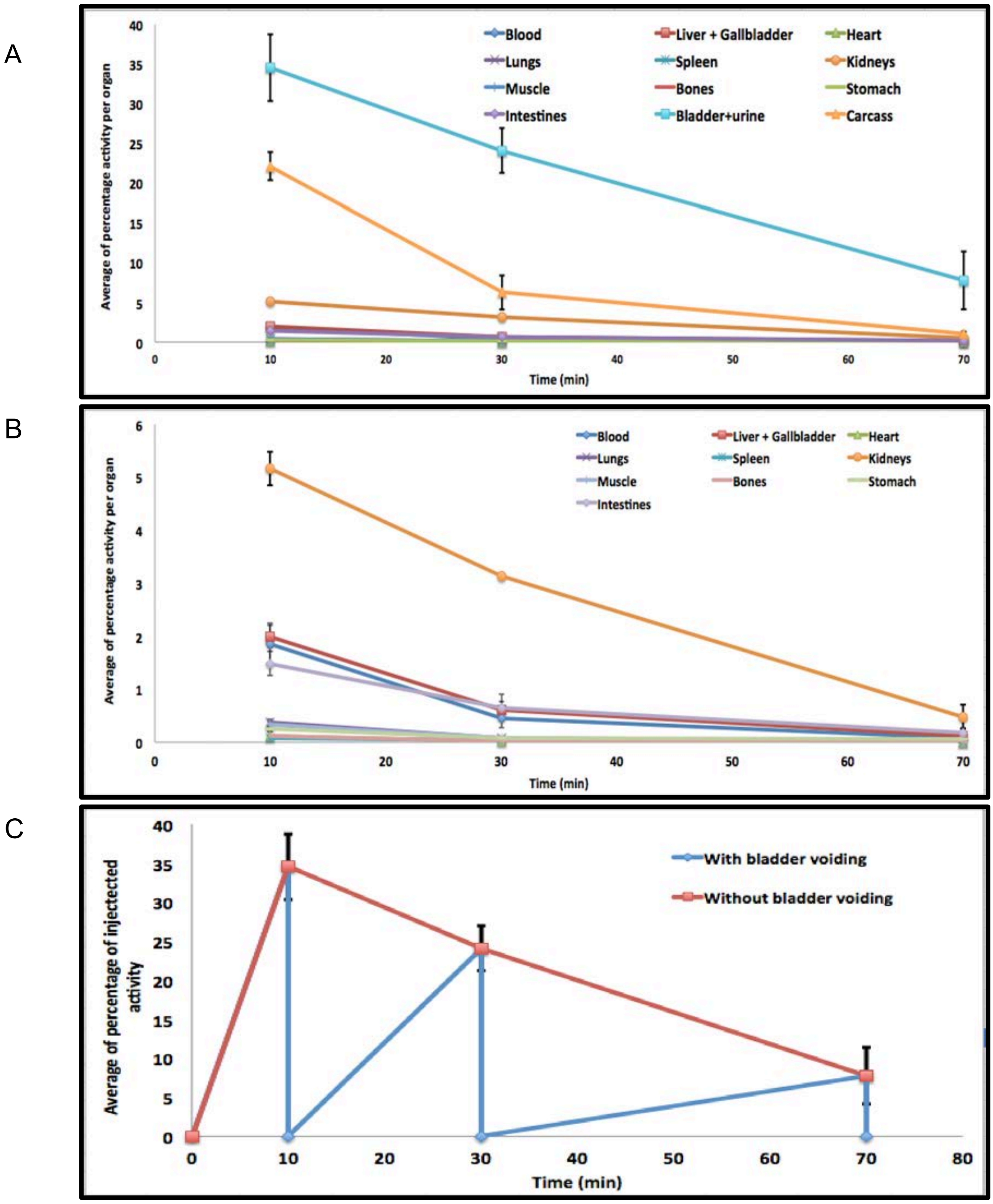

Figure 2.3: Average percentage of administrated activity per organ for [^{11}C]SAM per mice time group. A: All measured organs; B: all organs except bladder+urine and carcass; C: bladder+urine compartment with and without bladder voiding. Figure adapted from (Zoppolo et al., 2018), with permission from authors.

The residence time in hours for mice organs is shown in Table 2.6, bladder+urine, kidneys and carcass had high values. The highest value was observed for the remainder when the bladder+urine without bladder voiding was considered. The difference between bladder+urine residence time with and without bladder voiding is about 2.5 times.

Table 2.6. Residence times (T) for each mice organ using [^{11}C]SAM.

Organ	Residence time (h)
Blood	7.14E-03
Liver-Gallbladder	8.53E-03
Heart wall	4.22E-04
Lungs	1.40E-03
Spleen	3.43E-04
Kidneys	3.03E-02
Muscle	1.27E-03
Bones	4.20E-04
Stomach contents	1.24E-03
Intestines contents	7.65E-03
Carcass	9.06E-02
Bladder contents without bladder voiding	2.36E-01
Bladder contents with bladder voiding	9.49E-02
Remainder	9.94E-02[a]

[a] Remainder is the sum of blood, muscles, bones and carcass.

Mass values for the male dosimetric model from OLINDA/EXM V2.0 are shown in Table 2.7, along with the S-factors for different organs, considering only self-irradiation. The difference in mass between human model and measured mice organs is between two to four orders of magnitude. This table also shows the residence times for the human model. These figures were used in OLINDA/EXM V2.0 to estimate the absorbed and effective dose. The highest residence time values for the male dosimetric model were for the remainder, bladder+urine and kidneys. The difference between bladder+urine residence time with and without bladder voiding is about 2.5 times.

Table 2.7. Organ mass values, for male model and mouse, used for mass scaling. Residence times used in OLINDA/EXM V2.0.

Organ	M_{male} (g)	S-factor[a] (mGy/MBq.s)	M_{mouse} (g)	T_{male}(h)
Heart Wall	330	2.11E-4	0.1400 ± 0.010	5.03E-04
Kidneys	310	2.36E-4	0.4746 ± 0.047	1.00E-02
Liver+Gallbladder	1858	---	1.8355 ± 0.203	4.36E-03
Liver	1800	4.91E-5	---	4.22E-03
Gallbladder contents	58	6.65E-4[b]	---	1.36E-04
Lungs	1200	5.72E-5	0.2018 ± 0.012	4.20E-03
Spleen	150	4.77E-4	0.1109 ± 0.015	2.34E-04
Stomach contents	250	1.62E-4[b]	0.1000[c]	1.57E-03
Intestines contents	650	---	3.3000[c]	7.61E-04
Left colon contents (LLI)	75	4.49E-4[b]	---	8.78E-4
Small intestine contents (SI)	350	1.05E-4[b]	---	4.10E-4
Right colon contents (ULI)	150	2.46E-4[b]		1.76E-4
Rectum contents	75	4.65E-4[b]	---	8.78E-4
Bladder contents without Bladder Voiding	211	1.91E-4[b]	0.1000[c]	2.52E-01
Bladder contents with Bladder Voiding	211	1.91E-4[b]	0.1000[c]	1.01E-01
Remainder	68031	---	30.7023	1.11E-01[d]
Whole Body	73000	1.65E-6	36.8650 ± 2.010	-----
Whole body mass for mice group at 10 min (g)			37.3633 ± 1.906	
Whole body mass for mice group at 30 min (g)			37.0567 ± 1.285	
Whole body mass for mice group at 70 min (g)			35.8300 ± 4.158	

[a] S-factor refers to self-irradiation; [b] S-factor for gallbladder wall, stomach wall, LLI wall, SI wall, ULI wall, rectum wall and urinary bladder wall, considering their contents as a source; [c] Mouse stomach, intestines and bladder contents masses taken from OLINDA/EXM V2.0; [d] Remainder considers blood, muscles, bones and carcass.

Table 2.8 shows the results for absorbed and effective dose estimations with and without bladder voiding using OLINDA/EXM V2.0. The total absorbed dose varies between 1.6 to 2.5 times for organs close to the bladder content (small intestine, rectum, prostate and testes), indicating the importance of taking bladder voiding into account. In addition, it is important to note the difference in the total absorbed dose to the urinary bladder wall, which is about 2.48 times. For organs far from the bladder contents compartment, the values of the total absorbed dose were in the same order of magnitude. Regarding the mean effective dose, its ratio was about 2.1 times for the same situations.

From OLINDA/EXM V2.0, for kidneys, when bladder voiding is considered, the ADC is 9.00×10^{-3} mGy/MBq, and without considering bladder voiding, this coefficient is 9.21×10^{-3} mGy/MBq.

Table 2.8. Absorbed dose coefficients (ADC) and contribution to effective dose factor (CEDF) results for adult male model from OLINDA/EXM V2.0, with and without bladder voiding consideration.

Target Organ	Without Bladder voiding		With Bladder voiding	
	ADC (mGy/MBq)	CEDF (mSv/MBq)	ADC (mGy/MBq)	CEDF (mSv/MBq)
Adrenals	1.85E-03	1.71E-05	1.70E-03	1.57E-05
Brain	6.27E-04	6.27E-06	6.27E-04	6.27E-06
Esophagus	8.61E-04	3.44E-05	8.26E-04	3.30E-05
Eyes	6.37E-04	-	6.30E-04	-
Gallbladder Wall	1.46E-03	1.35E-05	1.32E-03	1.22E-05
Left Colon	2.93E-03	1.42E-04	2.57E-03	1.24E-04
Small Intestine	2.60E-03	2.40E-05	1.65E-03	1.53E-05
Stomach Wall	1.81E-03	2.17E-04	1.75E-03	2.10E-04
Right Colon	1.69E-03	8.17E-05	1.27E-03	6.17E-05
Rectum	8.03E-03	1.85E-04	4.57E-03	1.05E-04
Heart Wall	8.93E-04	8.24E-06	8.61E-04	7.95E-06
Kidneys	9.21E-03	8.50E-05	9.00E-03	8.31E-05
Liver	1.25E-03	4.99E-05	1.17E-03	4.67E-05
Lungs	1.23E-03	1.48E-04	1.21E-03	1.45E-04
Pancreas	1.17E-03	1.08E-05	1.06E-03	9.81E-06
Prostate	9.32E-03	4.30E-05	4.23E-03	1.96E-05
Salivary Glands	7.08E-04	7.08E-06	7.07E-04	7.07E-06
Red Marrow	1.68E-03	2.01E-04	1.08E-03	1.30E-04
Osteogenic Cells	1.09E-03	1.09E-05	7.77E-04	7.77E-06
Spleen	1.12E-03	1.03E-05	1.05E-03	9.66E-06
Testes	2.66E-03	1.06E-04	1.47E-03	5.88E-05
Thymus	7.75E-04	7.15E-06	7.62E-04	7.03E-06
Thyroid	7.49E-04	3.00E-05	7.41E-04	2.96E-05
Urinary	1.74E-01	6.96E-03	7.02E-02	2.81E-03
Total Body	2.22E-03	-	1.36E-03	-
Total Effective	-	8.40E-03	-	3.96E-03

Table 2.9 shows similar results as in table 2.8, but using IDAC 2.1. For small intestine, rectum, prostate, testes, ureters and urinary bladder wall similar differences for ADCs can be seen for OLINDA/EXM V2.

According to ICRP-103 the mean effective dose must be estimated for male and female reference models, but this radiopharmaceutical will be used for male patients. Consequently, another quantity should be used instead of effective dose, in the case of radiopharmaceuticals used only for male or female patients. Taking into account this idea, in a publication from Giussani et al. (Giussani et al., 2012), a quantity called “risk-weighted absorbed dose coefficient” was reported, using information from ICRP-60. Following this idea and applying ICRP-103 recommendations, in table 2.8, a contribution to the effective dose factor is calculated to find the “risk-weighted effective dose coefficient” (RWEDC) with and without bladder voiding, which is almost a factor of two for these situations.

Table 2.9. Absorbed dose coefficients (ADC) for adult male model using IDAC 2.1. Risk-weighted effective dose coefficient (RWEDC) using information from ICRP-103.

Target organ	Without Bladder voiding		With Bladder voiding	
	ADC (mGy/MBq)	RWEDC (mSv/MBq)	ADC (mGy/MBq)	RWEDC (mSv/MBq)
Adipose/residual tissue	1.72E-03	-	1.12E-03	-
Adrenals	1.73E-03	-	1.65E-03	-
Alveolar-interstitial	1.44E-03	-	1.43E-03	-
Brain	6.42E-04	6.42E-06	6.41E-04	6.41E-06
Breast	6.70E-04	8.04E-05	6.53E-04	7.84E-05
Bronchi bound	9.58E-04	-	9.41E-04	-
Bronchi sequestered	9.56E-04	-	9.39E-04	-
Bronchioles	1.46E-03	-	1.44E-03	-
Colon Wall	3.04E-03	3.65E-04	1.73E-03	2.08E-04
Endosteum (bone surface)	1.61E-03	1.61E-05	1.11E-03	1.11E-05
ET región	4.25E-04	-	4.23E-04	-
ET1 basal cells	2.85E-04	-	2.84E-04	-
ET2 basal cells	4.25E-04	-	4.24E-04	-
Eye lenses	4.66E-04	-	4.66E-04	-
Gallbladder wall	1.25E-03	-	1.14E-03	-
Heart Wall	8.46E-04	-	8.21E-04	-
Kidneys	6.79E-03	-	6.65E-03	-
Left colon wall	1.21E-03	-	1.02E-03	-
Liver	1.09E-03	4.36E-05	1.03E-03	4.12E-05
Lung	1.29E-03	1.55E-04	1.27E-03	1.52E-04
Lymphatic nodes	2.96E-03	-	1.68E-03	-
Lymph nodes in ET region	7.20E-04	-	7.18E-04	-
Lymph nodes in sys	3.38E-03	-	1.85E-03	-
Lymph nodes in thoracic Region	8.27E-04	-	8.17E-04	-
Muscle	1.43E-03	-	9.96E-04	-
Oesophagus	7.79E-04	3.12E-05	7.61E-04	3.04E-05
Oral mucosa	6.60E-04	-	6.58E-04	-
Ovaries	-	-	-	-
Pancreas	1.23E-03	-	1.09E-03	-
Pituitary gland	6.71E-04	-	6.71E-04	-
Prostate	1.76E-02	-	7.52E-03	-
Recto-sigmoid colon wall	1.00E-02	-	4.57E-03	-
Red (active) bone marrow	2.33E-03	2.80E-04	1.45E-03	1.74E-04
Right colon wall	1.38E-03	-	1.02E-03	-
Salivary glands	6.28E-04	6.28E-06	6.27E-04	6.27E-06
Skin	8.15E-04	8.15E-06	6.48E-04	6.48E-06
Small intestine wall	3.69E-03	-	1.95E-03	-
Spleen	9.13E-04	-	8.64E-04	-
Stomach wall	1.70E-03	2.04E-04	1.63E-03	1.96E-04
Testes	1.73E-03	1.38E-04	1.10E-03	8.80E-05
Thymus	7.58E-04	-	7.50E-04	-
Thyroid	6.83E-04	2.73E-05	6.78E-04	2.71E-05
Tongue	4.52E-04	-	4.50E-04	-
Tonsils	6.92E-04	-	6.91E-04	-
Ureters	5.28E-03	-	2.70E-03	-
Urinary bladder wall	5.83E-02	2.33E-03	2.38E-02	9.52E-04
Uterus/cervix	-	-	-	-
Remainder	3.10E-03	3.72E-04	2.01E-03	2.42E-04
Effective dose 60 [mSv/MBq]	4.52E-03	-	2.36E-03	-
Risk-weighted effective dose 103 [mSv/MBq]	-	4.06E-3	-	2.22E-03

The mean effective doses using OLINDA/EXM V2.0 are 8.40x10^{-3} mSv/MBq and 3.96x10^{-3} mSv/MBq without and with the bladder voiding, respectively. According to CUDIM protocols, the injected activity of this product will be between 4-6 MBq/kg, which is between 292–438 MBq for a 73 kg patient. Without bladder voiding, the mean effective dose range is between 2.45–3.68 mSv, and with bladder voiding, the effective dose ranged from 1.16–1.73 mSv.

Using information from IDAC 2.1, the risk-weighted effective dose would be 4.06 x10^{-3} mSv/MBq and 2.22 x10^{-3} mSv/MBq without and with the bladder voiding consideration, respectively. Without bladder voiding, the mean effective dose range is between 1.19–1.78 mSv, and with bladder voiding, the effective dose ranged from 0.65–0.97 mSv, for the same injected activities. Considering ICRP-60 recommendations, the effective dose would be 4.52 x10^{-3} mSv/MBq and 2.36 x10^{-3} mSv/MBq without and with the bladder voiding consideration, respectively. This would correspond to mean effective doses ranging from 1.32-1.98 mSv and 0.69-1.03 mSv without and with the bladder voiding consideration, respectively.

In table 2.10 effective dose factor results can be seen, with and without bladder voiding consideration. Without bladder voiding consideration, both OLINDAs version results are higher than those values obtained with IDAC 2.1. In the case of OLINDA/EXM V2.0 the result can be twice of the values from IDAC 2.1. The same effect occurs with bladder voiding consideration.

Table 2.10. Summary of effective dose factor results (mSv/MBq) for [^{11}C]SAM, in the case of male model with and without bladder voiding considerations.

OLINDA/EXM V1.0		OLINDA/EXM V2.0		IDAC 2.1(RWEDC)			
				ICRP-60		ICRP-103	
With	**Without**	**With**	**Without**	**With**	**Without**	**With**	**Without**
3.32E-03	6.82E-03	3.96E-03	8.40E-03	2.36E-03	4.52E-03	2.22E-03	4.06E-03

In table 2.11 the percentage of relative difference (PRD) for the absorbed dose coefficients (ADC) between IDAC 2.1 (used as reference) and OLINDA/EXM V2.0. The first difference to highlight between the two software is the amount of target organs used, IDAC 2.1 complies with ICRP recommendations in those terms. Second for left colon wall differences are higher than 140% and urinary bladder wall more than 190%. Other organs exhibit differences higher than ± 20% are: endosteum, eye lens, kidneys, prostate, red bone marrow, right colon, small intestine, spleen and testes.

Table 2.11. Percentage of relative difference (PRD) for the absorbed dose coefficients (ADC) between IDAC 2.1 (used as reference) and OLINDA/EXM V2.0 for [^{11}C]SAM.

Target organ	PRD with bladder voiding	PRD without bladder voiding
Adipose/residual tissue	---	---
Adrenals	3,03	6,94
Alveolar-interstitial	---	---
Brain	-2,18	-2,34
Breast	---	---
Bronchi bound	---	---
Bronchi sequestered	---	---
Bronchioles	---	---
Colon wall	---	---
Endosteum (bone surface)	-30,00	-32,30
ET region	---	---
ET1 basal cells	---	---
ET2 basal cells	---	---
Eye lenses	35,19	36,70
Gallbladder wall	15,79	16,80
Heart wall	4,87	5,56
Kidneys	35,34	35,64
Left colon wall	151,96	142,15
Liver	13,59	14,68
Lung	-4,72	-4,65
Lymphatic nodes	---	---
Lymph nodes in ET region	---	---
Lymph nodes in sys	---	---
Lymph nodes in thoracic region	---	---
Muscle	---	---
Oesophagus	8,54	10,53
Oral mucosa	---	---
Ovaries	---	---
Pancreas	-2,75	-4,88
Pituitary gland	---	---
Prostate	-43,75	-47,05
Recto-sigmoid colon wall	0,00	-19,70
Red (active) bone marrow	-25,52	-27,90
Right colon wall	24,51	22,46
Salivary glands	12,76	12,74
Skin	---	---
Small intestine wall	-15,38	-29,54
Spleen	21,53	22,67
Stomach wall	7,36	6,47
Testes	33,64	53,76
Thymus	1,60	2,24
Thyroid	9,29	9,66
Tongue	---	---
Tonsils	---	---
Ureters	---	---
Urinary bladder wall	194,96	198,46
Uterus/cervix	---	---

3.3. Residence times and absorbed dose estimations for [^{18}F]SFR101

Figure 2.4.A. shows the variations in the averages of percentages of injected activity per mice group for all organs. High uptake can be observed in the intestines and liver, demonstrating the clearance pathway of this radiopharmaceutical. The uptake for the other organs is little, as it can be observed in figure 2.4.B.

The residence times for each mice organ and the mass values considered for mass scaling are described in Table 2.12. As it is expected, the highest residence time is for the intestines. The remainder, liver, kidneys, carcass and stomach showed high values as well.

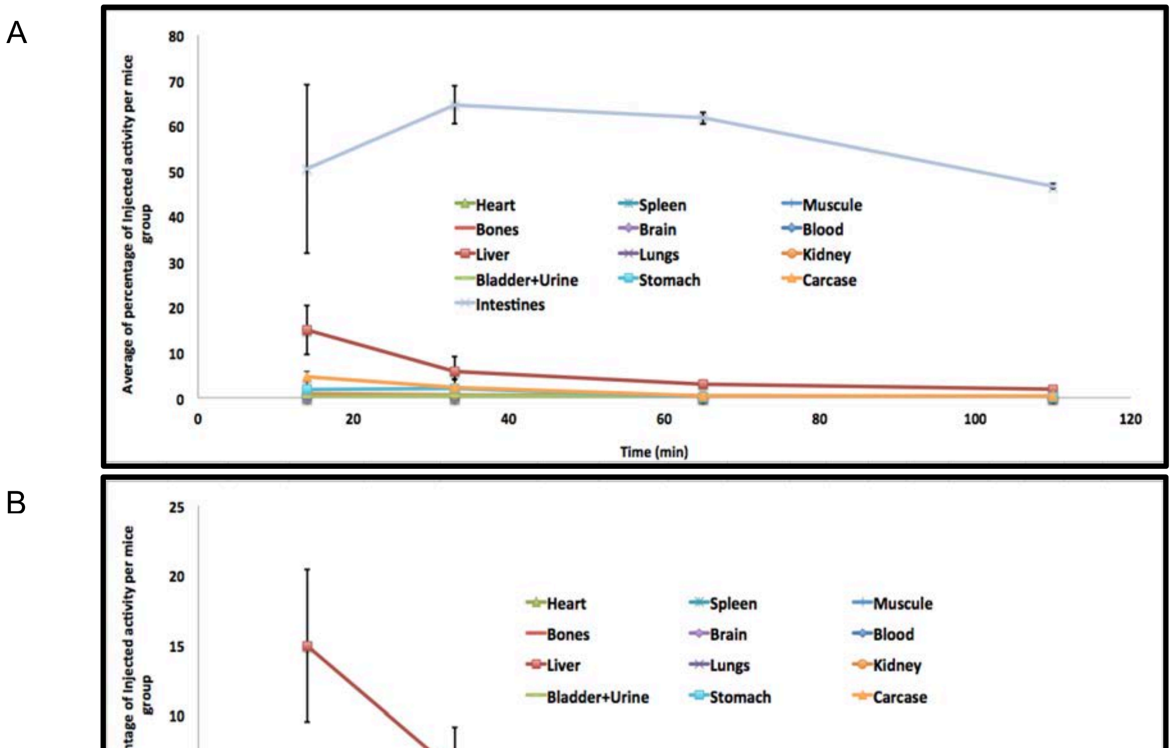

Figure 2.4: Percentage of administrated activity per mice time group for [^{18}F]SFR101. A: all measured organs. B: all organs except intestines. Figure adapted from (Kreimerman et al., 2018), also with permission from authors.

Table 2.12. Residence times (T) for each organ for [^{18}F]SFR101 in mice. Average measure of the mice organ masses used for the mass scaling process for some organs. Mass average and standard deviation for each mice group.

Organ	Residence time (h)	Organ mass (g)
Blood	3.11E-03	---
Brain	1.37E-04	0.4090 ± 0.0731
Liver	1.16E-01	1.8596 ± 0.2463
Heart wall	9.52E-05	0.1646 ± 0.0286
Lungs	9.75E-04	0.2193 ± 0.0319
Spleen	5.48E-05	0.0963 ± 0.0285
Kidneys	1.29E-02	0.4204 ± 0.0425
Muscles	2.63E-04	---
Bones	2.18E-04	---
Stomach contents	1.77E-02	0.1000[a]
Intestines	1.69E+00	3.3000[a]
Bladder contents	7.65E-03	0.1000[a]
Carcass	3.11E-02	---
Remainder	3.47E-02	28.2063[b]
Whole body mass	---	34.8755 ± 3.4749
Whole body mass for mice group 14 min (g)	32.02 ± 3.47	
Whole body mass for mice group 33 min (g)	37.52 ± 3.13	
Whole body mass for mice group 65 min (g)	33.67 ± 2.34	
Whole body mass for mice group 110 min (g)	37.00 ± 2.69	

[a] Mice intestines, stomach and bladder contents masses taken from OLINDA/EXM V2.0; [b] Remainder takes into account the blood, muscles, bones and carcass.

The mass values used for the male and female dosimetric models of OLINDA/EXM V2.0 and the self-irradiation S-factor for each organ are included in Table 2.13. As was observed in the previous cases, the differences in mass between human dosimetric models and measured mice organs are between two or four orders of magnitude.

Table 2.13. Mass values used for mass scaling and self-irradiation S-factor for each organ, taken from male/female models available in OLINDA/EXM V2.0.

Organ	m_{male} (g)	S-factor [a] (mGy/MBq-s)	m_{female} (g)	S-factor [a] (mGy/MBq-s)
Brain	1450	4.44E-05	1300	4.89E-05
Heart wall	330	1.42E-04	250	1.86E-04
Kidneys	310	1.64E-04	275.5	1.82E-04
Intestines contents	650[c]	---	600[c]	---
Left colon contents (LLI)	75	2.95E-04[b]	80	2.77E-04[b]
Small intestine contents (SI)	350	7.17E-05[b]	280	8.71E-05[b]
Right colon contents (ULI)	150	1.68E-04[b]	160	1.57E-04[b]
Rectum contents	75	3.10E-04[b]	80	3.00E-04[b]
Liver	1800	3.62E-05	1400	4.53E-05
Lungs	1200	3.90E-05	950	4.80E-05
Spleen	150	3.29E-04	130	3.76E-04
Stomach contents	250[c]	1.15E-04[b]	230[c]	1.26E-04[b]
Bladder contents	211[c]	1.35E-04[b]	160[c]	1.56E-04[b]
Remainder	66649	1.29E-06	54704.5	1.57E-06
Whole body	73000	---	60000	---

[a] S-factor refers to self-irradiation; [b] S-factor for LLI wall, SI wall, ULI wall, rectum wall, stomach wall and urinary bladder wall, considering their contents as a source; [c] Intestines, stomach and urinary bladder contents masses taken from OLINDA/EXM V2.0;

Human residence times used in OLINDA/EXM V2.0 after mass scaling are shown in Table 2.14. The highest values are for the remainder, intestines and stomach contents and liver, for both dosimetric models.

Table 2.14. Residence times (T) used for dosimetric estimations in OLINDA/EXM V2.0.

Organ	**T_{male}(h)**	**T_{female}(h)**
Brain	2.31E-04	2.52E-04
Heart wall	9.12E-05	8.41E-05
Kidneys	4.56E-03	4.93E-03
Intestines contents	1.59E-01	1.79E-01
Left colon contents (LLI)	1.84E-02	2.39E-02
Small intestine contents (SI)	8.56E-02	8.35E-02
Right colon contents (ULI)	3.67E-02	4.77E-02
Rectum contents	1.84E-02	2.39E-02
Liver	5.37E-02	5.08E-02
Lungs	2.55E-03	2.46E-03
Spleen	4.07E-05	4.30E-05
Stomach contents	2.11E-02	2.36E-02
Bladder contents	7.72E-03	7.12E-03
Remainder	3.91E-02[a]	3.91E-02[a]

[a] Remainder considers the blood, muscles, bones and carcass.

The absorbed and effective doses estimated by OLINDA/EXM V2.0 are shown in table 2.15. The highest ADCs values are for the different sections of the wall intestines (left colon, small intestine, right colon and rectum). For the male dosimetric model, other organs exhibiting a high ADCs, for instance, gallbladder wall, kidneys, liver, pancreas and urinary bladder wall. For the female dosimetric model, the uterus also exhibits high ADC in addition to the mentioned organs. The mean effective doses according to OLINDA/EXM V2.0 were 5.26×10^{-3} mSv/MBq and 6.51×10^{-3} mSv/MBq for the male and female dosimetric models, respectively. When an administered activity of 350 MBq is injected to a patient (according to CUDIM protocols), it would correspond to 1.44 mSv and 2.28 mSv for male and female dosimetric models, respectively.

The absorbed and effective doses estimated by IDAC 2.1 are shown in table 2.16. For both dosimetric models the highest ADCs values are for the different sections of the wall intestines (left colon, small intestine, right colon and rectum), gallbladder wall, kidneys, liver and pancreas. Then for IDAC 2.1, the effective doses are 3.12×10^{-3} mSv/MBq and 3.59×10^{-3} mSv/MBq for male and female models respectively (for a reference person 3.36×10^{-3} mSv/MBq). This would correspond to effective doses of 1.18 mSv and 1.28 mSv, for male and female models respectively, for the same administrated activity (for a reference person 1.18 mSv). In the case of ICRP-60 recommendations the effective dose for male model varies between 2.91×10^{-3} mSv/MBq and 3.17×10^{-3} mSv/MBq and for the female model varies between 3.75×10^{-3} mSv/MBq and 4.08×10^{-3} mSv/MBq.

Table 2.15. Absorbed dose coefficients (ADC) and contribution to the effective dose factor (CEDF) results for adult male and female models from OLINDA/EXM V2.0.

Target organ	Male		Female	
	ADC (mGy/MBq)	CEDF (mSv/MBq)	ADC (mGy/MBq)	CEDF (mSv/MBq)
Adrenals	3.23E-03	2.98E-05	3.23E-03	2.98E-05
Brain	9.94E-05	9.94E-07	1.22E-04	1.22E-06
Breast	---	---	5.57E-04	6.69E-05
Oesophagus	1.34E-03	5.37E-05	1.31E-03	5.25E-05
Eyes	1.84E-04	---	2.22E-04	---
Gallbladder Wall	4.29E-03	3.96E-05	4.64E-03	4.28E-05
Left colon	2.26E-02	1.10E-03	2.65E-02	1.28E-03
Small Intestine	2.40E-02	2.21E-04	2.83E-02	2.61E-04
Stomach Wall	1.00E-02	1.20E-03	1.25E-02	1.50E-03
Right colon	2.41E-02	1.17E-03	2.91E-02	1.41E-03
Rectum	2.21E-02	5.09E-04	2.74E-02	6.30E-04
Heart Wall	1.45E-03	1.34E-05	1.08E-03	1.00E-05
Kidneys	4.50E-03	4.15E-05	5.58E-03	5.15E-05
Liver	7.98E-03	3.19E-04	9.43E-03	3.77E-04
Lungs	1.24E-03	1.49E-04	1.33E-03	1.59E-04
Ovaries	---	---	2.94E-03	1.18E-04
Pancreas	4.58E-03	4.23E-05	4.32E-03	3.99E-05
Prostate	1.94E-03	8.98E-06	-	-
Salivary Glands	2.31E-04	2.31E-06	2.62E-04	2.62E-06
Red Marrow	9.00E-04	1.08E-04	1.22E-03	1.47E-04
Osteogenic Cells	6.11E-04	6.11E-06	7.54E-04	7.54E-06
Spleen	1.54E-03	1.42E-05	2.58E-03	2.38E-05
Testes	3.76E-04	1.50E-05	---	---
Thymus	5.97E-04	5.51E-06	6.41E-04	5.92E-06
Thyroid	3.65E-04	1.46E-05	4.00E-04	1.60E-05
Urinary Bladder Wall	4.89E-03	1.96E-04	6.31E-03	2.52E-04
Uterus	---	---	4.81E-03	2.22E-05
Total Body	1.18E-03	---	1.87E-03	---
Effective dose (mSv/MBq)	---	5.26E-03	---	6.51E-03

Table 2.16. Absorbed dose coefficients (ADC) for adult male and female models using IDAC 2.1.

Target organ	From male bio-kinetics		From female bio-kinetics	
	Male ADC (mGy/MBq)	Female ADC (mGy/MBq)	Male ADC (mGy/MBq)	Female ADC (mGy/MBq)
Adipose/residual tissue	1.03E-03	8.86E-04	1.10E-03	9.47E-04
Adrenals	3.21E-03	3.84E-03	3.30E-03	3.86E-03
Alveolar-interstitial	1.36E-03	1.39E-03	1.37E-03	1.38E-03
Brain	9.46E-05	1.04E-04	9.84E-05	1.08E-04
Breast	9.07E-04	7.04E-04	9.39E-04	7.06E-04
Bronchi bound	1.03E-03	8.77E-04	1.05E-03	8.75E-04
Bronchi sequestered	1.03E-03	8.77E-04	1.05E-03	8.74E-04
Bronchioles	1.36E-03	1.39E-03	1.37E-03	1.38E-03
Colon Wall	5.99E-03	6.54E-03	7.07E-03	7.85E-03
Endosteum (bone surface)	6.18E-04	8.72E-04	6.48E-04	9.25E-04
ET región	1.68E-04	2.01E-04	1.70E-04	2.02E-04
ET1 basal cells	1.23E-04	1.58E-04	1.25E-04	1.59E-04
ET2 basal cells	1.68E-04	2.01E-04	1.70E-04	2.02E-04
Eye lenses	1.48E-04	1.85E-04	1.48E-04	1.86E-04
Gallbladder wall	5.69E-03	5.13E-03	6.02E-03	5.09E-03
Heart Wall	1.55E-03	1.34E-03	1.60E-03	1.35E-03
Kidneys	4.95E-03	5.61E-03	5.25E-03	5.92E-03
Left colon wall	6.01E-03	5.82E-03	6.86E-03	6.90E-03
Liver	6.80E-03	7.85E-03	6.71E-03	7.58E-03
Lung	1.25E-03	1.22E-03	1.26E-03	1.21E-03
Lymphatic nodes	2.05E-03	2.38E-03	2.18E-03	2.55E-03
Lymph nodes in ET region	2.76E-04	3.23E-04	2.79E-04	3.23E-04
Lymph nodes in sys	2.35E-03	2.75E-03	2.51E-03	2.94E-03
Lymph nodes in thoracic region	6.32E-04	6.07E-04	6.42E-04	6.04E-04
Muscle	6.35E-04	8.77E-04	6.73E-04	9.40E-04
Oesophagus	1.20E-03	1.09E-03	1.23E-03	1.09E-03
Oral mucosa	2.32E-04	2.70E-04	2.34E-04	2.71E-04
Ovaries	---	3.28E-03	---	3.61E-03
Pancreas	6.03E-03	5.85E-03	6.30E-03	5.98E-03
Pituitary gland	1.64E-04	2.09E-04	1.67E-04	2.10E-04
Prostate	1.10E-03	---	1.13E-03	---
Recto-sigmoid colon wall	4.32E-03	6.21E-03	5.33E-03	7.39E-03
Red (active) bone marrow	1.20E-03	1.63E-03	1.26E-03	1.73E-03
Right colon wall	6.81E-03	7.41E-03	8.14E-03	9.04E-03
Salivary glands	2.16E-04	2.55E-04	2.18E-04	2.56E-04
Skin	4.21E-04	5.03E-04	4.44E-04	5.28E-04
Small intestine wall	7.93E-03	9.59E-03	8.08E-03	9.86E-03
Spleen	2.04E-03	2.34E-03	2.18E-03	2.47E-03
Stomach wall	1.00E-02	1.01E-02	1.10E-02	1.09E-02
Testes	2.94E-04	0.00E+00	3.03E-04	0.00E+00
Thymus	5.06E-04	5.24E-04	5.14E-04	5.23E-04
Thyroid	3.51E-04	3.61E-04	3.56E-04	3.61E-04
Tongue	1.85E-04	2.00E-04	1.87E-04	2.01E-04
Tonsils	2.13E-04	2.62E-04	2.15E-04	2.62E-04
Ureters	3.25E-03	4.29E-03	3.41E-03	4.64E-03
Urinary bladder wall	2.39E-03	3.86E-03	2.42E-03	4.01E-03
Uterus/cervix	---	4.01E-03	---	4.40E-03
Effective dose 60 [mSv/MBq]	2.91E-03	3.75E-03	3.17E-03	4.08E-03
Risk-weighted effective dose 103 [mSv/MBq]	3.12E-03	-	-	3.59E-03

In table 2.17 effective dose factor results are presented. For both models, for both versions of OLINDA results are higher than those values obtained with IDAC 2.1. For female model, results are higher that male model for all software. For this model, for both versions of OLINDA results are almost twice those results obtained using IDAC 2.1. The same effect occurs for male model.

Table 2.17. Summary of effective dose factor results (mSv/MBq) for [^{18}F]SFR-101.

OLINDA/EXM V1.0		OLINDA/EXM V2.0		IDAC 2.1		
				ICRP-60		ICRP-103
Male	**Female**	**Male**	**Female**	**Male**	**Female**	**Reference person**
6.55E-03	8.77E-03	5.26E-03	6.51E-03	2.91E-03	4.08E-03	3.36E-03

4. Discussion

In this chapter, three different radiopharmaceuticals were studied from the dosimetric point of view. Also, the biodistribution of these products were established by using images or by dissection of the animals. Most of the time, the preferred animals to study these products are among mammalians species, because they approximate well the human response. Hence, by knowing the biodistribution in the animal, pharmacokinetics assessment can take place by using empirical approaches, considering the body surface area (BSA), rates of metabolism and allometric approaches, which are relative mass scaling between organ masses and whole-body masses. However, there are aspects that need to be considered in order to quantify the activity accurately as possible independently of the chosen method to study the bio-kinetics of the radiopharmaceutical. For instance:

4.1. Scaling to human’s method and differences in organs sizes

McParland (McParland, 2010) discussed different scaling methods. One of the simplest approaches is to consider the same pharmacokinetics between humans and animals. Depending on the chosen animals some differences cannot be neglected, for instance, a) the rat does not have gallbladder, and therefore, the liver behaviour is not the same; b) organ sizes, the weight of the rat testes can be higher comparing to a reference man. Consequently, assuming no specificity, the testicular uptake is higher than expected, with a subsequent overestimation of testicular absorbed dose in man; c) the metabolism rate between species will typically differ.

Conversely, assuming same pharmacokinetics between different species, the pharmacokinetics result can be scaled with the organ mass as a fraction of the total body mass. Tolvanen et al. (Tolvanen et al., 2010) mentioned that due to the faster physiology of rodents, the absorbed and effective doses extrapolated from mice may be lower than in data obtained directly from humans. In particular, there are qualitative differences in liver metabolism between species that can introduce bias in the results. Beykan et al. (Beykan et al., 2016) highlighted that pig models studies are more suitable than small animals (mice/rats) due to the similarity in physical properties and biodistribution compared to human physiology. Moreover, Kranz et al.

(Kranz, Sattler, Wüst, et al., 2016) concluded that the extrapolation of preclinical data obtained from studies in small animals (primates (Macaca fascicularis), rats, squirrels monkeys, piglets or rabbits), either by organ harvesting or PET images, would result in an underestimation of the human effective dose due to limitations in allometric scaling and species-specific target expression.

Avila-Rodriguez et al. (Avila-Rodriguez et al., 2017) examined [^{64}Cu]CuCl$_2$ in healthy rats and human volunteers. Initially they performed MicroPET imaging (Manrique-Arias et al., 2016) to rats and then extrapolation to human was carried out by mass scaling. When they compared the extrapolated data with images from human volunteers, they found discrepancies in the results due to differences in sizes between species, metabolic rate and in assumptions in the dose calculations.

Also Beykan et al. (Beykan et al., 2016) and McParland (McParland, 2010) mentioned that sources of errors due to the allometric approach can be introduced because scaling increases or decreases the values of residence times, and consequently, the same effect will be present on absorbed doses. In our results, residence times suffer these variations, for instance, for brain and lung, for [^{18}F]FNM and [^{18}F]SFR-101, an increment occurs ranging between 1.8 to 3.4 times. For the three products, these results depend on the dosimetric model used, reduction in kidneys occurs between 0.34 to 0.57 times and in liver between 0.46 to 0.99 times.

4.2. Gender of the animals

The ideal would be to have the pharmacokinetic of male and female animals, but the number of animals must be kept minimum, due to ethical and financial reasons. Consequently, in our studies one gender was used to assess the products. Since we had no specific assessment of male/female pharmacokinetics from animal experiments, the gender specific estimate was obtained during the extrapolation phase, by scaling differently the same animal pharmacokinetics. This is clearly a bias that would require further studies.

4.3. Half-life of the radionuclide and measured time points

Our study considered two isotopes with short half-lives; furthermore, ^{11}C has a shorter half-life than ^{18}F. Hence, regarding data acquisition and/or measuring times McParland (McParland, 2010) provided two recommendations: a) include data measurements between 2 and 5 min to determine the uptake of the radiopharmaceutical and b) the last point measurement should be at $t=4*T_{1/2p}$ (four times the physical half-life).

For [^{11}C]SAM Ishiwata et al. reported an increase in ^{11}C concentration until 10 min after injection in rats (Ishiwata et al., 1986) but they started measurements before 5 min. Bearing in mind that our measurements began at t=10 min in the current study to reduce the number of animals. On the other hand, for this product, last measure data time point was near to the criterion given by McParland

(McParland, 2010). In case of both products with ^{18}F, it was really difficult to follow the recommendation for the last data time point.

On one hand, for the organ harvesting studies the number of animals were kept as low as possible, trying to keep financial cost as minimum as possible, but also to be representative enough in terms of time point measurements. On the other hand, for [^{18}F]FNM the issue was not the number of animals, but how to keep the rats under anaesthesia to acquire images at late time points. This was the main reason to stop image acquisition at 70 min.

4.4. Calibration of the equipment used to quantify activity

4.4.1. PET/CT units

It is well known that issues such as acquisition settings, reconstruction parameters, attenuation/scatter/partial volume effect may impact the quantification. Corrections have been studied and optimization can be done in each step if necessary. Other important aspect to consider is how to obtain the calibration factor for the system. This is linked to the previous steps and for small animal imaging it's also critical due to the small structures present, due to the possibility of errors induced by the partial volume effect. In our study, image registration and segmentation took place using validated software called Sysiphe (Ducassou et al., 2013; Ken et al., 2015; Salabert et al., 2017; Tensaouti et al., 2018) developed in Toulouse, which was available at the moment of this study and was used by a well-trained professional.

4.4.2. Well counters

Well counters are used most of the time following a dissection. This procedure can be highly user-dependent; therefore, activity loss can happen. Measuring settings (centre of the channel of measure and energy width) were similar for both isotopes due to the γ-emission. Background corrections were performed before measurement. Volume corrections were considered due to the difference in the dissected organs, therefore, CUDIM has a reference volume to compare with, and from it the correction took place. This correction is very important to be taken into account as great errors can happen in terms of quantification. Finally, time of measurements was kept constant.

4.5. Applied fitting method

Depending on the number of data time points, bi-exponential analysis can be done, as it was the case of some organs for [^{18}F]FNM. However, when is not possible, the trapezoidal method is normally used. Guerriero et al. (Guerriero et al., 2013), mentioned an overestimation of time-integrated activities using the trapezoidal method (also considering physical decay from the last point measurement) compared to those generated by bi-exponential or other methods. However, in the case of

[^{11}C]SAM and [^{18}F]SFR-101, the time-integrated activity curves of the different organs did not show an exponential behaviour. Therefore, the best way to estimate the cumulated activity was by applying the trapezoidal method. To evaluate the best fit, the Pearson correlation coefficient (R^2) was used (being > 0.98 in all cases) for the linear functions. In our case *Mathematica* (Mathematica, 2015) was used applying non-linear fitting for some organs when [^{18}F]FNM was employed. For the other products, *Mathematica* was used to assess the linear fitting in the trapezoidal method. In the case of Boschi et al. (Boschi et al., 2016a) and other authors (Beykan et al., 2016; Boschi et al., 2016b; Herrmann et al., 2015; Schottelius et al., 2017; Weineisen et al., 2015) for dosimetric analysis and calculations using NUKFIT, which may have advantages over *Mathematica*, because this software can incorporate the systematic error in activity determination, and error propagation also can be taken into account. Finally, we assumed no activity at t= 0 h, therefore between this time and the first data time point, we assumed a line to join the two points (forming a triangle). For each organ we could assume different approaches, but this is time consuming and depending on the organ the impact would be low. Some software, such as the fitting module from Dosisoft (Gardin et al., 2017), allows the user to choose between three options to create the fitting from t=0h to the first data time point, but entering data is not possible within this module.

4.6. Reference model used

Differences between OLINDA/EXM V1.0, V2.0 and IDAC 2.1 are the following:

4.6.1. Organ geometries, composition and masses

The human models (stylised) from Cristy and Eckerman are used in OLINDA/EXM V1.0. These models were created considering anatomical information from ICRP-23, in terms of organ mass and composition. In case of OLINDA/EXM V2.0, non-uniform rational B-splines (NURBS) body and organ models were scaled and shaped to fulfil the ICRP-89 values, in terms of organ mass and its composition. This means that human models considered in OLINDA/EXM V2.0 are not the same as those presented in ICRP-110, but most characteristics are similar. However, organ shapes and positions within the human models may vary from the ICRP-110. In IDAC 2.1, the ICRP-110 human models (voxelized) are used.

4.6.2. S-value estimation

In OLINDA/EXM V1.0, the absorbed fraction (AF) is considered = 1 for alpha and beta emissions when the source region is the same as the target region. Hence, a linear mass scaling can be performed in order to adjust the AF to a particular organ mass value. Also, in this case AF = 0 when the source region is different from the target region for the same emissions. In the case of photons, AF≠1, because cross-irradiation will occur from the source region to the target region. Then, if mass adjustment is needed, the AF can be adjusted with the cube root of the new organ mass.

In OLINDA/EXM V2.0 and IDAC 2.1, the AF was estimated using MC codes. In the case of OLINDA/EXM V2.0, GEANT4 was used for SAF estimations. In the case of IDAC 2.1 references from ICRP-133 were used using EGS4.

4.6.3. Radiation and tissue weight factors employed and effective dose estimation

OLINDA versions do not strictly follow ICRP recommendations for the estimations of effective dose. Conversely, IDAC 2.1 strictly complies with ICRP recommendations, for both effective dose estimations under ICRP-60 and ICRP-103.

In the case of OLINDA/EXM V1.0 / ICRP-60, some organs are missing, for example, oesophagus. The colon is divided in two sections, the Lower Large Intestine (LLI) is part of colon and the Upper Large Intestine (ULI) is part of the remainder. For gonads a value is assigned for ovaries and not for testes, only when they are considered as a source. Also, in the case of the estimation of the remainder, there are some ICRP-60 recommendations not followed in OLINDA/EXM. For gallbladder, heart wall and testes there is no weighting tissue factor assigned, meaning that they do not contribute to the effective dose.

In the case of OLINDA/EXM V2.0 / ICRP-103, some organs are missing, for instance skin, breast for adult male. Weighting tissue factor for ovaries, testes, prostate and ureters are different comparing to ICRP-103 recommendations. For the remainder, four organs are not taken into account, extrathoracic region (ET), lymphatic tissue (Lymph), muscle and oral-mucosa (O-mucosa).

In terms of radiation weighting factor, for alpha emissions, OLINDA/EXM V1.0 and V2.0 consider a value of 5 (Feinendegen & McClure, 1997), instead of 20 as is recommended by ICRP-103. This is to give account of deterministic effects, but certainly deviates from ICRP concepts.

In the case of [^{18}F]FNM results from table 2.5 are lower than those observed in other ^{18}F-PET tracers used in neurology. For example, [^{18}F] DPA714 is around 17.2 µSv/MBq (Arlicot et al., 2012), [^{18}F]FEDDA is around 36 µSv/MBq (Takano et al., 2011) and the [^{18}F] amyloid tracer flutemetamol, is around 25-30 µSv/MBq (Koole et al., 2009). This may be associated to the fast clearance of the radiopharmaceutical through the kidneys. On the other hand, comparing results between OLINDA/EXM V1.0 and IDAC 2.1 (ICRP-60), these are very similar even though the mean effective doses from IDAC 2.1 were obtained using a different mass scaling and different dosimetric models.

Moreover, comparing OLINDA/EXM V2.0 with IDAC 2.1 (ICRP-103), mean effective dose values are in the same order of magnitude, but with OLINDA/EXM V2.0 some organs are not considered. Moreover, in IDAC 2.1 the mean effective dose for the reference person are from averaging male and female models results.

In the case of [^{11}C]SAM, as described by Ishiwata et al. and Tolvanen et al. in rats (Ishiwata et al., 1986; Tolvanen et al., 2010), the highest total absorbed dose is for the kidneys as it was in our case. Tolvanen et al. (Tolvanen et al., 2010) reported effective dose values varying from 3.2×10^{-3} to 1.41×10^{-2} mSv/MBq for ^{11}C-radiopharmaceuticals in humans, and the current results are comparable to those figures.

Moreover, looking at table 2.10, results for OLINDA/EXM V1.0 and IDAC 2.1 (ICRP-60) are in the same order of magnitude, but some differences can be highlighted. First, the organ mass for the bladder contents is almost twice higher in IDAC 2.1 than OLINDA/EXM V1.0. In OLINDA/EXM V1.0, the SAF for the urinary bladder wall due to the bladder contents irradiation is estimated as 0.5xbladder contents mass. However, in IDAC 2.1 the SAF is estimated from MC simulations. Also, there are differences regarding the estimation of the remainder and the contribution of the intestines (especially the large intestine) to the mean effective dose.

Also, comparing results between OLINDA/EXM V2.0 and IDAC 2.1 (ICRP-103) in table 2.11 the percentage of relative difference for the ADC, with and without bladder voiding. For left colon wall and urinary bladder wall, these values are almost 200%, which means that the model generated in OLINDA/EXM V2.0 has an impact on the absorbed dose calculation. Hence, for hollow organs, which mean the ones having no-contents, may also be important in absorbed dose calculations. Moreover, other organs exhibit percentage of relative differences more than 30% are the endosteum, eyes lens, kidneys, prostate and testes. In the case of kidneys, prostate and testes are close to the bladder, and then irradiation should be important. Finally, tissue weighting factors, the way in which the remainder is estimated, and the organs used to compute the mean effective dose are not exactly the same between the two software.

In the case of [^{18}F]SFR-101, values of mean effective dose in table 2.17 are lower but comparable to different radiopharmaceuticals previously published: 12.1 μSv/MBq for [^{18}F]-Flubatine (Kranz et al., 2016); 6.23 μSv/MBq for [^{18}F]-PMSA [27]; 25 μSv/MBq for [^{18}F]-Tetrafluoroborate (Marti-Climent et al., 2015); 19 μSv/MBq for [^{18}F]-VAT (Karimi et al., 2015); 21 μSv/MBq for [^{18}F]-Fluspidine [28], 20 μGy/MBq for [^{18}F]-SFE (Waterhouse et al., 2006); and 20 μGy/MBq for [^{18}F]-FPS [29]. The differences between the two versions of OLINDA/EXM and IDAC 2.1 that were mentioned before for [^{11}C]SAM, apply here also. For [^{18}F]SFR-101, the highest residence times were for intestines. Therefore, the greatest percentages of relative differences can be seen for the intestine's walls, again showing that contents are important to be considered as source.

5. Conclusions

In this chapter biodistribution and bio-kinetics for three radiopharmaceuticals have been shown. These data were obtained from small animals (rats and mice). For the three products extrapolations to humans was carried out. This procedure was performed by allometric scaling of the normalised cumulated activity by using mass organ information from ICRP-23 and ICRP-89. The extrapolated results to humans were assessed using three software. OLINDA/EXM V1.0 is nowadays the gold standard in this field. However, its new version is in the market as well as IDAC 2.1, which can be used for same purposes, claiming the fulfilment of ICRP-103 recommendations. Main characteristics between the software have been addressed in order to explain differences in their results. Despite the differences in the methods used to assess dosimetric estimations, the current data provide a reasonable basis for evaluating human dosimetry, that can be better-established in human subjects, to verify or to compare the obtained results at a pre-clinical level.

As a future work, we are expecting to perform dosimetry for healthy volunteers and patients for the three radiopharmaceuticals studied in this chapter. At the moment the final approval of the national/local ethics committees and the revision of the clinical protocols proposed by each research centre are under study.

6. References of the chapter

Andersson, M., et al., (2017). IDAC-Dose 2.1, an internal dosimetry program for diagnostic nuclear medicine based on the ICRP adult reference voxel phantoms. *EJNMMI Research*, *7*, 1–10.

Arlicot, N., et al,. (2012). Initial evaluation in healthy humans of [18F]DPA-714, a potential PET biomarker for neuroinflammation. *Nucl Med Biol*, *39*(4), 570–578.

Avila-Rodriguez, et al., (2017). Biodistribution and radiation dosimetry of [64Cu]copper dichloride: first-in-human study in healthy volunteers. *EJNMMI Research*, *7*(1), 98.

Beykan, S., et al., (2016). [177Lu]-OPS201 targeting somatostatin receptors: In vivo biodistribution and dosimetry in a pig model. *EJNMMI Research*, *6*(1), 1–9.

Boschi, S., et al., (2016a). Synthesis and preclinical evaluation of an Al(18)F radiofluorinated GLU-UREA-LYS(AHX)-HBED-CC PSMA ligand. *Eur J Nucl Med Mol Imaging*, *43*(12), 2122–2130.

Boschi, S., et al,. (2016b). Synthesis and preclinical evaluation of an Al18F radiofluorinated GLU-UREA-LYS(AHX)-HBED-CC PSMA ligand. *Eur J Nucl Med Mol Imaging*, *43*(12), 2122–2130.

Cristy, M., Eckerman, K. F. (1987). *Specific Adsorbed Fractions of Energy at Various Ages From Internal Photon Sources*. *TN: Oak Ridge National Laboratory. Ornl/Tm-8381 V1-V7*.

Ducassou, A., et al., (2013). αvβ3 Integrin and Fibroblast growth factor receptor 1 (FGFR1): Prognostic factors in a phase I-II clinical trial associating continuous administration of Tipifarnib with radiotherapy for patients with newly diagnosed glioblastoma. *Eur J Cancer*, *49*(9), 2161–2169.

Eckerman, K., & Endo, A. (2008). MIRD: radionuclide data and decay schemes 2nd edn (Reston, VA: Society for Nuclear Medicine).

Feinendegen, L. E., McClure, J. (1997). Alpha-Emitters for Medical Therapy-Workshop of the United States Department of Energy, *148*(2), 195–201.

Gardin, I., et al., (2017). Predictive value of dosimetry indices for treatment response in liver cancer patients treated with yttrium 90 microspheres using a random forest algorithm. *J Nucl Med*, *58*(supplement 1), 197.

Giussani, A., et al., (2012). A Compartmental Model for Biokinetics and Dosimetry of 18F-Choline in Prostate Cancer Patients. *J Nucl Med*, *53*(6), 985–993.

Guerriero, F., et al., (2013). Kidney dosimetry in 177Lu and 90Y peptide receptor radionuclide therapy: Influence of image timing, time-activity integration method, and risk factors. *Bio Med Res Int.*, *2013*, 1–12.

Herrmann, K., et al., (2015). Biodistribution and Radiation Dosimetry for a Probe Targeting Prostate-Specific Membrane Antigen for Imaging and Therapy. *J Nucl Med*, *56*(6), 855–861.

ICRP. (1975). ICRP 23: Report of the task group on reference man. *Ann ICRP*, 0–480.

ICRP. (1991). 1990 Recommendations of the International Commission on Radiological Protection. ICRP Publication 60. *Ann ICRP*, *21*, 1–201.

ICRP. (2007). ICRP publication 103. *Ann ICRP*, *37*(2.4), 2.

Ishiwata, K., et al., (1988). Tumor Uptake Studies of S-Adenosyl-L- [methyl-11C] Methionine L- [methyl-11C] Methionine. *Nucl Med and Biol*, *15*(2), 123–126.

Ishiwata, K., et al., (1986). Simplified enzymatic synthesis and biodistribution of 11C-S-adenosyl-L- methionine. *Eur J Nucl Med*, *11*(11), 449–452.

Karimi, M., et al., (2015). Radiation dosimetry of [18F]VAT in nonhuman primates.

EJNMMI Research, *5*(1), 1–6.

Ken, S., et al., (2015). Voxel-based evidence of perfusion normalization in glioblastoma patients included in a phase I–II trial of radiotherapy/tipifarnib combination. *J Neuro-Onc*, *124*(3), 465–473.

Koole, M., et al., (2009). Whole-Body Biodistribution and Radiation Dosimetry of 18F-GE067: A Radioligand for In Vivo Brain Amyloid Imaging. *J Nucl Med*, *50*(5), 818–822.

Kranz, M., et al., (2016). Radiation dosimetry of the alpha4beta2 nicotinic receptor ligand (+)-[18F]flubatine, comparing preclinical PET/MRI and PET/CT to first-in-human PET/CT results. *EJNMMI Physics*, *3*(1), 1–17.

Kranz, M., et al., (2016). Evaluation of the enantiomer specific biokinetics and radiation doses of [18 F]fluspidine-A New tracer in clinical translation for imaging of Σ1Receptors. *Molecules*, *21*(9), 1164–78.

Kreimerman, I., et al., (2018). Dosimetry and toxicity studies of the novel sulfonamide derivative of Sulforhodamine 101([18F]SRF101) at a preclinical level. *Cur Radiopharm*, *11*.

Kreimerman, I., et al., (2017). Synthesis of [18F] 2B-SRF101: A sulfonamide derivative of the fluorescent dye Sulforhodamine 101. *Cur Radiopharm*, *10*(3), 212–220.

Manrique-Arias, J. C., et al., (2016). Biodistribution in rats and estimates of doses to humans from 64CuCl2, a potential theranostic tracer. *App Rad Iso*, *115*, 18–22.

Marti-Climent, J. M., et al., (2015). Radiation dosimetry and biodistribution in non-human primates of the sodium/iodide PET ligand [18F]-tetrafluoroborate. *EJNMMI Research*, *5*(1), 1–9.

Mathematica, W. (2015). Wolfram Research. *Inc., Champaign, Illinois*.

McParland, B. J. (2010). *Nuclear Medicine Radiation Dosimetry: Advanced Theoretical Principles*. Springer Science & Business Media.

Ryman, J. C., et al., (1987). ALGAMP--A Monte Carlo radiation transport code for calculating specific absorbed fractions of energy from internal or external photon sources. *ORNL/TM-8377) Oak Ridge National Laboratory, Oak Ridge, TN*.

Salabert, A.S., et al., (2018). Evaluation of [18 F] FNM biodistribution and dosimetry based on whole-body PET imaging of rats. *Nucl Med Biol*, *59*, 1–8.

Salabert, A.S., et al., (2017). Imaging grafted cells with [F-18] FHBG using an optimized HSV1-TK mammalian expression vector in a brain injury rodent model. *Plos One*, *12*(9), 1–9.

Salabert, A., et al., (2015). Radiolabeling of [18 F]-fluoroethylnormemantine and initial in vivo evaluation of this innovative PET tracer for imaging the PCP sites of NMDA receptors. *Nucl Med Biol*, *42*, 643–653.

Schottelius, M., et al., (2017). [177Lu]pentixather: Comprehensive preclinical characterization of a first CXCR4-directed endoradiotherapeutic agent. *Theranostics*, *7*(9), 2350–2362.

Stabin, M., et al., (2008). ICRP-89 based adult and pediatric phantom series. *J Nucl Med*, *49*(supplement 1), 14P–14P.

Stabin, M., Farmer, A. (2012). OLINDA/EXM 2 .0: The new generation dosimetry modeling code. *J Nucl Med*, *53*(Suppl 1), 585.

Stabin, M. G., et al., OLINDA/EXM: the second-generation personal computer software for internal dose assessment in nuclear medicine. *J Nucl Med*, *46*(6), 1023–1027.

Stabin, M., Siegel, J. A. (2018). Radar Dose Estimate Report: a Compendium of Radiopharmaceutical Dose Estimates Based on Olinda/Exm Version 2.0. *J Nucl Med*, *59*(1), 154–160.

Takano, A., et al., (2011). Biodistribution and radiation dosimetry of the 18 kDa translocator protein (TSPO) radioligand [18F]FEDAA1106: a human whole-body PET study. *Eur J Nucl Med Mol Imaging*, *38*(11), 2058–2065.

Tensaouti, F., et al., (2018). Imaging biomarkers of outcome after radiotherapy for pediatric ependymoma. *Radioth Onc*, *127*(1), 103–107.

Tensaouti, F., et al., (2008). Sysiphe-neuroimaging software toolbox. *Eur Soc Mag Res Med Biol*, *21*(1), 489.

Tolvanen, T., et al., (2010). Biodistribution and radiation dosimetry of [11C]choline: A comparison between rat and human data. *Eur J Nucl Med Mol Imaging*, *37*(5), 874–883.

Waterhouse, R. N., et al., (2003). Preclinical acute toxicity studies and rodent-based dosimetry estimates of the novel sigma-1 receptor radiotracer [18 F] FPS. *Nucl Med Biol*, *30*, 555–563.

Waterhouse, R. N., et al., (2006). Preclinical acute toxicity studies and dosimetry estimates of the novel sigma-1 receptor radiotracer, [18F]SFE. *Mol Imaging Biol*, *8*(5), 284–291.

Weineisen, M., et al., (2015). *68Ga- and 177Lu-Labeled PSMA I&T: Optimization of a PSMA-Targeted Theranostic Concept and First Proof-of-Concept Human Studies. J Nucl Med* (Vol. 56).

Zoppolo, F., et al., (2018). Biological and dosimetric evaluation of [11 C] S-adenosyl Methionine as a potential agent for prostate cancer diagnosis. *Cancer Research Frontiers*, *4*(1), 27-.

Zoppolo, F., et al., (2017). Automated One-pot Radiosynthesis of [11C]S-adenosyl Methionine. *Cur Radiopharm*, *10*(3), 203–211.

1. Introduction

Gamma camera calibration is a key factor for quantitative imaging, and therefore participates to the dosimetric chain. SPECT/CT systems from different manufacturers have been studied to derive calibration procedures (Beauregard et al. 2011; de Nijs et al., 2014; Sandström al., 2010). For ^{177}Lu, several publications can be found showing acquisition protocols to perform calibration. In tables 3.1 and 3.2, a resume of the protocols used to achieve this goal is shown. As can be seen, the comparison between calibration procedures can be a difficult task.

Table 3.1 shows differences in crystal thickness (3/8”, 5/8”, 1”), collimator type (LEHR, LEGP, MELP, MEGP), acquisition time (20 s, 30 s, 40 s, 45 s, 60 s), number of projections (60, 64, 120, 128), number of energy windows per photo-peak (113 keV @ 20%, 208 keV @ 20%, 208 keV @ 15%), the matrix size (generally 128x128 is used but there is one study also showing results with 256x256) (Sanders et al. 2015), acquisition orbit (frequently is auto-contouring, but circular orbits have been used with a fixed radius of 25cm) (de Nijs et al., 2014; Robinson et al. 2016), and pixel size (in the majority of the cases it varies from 4.4 mm to 4.8 mm). In the same table regarding the reconstruction process, in most of the cases OSEM was used. de Nijs et al. (de Nijs et al., 2014) and Sanders et al. (Sanders et al., 2015) have explored the influence of the combination in iterations and subsets. In most of publications, TEW (Ichiharaet al., 1993; Ogawa et al., 1991) is used as scatter correction method. However, de Nijs et al. (de Nijs et al., 2014) compared different scatter corrections methods, for instance, the effective scatter source estimation (ESSE) (Kadrmas et al. 1998), DEW (Jaszczak et al. 1984), TEW (Ogawa et al., 1991), downscatter correction (de Nijs et al. 2010), combined scatter and downscatter correction (de Nijs & Svarer, 2007), and dual-photopeak window (Ljungberg et al. 1994). Other corrections can also be seen in the same table for example, collimator-detector response, pre- and post-filtering, recovery coefficient and dead time.

Table 3.2 presents differences in the CT acquisition protocols (kV and mAs applied), the calibration procedure, the registration and segmentation procedures, absorbed dose results, residence times estimations, phantoms used for calibration, sensitivity units and sensitivity results. This shows that, to date, there is not standardized procedure to acquire, reconstruct, register and segment phantom/patient data. However, Wevrett et al. (Wevrett et al., 2017) proposed a calibration protocol for quantitative imaging for molecular radiotherapy dosimetry. Although they did not address all possible corrections that could be implemented, they suggested clearly how to perform the calibration of the SPECT/CT system. In addition, the MIRD committee has produced extensive and comprehensive documents to address quantitative planar (Siegel et al., 1999) and SPECT (Dewaraja et al., 2012) imaging.

Following the quantitative imaging general principles presented in Dewaraja et al. (Dewaraja et al., 2012), in 2016 the EANM and MIRD (Ljungberg et al., 2016) generated guidelines for quantitative ^{177}Lu-SPECT; illustrating the results of Monte

Carlo simulations, phantoms experiments and examples of patients protocols used in clinic. The importance of this effort from EANM/MIRD is related to the review of the literature regarding some of the effects degrading images for quantitative SPECT with this isotope specifically. Moreover, in this work the information is very rich as it provides a series of recommendations to estimate activity accurately. Tran-Gia and Lassmann (Tran-Gia & Lassmann, 2017) created a 3D realistic 2-compartment kidney phantom, to study partial volume correction methods on quantitative SPECT/CT imaging for ^{177}Lu, using two commercially available reconstruction methods. They mentioned that in sphere-like objects, the central voxels are far away from the object edges and, therefore, are largely unaffected by partial volume errors. In contrast, in complex structures such as renal cortex, most voxels are close to one of the object edges, thus, affecting these voxels by partial volume errors. Moreover, they showed an example where Gibbs ringing occurs after certain number of iterations, without post-filtering, for the two reconstruction methods evaluated.

In this work four commercial workstation were studied, GE Dosimetry Toolkit (DTK), Hermes Hybrid dosimetry Module™ (HDM), Philips STRATOS and Dosisoft PLANET® Onco Dose (PDOSE). The calibration factor used in each workstation and the units in which this parameter is expressed may differ. An overview of these software is presented as follows:

- DTK is an application from the GE Xeleris® workstation, that is working in Windows. The user can upload either serial Anterior-Posterior WB scans; serial Anterior-Posterior WBs and one SPECT (or SPECT/CT) study, or 3 serial SPECT (or SPECT/CT) studies. DTK requires two steps: first the "preparation for dosimetry toolkit" is used for the reconstruction of SPECT/CT raw data and the definition of a reference for later registration of the CT scans; second, the "Dosimetry toolkit" is used to segment different organs, to create time activity curves and to fit them by a mono-exponential, in order to calculate residence times for each organ. Finally the residence times can be exported to OLINDA/EXM V1.0 (Stabin et al., 2005). A calibration method is proposed by this company based-on planar measurements, estimating the calibration factor in units of cps/MBq.

Table 3.1. Acquisition protocols used with ^{177}Lu for patient treatments or SPECT/CT calibration.

Parameters	*de Nijs et al.* (de Nijs et al., 2014)	*Sandström et al.* (Sandström et al., 2010)	*Robinson et al.* (Robinson et al., 2016)	*Garkavij et al.* (Garkavij et al., 2010)	*Gustafsson et al.* (Gustafsson et al., 2015)	*Ilan et al.* (Ilan et al., 2015)	*Beauregard et al.* (Beauregard et al., 2011)	*Sanders et al.* (Sanders et al., 2015)	*Hippeläinen et al.* (Hippeläinen et al., 2016)
Model	Phillips, Precedence SPECT/16MDCT	GE, Hawkeye Millennium VG	GE, Infinia Hawkeye-4	GE, Discovery VH HawkeyeCT	GE, Discovery 670	GE, Infinia Hawkeye	Siemens, Symbia True Point T6	Siemens, Symbia True Point T2	Siemens, Symbia T2
Crystal thickness	9.5mm	15.9mm	---	25.4mm	---	9.5mm	15.8mm	9.5mm	---
Planar-SPECT/CT acquisitions	SPECT/CT	Planar-SPECT/CT	SPECT/CT	Planar-SPECT/CT	SPECT/CT	SPECT/CT	SPECT/CT	SPECT/CT	SPECT/CT
Main photo-peak energy window set.	208keV, 113keV @ 20%	208keV, 113keV @ 20%	208keV, 113keV @ 20%	208keV @ 20%	208keV @ 15%	208keV @ 20%	208keV @ 20%	208keV, 113keV @ 20%	208keV @ 20%
Total projections	128	60	60	60	60	120	96	120	64
Time (s) per proj.	30	60	40	45	45	30	10-15(Pat) 10-40 (Cal)	15 (Pat) 30 (Cal)	20
Collimator	LEHR, LEGP, MEGP	MEGP	MEGP	MEGP	MEGP	MEGP	MELP	MELP	MELP
Matrix size	128x128	---	128x128	128x128	128x128	---	128x128	128x128 256x256	128x128
Pixel size	3.195mm	---	---	4.02cm	4.4mm	---	4.8mm	4.8mm 2.4mm	4.8mm
Zoom	---	---	---	---	---	---	1	1	---
Orbit	Circular, 25cm	---	Circular, 25cm	Auto	Auto	---	Auto	Auto	Auto
Step & shoot	Yes	---	---	---	---	---	Yes	Yes	Yes
Reconst. algorithm	OSEM(Astonish)	OSEM(Xeleris)	OSEM(Xeleris)	LundADose software	OSEM	OSEM(Xeleris)	OSEM (Siemens-Flash 3D)	OSEM (Siemens-Flash 3D)	OSEM (Hermes)
Updates	24/48/64/128	32	40	80	80	32	32	4/8/12/16/20 /24/28	240
Iterations, subsets	3,8/3,16/4,16/8,16	4,8	4,10	8,10	8,10	4,8	4,8	x,8/x,8/x,8/x, 8/x,8/x,8/x,8	15,16
Scatter correction	ESSE, TEW, DEW, Downscatter, DPW	---	TEW	ESSE	ESSE	---	DEW	TEW	MC Simulation
Collim. correction	Yes	---	---	Yes	Yes	---	Yes	Yes	Yes
Pre-filtering	No	---	Yes	---	---	---	No	Yes	---
Post-filtering	No	Yes	Yes	---	---	Yes	No	No	No
Recovery coeff.	Yes	---	Yes	---	Yes	Yes	No	Yes	Yes
Partial volume correction	No	---	Yes	---	Yes	Yes	No	Yes	No
Dead time correction	No	---	No	---	No	---	Yes	---	---

Table 3.2. CT protocols, dosimetric units and reference parameters for SPECT/CT calibration.

	de Nijs et al. (de Nijs et al., 2014)	*Sandström et al.* (Sandström et al., 2010)	*Robinson et al.* (Robinson et al., 2016)	*Garkavij et al.* (Garkavij et al., 2010)	*Gustafsson et al.* (Gustafsson et al., 2015)	*Ilan et al.* (Ilan et al., 2015)	*Beauregard et al.* (Beauregard et al., 2011)	*Sanders et al.* (Sanders et al., 2015)	*Hippeläinen et al.*(Hippeläinen et al., 2016)
CT Protocol	Low dose	Hawkeye	Manufacturer	Hawkeye	Low dose	Hawkeye	CARE Dose4D	CARE Dose4D	CARE Dose4D
CT parameters	140kVp, ---	140kV, 3.0mA	---	140kV, 2.5mAs	120kV, ---	140kV, 3.0mA	130kV, 70mAs	130kVp, 30mAs	130kV, 100mAs
Resampling CT	---	---	---	Yes	---	---	Yes	---	---
Registration	---	---	---	Yes	---	---	Yes	---	Yes
Segmentation	*Tossici-Bolt et al.* (Tossici-Bolt et al., 2006)	Manually based-on a combination emission and attenuation maps	Manually based-on CT	Based on SPECT/CT with guidance from CT	Manually based-on CT	Based-on SPECT/CT, automatic threshold using a 42% isocontour	Based on emission map, using threshold varying 1-40%	Manually based-on CT	Based on CT drawing physical boundaries
Absorbed dose results	No	Yes, Gy	No	Yes	Yes, Gy /BED	Yes, Gy	No	No	Yes, Gy
Residence times estimation	No	Yes	No	Yes	TAC and absorbed dose rate function	*Sandström et al.* (Sandström et al., 2010)	No	No	TAC
Phantom geometry	NEMA2007/IEC2008	Cylindrical	Cylindrical	Petri dishes and elliptical phantoms	Petri dishes		Cylindrical	Cylindrical	Cylindrical, Jaszczak
Insert (#)	Yes (6)	Yes (1)	Yes (3)	---	---		Yes (3)	Yes (6)	Yes (1)
Shape inserts	Spherical	Spherical	Cylindrical	---	---		Cylindrical	Spherical	Bottle
Sensitivity (Units)	cps/kBq	counts/MBq	cps/MBq	cycles per second/MBq	Count rate per unit activity in air, *Ljungberg* (Ljungberg et al., 2003)		$(Bq*s)^{-1}$	cpm/kBq	kBq/ml
Sensitivity results	Results are different depending on each photo-peak and applied scatter correction method	Planar= 7.396 $SPECT_{Large}$= 28.620 $SPECT_{Small}$= 36.814	---	Planar= 1.32 SPECT= 8.0	---		$1.078x10^{-5}$	PP_{113} = 1.25 PP_{208} = 1.13	---

- In the case of the Hermes workstation, reconstruction can be performed. This workstation also contains HDM version 1.0, which has been used with ^{177}Lu-DOTATATE patient data (Hippeläinen et al., 2016). Patient data can be used under different scenarios, for example, either a minimum of 3 serial Anterior-Posterior WBs; or 3 serial Anterior-Posterior WBs and one SPECT (or SPECT/CT study) or 3 serial SPECT (or SPECT/CT studies). A calibration method is proposed based on a uniformly filled cylindrical phantom. HDM requires a calibration factor in MBq/counts obtained from SPECT/CT acquisitions. Fitting can be done using mono-exponential or bi-exponential approaches. By knowing the injected activity and injection time, the residence times can be estimated in HDM and its results can be exported to OLINDA/EXM V2.0 (Stabin & Farmer, 2012).
- STRATOS is a software which part of Phillips IMALYTICS research workstation (3.2, Rev 6289(64)), reconstructions cannot be performed and no calibration method is suggested. This software can be used only with 3D SPECT/CT data. A relationship between the number of counts and intensity can be established by setting the number of counts equal to the level of intensity in the NM image. The calibration factor is therefore expressed in Bq/Intensity. Fitting can be done voxel by voxel using the trapezoidal method, and also considering a mono-exponential decay from last measure time point. Absorbed doses are calculated by convolution at the voxel level. DVHs can be generated. STRATOS has been used by some authors, for instance for comparison with an internally-developed software (Grassi et al., 2015), to OLINDA/EXM and GATE Monte Carlo code (Marcatili et al., 2015).
- PDOSE (version 3.1.1RC-2018-03-16), from DOSISOFT works only with SPECT/CT acquisitions and no calibration method is suggested by this company, also operates on Linux (7.3.1611, CentOS7-64bits)~~.~~ The calibration factor can be expressed in units of Bq/counts, but other options are available. PDOSE allows the usage of different calibration factors, thus, the user can vary acquisition time. Fitting can be done by different approaches, for instance, using the trapezoidal method, mono-exponential, bi- or tri-exponentials. PDOSE can calculate the mean absorbed doses by considering both organ-based and voxel-based approaches. PDOSE can estimate the mean absorbed dose by convolution (Dieudonne et al., 2011, 2013; Dieudonne et al., 2010) and assuming local energy deposition (Pasciak et al., 2014). This software have been used for other applications, for instance in PET/CT for radiotherapy purposes (Desbordes et al., 2017; Desbordes et al., 2014; Vera et al., 2013) and in the treatment of liver cancers with ^{90}Y microspheres (Gardin et al., 2017).

In summary, DTK and HDM are able to perform image reconstruction. However, they propose only model-based dosimetry at the organ level. STRATOS performs dosimetry at the voxel level. PDOSE can do both. DTK, being part of Xeleris®, is a medical device that can be used in a clinical context. HDM and PDOSE are both aiming for that (PDOSE got the CE marking during this work). STRATOS is and will remain a research tool.

In this chapter the calibration of a SPECT/CT system using different source geometries is presented. The calibration factor was determined for several reconstructions to show the influence of the reconstruction method on the determination of this parameter. Recovery coefficient results were obtained from phantom studies. A phantom study was performed to test the calibration factor chosen in several workstations.

In this chapter two main objective are addressed:

1. To calibrate a SPECT/CT.
    a. To generate the CT calibration curve.
    b. To determine the sensitivity of the system.
        i. Planar sensitivity.
        ii. SPECT sensitivity.
    c. To determine the calibration factor.
    d. To generate the recovery coefficient curve.
2. To test the performance of three commercial workstations using phantom data sets by:
    a. Estimating the activity for a phantom configuration.
    b. Assessing the dosimetric workflow to calculate residence times.

2. Materials and Methods

Phantom experiments were carried out at the Institut régional du cancer de Montpellier (ICM) in the Nuclear Medicine Department, using a SPECT/CT unit GE-Discovery NM/CT 670, 9.5 mm crystal thickness. All activity measurements were done in an accurate activimeter calibrated for ^{177}Lu measurements. Projections were acquired, reconstructed and analyzed independently at the ICM and the Centre de Recherches en Cancérologie de Toulouse (CRCT). All activity measurements were done in an accurate activimeter calibrated for ^{177}Lu measurements.

At ICM images were reconstructed using Dosimetry Toolkit®. At CRCT reconstruction was performed using HybridRecon-Oncology version_1.3_Dicom (HROD) from Hermes without using the SPECT Standard Uptake Value (SUV) (Kangasmaa et al., 2016) option.

2.1. CT calibration curve

To correct for the attenuation effect, a CT calibration curve was generated using the Catphan 500 phantom. This phantom can be also used in the quality assurance program. In figure 3.1 a representation of a slice of the phantom can be observed, showing materials such as teflon, LDPE, acrylic, etc. In table 3.3, information regarding data from the Catphan500 inserts can be seen. The phantom was placed in the SPECT/CT and CT acquisition protocol was as follows: 140 kV, mA was set in auto, matrix size 512x512, noise index 6.4, slice thickness 5 mm, pitch 1.375 and standard reconstruction filter.

Table 3.3. Information regarding data from the Catphan 500.

Material	Density (g/cm^3)	Other information	µ (cm^{-1}) at 80 keV from ICM	µ (cm^{-1}) at 80 keV from NIST	Hounsfield units (HU)
Air			0		-972.21
H_2O	1		0.184	0.184	0
Polystyrene	0.96 – 1.04		0.180	0.183	-35.37
LDPE	0.910 – 0.940	Low density polyethylene (LDPE)	0.167	0.170	-78.12
Acrylic	1.18	Poly(methyl methacrylate (PMMA)	0.207	0.208	133.06
Teflon	2.2	Polytetrafluoroethylene (PTFE)	0.342	0.367	910.1

The effective energy associated at 140 kV is 80 keV. The same information to generate the calibration curve was used for reconstruction purposes in HROD and Xeleris®. The ICM provided information for the linear attenuation coefficient and its associate Hounsfield Units (HU). This information is needed in HROD to perform the attenuation correction in the reconstruction process. This information is required at 140 keV, and HROD automatically converts to the energy of the isotope (in this case ^{177}Lu). Hermes provides a software called, "CT-based attenuation map calibration-Hybrid Recon™", to estimate the equations associated to these parameters (Hermes Medical Solutions, 2014).

Linear attenuation coefficients at 80 keV were compared to those from National Institute of Standards and Technology (https://www.nist.gov/) (NIST). Linear attenuation coefficients at 100 keV and 150 keV were extracted from this database in order to estimate the respective values at 140 keV, using a first-degree polynomial approximation, because the attenuation coefficient is not provided at this energy.

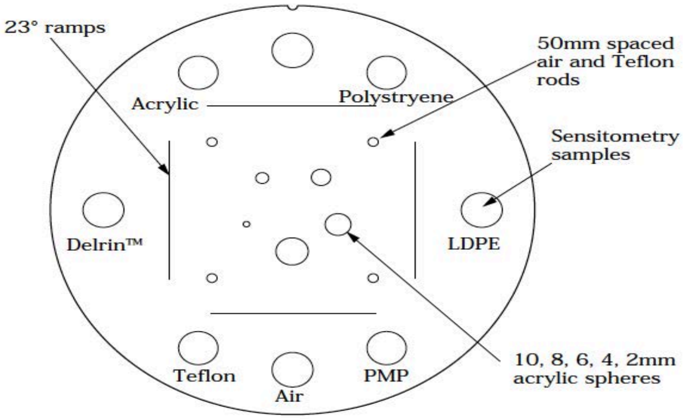

Figure 3.1: CTP404 module with slice width, sensitometry and pixel size.

2.2. Data acquisition for sensitivity determination

2.2.1. Planar sensitivity tests

At the ICM the sensitivity factor (cps/MBq) was determined from planar images, this was requirement by DTK. The estimation of the planar sensitivity occurred using a spherical source at different source-to-collimator distances. The acquisition protocol was as follows: matrix size 128x128, zoom=1, two energy windows were used, the principal centered at 208 keV with 20% of energy window width, a secondary energy window, centered at 177 keV with 10% of energy window width, acquisition time 5 min, medium energy general-purpose (MEGP) collimator. Figure 3.2 shows the energy windows set-up generated by the gamma camera. The activity in the source was 75.88 MBq. Images were generated at different source-to-collimator distances (d=8 cm, 13 cm, 18 cm) using a fillable sphere (external diameter 33.27 mm) placed in air.

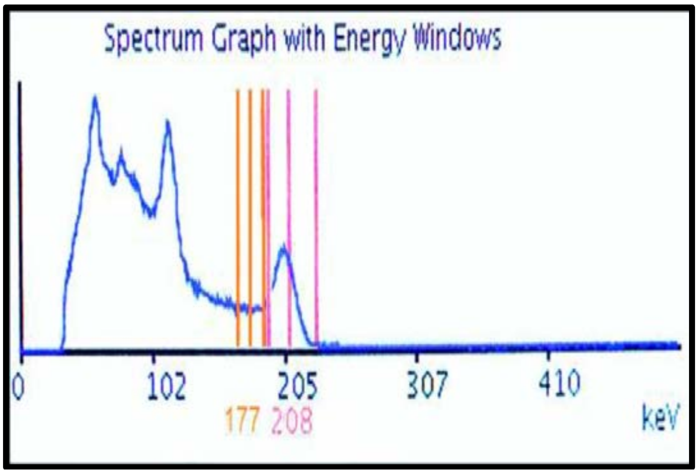

Figure 3.2: Energy spectrum of ^{177}Lu acquired on SPECT/CT unit GE-Discovery NM/CT 670. The main energy window was set at 208 keV @ 20%, the secondary energy window was set at 177 keV @ 10%. Images provided by ICM nuclear medicine department.

For each distance, planar sensitivities were estimated from geometric mean images using ImageJ (Schneider et al. 2012): a) using one ROI covering the whole image, b) drawing a circular ROI 4 and 10 pixels in diameter, which were centered on the maximal pixel counts. Moreover, using results from ImageJ planar sensitivity variation with distance for the two collimators and the geometric mean (without scatter correction) were plotted for the same distances.

2.2.2. SPECT sensitivity tests

To estimate the SPECT sensitivity different options were addressed in terms of phantom configuration, acquisition time and reconstruction. Table 3.4 shows different characteristics for each phantom configuration along with acquisition and reconstruction parameters. Phantom configurations 3 and 4 were used to partially replicate the procedure implemented in the MetroMRT European project (Wevrett et al., 2017). Figure 3.3 shows phantom set-up for each configuration. Phantom configurations showed in table 3.4 are going to be used in the following sections. At ICM the only configuration analyzed was configuration 1.

Table 3.4. Phantom models and configurations, source geometry, used activities.

Phantom config.	Phantom model	Source geo.	Source Activity (MBq)	Attenuation medium	Time(s)/ projection	Post-filter (cm)	Number of iterations and subsets	Dosimetric analysis
1	NEMA 2012/IEC 2008 PET Elliptical	Bottle (500 ml)	A_o= 272.80	Cold water, no background activity	120	0.0 0.1 1.0	OSEM, 6i, 10ss	N/A
2			A_1= 535.44		60			HDM PDOSE STRATOS
3	Jaszczak SPECT cylindrical	Hollow sphere (16 ml)	A_2= 78.07	Air	45		OSEM, 4i, 5ss 4i, 10ss 6i, 10ss 8i, 10ss 16i, 10ss 32i, 10ss	N/A
4				Cold water, no background activity				

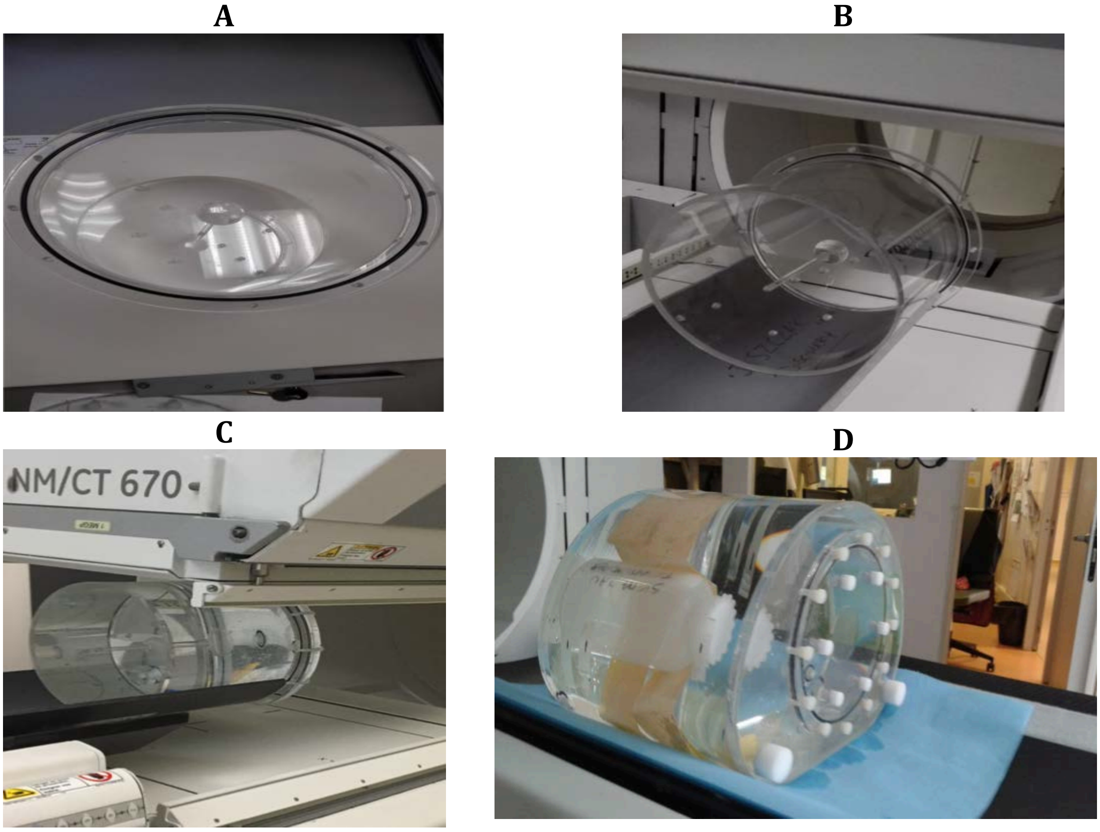

Figure 3.3: A. Spherical source placed at the centre of an empty cylindrical phantom. B. Placement of spherical source at the centre of an empty cylindrical phantom in the SPECT/CT. C. Placement of spherical source in the centre of a cylindrical phantom filled with water in the SPECT/CT. D. Placement in the SPECT/CT of the NEMA 2012/IEC 2008 phantom filled with water (no background activity) and containing a fillable bottle (500ml). Images provided by ICM nuclear medicine department.

SPECT acquisitions were as follows: one FOV covering the whole phantom, 60 projections in total, zoom 1, matrix size 128x128, using two energy windows one centered at 208 keV at 20% and one at 177 keV at 10%, parallel-hole medium energy general purpose (MEGP) collimator, step & shoot, and body auto-contour. CT acquisition protocol was as follows: 120 kV, mA was set in auto, matrix size 512x512, noise index 6.4, slice thickness 5 mm, pitch 1.375 and standard reconstruction filter.

2.3. SPECT data reconstruction

Reconstructions at CRCT were as follows: for phantom configurations 1 and 2, OSEM (Hudson & Larkin, 1994) (6i, 10ss) was used; for phantom configurations 3 and 4, several OSEM combinations were used, varying between number of iterations (4, 6, 8, 16, 32) and subsets (5, 10). Gaussian post-filter was set at 0.0, 0.11 and 1.00 cm.

For all phantom configurations, different correction methods available were applied, such as attenuation, collimator-detector response and Monte Carlo Scatter Modelling (MCSM) (Sohlberg et al., 2008). In order to apply the MCSM, a modification of the DICOM header from the original images took place using the Dicom Editor Tool 3.2.6 (DVTk Library 3.1.9, www.dvtk.org) because the MCSM works with the main energy windows.

As described by other authors (Hippeläinen et al., 2016; Sohlberg et al., 2008), the CT attenuation map, when using HROD, was generated using a bilinear conversion from HU to linear attenuation coefficient values and the collimator correction was based on the Gaussian convolution. Then, the projection data was loaded with the attenuation map into the HROD Reconstruction Module. The attenuation map was resampled to correct size/energy, this resampling was performed automatically by the workstation (Hermes Medical Solutions, 2015).

At the ICM the configuration 1 was reconstructed as follows: OSEM (6i, 10ss), using all corrections methods available (scatter, attenuation and collimator-detector response correction) and using Gaussian post-filter set at 0.11 cm.

2.4. Segmentation and image analysis for SPECT sensitivity

Using the Hybrid Viewer Multi (HVM) version 2.7 from Hermes, for configurations 3 and 4, a VOI was generated on the CT image creating a spherical volume. The diameter of the generated sphere was 3.13 cm in order to have a volume of 16 ml. In order to place the center of the generated VOI, the biggest diameter of the spherical volume in the CT image was chosen, and correct positioning was assessed visually. The volume created on the CT image was copied to the NM reconstructed images. On average, the generated volume on the NM reconstructed images for the empty phantom was 15.88 ml and for the water-filled phantom was 16.51 ml.

Manual segmentation of the bottle was not easy to perform using HVM, because of the bottle wall thickness. Therefore, for configuration 1, an automatic segmentation was used by absolute thresholding in the NM signal. Hence, by using different percentages (23% and 24%) relative to the maximum number of counts within the VOI, the automatic segmentation tool was tested.

For phantom configuration 4, with all correction methods were tested, with gaussian post-filter set at 0.0, 0.11 and 1.0 cm. Line-profiles crossing the sphere source were generated using ImageJ (Schneider et al., 2012), for the same slice of the phantom, for each NM reconstructed image. For every image, the same position in the "y-axis" was used in order to draw the profiles. Gray values in these profiles are related to the number of counts present in each voxel of the line.

2.5. Calibration factor determination

The calibration factor was found as the inverse of the system volumetric sensitivity. As described by Sanders et al. (Sanders et al., 2015), the system's volumetric sensitivity, expressed in (cps/ml)/(MBq/ml), is estimated as follows:

$$S = \frac{c_{mes}}{\tau_{acq} \times C_o \times exp\left(\frac{-ln(2) \times \Delta t}{\mathrm{T}_{1/2}}\right)} \qquad 3.1$$

Where c_{mes} is the number of counts in the generated VOI, τ_{acq} is the acquisition duration (i.e., time per projection multiplied by the total number of projections), C_o is the prepared activity concentration, Δt is the time between the source activity preparation and the SPECT/CT acquisition, and $\mathrm{T}_{1/2}$is the physical half-life of the radionuclide. This expression of the calibration factor was also used by Marin et al. (Marin et al., 2017).

For all configurations, average of respective volumetric sensitivities were estimated, as it is recommended by Wevrett et al. (Wevrett et al., 2017): with Gaussian post-filtering set at 0.0, 0.11 and 1.0 cm, this was done for: all corrections methods used in the reconstruction algorithm; using only attenuation + collimator response correction and using only attenuation.

These figures were used directly into three different workstations, Hermes, PDOSE and STRATOS. For the three workstations the same calibration factor can be used with the appropriate units (activity/counts). Also, in the case of STRATOS the intensity of the displayed image can be associated with the number of counts in the NM image. For each configuration, the calibration factor was found by multiplying the estimated volumetric sensitivity by the acquisition time.

Finally, these results were helpful for the evaluation of the residence times when a phantom with a cylindrical source was used as it is explained in the next section.

2.6. Recovery coefficients determination

In order to determinate the recovery coefficient, two experiments were carried out using two cylindrical phantoms (Jaszczak, 6.4 L) one filled with background activity and another without background activity, using two sets of 6 fillable spherical sources (16, 8, 4, 2, 1, 0.5 ml). The volumetric activity used with each source was 0.54 MBq/ml. The volumetric activity used such as background was 0.07 MBq/ml.

Acquisition protocol was as follows: one FOV covering the whole phantom, 60 projections in total, 120 seconds per projection, zoom 1, matrix size 128x128, using two energy windows one centred at 208 keV at 20% and one at 177 keV at 10%, MEGP collimator, step & shoot and body auto-contour. The CT acquisition protocol was 120 kV, mA was set in auto, matrix size 512x512, noise index 6.4, slice thickness 5 mm, pitch 1.375 and standard reconstruction filter.

VOI's were created in the CT image for each sphere and then copied in the NM images. In the case of the phantom with background activity, spheres of same volumes in the background region were create and these figures were subtracted from the values obtained from the counts in each sphere. All image analysis occurred with HVM.

2.7. Assessment on three commercial workstations

The dosimetric workflow implemented in each work station not only considered the determination of activity at a given time point from a calibration factor, but also how different time points were integrated to provide for cumulated activity/residence time before absorbed dose calculation. Therefore, we decided to test the whole chain of processing on phantom experiments. We performed SPECT/CT acquisitions of phantom configuration 2, imaged at approximately 2.5, 25, 48, 146 and 165 h. The phantom placement was not exactly the same between the different time point measurements, in order to assess the (rigid) registration tools provided by each workstation. This configuration was used, because the source can mimic one kidney.

As only physical decay of the radionuclide occurred during the experiments, the residence time for ^{177}Lu should be equal to 230.15h (230.15h =$\left[\frac{1}{ln2} * \mathrm{T}_{1/2phys}\right]$).

2.7.1. Activity determination

In collaboration with Montpellier we decided to perform an initial evaluation using the calibration factor resulting from the OSEM reconstruction, with 6 iterations, 10 subsets, using all corrections methods and Gaussian post-filter at 0.11 cm. Then, uploading reconstructed images from the previous phantom in Hermes, PDOSE and STRATOS, an estimation of the activity at each time point and associated relative difference was found.

The dosimetry workflow using HDM was as follows: automatic registration by conducting a rigid registration (translation) taking as reference the first SPECT/CT was performed; the software synchronized two SPECT/CT series at the time. The VOIs were created using the automatic segmentation tool, as mentioned before. A mono-exponential fit was applied, and integration from t=0 to infinity was done to find the residence time.

In the case of PDOSE the workflow was as follows: segmentation was carried out manually on the reference CT slices. This software also synchronized two SPECT/CT series at the time. Rigid registration was performed taking as reference the first SPECT/CT. PDOSE has many fitting options available but we decided to use mono-exponential fitting. Integration from t=0 to infinity was done to find the residence time, by knowing the initial activity, also PRD was found.

In the case of STRATOS, automatic rigid registration was performed by rigid registration, between each NM study and the first CT study (which was taken as a reference). Segmentation was carried out manually on the reference CT slices. Here fitting was carried out by segments applying the trapezoidal method, and from the last data point, extrapolation to infinity, assuming mono-exponential decay (called tail integration) and considering physical half-life only. To estimate the residence time, the software performed integration of each segment automatically and also PRD was found.

2.7.2. Residence times evaluation and phantom validation

The VOI of the bottle was generated using automatic segmentation, based on absolute thresholding, in HDM. Hence, two different percentages (23% and 24%) relative to the maximum number of counts within the VOI, were generated. The segmented VOI's were copied to the other SPECT/CT data points. Fitting was applied by using a mono-exponential function. Finally residence times were calculated for each calibration factor, from phantom configurations 1 to 4. The approach described in the previous section was implemented in STRATOS and PDOSE. The relative difference is calculated between the theoretical and estimated residence times for all software.

3. Results

3.1. CT calibration curve

In table 3.5 results for linear attenuation coefficient and HU are presented. The values from GE and NIST at 80 keV are similar for the majority of the materials. Only 5 materials were chosen for this analysis. In the case of Polystyrene results were not similar, therefore we did not use this material to generate our calibration curve.

In figure 3.4, calibration curve results using the software provided by Hermes can be seen, showing the bilinear fitting. In figure 3.4.A, coefficients for the slope and intercept of the two equations are shown. In figure 3.4.B, an image of how these coefficients were introduced in HROD to perform the reconstruction is presented.

Table 3.5. Linear attenuation coefficient and HU results for the CT calibration curve.

Material	Linear attenuation coefficient μ (cm^{-1})				
	GE 80 keV	NIST 80 keV	NIST 100 keV	NIST 140 keV	NIST 150 keV
H_2O	0.1837	0.1837	0.1707	0.1545	0.1505
POLYSTYRENE (PS)	0.18	0.1829	0.1721	0.1572	0.1535
L-POLYETHYLENE (LDPE)	0.167	0.1695	0.1599	0.1461	0.1427
Polymethylmethacrylate (PMMA)	0.207	0.2084	0.1953	0.1777	0.1733
Polytetrafluoroethylene (PTFE), ρ=2,25	0.342	0.3672	0.3375	0.3033	0.2948

Material	Hounsfield units (# CT)				
	GE 80 keV	NIST 80 keV	NIST 100 keV	NIST 140 keV	NIST 150 keV
H_2O	0.000	0.000	0.000	0.000	0.000
POLYSTYRENE (PS)	-35.75	-4.63	8.46	17.34	19.85
L-POLYETHYLENE (LDPE)	-78.12	-77.09	-63.46	-54.59	-52.08
Polymethylmethacrylate (PMMA)	133.06	134.29	143.99	149.65	151.26
Polytetrafluoroethylene (PTFE), ρ=2,25	910.1	998.91	977.15	962.60	958.47

CT calibration curve used in HU-fit software (from HERMES)

Material	Hounsfield units (# CT)	Linear attenuation coefficient μ (cm^{-1})
Air	-972.21	0.000
L-POLYETHYLENE (LDPE)	-54.60	0.146
H_2O	0.00	0.155
Polymethylmethacrylate (PMMA)	149.65	0.178
Polytetrafluoroethylene (PTFE), ρ=2,25	962.60	0.303

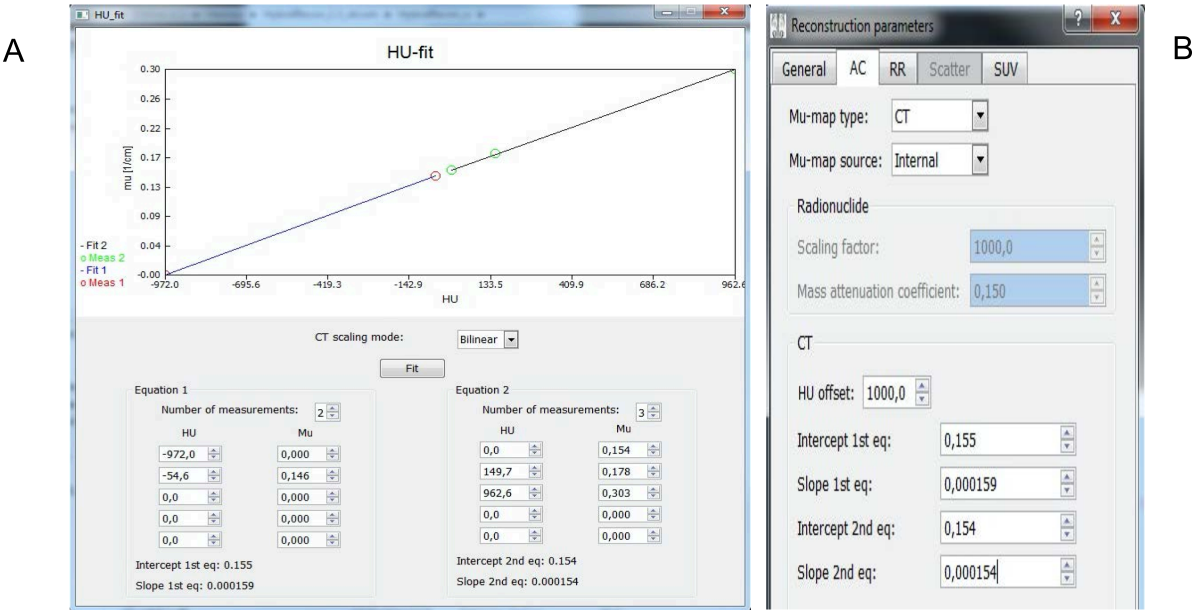

CT scaling mode: Bilinear

Equation 1

Number of measurements: 2

HU	Mu
-972,0	0,000
-54,6	0,146
0,0	0,000
0,0	0,000
0,0	0,000

Intercept 1st eq: 0.155

Slope 1st eq: 0.000159

Equation 2

Number of measurements: 3

HU	Mu
0,0	0,154
149,7	0,178
962,6	0,303
0,0	0,000
0,0	0,000

Intercept 2nd eq: 0.154

Slope 2nd eq: 0.000154

Mu-map type: CT

Mu-map source: Internal

Scaling factor: 1000,0

Mass attenuation coefficient: 0,150

HU offset: 1000,0

Intercept 1st eq: 0,155

Slope 1st eq: 0,000159

Intercept 2nd eq: 0,154

Slope 2nd eq: 0,000154

Figure 3.4: Results from bilinear fitting using software provided by HERMES. A: coefficients generated for the two linear equations. B: Attenuation correction menu from HROD.

3.2. Sensitivity determination results

3.2.1. Planar sensitivity test results

In terms of planar sensitivity, figure 3.5 shows sensitivity results for detector and the geometric mean (GM) of both results when the measured ROI size increases (from 4 to 10 pixels). This figure shows that for the same distance, sensitivity increases with ROI size. Moreover, as the source–to–collimator distance increases, the sensitivity decreases for the same measured ROI. The relative difference (taking 18 cm data as reference) in GM sensitivity varies from 14.50% to 4.80%, between 4- and 10-pixels ROI measured size, for 8 cm and 18 cm.

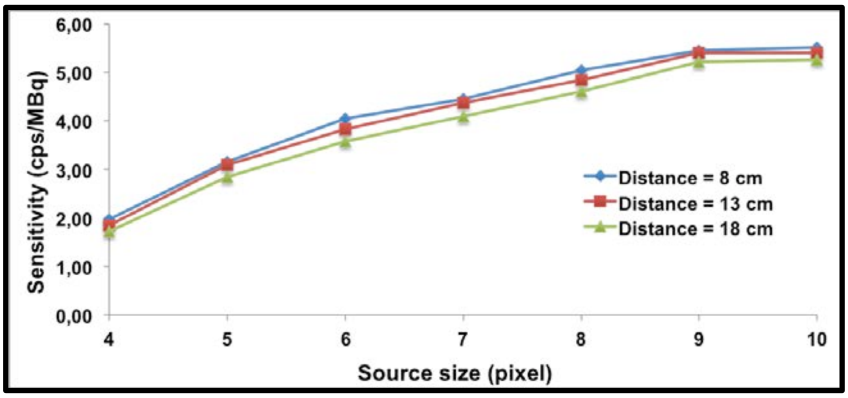

Figure 3.5: Planar sensitivity variation in air, for a matrix size of 128x128, for different source–to–collimator distance for GE-Discovery NM/CT 670, for each gamma camera detector and for the geometric mean (GM) for different ROI sizes. D: GM sensitivity results for different source–to–collimator distance.

3.2.2. SPECT sensitivity test results

3.2.2.1. Spherical source geometry

Table 3.6 shows results for sensitivity factors from phantom configurations 3 and 4 and its average for different reconstructions. Sensitivity results for 0.0 and 0.11 cm are similar, variation occurs after the second significant number. *Then from now and towards, without post-filter results are the same for 0.0 and 0.11cm.* For the same post-filter, as the number of iterations increases, the sensitivity increases. For the same number of iterations and subsets, without post-filter, sensitivity values for the source placed inside the empty phantom are higher than the results for the source placed in the phantom containing water.

The absolute difference between sensitivity values for the source placed inside the phantoms (in air and containing water) varies from 0.55 to 0.73 cps/MBq without post-filtering, and in the when post-filter is set to 1cm, these differences decreases varying from 0.04 to 0.28 cps/MBq. For all the cases, the post-filtering effect on sensitivity results is important because the values can be reduced up to 1.98 cps/MBq.

On the other hand, considering all correction methods applied within OSEM and non-post-filter, sensitivity varies from 9.32 to 10.41 cps/MBq (average 9.91

cps/MBq); for Gaussian post-filter = 1.0 cm, sensitivity varies from 7.61 to 7.90 cps/MBq (average 7.76 cps/MBq).

Table 3.6. Sensitivity results for spherical source centered either in an empty phantom or in a phantom filled with water using attenuation, scatter and collimator response corrections within OSEM and Gaussian post-filter.

Id	Gaussian post-filter (cm)	Iterations	Subsets	Sensitivity (cps/MBq)		
				Empty phantom	Phantom filled with Water	Average±σ
1	Without post-filter	4	5	9.32	9.04	9.18±0.20
2	1			7.61	7.63	7.62±0.01
3	Without post-filter	4	10	9.69	9.38	9.54±0.22
4	1			7.72	7.79	7.76±0.05
5	Without post-filter	6	10	9.84	9.51	9.68±0.24
6	1			7.72	7.79	7.76±0.05
7	Without post-filter	8	10	9.95	9.59	9.77±0.25
8	1			7.73	7.81	7.77±.0.06
9	Without post-filter	16	10	10.22	9.83	10.03±0.27
10	1			7.74	7.86	7.80±0.08
11	Without post-filter	32	10	10.41	10.05	10.23±0.26
12	1			7.76	7.90	7.83±0.01

In the appendix of this chapter figures A.1 and A.2 show an artifact that may be associate to the use of the collimator-response-correction, this is known as Gibbs-like artifact.

3.2.2.2. Cylindrical source geometry

Table 3.7 shows results for the sensitivity factors obtained with configurations 1 and 2. Different activities and different acquisition times were used. In both cases, as expected, segmentation produces different volumes depending on the modality. With threshold set at 23 and 24%, volumes close to the real source distribution are generated. However, regardless the threshold, the sensitivity values are very similar, for two different initial activities and acquisition times. For the two activities and two thresholds used, sensitivities vary between 10.10 and 10.21 cps/MBq. Moreover, comparing these results with the ones of 3 and 4 configurations (considering the variation in source geometry), sensitivity results are in the same order of magnitude and comparable to those values generated when non-post-filter was used.

Table 3.7. Sensitivity results for activity placed in a bottle (to mimic a kidney) placed into a phantom filled with water, using a reconstructed image with OSEM (6i, 10ss) +AC+S+CR+non-GPF.

Activity in the bottle	NM volume (ml)	CT volume (ml)	Initial activity (MBq)	Sensitivity (cps/MBq)
Threshold curve 23 %	497.90	505.11	A_1=535.44	10.10
Threshold curve 24 %	493.33	500.88		10.15
Threshold curve 23 %	494.88	504.39	A_0=272.80	10.18
Threshold curve 24 %	491.61	499.55		10.21

3.2.2.3. Recovery coefficient results

Figure 3.6 shows the recovery coefficient results using a phantom with and without background activity, when non-Gaussian post-filter is used. In both cases, images were reconstructed using OSEM, applying all correction methods. As the number of updates increase, the recovery coefficient increase. In the case figure 3.6.A., for spheres volumes 2 and 4 ml, as the number of updates increase, the recovery coefficient increases reaching more than 100% (for 320 updates). For spheres volumes between 8 and 16 ml, the same effect is observed, as the number of updates increase, the recovery coefficient also increases, but for these spheres reaching values less than 100%. Similar tendency occurs in the presence of background activity (figure 3.6.B.), for the 2 ml sphere the variation in the recovery coefficient is between 23% and 68%; for the 4 ml sphere the variation is between 45% and 87%, for 8 ml sphere the variation is between 56% and 77% and for the 16 ml sphere is between 69% and 81%, from 20 to 320 updates, respectively. From both figures, an overestimation in the recovery coefficient occurs for spheres of 2 and 4 ml, as the number of updates increases.

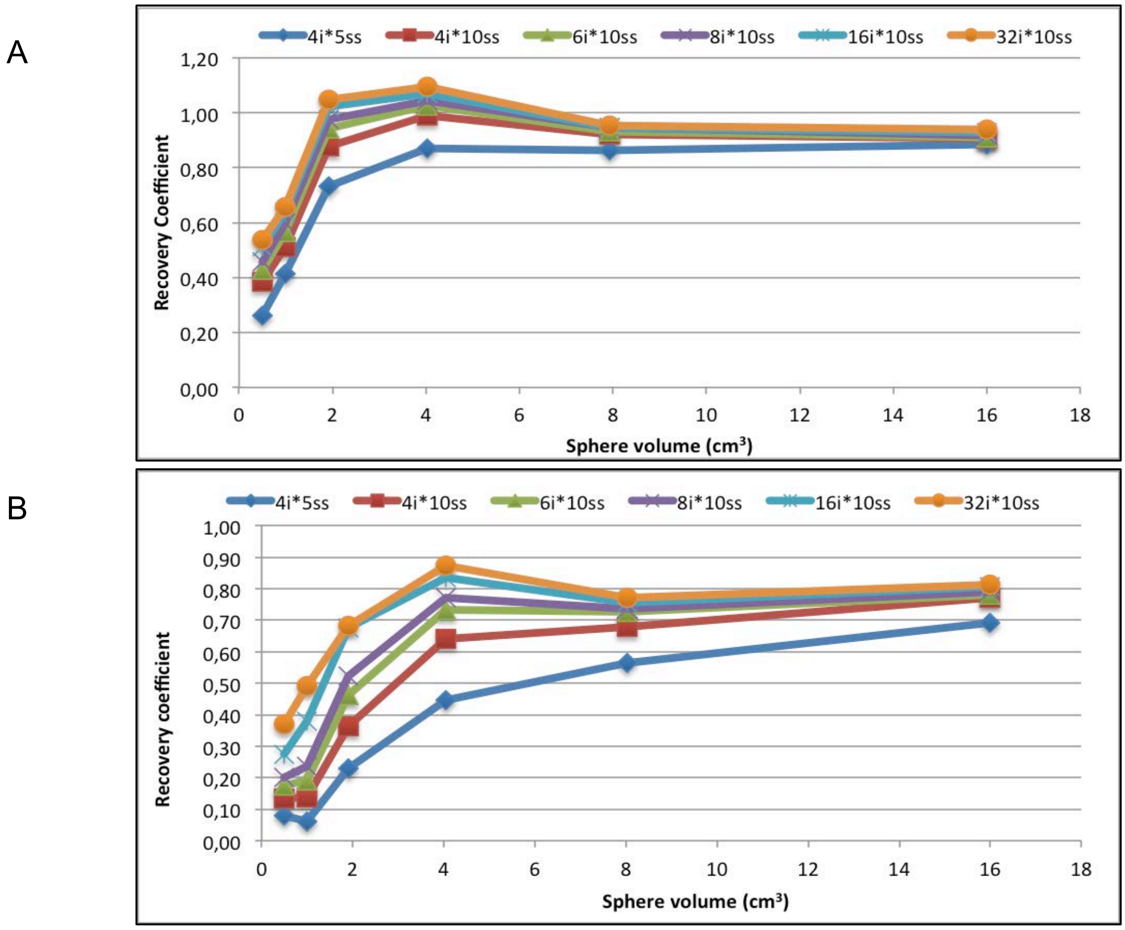

Figure 3.6: Recovery coefficient for OSEM reconstructed images of a phantom using attenuation, collimator response and scatter corrections, without Gaussian post-filter. A: without background activity. B: with background activity.

3.2.3. Phantom evaluation on three commercially available workstations

3.2.3.1. Activity determination

Looking at the results in table 3.8, good results in terms of the activity estimation and residence times can be seen for HDM and PDOSE, less so for STRATOS. In the case of HDM the relative difference (%) in activity varies from -7.02% to -3.80% and for the residence time results the relative difference (%) is 4.44%. For PDOSE the relative difference (%) varies from -2.20% to 3.20% and -3.54% in activity and residence times, respectively. In the case of STRATOS the percentage of relative difference varies from -61.22% to 5.70% and -50.52% in activity and residence times, respectively.

Table 3.8. Activity estimation for each software for reconstruction OSEM (6i,10ss) +A+S+CR+Non-Gaussian post-filter.

ΔT (hours)	Activity (MBq)		Relative difference (%)	Residence time (h)	Relative difference (%)	Software
	Theory	Estimation				
2.50	529.80	550.62	-3,93	241.93	4.44	HDM
24.97	480.53	499.73	-4,00			
49.05	432.78	463.17	-7,02			
146.28	283.66	297.51	-4,88			
168.70	257.33	267.11	-3,80			
2.50	529.80	546.72	3,20	222.00	-3.54	PDOSE
24.97	480.53	480.75	0,05			
49.05	432.78	432.86	0,02			
146.28	283.66	283.18	-0,17			
168.70	257.33	251.72	-2,20			
2.50	529.80	560.00	5.70	114.00	-50.52	STRATOS
24.97	480.53	390.00	-18.84			
49.05	432.78	350.00	-19.13			
146.28	283.66	110.00	-61.22			
168.70	257.33	100.00	-61.14			

Figures 3.7.A and 3.7.B show the positioning and placement variation of the phantom using HDM and PDose for each time point measurement, after the registration process. These images are not possible to extract from STRATOS. In the case of HDM and PDOSE results regarding the mono-exponential fit can be seen. STRATOS does not provide this information. PDOSE provides a tool to verify the goodness of the fit by using the Spearman coefficient, while the other software do not provide such tools for this evaluation.

Figure 3.7. (C, D, E) shows mono-exponential fit results for HDM, PDOSE, and STRATOS. With HDM and PDOSE, the point measurements almost fit a mono-exponential function. However, with STRATOS, the point measurements are fitted by the trapezoidal method.

3.2.3.2. Residence time evaluation and phantom validation

Tables 3.9, 3.10 and 3.11 used the average sensitivity values from tables 3.6 and 3.7 and show results for relative difference (%) between the theoretical residence time and the estimated residence time using HDV, STRATOS, and PDOSE.

In case of table 3.9, for the two thresholds applied, as the sensitivity values increases, the percentage of error decreases. For sensitivity values obtained without post-filter (same Id), the relative differences (%) are lower than 5%, as it can be seen for sensitivity values varying from 9.78 to 10.23 cps/MBq. For these reconstructions a Gibbslike artifact can be observed (see appendix chapter 3). Moreover, for sensitivity values obtained using a Gaussian post-filter at 1.0 cm, the percentage of relative difference varies from 29.90 to 33.74%.

In table 3.10, percentage of relative difference are lower than 1% when the calibration factors are coming from the sensitivity values obtained using the same source configuration. In this case Gibbslike artifacts are less important because the reconstruction was carried out using 60 updates (see appendix chapter 3).

In table 3.11, for STRATOS, the relative difference (%) results vary from -44.48 to -50.52% and -28.79 to -38.45%, for non-post-filter and post-filter at 1.0 cm, respectively. For PDOSE these figures vary from -8.58 to 1.83% and 19.31 to 22.67%, for non-post-filter and post-filter at 1.0 cm, respectively.

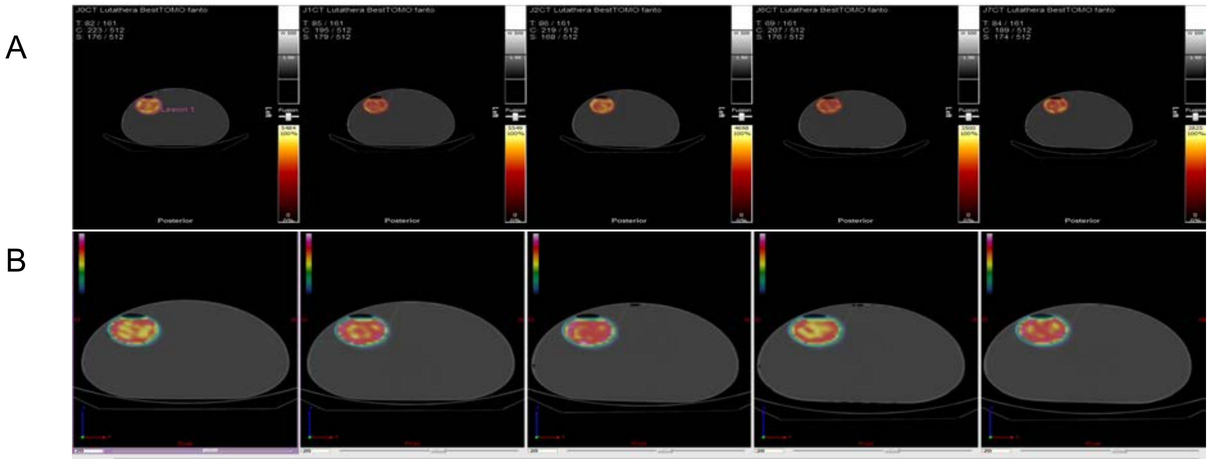

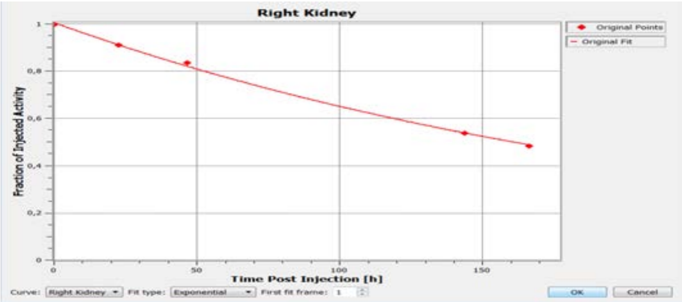

C: Fraction of injected activity and Mono-exponential fitting by HDM

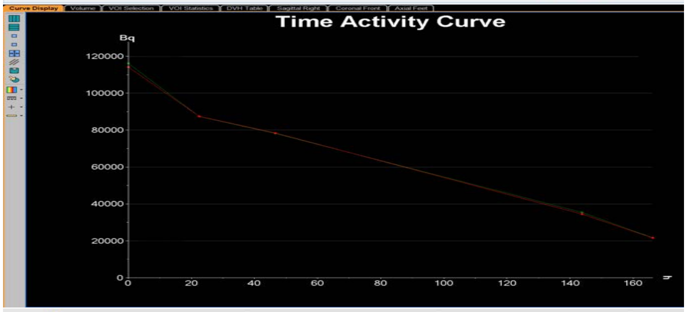

D: Time activity curve for the generated volumes and trapezoidal fitting by STRATOS

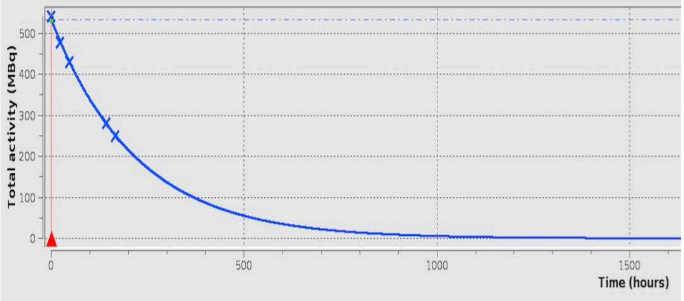

E: Time activity curve for the generated volume and Mono-exponential fitting by PDose

Figure 3.7: A: Axial view of phantom placement after registration process using HDM and B: PDOSE.

Table 3.9. Percentage of relative difference (PRD) results for residence time estimations entering into HDM sensitivities values from table 3.6.

Id	Average Sensitivity (cps/MBq)	PRD in residence times Segmentation threshold applied	
		23%	24%
1	9.18	11.02	10.77
2	7.62	33.74	33.45
3	9.54	6.91	6.67
4	7.76	31.45	31.16
5	9.68	5.12	5.35
6	7.76	31.37	31.09
7	9.77	4.07	4.29
8	7.77	30.87	31.16
9	10.03	1.51	1.73
10	7.80	30.35	30.63
11	10.23	-0.56	-0.35
12	7.83	29.90	30.19

Table 3.10. Percentage of relative difference (PRD) results for residence time estimations entering into HDM sensitivities values from table 3.7.

Sensitivity (cps/MBq)	PRD in residence times Segmentation threshold applied	
	23%	24%
10.10	0.95	0.73
10.15	0.38	0.16
10.21	0.11	-0.11
10.18	-0.19	-0.41

Table 3.11. Percentage of relative difference (PRD) results for residence time estimations entering into STRATOS and PDose sensitivities values from table 3.6.

Id	Average Sensitivity (cps/MBq)	PRD in residence times for STRATOS	PRD in residence times for PDose
1	9.18	-48.10	1.83
2	7.62	-34.83	22.67
3	9.54	-50.52	-2.20
4	7.76	-33.62	20.32
5	9.68	-48.10	-3.54
6	7.76	-31.20	20.32
7	9.77	-46.86	-4.55
8	7.77	-38.45	20.32
9	10.03	-44.48	-6.90
10	7.80	-28.79	19.65
11	10.23	-49.31	-8.58
12	7.83	-38.45	19.31

From the previous results, the calibration factor providing the best residence times are for reconstructions using OSEM (6 or 8 iterations, 10 subsets), with all corrections and gaussian post-filter set at 0.0 cm, for all workstations except for STRATOS. Higher number of updates provided good results as well, but Gibbs-like artifacts are presented.

4. Discussion

In table 3.1, an overview of different SPECT acquisitions protocols was presented. Most publications used gamma cameras with the same crystal thickness and the same collimator type. Therefore, one should expect similar results because intrinsic and extrinsic sensitivities should be close. Our SPECT/CT was from GE, therefore, our acquisition protocol was very similar those using this SPECT/CT system. Energy windows selected in our studies were similar to the majority of the references and chosen according to the recommendations from Ljungberg (Ljungberg et al., 2016).

Four out of five of GE SPECT/CT systems used 60 projections in total, with more than 40 seconds per projection. On the other hand, for the three references using Siemens SPECT/CT systems the number of projections was variable, and times per projection were equal to or lower than 40 seconds. Also, two out of three reference used different acquisition times for calibration and patient acquisition. The Phillips SPECT/CT system was used with 128 projections and 30 seconds per projection.

For acquisition, the preferred matrix size was 128x128 matrix size. The preferred acquisition mode was step&shoot rather than continuous. Auto-contouring was preferred because most reconstruction algorithms contains the collimator response correction. From these references an acquisition protocol can be drafted.

In terms of reconstruction, two out of nine references used reconstruction software different from that of the manufacturer. The reconstruction algorithm chosen was OSEM. In terms of number of iterations and subsets, references using Phillips and Siemens systems there were not seem to be a clear relation, but for GE systems 4 or 8 iterations, with 8 or 10 subsets where chosen.

In terms of SPECT corrections, all references cited used attenuation correction. For scatter, one reference used different methods, one used DEW, one used a Monte Carlo Simulation approach, two used TEW, two used ESSE and two did not mentioned their selected approach. For collimator response, three out of nine references did not mention if they used any. For dead time, one out of nine took this correction into account. According to MIRD recommendation (Ljungberg et al., 2016), for scans acquired shortly after injection time, dead time may have little effect on the overall absorbed dose calculation. For partial volume effect correction, three publications clearly mentioned that they did not use any, and in two there was no mention of its use. Six out of nine reference used recovery coefficients to correct this effect.

Our reconstruction method was based-on HROD considering all corrections available in this workstation. We did not perform any dead time correction because for the calibration process we did not used high activity.

The SUV option in the HROD module from Hermes allows the comparison of SPECT sensitivity results with other workstations. However, at the time of performing this study, this option was not available.

Regarding calibration factors presented in the same table, some of the authors have used them with similar units cps/kBq (de Nijs et al., 2014) and cpm/kBq

(Sanders et al., 2015) or identical units as those presented in this work, cps/MBq. In the majority of cases, cylinders were preferred as phantom geometries to contain several inserts that were used as a calibration source. Cylinders, spheres and bottles inserts were chosen as source geometry. In planar studies petri dishes were preferred.

4.1. CT calibration curve

Most of the SPECT/CT systems can use the information regarding this CT calibration directly by following manufacturer recommendations. Hermes is an independent workstation to perform reconstructions. The determination of the CT calibration curve was a challenge, because we were using the results at 80 keV, from the measurements using the Catphan phantom, to establish the bilinear equations at 140 keV. Using information from NIST our results for water are slightly higher compared to those reported by Brown (Brown et al., 2008). Knowing this difference all reconstructions were performed in the same way, for phantom calibrations and patient data, therefore creating a systematic bias.

Brown et al. has investigated how to obtain these relationships using different radionuclides and slabs of different materials by creating a narrow beam geometry and measuring directly in the gamma camera (Brown et al., 2008). At 140 keV, for water, they reported a linear attenuation coefficient of 0.149 cm^{-1}. They reported differences for all measured material in less than 2% at this energy, comparing to NIST. Our results at 140 keV are slightly higher than those reported by the same group.

McParland (McParland, 2010) developed an interesting methodology to create this curve (see chapter 1), nevertheless, by using the linear attenuation coefficient information for bone, from the emissions photons and the CT component, these data was not available, hence we could not test this approach.

4.2. Sensitivity determination

4.2.1. Planar sensitivity

Barquero et al. has shown planar sensitivity results for a Siemens e-cam system (Barquero et al., 2017). Their results are for ^{131}I from measurements and Monte Carlo simulations using SIMIND. They showed sensitivity increases with size (ROI) for any distance, and decreases with distance for any size. Similar results were seen using ImageJ at CRCT. Using Xeleris^{TM} at ICM and creating a circular ROI to cover the source distribution, insignificant variation of sensitivity was observed for all distances.

Uribe et al. (Uribe et al., 2017) and Zhao et al. (Zhao et al., 2018) have performed studies using a point source in air, in both cases TEW corrections were applied. In both cases they used a collimator-to-source distance between 25 and 30cm. They concluded that *camera sensitivity does not depend on the source-collimator distance although increase in recorded counts may occur due to septal* *penetration if sources are placed very close to the collimator*. The previous conclusion can be confirmed by looking at figure 3.5.

In our case scatter correction was not performed, because we did not found an agreement in the value of "k" that is necessary to be applied with the Dual Energy Window (DEW), for instance, de Nijs et al. (de Nijs et al., 2014) mentioned that further studies should be perform with patient data, because "k" values may differ from the ones that they studied (k= 0.5, 0.8, 0.9). Then, our planar sensitivity results are higher than expected because DEW was not performed. However, if DEW was performed, results should be comparable, because the scatter counts from a spherical source in air are not high.

4.2.2. SPECT sensitivity

4.2.2.1. Spherical source – Gibbslike artifacts

From table 3.6, as expected, when the number of updates increases, the counts will increase and then converge to a certain level; this phenomenon is present under OSEM reconstructions. For both phantom configurations (3 and 4), sensitivity results are very similar but not equal. On the other hand, the impact on reconstructed images due to the post-filtering (1.0 cm) is very important, therefore it may be necessary to perform two different reconstructions, one for clinicians (for patient reports) and one for physicists (for quantification procedures).

Considering phantom model and the source placement, in the work of Wevrett et al. (Wevrett et al., 2017), different phantom configurations were used in order to determine the calibration factor for a specific equipment. They recommended to use the mean value of the sensitivity obtained from three configurations, which are the source centrally in air, source centrally in a phantom filled with water and source with an offset in a phantom filled with water. They also mentioned that adding resolution recovery reduces the variation in the calibration factor by 50% or more, depending on the camera system but maintains the geometry dependence, with the overestimation of the calibration factor increasing with distance from the centre of the phantom. We did not perform the offset configuration because we were satisfied with the obtained results with the source centered in air and in a phantom with water.

In terms of Gibbslike artifacts, according to Ljungberg et al. (Ljungberg et al., 2016), using collimator response correction can benefit NM images in several ways. For instance, it can modify the distribution of counts in the image without changing their total number. Therefore, the quantification in the field of view should not be affected. Also, it decreases the resolution-induced spill-out of counts from hot regions. However, it may create Gibbslike artifacts in the vicinity of sharp boundaries. This phenomenon is presented in our reconstructed images, especially in phantoms where no background activity and no post-filtering were employed (figures in appendix of chapter 3). Also, when post-filtering is used this phenomenon is highly reduced and it only starts to appear at 320 updates. However, in clinical practice these situations will not be seen, because background activity will be within the patient, surrounding different VOI's. We did not study deeply this effect in the background:spheres ratio activity. In our case, an activity ratio of 8:1 was employed and this effect is still present at 160 updates.

A decision was taken in terms of the reconstruction, considering only using OSEM 6 iteration and 10 subsets. Gibbslike artifacts may be reduced at this number of updates, without Gaussian post-filter. The speed of reconstruction was fast, then optimal for clinical implementation.

4.2.2.2. Cylindrical source

In table 3.7, sensitivity results for different source geometry can be seen. Using the threshold at 24% generated a CT volume close to the real source volume. The bottle was segmented automatically considering that it was not easy to do it manually, due to the thickness of the bottle wall. Moreover, source and phantom were filled with water increasing the difficulty to segment volumes correctly. By using the automatic segmentation tool same volumes were generated, in a reproducible way. However, when manual segmentation was performed volumes close to 500 ml were generated.

The sensitivity results presented in this table were obtained using two initial activities; results vary from 10.10 and 10.21 cps/MBq (average 10.18 cps/MBq). These results are 1.01 cps/MBq higher than sensitivity results of reconstruction Id #5 from table 3.6. This insignificant difference can be associated to difference in source geometry, phantom model (cylindrical vs elliptical), and acquisition time.

Considering source geometry (sphere vs bottle), less partial volume effect may be expected for the bottle source geometry than the sphere source geometry due to the difference in diameter size, therefore better results in terms of sensitivity should be expected.

Robinson et al. (Robinson et al., 2016) used a large cylinder phantom to determine whole-body sensitivity but their conclusions are related with the TEW scatter correction and they do not use collimator response correction in their work. Dewaraja et al. (Dewaraja et al., 2012) proposed to have calibration factors based-on the studied volume. Tran-Gia and Lassmann (Tran-Gia & Lassmann, 2017), created a 3D realistic 2-compartment kidney phantom. They considered the effect of source geometry and its placement, observed Gibbslike artifacts, and partial volume effect. Zhao et al. (Zhao et al., 2018) mentioned that its calibration factor value *corresponds purely to the camera efficiency for given radioisotope, collimator and energy window settings. It does not depend on the camera and image resolution, the size and shape of the imaged object, the signal-to-background ratio and other factors.*

The HROD user's manual (Hermes Medical Solutions, 2015), presents an in-house study using an Jaszczak phantom filled with water and ^{99m}Tc. The acquisition was performed using a Siemens® Symbia-T SPECT/CT, with LEHR collimators. They explain the reconstructing procedure and they draw spherical ROIs of 3.0cm in diameter in 5 different locations. They find good activity concentration results; however, they did not used the whole Jaszczak phantom filled water as source geometry to perform the calibration itself.

For calibration purposes it may be important to consider a bigger geometry source, such as the whole Jaszczak phantom (without the inner structures) at least to reduce partial volume effect. But in the case of quality control, in order to check the stability of the gamma camera for ^{177}Lu, a planar acquisition of a point source in air can be implemented in clinical practice.

Regarding the calibration factor estimation, acquisition time will not have an impact on our results, at least for HDM, STRATOS and PDOSE, because for these workstations calibration factor it is not time dependent. This is not true in the case of DTK.

SPECT sensitivity results (cps/MBq) for ^{177}Lu obtained after reconstruction with HROD, Marin et al. (Marin et al., 2017)*,* Uribe et al. (Uribe et al., 2017) *and* Zhao et al. (Zhao et al., 2018) showed similar results using another gamma camera type.

4.2.3. Recovery coefficients

Marin et al., used a similar phantom configuration and similar set of spheres, different SPECT/CT (Symbia TruePoint T), different reconstruction algorithm (Syngo MI Applications 8.5) and different collimator type - medium energy, low penetration collimator (MELP), In their results as the number of updates increases, the recovery coefficient increases for different Gaussian post-filters, for two different sphere sizes. Their recovery coefficient values are comparable to our results using a Gaussian post-filter set at 1.0 cm. It is important to notice the behavior of the recovery coefficient when non-Gaussian post-filter was applied for spheres between 2 and 4 ml, showing an overestimation of the real activity in the sources. Nonetheless, for the same spheres with Gaussian post-filter this overestimation is reduced up to 38% and 50%, respectively; this is due to the smoothing of counts generated when the post-filter is applied. The overestimation effect, for these two spheres, increases as the number of updates increases. When Gaussian post-filter at 1.0 cm is applied our results are similar to those presented by Marin et al. (Marin et al., 2017) for an equivalent number of updates. In our case, the recovery coefficient results are just to benchmark the SPECT/CT, because in our clinical implementation (see chapter 4) the segmented volumes are bigger than 70 ml, then the recovery coefficient should be 1 (or very close).

According to Dewaraja et al. (Dewaraja et al., 2012), in iterative reconstruction, using the distance-dependent collimator-detector response function will reduce partial-volume effects but complete resolution recovery will not take place. Therefore, this correction should be applied for some small structures.

4.2.4. Phantom evaluation on three commercially available workstations

To evaluate (part of) the dosimetric chain, rather than just activity quantification, we evaluated the residence times in HDM, PDOSE, and STRATOS. One idea was to check the registration process in a multi-SPECT/CT scenario, especially considering the misplacement of the phantom. Obviously, the phantom being rigid, this is an oversimplified use of registration algorithms implemented in the workstations. In real patient acquisitions the situation would be much worse, due to patient placement, internal organs movements, related or not to respiratory motion. Looking at figure 3.7.A and 3.7.B, using HDM and PDOSE, the phantom positioning can be visually assessed after registration (for instance, in the axial view); with STRATOS, the registration cannot be checked in a similar way.

4.2.4.1. Activity determination

The initial idea was to compare the three workstations according to the reconstruction method, to measure the activity at each time point for each workstation and to estimate the residence time.

From our results in table 3.8, HDM performed similarly as PDOSE, showing that the registration method was able to see the variations in phantom positioning. The variations in segmentation for both software are not very important, because at each time point the PRD is less than ±10%, and in the case of PDOSE the PRD are less than ± 3.3%. In the case of STRATOS, for the first three data points the activity estimation was good, reaching PRD values less than ± 20%. For the last two data points the phantom position varied, hence the activity estimation was not good. Most probably the error in quantification is associated to the registration method, in which only one CT (reference CT) is used to register all NM data points. From this experience, it could be advisable to perform the registration using CT data only.

4.2.4.2. Residence time evaluation

For each average sensitivity, a calibration factor was estimated in order to be used in each software. Looking at table 3.9 for calibrations factors derived from reconstructions with non-Gaussian post-filter, PRDs are lower than 11.02%, for the two segmentation thresholds applied. In fact, when average sensitivity is close to 10 cps/MBq, the relative difference (%) between the theoretical and estimated residence time is close to 0%. Relative differences (%) derived from reconstructions using post-filter 1.0 cm are the worst for the tested calibrations factors. These results confirm that one set of reconstructed images with non-Gaussian post-filter must be used for quantification. From this table, the sensitivity factors 9.68 or 9.77 cps/MBq, should be chosen for quantification purposes.

In the case of results from table 3.10, calibration factors come from sensitivities values close to 10 cps/MBq, therefore percentage of relative differences are lower than 1%.

Table 3.11 the percentage of relative differences using STRATOS and PDOSE can be observed. When using PDOSE similar tendency as HDM can be observed. The best results are obtained with non-Gaussian post-filter. However, this occurs for the sensitivities lower than 10 cps/MBq. In this case, the segmentation process was manual, generating a source volume of 492 ml, very close to the real volume in the bottle. With this software the goodness of the fitting can be evaluated quantitatively and qualitatively by using the Spearman's coefficient. Nevertheless, no explanation has been found to the opposite behavior of HDM and PDose.

On the other side, table 3.11 shows percentage of relative differences using STRATOS, for this software no trend in the results can be seen for any of the calibration factors used.

Comparing HDM and PDOSE, both performed similarly in terms of residence time and activity estimations, as shown in table 3.8. Both show the final registration result and the user can evaluate qualitatively its performance. On the other hand, HDM shows the highest percentage of relative difference (7%) in activity estimation (for time point at 49h), this effect can be seen also in figure 3.7.C.

STRATOS could not recognize the phantom misplacements, therefore, registration process between the first CT and the others NM images may generate great variations in the estimated activity for each measured time point (and voxel per voxel); hence, estimation of residence time for ^{177}Lu will not be optimal. Our version of the software does not provide manual registration option; hence, we applied the same automatic registration algorithm, but it was not possible to obtain the same registration parameters results when reprocessing phantom data. These results can be confirmed by looking at table 3.8, in which the highest percentages of relative differences in activity were seen when the positioning of the phantom varied importantly, creating a bias in residence time estimation.

5. Conclusions

As could be seen, calibration procedure is a complex process that is far from being standardized. This is reflected in the different dosimetric software.

CT calibration curve, planar and SPECT sensitivity factors were estimated and established for a SPECT/CT system at the ICM.

In this study, two phantom models using different source geometries were used. One important effect degrading image quality is the partial volume effect, but using collimator-response correction (and recovery coefficients) this phenomenon could be reduced in small structures. Nevertheless, this correction can generate Gibbslike artifacts.

Although there are several publications regarding ^{177}Lu, further investigations should be done to assess Gibbslike artifacts in clinical practice, especially when high numbers of updates are used with OSEM reconstruction algorithm.

One possible solution to avoid PVE artifacts is to use big sources for the calibration process and to use point sources for quality control purposes (to assess the constancy of the detector).

In the case of HDM and PDOSE, preliminary results show best calibration factors derived from sensitivity values close to 10 cps/MBq. For STRATOS it was not possible to obtain a calibration factor.

HDM and STRATOS allow using one calibration factor only. PDOSE allows more than one calibration factor (if the user needed). This option should be managed carefully in clinical routine as there is no built-in verification process (i.e. sanity check of entered values).

We presented an indirect validation method to assess the dosimetric chain in three workstations. This method was implemented by finding the theoretical residence time in a phantom study (considering phantom displacements). From residence time results assessed in a phantom study, HDM and PDOSE performed similarly and STRATOS shows a bias that may be associated to the registration process (even in simple situations as that of a rigid phantom).

Having established the best reconstruction set-up, its associated calibration factor and validated three workstations, clinical patient data can be processed and analyzed. Moreover, dosimetric results can be obtained for segmented structures.

6. References of the chapter

Barquero, R., et al. (2017). ^{131} I activity quantification of gamma camera planar images. *Phys Med Biol*, *62*(3), 909–926.

Beauregard, J. M., et al. (2011). Quantitative 177Lu SPECT (QSPECT) imaging using a commercially available SPECT/CT system. *Cancer Imaging*, *11*, 56–66.

Brown, S., et al. (2008). Investigation of the relationship between linear attenuation coefficients and CT Hounsfield units using radionuclides for SPECT. *Applied Radiation and Isotopes*, *66*(9), 1206–1212.

de Nijs, R., & Svarer, C. (2007). Combined backscatter and scatter correction for low count I-123 SPECT studies. *J Nucl Med*, *48*(S1), 424.

de Nijs, R., et al. (2010). Experimental determination of the weighting factor for the energy window subtraction-based downscatter correction for I-123 in brain SPECT studies. *J Med Phys*, *35*(4), 215–22.

de Nijs, R., et al.. (2014). Improving quantitative dosimetry in 177Lu-DOTATATE SPECT by energy window-based scatter corrections. *Nucl Med Commun*, *35*(5), 522–533.

Desbordes, P., et al. (2014). 3D automated lymphoma segmentation in PET images based on cellular automata. In *Image Processing Theory, Tools and Applications* (pp. 1–6). IEEE.

Desbordes, P., et al. (2017). Predictive value of initial FDG-PET features for treatment response and survival in esophageal cancer patients treated with chemo-radiation therapy using a random forest classifier. *PloS One*, *12*(3), e0173208.

Dewaraja, Y. K., et al. (2012). MIRD pamphlet No. 23: quantitative SPECT for patient-specific 3-dimensional dosimetry in internal radionuclide therapy. *J Nucl Med*, *53*(8), 1310–25.

Dieudonne, A., et al. (2010). Fine-Resolution Voxel S Values for Constructing Absorbed Dose Distributions at Variable Voxel Size. *J Nucl Med*, *51*(10), 1600–1607.

Dieudonne, A., et al. (2011). Clinical Feasibility of Fast 3-Dimensional Dosimetry of the Liver for Treatment Planning of Hepatocellular Carcinoma with 90Y-Microspheres. *J Nucl Med*, *52*(12), 1930–1937.

Dieudonne, A., et al. (2013). Study of the Impact of Tissue Density Heterogeneities on 3-Dimensional Abdominal Dosimetry: Comparison Between Dose Kernel Convolution and Direct Monte Carlo Methods. *J Nucl Med*, *54*(2), 236–243.

Gardin, I., et al. (2017). Predictive value of dosimetry indices for treatment response in liver cancer patients treated with yttrium 90 microspheres using a random forest algorithm. *J Nucl Med*, *58*(supplement 1), 197.

Garkavij, M., et al. (2010). 177Lu-[DOTA0,Tyr3] Octreotate therapy in patients with disseminated neuroendocrine tumors: Analysis of dosimetry with impact on future therapeutic strategy. *Cancer*, *116*(Supple 4), 1084–1092.

Grassi, E., et al. (2015). Quantitative comparison between the commercial software STRATOS®by Philips and a homemade software for voxel-dosimetry in radiopeptide therapy. *Phys Medica*, *31*(1), 72–79.

Gustafsson, J., et al. (2015). Uncertainty propagation for SPECT/CT-based renal dosimetry in 177Lu peptide receptor radionuclide therapy. *Phys Med Biol*, *60*, 8329–8346.

Hermes Medical Solutions. (2014). Hybrid Recon^{TM} - CT-based attenuation map calibration, (CD301.3_P21V1.1), 1–6.

Hermes Medical Solutions. (2015). *Handbook Hybrid Recon^{TM} - Oncology*.

Hippeläinen, E., et al. (2016). Quantitative accuracy of 177Lu SPECT reconstruction using different compensation methods: phantom and patient studies. *EJNMMI Research*, *6*, 16.

Hudson, H. M., & Larkin, R. S. (1994). Ordered Subsets of Projection Data. *IEEE Transactions on Medical Imaging*, *13*(4), 601–609.

Ichihara, T., et al. (1993). Compton Scatter Compensation the Triple-Energy Window Method for Single- and Dual-Isotope SPECT. *J Nucl Med*, *34*(12), 2216–2221.

Ilan, E., et al. (2015). Dose response of pancreatic neuroendocrine tumors treated with peptide receptor radionuclide therapy using 177Lu-DOTATATE. *J Nucl Med*, *56*(2), 177–182.

Jaszczak, J., et al. (1984). Improved SPECT Quantification Using Compensation for Scattered Photons. *J Nucl Med*, *25*(8), 893–900.

Kadrmas, D., et al. (1998). NIH Public Access. *Phys Med Biol*, *43*(4), 857–873.

Kangasmaa, T. S., et al. (2016). Multicenter evaluation of single-photon emission computed tomography quantification with third-party reconstruction software. *Nucl Med Commun*, *37*(9), 983–987.

Ljungberg, M., et al. (1994). Comparison of four scatter correction methods using Monte Carlo simulated source distributions. *J Nucl Med*, *35*(1), 143–151.

Ljungberg, M., et al. (2003). 3D absorbed dose calculations based on SPECT: evaluation for 111-In/90-Y therapy using Monte Carlo simulations. *Cancer Bioth Radiopharm*, *18*(1), 99–107.

Ljungberg, M., et al. (2016). MIRD Pamphlet No. 26: Joint EANM/MIRD Guidelines for Quantitative 177Lu SPECT Applied for Dosimetry of Radiopharmaceutical Therapy. *J Nucl Med*, *57*, 151–162.

Marcatili, S., et al., (2015). Model-based versus specific dosimetry in diagnostic context: Comparison of three dosimetric approaches. *Med Physics*, *42*(3), 1288–1296.

Marin, G., et al. (2017). Accuracy and precision assessment for activity quantification in individualized dosimetry of 177 Lu-DOTATATE therapy. *EJNMMI Physics*, *4*, 7.

McParland, B. J. (2010). *Nuclear Medicine Radiation Dosimetry: Advanced Theoretical Principles*. Springer Science & Business Media.

Ogawa, K., et al. (1991). A Practical Method for Position-Dependent Compton-Scatter Correction in Single Photon Emission CT. *IEEE Transactions on Medical Imaging*, *10*(3), 408–412.

Pasciak, A. S., et al. (2014). A Comparison of Techniques for 90Y PET/CT Image-Based Dosimetry Following Radioembolization with Resin Microspheres. *Frontiers in Oncology*, *4*(May), 1–10.

Robinson, A. P., et al. (2016). The influence of triple energy window scatter correction on activity quantification for 177Lu molecular radiotherapy. *Phys Med Biol*, *61*, 5107–5127.

Sanders, J. C., et al. (2015). Quantitative SPECT/CT Imaging of 177Lu with In Vivo Validation in Patients Undergoing Peptide Receptor Radionuclide Therapy. *Mol Imaging Biol*, *17*(4), 585–593.

Sandström, M., et al. (2010). Individualized dosimetry in patients undergoing therapy with 177Lu-DOTA-D-Phe1-Tyr3-octreotate. *Eur J Nucl Med Mol Imaging*, *37*(2), 212–225.

Schneider, C. A., et al. (2012). NIH Image to ImageJ: 25 years of image analysis. *Nature Methods*, *9*(7), 671–675.

Siegel, J. A., et al. (1999). MIRD pamphlet no. 16: Techniques for quantitative radiopharmaceutical biodistribution data acquisition and analysis for use in human radiation dose estimates. *J Nucl Med*, *40*(2), 37S–61S.

Sohlberg, A., et al. (2008). Acceleration of Monte Carlo-based scatter compensation for cardiac SPECT. *Phys Med Biol*, *53*(14), N277–N285.

Sohlberg, A., et al. (2008). Three-dimensional SPECT reconstruction with transmission-dependent scatter correction. *Ann Nucl Med*, *22*(7), 549–556.

Stabin, M., Farmer, A. (2012). OLINDA/EXM 2 .0: The new generation dosimetry modeling code. *J Nucl Med*, *53*(Suppl 1), 585.

Stabin, M., et al. (2005). OLINDA/EXM: the second-generation personal computer software for internal dose assessment in nuclear medicine. *J Nucl Med*, *46*(6), 1023–1027.

Tossici-Bolt, L., et al. (2006). Quantification of 123IFP-CIT SPECT brain images: An accurate technique for measurement of the specific binding ratio. *Eur J Nucl Med Mol Imaging*, *33*(12), 1491–1499.

Tran-Gia, J., Lassmann, M. (2017). Optimizing Image Quantification for Lu-177 SPECT/CT Based on a 3D Printed 2-Compartment Kidney Phantom. *J Nucl Med*, *59*(4), 616–624.

Uribe, C. F., et al. (2017). Accuracy of 177Lu activity quantification in SPECT imaging: a phantom study. *EJNMMI Physics*, *4*, 2.

Vera, P., et al. (2013). Does enhanced CT influence the biological GTV measurement on FDG-PET images? *Radiotherapy and Oncology*, *108*(1), 86–90.

Wevrett, J., et al. (2017). Development of a calibration protocol for quantitative imaging for molecular radiotherapy dosimetry. *Rad Phys Chem*, *140*, 355–360.

Zhao, W., et al. (2018). Determination of gamma camera calibration factors for quantitation of therapeutic radioisotopes. *EJNMMI Physics*, *5*, 8.

1. Introduction

Lutetium 177 (^{177}Lu) is a good candidate for targeted radionuclide therapy, due to the possibility of reliable labeling on biomolecules used for tumour targeting and its decay characteristics (Ljungberg et al., 2016). It has been used for example in peptide receptor radionuclide therapy (PRRT). The agent ^{177}Lu-DOTA-octreotate enables the targeting of somatostatin receptors (SSTR) expressed at the surface of neuroendocrine tumours (NET) (Kashyap et al., 2014).

PRRT has been used for several years proving to be safe, efficient and well-tolerated to treat patients with NETs (Bodei et al., 2011; Strosberg et al., 2017). Lutathera (^{177}Lu-labelled DOTATATE) has recently received EMA and FDA approval, with an administration scheme of 4 cycles of fixed (7.4 GBq) activity. This has triggered a debate within the nuclear medicine community regarding the relevance of advocating “one-size-fits-all” approaches in the personalized medicine era (Chiesa et al., 2017; Flux et al., 2017; Giammarile et al., 2017). Regardless of the obvious clash between the Euratom Directive and EMA decision (one EU body enforcing patient-specific dosimetry whereas another one *de facto* limits its implementation), publications have demonstrated the added value of dosimetry in a context of PRRT with ^{177}Lu.

Treatment optimization can be based on the evaluation of absorbed doses delivered to critical organs (kidneys, red or active bone marrow) or tumours (Bergsma et al., 2016; Garske-Román et al., 2018; Astrid Gosewisch et al., 2018; Sundlöv et al., 2017; Valkema et al., 2005).

Different approaches to clinical dosimetry have been proposed. They are based on whole body (WB) planar images (Cremonesi, et al. 2006; Mirzaei, et al., 2013; Schuchardt, et al., 2013; Svensson et al., 2016), SPECT/CT images (Beauregard, et al., 2011; Hänscheid, et al., 2018; Ilan et al., 2015; Sanders, et al., 2015) or hybrid methods combining WB planar images with one or two SPECT/CT (Bailey et al., 2015; Brolin, et al., 2015; Garkavij et al., 2010; Guerriero et al., 2013; Sandström, et al., 2010). Comparison between planar and SPECT activity quantification treating NET patients has shown an overestimation of kidney activity using planar methods, due to overlapping of high activity areas (Garkavij et al., 2010).

Up to recently, there was no dosimetry software in commercial nuclear medicine workstations. Therefore academic/research institutions/hospitals developed *ad hoc* dosimetric software. Among these software are: DOSIMG (Tagesson, et al., 1996), MABDOSE (Johnson, et al., 1999), DOSE3D (Clairand, et al., 1999), RMDP (Guy, et al., 2003), VoxelDose (Gardin et al., 2003), MrVoxel (McKay, 2003), 3D-ID (Sgouros et al., 2004), LundADose (Sjögreen et al., 2005), OEDIPE (Chiavassa et al., 2006), MINERVA (Lehmann et al., 2005), 3D-RD (Prideaux et al., 2007), RAYDOSE (Marcatili et al., 2013), VIDA (Kost et al., 2015) and NUKDOS (Kletting et al., 2015).

Beyond these efforts, commercial packages are arriving on the market, providing solutions that include different modules for dealing with raw data or uploading reconstructed DICOM images, allowing registration and segmentation processes, data fitting and absorbed dose estimations/reporting, i.e. addressing the different steps of the dosimetric workflow. Figure 4.1 shows a scheme of the dosimetric workflow.

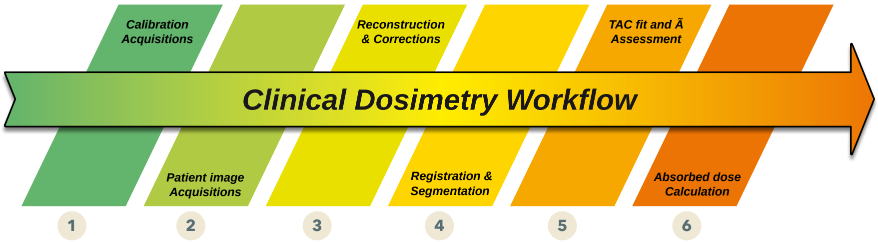

Figure 4.1: Clinical dosimetric workflow scheme. Created by Manuel Bardiès. Used with his permission.

In this chapter four commercial software are compared based-on clinical data from two patients with gastroenteropancreatic tumours of neuroendocrine origin treated with ^{177}Lu-DOTATATE. Two cycles of treatment for each patient were used to estimate residence times for the kidneys, liver, spleen, bone marrow and whole body.

In the case of the bone marrow, a new methodology is presented to estimate the absorbed dose without the need for whole-body measurements.

It can be seen that the registration of the images has an impact on the determination of the absorbed dose. The results are therefore calculated by employing an approach that involves independent registration of each volume of interest in the images.

Different calculation algorithms were used to determine the absorbed dose delivered to patients.

Several objectives are addressed to assess the reliability of four commercial workstations using patient data sets:

c. To calculate residence times for liver, spleen and kidneys.
d. To estimate the absorbed doses for the previous organs.
e. To estimate the absorbed dose to red bone marrow when whole body measurements were not performed.

2. Materials and Methods

All measurements and treatments were carried out at the Institut régional du Cancer de Montpellier (ICM) in the Nuclear Medicine Department, using a GE-Discovery NM/CT 670 SPECT/CT, 9.5 mm crystal thickness. One set of projections was acquired and was reconstructed and analyzed at the ICM and the Centre de Recherches en Cancérologie de Toulouse (CRCT). All activity measurements were done in an accurate activimeter calibrated for ^{177}Lu measurements.

At CRCT reconstruction was performed using HybridRecon-Oncology version_1.3_Dicom (HROD) from Hermes without using the SPECT Standard Uptake Value (SUV) (Kangasmaa, et al., 2016) option. At ICM images were reconstructed using Dosimetry Toolkit®, which is an application of the commercial workstation Xeleris®. A general overview of the four software was introduced in chapter 3.

2.1. Patient characteristics

Two patients (one male, one female) who benefited from PRRT with ^{177}Lu were considered in this study. Table 4.1 shows some characteristic of these patients. Each patient received four cycles of therapy, with an interval of approximately 8 weeks.

Table 4.1. Characteristics of patients treated with ^{177}Lu-DOTATATE for PRRT.

	Treatment cycle for female patient		**Treatment cycle for male patient**	
	First	**Second**	**First**	**Second**
Injected activity	7176.7	7239.4	7207.2	7188.2
Age (years)	82		59	
Weight (kg)	57		79	
Height (cm)	153		180	
Primary tumor	Pancreas NET		Small intestine NET	
Metastasis	Liver		Mesentery, liver	

2.1.1. Patient data acquisition and reconstruction

Using same equipment described in chapter 3, SPECT/CT images were acquired at 4, 24, 72 and 192 h. In one FOV, pelvic and thoracic regions were acquired using 60 projections in total, 45 s per projection, zoom 1, matrix size 128x128, using two energy windows (one centered at 208 keV at 20% and one at 177 keV at 10%), parallel-hole medium energy general purpose (MEGP) collimator and body auto-contour were used. The CT acquisition protocol was 120 kV, mA was set in auto, matrix size 512x512, noise index 6.4, slice thickness 5 mm, pitch 1.375 and standard reconstruction filter. For each patient and for each time point measurement, one set of images was generated.

At ICM transversal slices were reconstructed using “preparation for dosimetry Toolkit application”, this includes manufacturer corrections such as scatter, CT-based attenuation, collimator-detector response and uses the two energy windows for scatter correction.

At CRCT the reconstruction was performed with Hermes HybridRecon-Oncology version_1.3_Dicom (HROD) using the main energy window only and applying manufacturer corrections (Monte Carlo-based scatter correction (Sohlberg, et al., 2008), CT-based attenuation correction (Hippeläinen, et al., 2016), the attenuation map was resampled to correct size/energy (this resampling was performed automatically by the workstation), collimator-detector response correction. The SPECT standard uptake value (SUV) option (Kangasmaa et al., 2016) was not available at the time of this study. Both centers reconstructed images using OSEM

(6i, 10ss), and using a gaussian post-filter set at 0.11cm.

The reconstructed data generated at the ICM was uploaded in DTK from Xeleris®. Reconstructed data from HROD was uploaded in PLANET® Onco Dose (PDOSE) from DOSISOFT (version 3.1.1 RC-2018-03-16), STRATOS from Phillips (Imalytics 3.2, Rev 6289(64)) and Hybrid Dosimetry Module™ (HDM) from Hermes (Version 1.0).

2.1.2. Residence times and absorbed dose comparisons

The selected organs for this study were the liver, spleen and kidneys. Sandström (Sandström et al., 2010) in their study mentioned that most patients had a large number of metastases within the liver which made it virtually impossible to correct adequately for normal liver weight, then we decided to combine the whole normal liver and the tumors in one VOI, which may be wrong from a clinical point of view but does not limit the analysis of the dosimetric workstations.

2.1.2.1. GE Healthcare Dosimetry Toolkit® (DTK)

Automatic registration occurred by conducting a rigid registration between each CT scan and the first CT scan. The reconstruction results were uploaded in the "Dosimetry toolkit" application. Kidneys, liver and spleen organs were automatically segmented using the first CT and NM images. They were then subsequently replicated to the other time point measurements. The SPECT/CT calibration factor was used to find the activity per organ at each time point. Fitting was performed using a mono-exponential function. By integrating all fitted data, the software estimated the residence times per organ and it exported the results to OLINDA/EXM V1.0 to calculate the mean absorbed dose.

2.1.2.2. Hermes Hybrid Dosimetry Module™ (HDM)

Automatic rigid registration (translation and rotation) was performed taking the first SPECT/CT as a reference; the software synchronized two SPECT/CT series at a time. Segmentation was carried out manually on CT slices by creating ROI's for each organ. The software automatically created each ROI from the CT on the NM matrix. Segmented organs were copied to the following SPECT/CT series, keeping the volume constant. If the generated ROI's did not match the position in axial plane of the SPECT/CT series, manual ROI's replacement was performed. The calibration factor was entered in units of MBq/counts, with information regarding date; time of injection and injected activity. Extrapolation before the first data point was done by creating a horizontal line from t=0 to the first data point (constant activity). Then from the first to the last time point curve fitting was done assuming bi-exponential decay using the Levenburg-Marquardt algorithm (Mirzaei et al., 2013). From the last time point measurement to infinity, mono-exponential decay was assumed considering only physical half-life. By integrating all fitted data, the software estimated the residence time. Fitting was assessed visually because the software does not provide a tool to evaluate the goodness of the fit. Results were exported to OLINDA/EXM V2.0 to estimate mean absorbed dose, with first order mass correction.

2.1.2.3. DOSISOFT PLANET®Onco Dose (PDOSE)

Segmentation was carried out manually on the CT slices of the reference CT in order to create a VOI for each structure. The software automatically created the VOI from the CT on the NM matrix. By using the segmented structure an automatic registration was done organ-by-organ. Rigid registration was performed taking the first SPECT/CT series as a reference; the software synchronizes two SPECT/CT series at a time. Registered images were saved in a new space, called “registered space”. After the registration process was done, rigid propagation of the structure occurred in the registered space. In this case the generated volume was kept constant among all images in the registered space. The calibration factor was included at this stage in units of Bq/counts, with the date and injection time information. Within the different available fitting options (mono-, bi- or tri-exponential, or using the trapezoid method assuming mono-exponential decay from the last data point) the best possibility was chosen according to the Spearman coefficient. By integrating fitted data the software calculated cumulated activity or mean absorbed doses. Using the known injected activity, residence times were also estimated. Absorbed dose is estimated by using the local energy deposition method.

2.1.2.4. STRATOS by Phillips

Information regarding the calibration factor (in units of Bq/intensity), date and time of injection and injected activity were entered. Automatic rigid registration was performed between the NM study of each day and the first CT study, which was taken as a reference. Segmentation was carried out manually on CT slices of the reference CT by creating VOI’s for each organ. The NM images generated by HROD had voxel sizes of 4.42 x 4.42 x 4.42 mm^3. STRATOS generates cumulated activity maps with this voxel size, meaning that no resampling was necessary. Fitting was performed at the voxel level, assuming a straight line between zero and the first time point; then trapezoid method was applied between the rests of time points. From last time point mono-exponential decay (called “tail integration”) was employed considering only physical half-life. Voxel S-values in STRATOS are provided for the previous dimensions. The cumulated activity is calculated voxel by voxel. The 3D cumulated activity maps were then convolved with a pre-calculated water dose voxel kernels (DVKs) to obtain a 3D absorbed dose map. Knowing the injected activity, residence times can be calculated (Marcatili, et al., 2015).

2.1.3. Absorbed dose comparisons

Because DTK export results to OLINDA/EXM V1.0 and HDM export results to OLINDA/EXM V2.0, a decision was taken in order to estimate the mean absorbed doses (corrected by organ mass) using each version of the OLINDA (using residence times).

For all software, all organ masses were estimated using density values from GATE MC code (Jan, 2004). For liver and spleen this value was 1.06 g*cm^{-3} and for kidneys was 1.05 g*cm^{-3}. Also, to allow comparison with OLINDA, the mean absorbed dose to kidneys was performed weighting the left/right results by each kidney mass.

Aside of model-based absorbed dose calculation using S-values tables, other approaches are provided within the workstations. In the case of STRATOS mean absorbed dose is calculated by a convolution method. In the case of PDOSE, local energy deposition method (LDM) is available.

2.1.3.1. Local energy deposition (LDM) method

In the case of LDM, this methodology was derived from an image-based dosimetry approach developed for radioembolization with resin microspheres. The methodology employed by Dosisoft was described in section 5.5.1 from chapter 1.

The general MIRD equation gives:

$$\overline{D}_{(k\leftarrow h)} = \tilde{A}_h \sum_i n_i\, E_i \frac{\phi_i(k \leftarrow h)}{m_k} \qquad 4.1$$

Where $\tilde{A}_h$ is the cumulated activity for an organ source, E_i is the mean energy of the ith nuclear transition; n_i is the number of ith nuclear transition per nuclear transformation. $\phi_i(k \leftarrow h)$ is the absorbed fraction, which is the fraction of radiation energy emitted E_i within the source tissue h that is absorbed in the target tissue k. Finally, m_k is the mass of the organ target. When $\phi_i(h \leftarrow h)$=1 (for non-penetrating radiation), all emitted energy can be considered as locally absorbed.

The equation 4.1 becomes:

$$\overline{D}_{(h\leftarrow h)} = \tilde{A}_h \frac{\Delta}{m_h} \qquad 4.2$$

Where Δ (in J. Bq^{-1}.s^{-1}) is the emitted energy per decay for the isotope. If LED conditions are met, the equation can easily be transposed to voxel-based dosimetry.

With PDOSE, the average absorbed dose rate will be estimated for each time point measurement. Then integrating over time, the average absorbed dose can be estimated.

2.1.4. Absorbed dose estimation for red bone marrow

According to Medical Internal Radiation Dose Committee (MIRD) scheme, Red Marrow (RM) absorbed doses can be estimated by summing the contributions of self- (contribution from RM to RM) and cross-irradiation (from organ sources to RM and from remainder of the body (RB) to RM) (Ferrer et al., 2010), as it is shown in equation 4.5.

$$D_{RM} = \tilde{A}_{RM} \times S_{(RM \leftarrow RM)} + \sum_{h} \tilde{A}_{h} \times S_{(RM \leftarrow h)} + \tilde{A}_{RB} \times S_{(RM \leftarrow RB)} \qquad 4.5$$

Where $\tilde{A}_{RM}$, $\tilde{A}_{h}$ and $\tilde{A}_{RB}$ are the cumulated activities in red marrow, other organs and the remainder, respectively. $S_{(RM \leftarrow RM)}$, $S_{(RM \leftarrow h)}$ and $S_{(RM \leftarrow RB)}$ are S-values associated to the previous source-target structures, those values can be found in OLINDA/EXM V2.0.

Manual segmentation of trabecular L_2-L_4 vertebrae is performed following recommendations from Pacilio (Pacilio et al., 2014), also manual segmentation of the thoraco-abdominal (TH-AB-FOV) region is performed. In both cases the objective is to estimate the volume of each structure. For these two regions residence times are calculated, which means, we also applied rigid registration and rigid propagation as it was performed for the previous cases. Figure 4.2 shows examples of the performed segmentation.

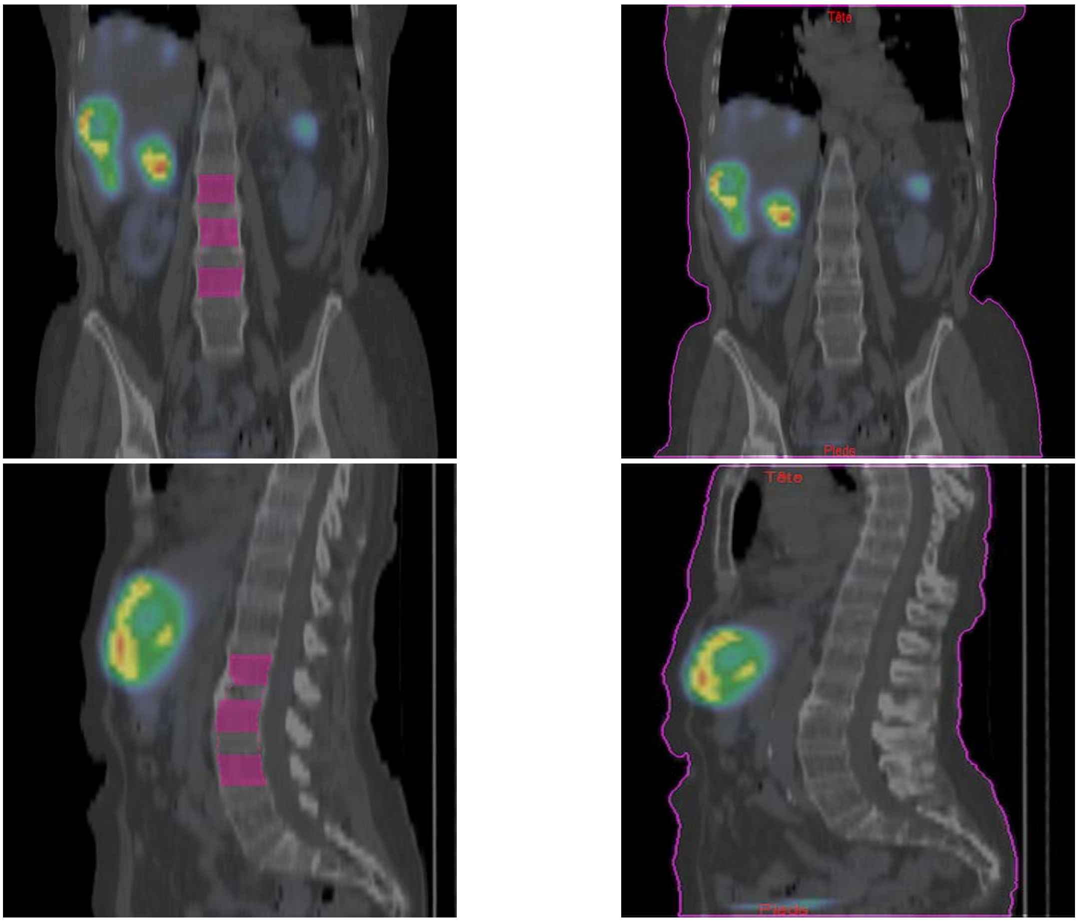

Figure 4.2: Example of segmentation (sagital and lateral views) of L_2-L_4 trabecular vertebrae and the thoraco-abdominal region in female patient.

Using residence time results for liver, spleen and kidneys from section 2.1.2.3, estimation the remainder of the body (RB) residence time can be obtained by summing all other residence times associated to each organs source (liver, kidneys, spleen and L_2-L_4 trabecular vertebrae) and subtracting them from the TH-AB-FOV residence time.

Quantification of RM is possible by using information provided from L_2-L_4 trabecular vertebrae, several authors have implemented this quantification (Ferrer et al., 2010; Pacilio et al., 2014; Shen et al., 2002). The volume of L_2-L_4 trabecular vertebrae for a female and male reference were 49 ml and 70 ml (Pacilio et al., 2014), respectively. Then, the L_2-L_4 trabecular vertebrae residence time previously found is scaled; thus, the remainder residence time is corrected by this new estimation.

On the other hand, S-value $S_{(RM \leftarrow RM)}$ is also scaled, by the ratio reference:patient volume of the trabecular vertebrae. Hence, D_{RM} is estimated according to equation 4.6.

$$D_{RM} = \tilde{A}_{RM} \times S_{(RM \leftarrow RM)} = \frac{\tilde{A}_{L_2-L_4}}{0.067} \times \left(S_{(RM \leftarrow RM)} \times \frac{V^{refman}_{trab\ L_2-L_4}}{V^{patient}_{trab\ L_2-L_4}} \right) \quad 4.6$$

The images of the patients were focussed in the thoraco-abdominal (TH-AB-FOV) region and whole-body measurements were not performed. Then, the activity determination of the remainder of the body only on acquisitions SPECT is challenging, because whole-body (WB)-SPECT was not performed.

The previous residence time of the remainder of the body is relative to the TH-AB-FOV, then an approximation to the real patient WB is proposed by the estimation of the ratio between the volume of TH-AB-FOV:WB on both patients, and the same ratio estimation is calculated for the ICRP-110 models, for validation purposes.

The WB volume of patients is calculated from their mass, assuming a density of 1.01g/cm^3, whereas the FOV volume of the patients is extracted from images (see figure 4.3.B).

For the models, the WB volume was known; and we extracted the FOV volume by dividing each model between: upper-part (with arms), FOV and lower-part. Figure 4.3.A, shows how this division occurred in the model.

Equation 4.7 shows how the ratios for the volume between patient and models are estimated.

$$R_{model} = \frac{V^{FOV}_{TH-AB}}{V_{WB}}, R_{patient} = \frac{V^{FOV}_{TH-AB}}{V_{WB}} \quad 4.7$$

Then, if the ratio between the model/patient volumes is similar, the cumulated activity of the remainder of the body is scaled as can be seen in equation 4.8

$$\tilde{A}^{scaled}_{RB} = \frac{\tilde{A}_{RB-FOV}}{R_{patient}} \quad 4.8$$

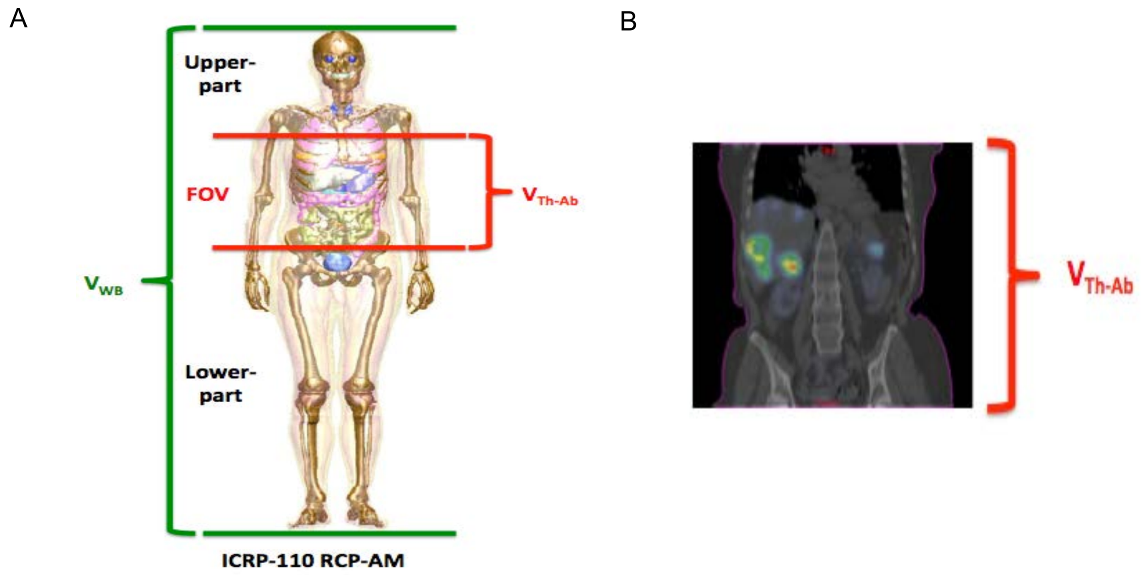

Figure 4.3: Estimation of ratio between the volume of TH-AB-FOV:WB for patient and model. A) Division of ICRP-110 RCP-AM model. B) Section of the TH-AB-FOV of a patient. Own creation. Patient image provided by ICM nuclear medicine department.

Finally, $S_{(RM \leftarrow RB)}$ is scaled according the ratio between the reference/patient mass, according to Traino (Traino, et al., 2007) and Woodard (Woodard, 1984). Then the last term of equation 4.5, can be expressed as it is shown in equation 4.9

$$D_{RM \leftarrow RB} = \tilde{A}_{RB}^{scaled} \times S_{(RM \leftarrow RB)}^{scaled} = \frac{\tilde{A}_{RB-FOV}}{R_{patient}} \times \left(S_{(RM \leftarrow RB)} \times \frac{m^{referece}}{m^{patient}} \right) \qquad 4.9$$

3. Results

To estimate the residence times in each workstation the calibration factors applied were as follows: for DTK 5.67 cps/MBq, for HERMES 38.3E-06 MBq/counts, for STRATOS 38.3 Bq/intensity and PDOSE 38.3 Bq/counts. The calibration factors for Hermes, STRATOS and PDOSE were estimated considering the patients were acquired 60 projections in total, 45 seconds per projection. This is equivalent to 9.68 cps/MBq.

3.1. Residence times determination and absorbed dose results

Figure 4.4, shows an example of segmentation of the studied organs, for male (MP) and female (FP) patients, in both cases using PDOSE. Images are from the reference SPECT/CT time point measurement. In the case of the FP, it's important to look at the metastasis within the liver. In the case of the MP, it's important to notice water within the stomach.

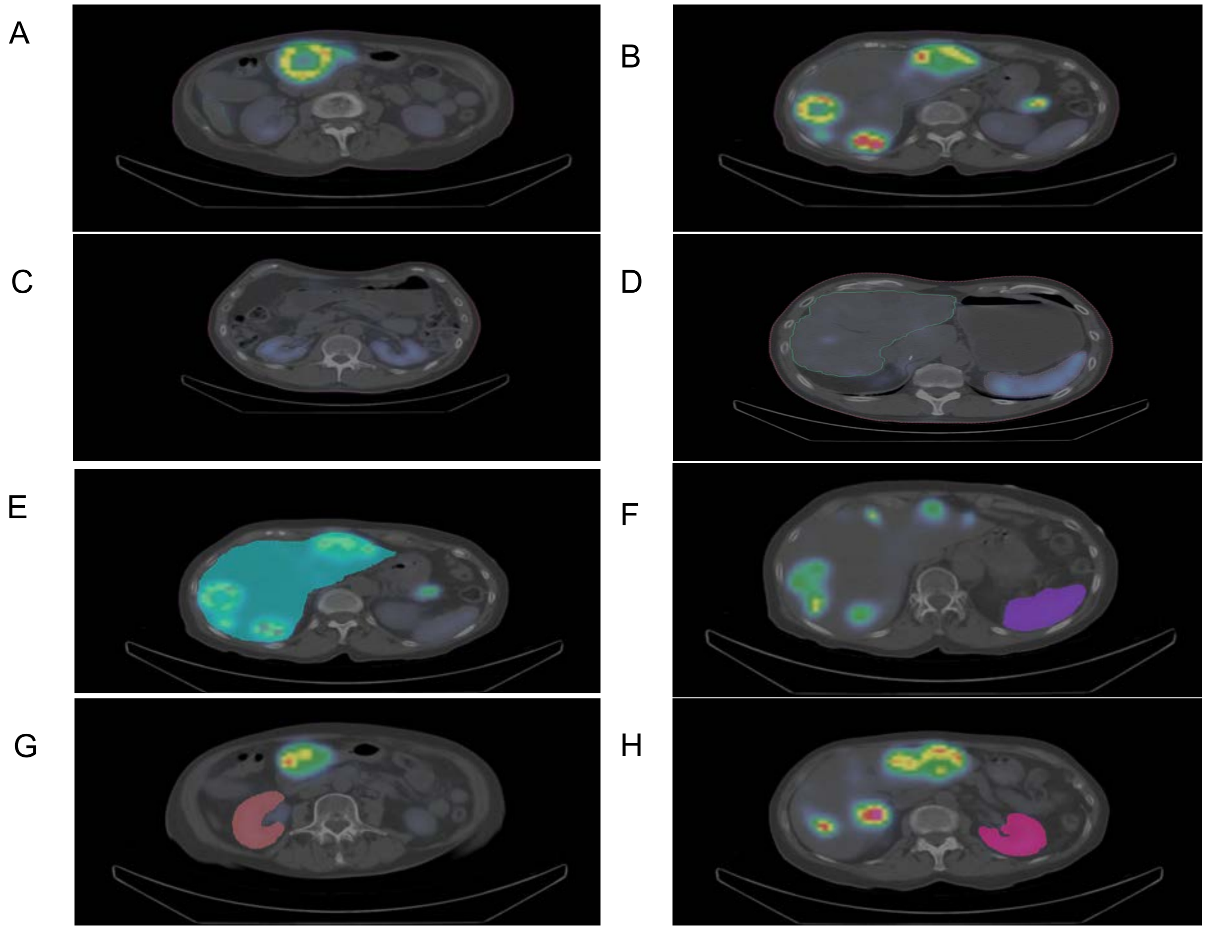

Figure 4.4: Axial slices showing segmented organs in the reference CT, using PDOSE workstation. A, B: female patient first treatment cycle, C, D: male patient first treatment cycle. For female patient E: liver, F: spleen, G: right kidney, H: left kidney. Own creation. Patient image provided by ICM nuclear medicine department.

Table 4.2 shows the obtained results for average residence time and average organ mass (± standard deviation) among all workstations.

Table 4.2. Results for average residence time (T) and average organ mass among all workstations.

Organ mass (g)	Treatment cycle for female patient First	Treatment cycle for female patient Second	Treatment cycle for male patient First	Treatment cycle for male patient Second
Liver	1624.8±43.6	1552.9±68.6	1338.8±87.9	1299.4±11.3
Spleen	105.9±6.0	106.5±7.8	243.2±8.7	251.6±7.8
Kidneys	273.7±3.8	275.4±15.1	437.0±44.0	442.3±41.8
Residence times (h)	**Treatment cycle for female patient First**	**Treatment cycle for female patient Second**	**Treatment cycle for male patient First**	**Treatment cycle for male patient Second**
Liver	42.9±3.2	23.7±1.8	2.7±0.6	3.0±0.3
Spleen	0.7±0.1	0.9±0.1	1.5±0.2	2.1±0.1
Kidneys	1.5±0.2	1.7±0.2	1.6±0.2	1.7±0.5

From table 4.2, among all workstations organ mass estimation varies less than 10% for all organs except for kidneys for MP. The relative standard deviation (standard deviation/mean) between organ mass obtained from different workstations is <6.7% for each cycle. On average equal to 5.0% (all results pooled). In the case of

MP the relative standard deviation for the kidneys, for both cycles of treatment is 10%. Detail results can be observed in the appendix of this chapter.

As a reference, for OLINDA/EXM V1.0 female and male models the liver mass is 1400g and 1910g, for spleen 150g and 183g, for kidneys 275g and 299g, respectively. For OLINDA/EXM V2.0 female and male models the liver mass is 1400g and 1800g, for spleen 130g and 150g, for kidneys 275.5g and 310g, respectively. For IDAC 2.1 female and male models the liver mass is 1810g and 2360g, for spleen 187g and 228g, for kidneys 357g and 422g, respectively.

Among all workstation, in the case of residence times, its standard deviation variation is less than 15% for all organs. In the case of spleen this variation tends to be higher than the other organs. In the case of the female patient, the average residence time for liver decreased by almost 50% from the first cycle to the second. The relative standard deviation between residence times obtained from different workstation is <17% for each cycle, and on average equal to 13.3% (all results pooled). However, in some situations the relative standard deviation can be quite high (i.e. MP, cycle 2 and kidneys: 31.5%), a variation largely induced by large discrepancies of the residence times obtained by STRATOS vs. the other possibilities.

Figures 4.5 and 4.6 show the residence times for female and male patients obtained using each workstation for liver, spleen and kidneys.

Regarding the S-values database for ^{177}Lu, for βeta, gamma emissions, for male and female models from OLINDA/EXM V1.0, OLINDA/EXM V2.0, for liver, spleen and kidneys, it can be seen that for the βeta emission the S-value is two orders of magnitude higher than the S-value for the gamma emission. Then, only results related to the βeta emissions are presented in the following sections. Spleen has the highest S-value value for all emissions for the two models.

All mean absorbed doses results are presented after organ mass correction (S-value mass scaling), expecting to have almost same results for both OLINDAs version, because S-values are almost the same after mass scaling.

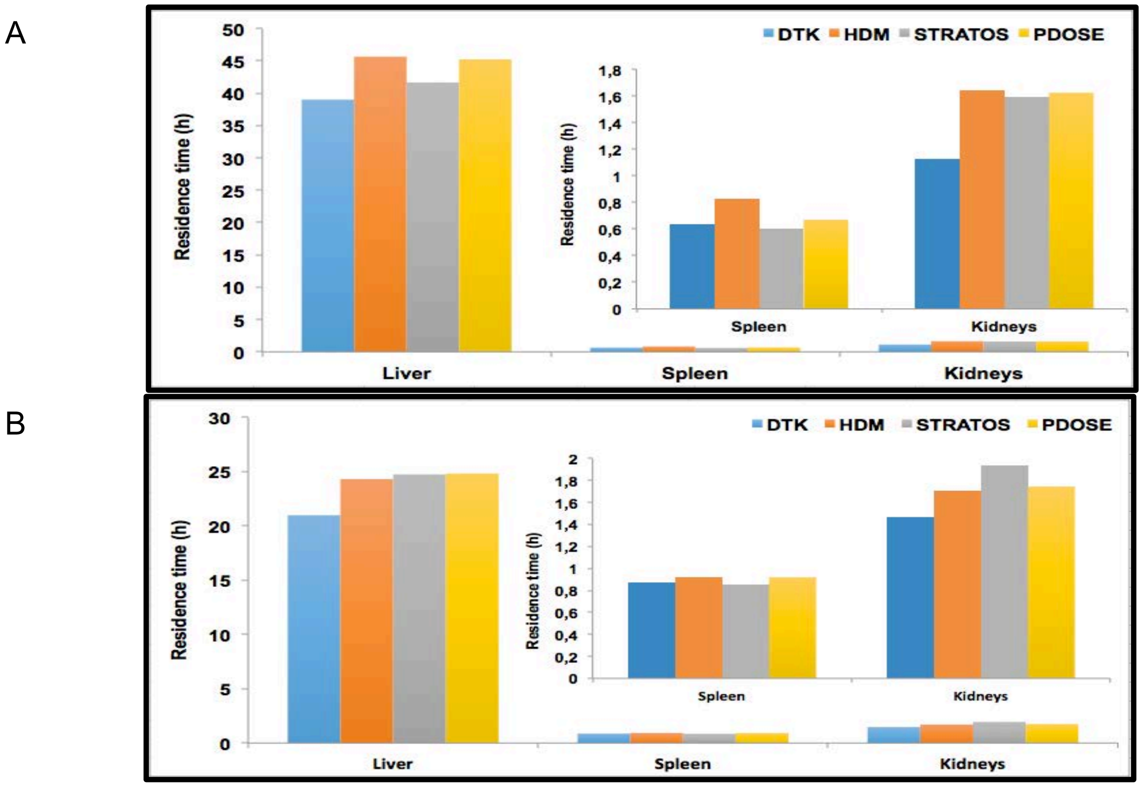

Figure 4.5: Residence times for liver, spleen and kidneys. Female patient, A: first treatment, B: second treatment. Own creation.

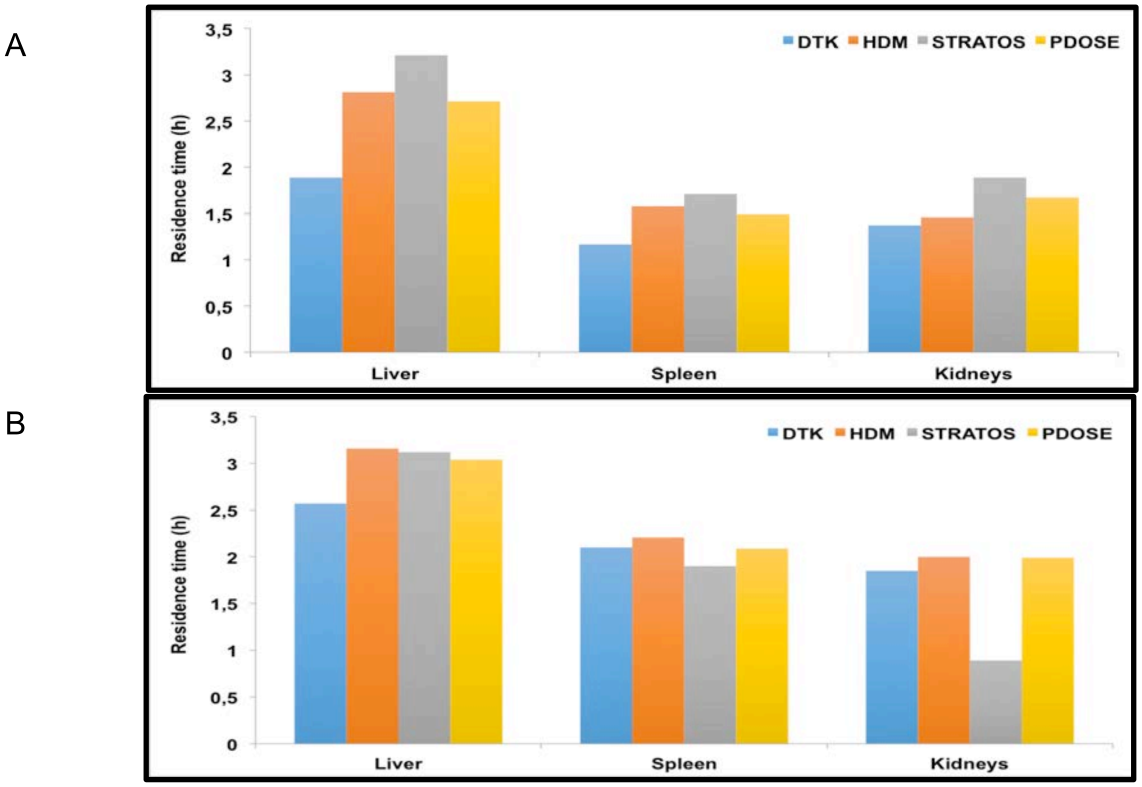

Figure 4.6: Residence times for liver, spleen and kidneys. Male patient, A: first treatment, B: second treatment. Own creation.

Mean absorbed doses obtained with the different workstations/software can be seen in figures 4.7 and 4.8, for female and male patients, for both treatment cycle. It can be seen that the results are in general quite close among software/workstations, at least in the same order of magnitude, despite the range of absorbed dose calculation solutions/algorithms. Also, the observed difference follows those observed in residence time (Figures 4.5 and 4.6).

Table 4.3 presents the mean absorbed doses obtained for the liver, spleen and kidneys and associated standard deviation. As compared to results from table 4.2, the relative standard deviation between residence times obtained from different workstation is <22.9% for each cycle, and on average equal to 16.7% (all results pooled). However, in some situations the relative standard deviation can be quite high (i.e. MP, cycle 2 and kidneys: 41.7%), a variation largely induced by large discrepancies of the residence times obtained by STRATOS vs. the other possibilities. Our mean absorbed dose results for kidneys are in the same order of magnitude to the ones reported by Sundlöv (Sundlöv et al., 2017), for the median renal absorbed dose = 4.5Gy/fraction, for 51 patients (199 treatment cycles).

Table 4.3. Results for mean absorbed dose (Gy) among all workstations.

Mean absorbed dose (Gy)	**Treatment cycle for female patient**		**Treatment cycle for male patient**	
	First	**Second**	**First**	**Second**
Liver	16.6±1.5	9.5±1.2	1.2±0.2	1.4±0.1
Spleen	3.8±0.5	4.9±0.6	4.0±0.8	5.3±0.9
Kidneys	3.3±0.6	3.8±0.5	2.3±0.4	2.3±1.0

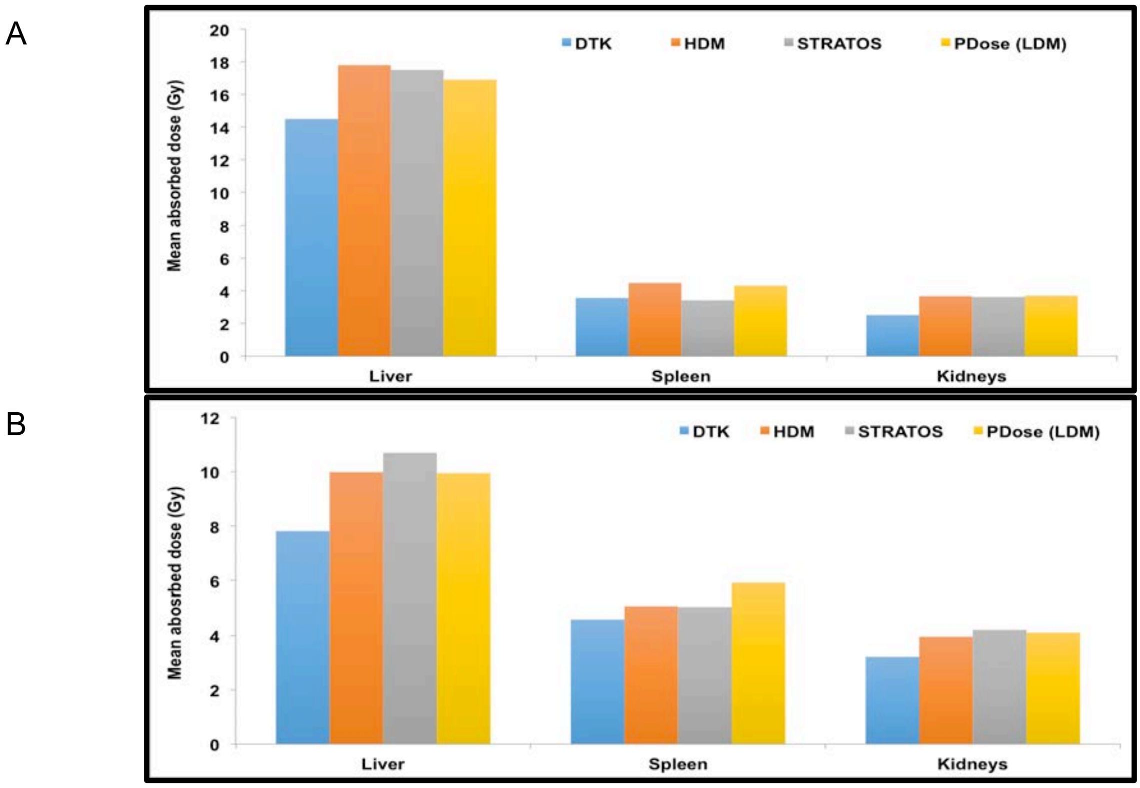

Figure 4.7: Mean absorbed dose results among all software for liver, spleen and kidneys. Female patient. A: first treatment, B: second treatment. Own creation.

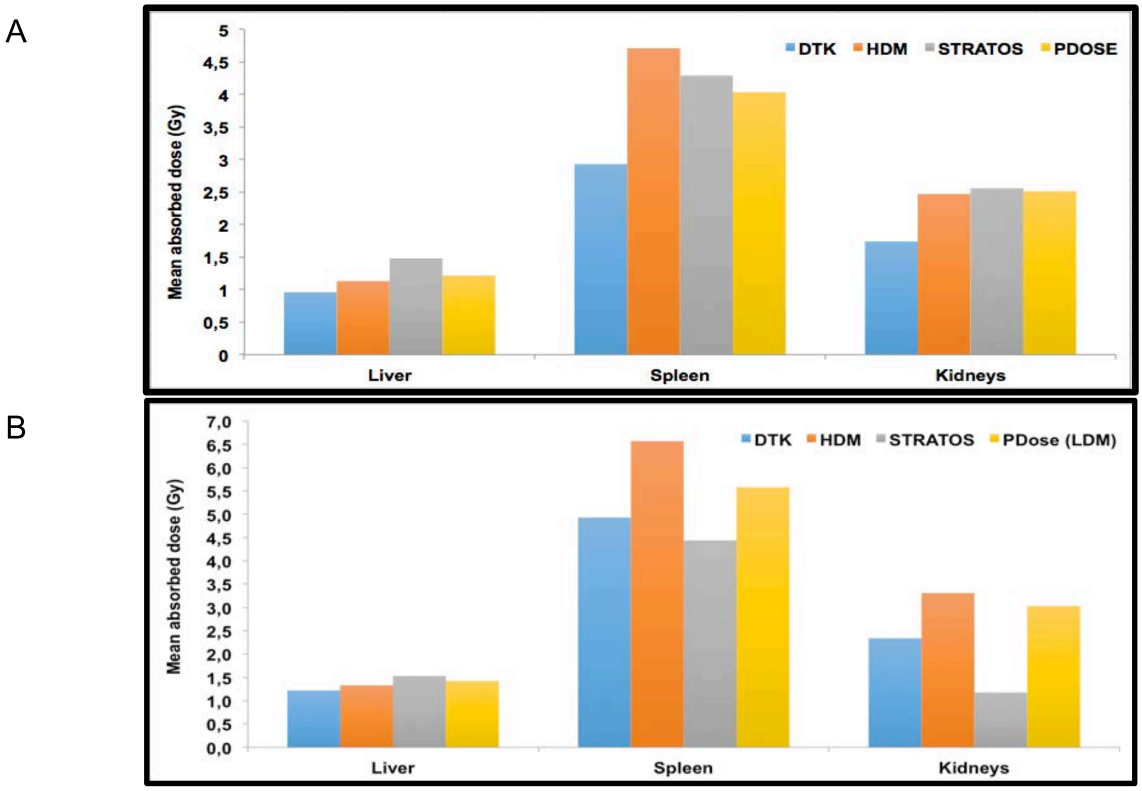

Figure 4.8: Mean absorbed dose results among all software for liver, spleen and kidneys. Male patient. A: first treatment, B: second treatment. Own creation.

3.1.1. Absorbed dose estimation for red bone marrow results

Table 4.4 shows the cumulated activities ratio between the two treatment cycles per patient. As it was described in the previous section, for both patients, in the second cycle of treatment the average absorbed dose was higher for the three organs, except for the liver, for female patient. The same effect can be seen for the red marrow and the remainder of the body.

Table 4.4. Cumulated activity ratio between treatment cycles (ctx), for organs source and RB, per patient.

Organs	**Female**	**Male**
$\tilde{A}_{Marrowctx2}/\tilde{A}_{Marrowctx1}$	1.14	1.38
$\tilde{A}_{R\_Bodyctx2}/\tilde{A}_{R\_Bodyctx1}$	1.12	1.18
Organs		
$\tilde{A}_{Liverctx2}/\tilde{A}_{Liverctx1}$	0.52	1.12
$\tilde{A}_{Kidneysctx2}/\tilde{A}_{Kidneysctx1}$	1.08	1.19
$\tilde{A}_{Spleenctx2}/\tilde{A}_{Spleenctx1}$	1.37	1.40

In table 4.5, mean absorbed dose results for the red bone marrow are presented, considered all contributions. Our results are similar to those presented by Forrer (Forrer et al., 2009). However, they used a different methodology for the same radiopharmaceutical. In the case of female patient, due to the high uptake of liver metastasis, the contribution to the red bone marrow due to all organs varies between 5 and 10%. In the case of male patient, this contribution is less than 2%. In the case of self-irradiation, for both patients, for the second treatment cycle this contribution increase slightly. The contribution from the remainder of the body to the red bone marrow is important, varies from 50 to almost 60% for both patients.

Table 4.5. Mean absorbed dose to RM and relative contributions from RM, organ sources (h) and RB.

Patient/cycle of treatment	D_{RM} *(mGy)*	*Relative contribution (%)**		
		$D_{RM\leftarrow RM}$	$D_{RM\leftarrow h}$	$D_{RM\leftarrow RB}$
Female/1st	475.6	34.0	9.3	56.2
Female/2nd	515.6	36.5	5.1	58.4
Male/1st	321.7	45.0	1.6	53.5
Male/2nd	409.1	49.2	1.5	49.3

*Similar results reported by Forrer (Forrer et al., 2009) in terms of relative contributions.

4. Discussion

One of the main challenges was to find a common parameter in order to be able to compare dosimetric results obtained from all workstations, since all of them have differences in the workflows. Each phase of the dosimetric workflow is a key factor that is going to affect the final result. Each step had been subject of multiple studies for several years and there are not meanings for assessing their performance along the dosimetric chain. Each workstation provides different acquisition protocols that could be applied for clinical dosimetry. Having available 2D and 3D protocols could allow the user to correlate results depending on the studied organ. A drawback to implement this idea, is the final acquisition time, due to the clinical condition of some patients this is not an easy task.

Having ways to assess the performance of each section of the dosimetric workflow, allow the user to clearly understand their connections and functioning; then, to try to estimate the uncertainties and to propagate them to the final result, as it is suggested by Gear (Gear et al., 2018). Unfortunately, none of the workstations evaluated provides this service, some of them provide tools to evaluate certain aspects, but none propose how to consider the uncertainties propagation.

Residence time was one common aspect found among these workstations that can be compared as a final output of the dosimetric workflow, nevertheless, organ masses and mean absorbed doses were indexes for comparison.

Therefore, in this section of the discussion aspects related to the comparison among the workstations are presented, them, further below, other features are considered for bone marrow dosimetry or the comparison of mean absorbed doses from different algorithms.

4.1.1.Segmentation

The final output of the segmentation process is the generation of a VOI, in which the organ mass can be associated. Using this parameter, the performance of the operators between the CRCT and the ICM was initially evaluated. In table 4.2 the organ masses were very close for the same patient data sets. We were interested in large organs to try to benchmark the evaluation among all workstations. Tumors and other small organs are more difficult to segment; then comparison could be more difficult.

In three workstations manual segmentation (slice by slice) was carried out and in one workstation an automatic segmentation tool was used. Manual segmentation is user-dependent process (Mortensen et al., 2014) and should be validated. The segmentation of several structures occurred using the first SPECT/CT as a reference. Copying segmented structures, from the reference SPECT/CT to other SPECT/CT (also so-called propagation of the VOI), the propagation of the structure occurred.

In this study we did not address the segmentation process itself, we were using the segmentation tools available in each workstation. The ideal situation would be to have patient data sets already segmented, in order to be uploaded in each workstation (for instance in DICOM RTStruct). However, this option was only available with PDOSE.

The structure propagation process has a strong dependence on the registration stage. If there are errors in the registration procedure, the placement of the structure will change or may not fit from one time-point SPECT/CT to another. HDM and PDOSE allow moving or modifying the size of the propagated structure. In our study displacement of structures occurred, but the size of the propagated structure remains constant. The idea was to keep constant the organ volume along the time-line to decrease the impact of the operator-dependence.

An idea that will be consider as a future work is to vary the organ volume at each time point measurement, then, to estimate the residence time.

4.1.2. Registration

The registration process normally is carried out using the CT reconstructed image within the whole nuclear medicine field of view image (FOV). Rigid registration is available in most of workstations and it is the first proposed method to be performed. Nonetheless, some workstations also provide elastic/deformable registration. The rigid registration was performed taking as a reference bone structures within the patient, but this does not consider aspects such as variation in the positioning of the patient in a multi-SPECT/CT scenario, movement of the patient between CT and SPECT acquisitions, respiratory motion, patient tilt and organs movements (due to respiratory motion or different placement). Looking at figure 4.4 (C, D), liquid can be seen in the stomach of the male patient, changing the position of the spleen and left kidney, comparing to other SPECT/CT time point measurements when the stomach was empty. All these aspects are sources of error, which negatively affect the registration process, therefore the accuracy of the image registration must be assessed and verified (Isambert, et al., 2008). Unfortunately, for the majority of the workstations, the user can assess this process visually. However, Dosisoft, proposed a method to optimize the registration process organ by organ, which might impact positively on the final result.

Grassi et al. (Grassi et al., 2018) compare the rigid registration using the Siemens E-Soft workstation versus the deformable registration using Velocity (from Varian), in order to assess their impact on absorbed dose calculations. They applied the deformable registration to the whole image. They compared both registrations techniques by using the structural similarity index (SSIM) implemented in MATLAB. Finally, the registered images were uploaded into Raydose for absorbed dose estimations. Although they found mean absorbed doses by deformable registration higher than those estimated by rigid registration, the effect of the image registration algorithm might be negligible for relatively large segmented structures.

Looking at the different tools used in radiotherapy to ensure the positioning of the patient during all sessions of therapy, one possible solution is to use the commercially available “Vac-lock” or similar devices, in which the patient can rest comfortably and the position of the patient on the table and its position on the SPECT/CT will be the same at all times. These devices must be evaluated prior to clinical implementation in Nuclear Medicine departments in order to evaluate their impact on images. Gosewisch et al. (Gosewisch et al., 2018) showed the impact of some patient movements on the absorbed dose estimations and techniques of correction to improve the final quantification. Finally, the effect of continuous respiratory motion on kidneys or other organs within the pelvic region, could be studied to understand its impact on NM SPECT images.

4.1.3. Time activity curve fitting and residence time determination

Every workstation provides fitting models, for instance, the trapezoidal method and/or mono- or bi-exponential. Some of them consider the time between t = 0 and the first data point. Few options are available to the user to choose the best possible fitting. Most of the software considers mono-exponential decay after last time point measurement, which might be a “safe” overestimation in the cumulated activity estimation. Most of the software computed cumulated activity based-on organ approaches and only STRATOS is clinical validated for voxel-based cumulated activity estimations. PDOSE has a platform to perform this type of calculations but it was not clinical validated at the time of performing this study. In the case of STRATOS its results are close to the other software, for the majority of the organs, this was not expected, due to the behavior showed in the software validation section. Most probably the variations in organ patient position, from one time point to another, are compensated with counts from one organ into another one. Also for the same software, the fitting is performed by segments, using the trapezoid method and according to Guerriero et al. (Guerriero et al., 2013) an overestimation of time-integrated activities has been observed compared to those generated by bi-exponentials. However, from our few results, we have not observed the same effect on residence time results.

In the case of DTK only mono-exponential fitting can be done. In the case of HDM, we applied bi-exponential fitting in almost most of the cases (for first treatment cycle of the male patient, mono-exponential fitting for kidneys). In the case of PDOSE, in order to assess the degree-of-goodness of the fitting, the Spearman coefficient was used for mono- or bi-exponential fitting, but sometimes best fitting was for a function such as $f(t) = A * t^{b} * e^{-c*t^{d}}$. From these results comparison between workstations, only considering time activity curve fit, is practically impossible, because applying same fitting among all workstations, will also have an impact on cumulated activity. NUKFIT (Kletting et al., 2013), is a software that it is interesting to compare with, therefore further investigation is planning using it.

4.1.4. Absorbed dose calculation

To estimate the mean absorbed dose (last section of dosimetric workflow) and following the MIRD formalism (Bolch, et al., 2009), two quantities are necessary, the cumulated activity (or the residence time) and the S-value. Until this point in the discussion, aspects related to the determination of the cumulated activity have been considered. For the second part of the equation, few aspects have to be considered in the case of reference dosimetry (because most of them have been discussed in chapter 2). In our study by using OLINDA/EXM V1.0 and V2.0 and considering patient organ mass adjustment, we can perform reference-adjusted dosimetry.

As it was previously mentioned, in the case of ^{177}Lu, the S-value associate to the βeta emission has a higher impact to the mean absorbed dose, up to two orders of magnitude higher than S-value associated to gamma emission.

For same organ and model (male or female), S-values will change depending on the OLINDA version, this is due to the calculation of the Specific Absorbed Fractions (SAF) available in the two OLINDA/EXM versions. In version V1.0, for photons, SAF's were estimated from the Cristy and Eckerman phantom series, developed in the Oak Ridge National Laboratory (ORNL) (Cristy & Eckerman, 1987). In version V2.0 models were based-on non-uniform rational B-splines (NURBS), with organ and body masses based on the references values from ICRP-89, and SAF's were estimated using GEANT4 (Stabin, et al., 2008). The geometry of each organ and phantom has changed importantly since 1987 with the Cristy and Eckerman phantom series. Consequently, anatomical differences in organs-shapes and organs-positions between the models may be one of the reasons to have these slightly differences in SAF values, as it has been shown by Ocampo et al. (Ocampo, et al., 2013). Moreover, the adjustment of organ mass from the model to patient has a relation with the emission, as we have previously talked in chapter 2.

In the case of the spleen for both patients, the standard deviation associated to the mean absorbed dose vary for each cycle of treatment. For this organ, the registration process was very difficult because at each time point measurement its position and organ size could change. Then for this organ it could be very helpful to consider the variation of organ mass per time point measurement, in order to estimate the residence time.

For most of the organs, the mean absorbed doses computed are comparable and in the same order of magnitude among all workstations. Further studies will take place considering voxel-based cumulated activity calculations (at least for STRATOS and possibly for PDOSE). Then, absorbed dose volume histograms could be studies to see its variation within the VOI.

The LDM from PDOSE considers β-particles as non-penetrating radiation (Pasciak, et al., 2014), then all energy deposition is with the voxel. Moreover, results from the two versions of OLINDA/EXM are close to each other. For most of the organs these results from both versions of OLINDA are close to the LDM from PDOSE. Therefore, both methods are comparable. Also because of the emission properties of ^{177}Lu, in which β-emissions are more important, the approach implemented in PDOSE could be a good approximation for the estimation of the mean absorbed dose.

In the case of mean absorbed doses from STRATOS, results are close to the others software (especially to those from PDOSE) for the majority of the organs, corresponding with the results from the residences times. Just in the case of the kidneys for male patient discrepancies can be seen. This software also considers that the irradiated volume was a uniform propagating medium. Also, the pre-calculated DVK was estimated in water and most probably its gamma contribution is lower compared to the βeta contribution.

Further improve/investigation can be done, if variation of organ mass is considered for the LDM implemented in PDOSE.

4.1.5. Absorbed dose estimation for red bone marrow

Following EANM recommendations (Hindorf, et al., 2010) for the estimation of absorbed dose to this organ, the cross- and the self- irradiation were considered. The cross-irradiation due to the whole body was challenging because in the clinical protocol no whole-body measurements were carried out. Our new proposed method allows estimating this contribution having measurement from the Whole-FOV. Some underestimations can occur if there are other uptake sources out of this region. Moreover, our approximation assumes a similar volume/mass between the patient and the reference model. This may not happen for some patients, then other phantom models available in the literature can be used to find the best approximation to the patient.

On the other hand, no PVE corrections were considered to correct the cumulated activity from the VOI generate within the vertebras, because the three vertebras were considered as one whole entity, with volumes varying from 50 ml to 70 ml for the female and male patient, respectively. One possible idea to improve further our results is to estimate the volume of each vertebra, then apply the appropriate recovery coefficient, to each vertebra, to correct the cumulated activity for this effect.

Our approximation allows reducing the patient time in the department and further inconvenient to the patient, for instance, when blood samples are taken. Also, this approximation has to be validated with more patients and possible considering blood samples. Beykan et al. (Beykan et al., 2018) showed dosimetric results variations between blood-based vs image-based dosimetry for this type of treatment, three times lower for the blood-based, however this has to be validated in more patients.

5. Conclusions

The dosimetric chain has been assessed on commercial workstations finding similar results, in terms of organ mass, residence times and mean absorbed doses, for patient data sets. The variations in residence times are in the same order of magnitude, regardless of the different processing modes in each section of the dosimetric chain.

On patient data, organ placement varies in al multi-SPECT/CT scenario, especially in the abdominal/thoracic regions, where the rigid-registration cannot perform adequately. Nonetheless, a promising tool to carry out this type of registration can be based-on organ approaches, this might be important to take into account patient movements between sequential studies, poor patient positioning, patient tilt (especially in the pelvic region) and movement of an organ from one day to another. In general, the segmentation tools provided by the different workstations are good enough for this type of dosimetry.

Options in terms of fitting are reduced for most of the workstations and it is generally not possible to perform an assessment of the goodness of the fitting.

None of the workstations incorporate uncertainty analysis in each section of the dosimetric chain, so it is impossible to provide a mean absorbed dose results including term.

On the other hand, we managed to see that the variations in terms of the calculation of the mean absorbed dose either using S values or using other approaches, in all cases generating results in the same order of magnitude.

From our point of view, the assessed workstations are lacking of some phases/sections:

- Diversity in processing clinical data, just two workstations allow to process 2D data and 3D patient data.
- Some platforms do not allow import/export patient data in DICOM RTStruct format.
- There is no possibility to incorporate the calibration data set from one gamma camera and to bind this data to a particular patient.
- There is no possibility to incorporate information about the “QC” regarding the sensibility stability of the SPECT/CT.
- There are no possibilities to have a “QC” assessment of patient data sets, to confirm if all-important DICOM tags (all important parameter) were acquire/process equally. For instance, acquisition time, number of projections, energy windows width and its positioning, radionuclide, reconstruction method, etc.
- There is no possibility to incorporate information regarding the recovery coefficient curve, to correct for PVE the VOI’s cumulated activity and/or mean absorbed dose.
- Few workstations allow the user to evaluate retrospectively the processing performed in each section of the dosimetric workflow.

- Uncertainty analysis must be included for each section of the dosimetry workflow.
- Few platforms provide the possibility to assess mean absorbed dose (or residence times) based-on organ mass variation.

Some of the previous points can be addressed in further evaluations that we are planning to develop as a future work.

In terms of red bone marrow mean absorbed dose, a method for calculating this parameter without having whole-body information has been proposed. Further evaluations can be carry-out to confirm our initial results. Moreover, comparison between image-based approaches and blood-based should be perform in a cohort of patients in targeted radionuclide therapy.

One possibility to study organ movements, for instance, due to respiratory motion, can be considering the possibility to incorporate 3D dynamic studies, but this is really depending on manufacturers interest.

As a future work we would like to assess the impact on residence time estimation due to different registrations to the same organ, performed by the same user or by different users. Also, to compare results from different fittings against NUKFIT.

Indeed, in this field of the nuclear medicine, optimization in several aspects can be considered in order to standardized the different sections of the dosimetric workflow, in this way, traceability of patient data can be processed allowing the user improve in patient-specific dosimetry.

6. References of the chapter

Bailey, D. L., et al. (2015). In vivo quantification of 177Lu with planar whole-body and SPECT/CT gamma camera imaging. *EJNMMI Physics*, *2*(1), 20.

Beauregard, J. M., et al. (2011). Quantitative 177Lu SPECT (QSPECT) imaging using a commercially available SPECT/CT system. *Cancer Imaging*, *11*, 56–66.

Bergsma, H., et al. (2016). Subacute haematotoxicity after PRRT with 177Lu-DOTA-octreotate: prognostic factors, incidence and course. *Eur J Nucl Med Mol Imaging*, *43*(3), 453–463.

Beykan, S., et al. (2018). Patient-specific dosimetry of 177Lu-DOTATATE peptide receptor therapy with high activities. *Eur J Nucl Med Mol Imaging*, *45*(Suppl 1), S33.

Bodei, L., et al. (2011). Peptide receptor radionuclide therapy with 177Lu-DOTATATE: The IEO phase I-II study. *Eur J Nucl Med Mol Imaging*, *38*(12), 2125–2135.

Bolch, W. E., et al. (2009). MIRD pamphlet No. 21: a generalized schema for radiopharmaceutical dosimetry--standardization of nomenclature. *J Nucl Med*, *50*(21), 477–484.

Brolin, G., et al. (2015). Pharmacokinetic digital phantoms for accuracy assessment of image-based dosimetry in (177)Lu-DOTATATE peptide receptor radionuclide therapy. *Phys Med Biol*, *60*(15), 6131–49.

Chiavassa, S., et al. (2006). Validation of a personalized dosimetric evaluation tool (Oedipe) for targeted radiotherapy based on the Monte Carlo MCNPX code. *Phys Med Biol*, *51*(3), 601–616.

Chiesa, C., et al. (2017). The conflict between treatment optimization and registration of radiopharmaceuticals with fixed activity posology in oncological nuclear medicine therapy Formalization of the optimization principle in the new European Council Directive 2013/59. *Eur J Nucl Med Mol Imaging*, 44(11), 1783-1786

Clairand, I., et al. (1999). DOSE3D: EGS4 Monte Carlo code-based software for internal radionuclide dosimetry. *J Nucl Med*, *40*(9), 1517–1523.

Cremonesi, M., et al. (2006). Dosimetry in Peptide radionuclide receptor therapy: a review. *J Nucl Med*, *47*(9), 1467–75.

Cristy, M., Eckerman, K. F. (1987). *Specific Adsorbed Fractions of Energy at Various Ages From Internal Photon Sources*. *TN: Oak Ridge National Laboratory. Ornl/Tm-8381 V1-V7*.

Ferrer, L., et al. (2010). Three methods assessing red marrow dosimetry in lymphoma patients treated with radioimmunotherapy. *Cancer*, *116*(SUPPL. 4), 1093–1100.

Flux, G. D., et al. (2017). From fixed activities to personalized treatments in radionuclide therapy: lost in translation? *Eur J Nucl Med Mol Imaging*, 12–14.

Forrer, F., et al. (2009). Bone marrow dosimetry in peptide receptor radionuclide therapy with [177Lu-DOTA0,Tyr3]octreotate. *Eur J Nucl Med Mol Imaging*, *36*(7), 1138–1146.

Gardin, I., et al. (2003). Voxeldose: A Computer Program for 3-D Dose Calculation in

Therapeutic Nuclear Medicine. *Cancer Bioth Radiopharm*, *18*(1), 109–115.

Garkavij, M., et al. 177Lu-[DOTA0,Tyr3] Octreotate therapy in patients with disseminated neuroendocrine tumors: Analysis of dosimetry with impact on future therapeutic strategy. *Cancer*, *116*(Supple 4), 1084–1092.

Garske-Román, U., et al. (2018). Prospective observational study of 177Lu-DOTA-octreotate therapy in 200 patients with advanced metastasized neuroendocrine tumours (NETs): feasibility and impact of a dosimetry-guided study protocol on outcome and toxicity. *Eur J Nucl Med Mol Imaging*, *45*(6), 970–988.

Gear, J. I., et al. (2018). EANM practical guidance on uncertainty analysis for molecular radiotherapy absorbed dose calculations. *Eur J Nucl Med Mol Imaging*, *45*, 2456–2474.

Giammarile, F., et al. (2017). Dosimetry in clinical radionuclide therapy: the devil is in the detail. *Eur J Nucl Med Mol Imaging*, 3–5.

Gosewisch, A., et al. (2018). Investigation of the effect of patient motion onto 3D dose estimates in Lu-177-PSMA therapy using Siemens xSPECT Quant reconstruction with integrated motion correction and dosimetry research tool. *Eur J Nucl Med Mol Imaging*, *45*(Suppl 1), S113.

Gosewisch, A., et al. (2018). Patient-specific image-based bone marrow Octreotate in Lu-177-DOTA,Try3-Octreotate and Lu-177-DKFZ-PSMA-617 therapy : investigation of a new hybrid image approach. *EJNMMI Research*, *8*, 76.

Grassi, E., et al. (2018). Effect of image registration on 3D absorbed dose calculations in177Lu-DOTATOC peptide receptor radionuclide therapy. *Phys Medica*, *45*, 177–185.

Guerriero, F., et al. (2013). Kidney dosimetry in 177Lu and 90Y peptide receptor radionuclide therapy: Influence of image timing, time-activity integration method, and risk factors. *BioMed Res Int.*, *2013*, 1–12.

Guy, M. J., et al. (2003). RMDP: A Dedicated Package For ^{131} I SPECT Quantification, Registration and Patient-Specific Dosimetry. *Cancer Bioth Radiopharm*, *18*(1), 61–69.

Hänscheid, H., et al. (2018). Dose Mapping after Endoradiotherapy with 177Lu-DOTATATE/-TOC by One Single Measurement after Four Days. *J Nucl Med*, *59*, 75–81.

Hindorf, C., et al. (2010). EANM dosimetry committee guidelines for bone marrow and whole-body dosimetry. *Eur J Nucl Med Mol Imaging*, *37*(6), 1238–1250.

Hippeläinen, E., et al. (2016). Quantitative accuracy of 177Lu SPECT reconstruction using different compensation methods: phantom and patient studies. *EJNMMI Research*, *6*, 16.

Ilan, E., et al. (2015). Dose response of pancreatic neuroendocrine tumors treated with peptide receptor radionuclide therapy using 177Lu-DOTATATE. *J Nucl Med*, *56*(2), 177–182.

Isambert, A., et al. (2008). A phantom study of the accuracy of CT, MR and PET image registrations with a block matching-based algorithm. *Cancer/Radiotherapie*, *12*(8), 800–808.

Jan, S. et al. (2004). GATE - Geant4 Application for Tomographic Emission: a simulation toolkit for PET and SPECT. *Phys Med Biol*, *49*(19), 4543–4561.

Johnson, T. K., et al. (1999). MABDOSE. I: Characterization of a general purpose dose estimation code. *Med Phys*, *26*(7), 1389–1395.

Kangasmaa, T. S., et al. (2016). Multicenter evaluation of single-photon emission computed tomography quantification with third-party reconstruction software. *Nucl Med Commun*, *37*(9), 983–987.

Kashyap, R., et al. (2014). Favourable outcomes of 177Lu-octreotate peptide receptor chemoradionuclide therapy in patients with FDG-avid neuroendocrine tumours. *Eur J Nucl Med Mol Imaging*, *42*(2), 176–185.

Kletting, P., et al. (2013). Molecular radiotherapy: the NUKFIT software for calculating the time-integrated activity coefficient. *Med Phys*, *40*(10), 102504-1-102504–9.

Kletting, P., et al. (2015). The NUKDOS software for treatment planning in molecular radiotherapy. *Zeitschrift Fur Medizinische Physik*, *25*(3), 264–274.

Kost, S. D., et al. (2015). VIDA: A Voxel-Based Dosimetry Method for Targeted Radionuclide Therapy Using Geant4. *Cancer Bioth Radiopharm*, *30*(1), 16–26.

Lehmann, J., et al. (2005). Monte Carlo treatment planning for molecular targeted radiotherapy within the MINERVA system. *Phys Med Biol*, *50*(5), 947–958.

Ljungberg, M., et al. (2016). MIRD Pamphlet No. 26: Joint EANM/MIRD Guidelines for Quantitative 177Lu SPECT Applied for Dosimetry of Radiopharmaceutical Therapy. *J Nucl Med*, *57*, 151–162.

Marcatili, S., et al. (2013). Development and validation of RAYDOSE: A Geant4-based application for molecular radiotherapy. *Phys Med Biol*, *58*(8), 2491–2508.

Marcatili, S., et al. (2015). Model-based versus specific dosimetry in diagnostic context: Comparison of three dosimetric approaches. *Med Phys*, *42*(3), 1288–1296.

McKay, E. (2003). A software tool for specifying voxel models for dosimetry estimation. *Cancer Bioth Radiopharm*, *18*(3), 379–92.

Mirzaei, S., et al. (2013). Easy-to-Use Online Software Package for Internal Dose Assessment After Radionuclide Treatment in Clinical Routine. *Clin Nucl Med*, *38*(9), 686–690.

Mortensen, N., et al. (2014). Inter-operator variability in manual image segmentation and its impact on the renal absorbed dose and biologically effective dose in 177Lu-Dotatate therapy. *Eur J Nucl Med Mol Imaging*, 41, S259–S259.

Ocampo, J. C., et al. (2013). Evaluation of specific absorbed fractions from internal photon sources in the ICRP reference male phantom. *Radiation Protection Dosimetry*, *157*(1), 133–141.

Pacilio, M., et al. (2014). Improving the dose-myelotoxicity correlation in radiometabolic therapy of bone metastases with 153Sm-EDTMP. *Eur J Nucl Med Mol Imaging*, *41*(2), 238–252.

Pasciak, A. S., et al. (2014). A Comparison of Techniques for 90Y PET/CT Image-Based Dosimetry Following Radioembolization with Resin Microspheres. *Frontiers in Oncology*, *4*(May), 1–10.

Prideaux, A. R., et al. (2007). Three-Dimensional Radiobiologic Dosimetry:

Application of Radiobiologic Modeling to Patient-Specific 3-Dimensional Imaging-Based Internal Dosimetry. *J Nucl Med*, *48*(6), 1008–1016.

Sanders, J. C., et al. (2015). Quantitative SPECT/CT Imaging of 177Lu with In Vivo Validation in Patients Undergoing Peptide Receptor Radionuclide Therapy. *Mol Imaging Biol*, *17*(4), 585–593.

Sandström, M., et al. (2010). Individualized dosimetry in patients undergoing therapy with 177Lu-DOTA-D-Phe1-Tyr3-octreotate. *Eur J Nucl Med Mol Imaging*, *37*(2), 212–225.

Schuchardt, C., et al. (2013). Dosimetry in Targeted Radionuclide Therapy : The Bad Berka Dose Protocol — Practical Experience. *Journal of Postgraduate Medicine, Education and Research*, *47*(March), 65–73.

Sgouros, G., et al. (2004). Patient-specific dosimetry for 131I thyroid cancer therapy using 124I PET and 3-dimensional-internal dosimetry (3D-ID) software. *J Nucl Med*, *45*(8), 1366–1372.

Shen, S., et al. (2002). Improved prediction of myelotoxicity using a patient-specific imaging dose estimate for non-marrow-targeting (90)Y-antibody therapy. *J Nucl Med*, *43*(9), 1245–1253.

Sjögreen, K., et al. (2005). The LundADose method for planar image activity quantification and absorbed-dose assessment in radionuclide therapy. *Cancer Bioth Radiopharm*, *20*(1), 92–7.

Sohlberg, A., et al. (2008). Acceleration of Monte Carlo-based scatter compensation for cardiac SPECT. *Phys Med Biol*, *53*(14), N277–N285.

Stabin, M., et al. (2008). ICRP-89 based adult and pediatric phantom series. *J Nucl Med*, *49*(supplement 1), 14P–14P.

Strosberg, J., et al. (2017). Phase 3 Trial of ^{177} Lu-Dotatate for Midgut Neuroendocrine Tumors. *New England Journal of Medicine*, *376*(2), 125–135.

Sundlöv, A., et al. (2017). Individualised 177Lu-DOTATATE treatment of neuroendocrine tumours based on kidney dosimetry. *Eur J Nucl Med Mol Imaging*, *44*(9), 1480–1489.

Svensson, J., et al. (2016). A novel planar image-based method for bone marrow dosimetry in 177Lu-DOTATATE treatment correlates with haematological toxicity. *EJNMMI Physics*, *3*(1), 21.

Tagesson, M., et al. (1996). A Monte Carlo program converting activity distributions to absorbed dose distributions in a radionuclide treatment planning system. *Acta Oncologica*, *35*(3), 367–372.

Traino, A. C., et al. (2007). Influence of total-body mass on the scaling of S-factors for patient-specific, blood-based red-marrow dosimetry. *Phys Med Biol*, *52*(17), 5231–48.

Valkema, R., et al. (2005). Long-term follow-up of renal function after peptide receptor radiation therapy with (90)Y-DOTA(0),Tyr(3)-octreotide and (177)Lu-DOTA(0), Tyr(3)-octreotate. *J Nucl Med*, *46 Suppl 1*, 83S–91S.

Woodard, H. Q. (1984). The relation of weight of haematopoietic marrow to body weight. *British Journal of Radiology*, *57*(October), 903–907.

Conclusion générale et perspectives futures (FR)

Dans le cadre de ce travail de doctorat, la formulation MIRD a été analysée. Cette formulation peut être exprimée, dans sa forme la plus simple, par trois variables : La dose absorbée, l'activité cumulée et la valeur S.

Chacune de ces variables pourrait être étudiée d'un point de vue préclinique et clinique. Dans chacun de ces deux domaines, il a été possible de comprendre le degré de complexité impliqué dans la détermination et l'utilisation de chacune d'elles.

Dans le deuxième chapitre de ce travail, l'estimation des doses absorbées et efficaces, qui peuvent être utilisées comme référence chez l'homme, a été réalisée, pour trois nouveaux produits radiopharmaceutiques, à partir de données au niveau préclinique. Dans ce cas, le calcul de l'activité cumulée a impliqué un défi particulier en fonction du type d'informations qui nous a été fourni.

Par exemple, dans le cas du médicament radiopharmaceutique (MRP) étudié par imagerie TEP/TDM, huit volumes d'intérêt ont été étudiés, chacun avec 16 points de mesure, ce qui a permis de générer des courbes d'activité-temps permettant d'identifier avec une certaine facilité et pour certains organes, les phases de captation et d'excrétion. Pour plusieurs organes, il a été possible d'établir un modèle biocinétique décrivant ces deux phases, mais pour d'autres, et malgré un bon nombre de points de mesure, il n'a pas été possible d'établir un tel modèle. Dans ces cas, la méthode des trapèzes a été choisie. Cette méthode peut être considérée comme une méthode conservatrice puisqu'elle peut surestimer les activités cumulées au moment de l'intégration de la courbe activité-temps.

Dans le cas des MRP pour lesquels on a utilisé la dissection d'organes, le nombre de points de mesure a été réduit, à trois ou quatre points, en raison du nombre d'animaux sacrifiés. Dans cette situation expérimentale, la méthode des trapèzes était préférable, car il n'y avait aucune possibilité d'établir un modèle biocinétique pour les organes à l'étude. On peut donc s'attendre à une surestimation des activités cumulées au moment de l'intégration de la courbe activité-temps. Pour ces deux cas, le nombre de volumes d'intérêts utilisés était de 13 et 14, si l'on considère les organes qui sont des moyens d'excrétion. Pour l'un des MRP, une étude a été développée considérant la vidange de l'urine présente dans la vessie. La même étude a montré d'importantes différences dans les résultats de dose absorbée lorsque cette considération n'était pas prise en compte. De ce point de vue, il a été montré que la prise en compte des activités cumulées provenant des organes qui sont des voies d'excrétion des MRP permet d’estimer les doses absorbées reçues par les organes environnants.

Dans le cas de ces deux produits radiopharmaceutiques, aucun facteur d'étalonnage du détecteur n'a été utilisé pour effectuer les mesures des organes à l'étude. Donc une méthodologie a été mise au point pour estimer le comptage total des coups dans tous les organes et l'activité totale injectée.

D'autre part, l'extrapolation des résultats précliniques à l'humain a été réalisée par pondération des masses des organes entre les deux espèces et cette méthode peut créer des erreurs dans les temps de résidence, donc dans le calcul des doses absorbées et efficaces entre animaux et êtres humains. Cette méthode permet d'augmenter ou de diminuer significativement les valeurs de temps de résidence.

En ce qui concerne l'utilisation de la valeur S fournie par plusieurs logiciels, on a pu constater que les différences sont principalement associées aux modèles anthropomorphiques et aux codes Monte-Carlo. Dans le cas des modèles anthropomorphiques, on constate des différences dans la position, les dimensions, la masse, le volume et la densité des organes. En outre, il a été possible de voir des différences entre les modèles en tant que tels, allant des modèles stylisés (qui ne reflètent pas l'anatomie des hommes et des femmes) aux modèles voxelizés (qui se rapprochent beaucoup de l'anatomie humaine). Dans le cas des codes Monte-Carlo, les différences peuvent être associées à l'interaction des particules chargées et non chargées avec la matière, c'est-à-dire les gammes d'énergie associées à ces particules, les spectres énergétiques utilisés, la manière dont ils ont été générés, etc. Cependant, il faut s'attendre à ce que dans les programmes les plus récents (OLINDA/EXM V2.0 et IDAC 2.1) les différences entre les codes Monte Carlo soient réduites.

Il est prévu que dans un proche avenir IDAC 2.1 (ou ses nouvelles versions) et OLINDA/EXM V2.0 (comme son prédécesseur) seront utilisés comme référence pour les estimations de dose absorbée et efficace pour les nouveaux MRP. Toutefois, cela dépendra de la disponibilité des logiciels et de leur approche des recommandations de la CIPR. De ce point de vue, IDAC 2.1 montre la voie car il s'agit d'un logiciel conforme à toutes ces recommandations. Par contre, OLINDA/EXM V2.0 n'est pas conforme à plusieurs des recommandations de cette institution. L'attention est portée sur le fait que le facteur de poids du rayonnement, pour les émissions alpha, est de 5 au lieu de 20 et que les organes, tels que la peau ou les seins pour le modèle masculin ne sont pas disponibles. Le facteur de poids des tissus tels que les ovaires, les testicules, la prostate et les uretères est également différent. La définition du « *remainder* » dans la CIPR-133 comprend 14 organes, mais dans OLINDA/EXM V2.0, on n'en trouve pas quatre : la région extrathoracique, le tissu lymphatique, le muscle et la muqueuse orale. Ces différences dans les deux programmes, en plus de celles mentionnées précédemment, génèrent des variations dans les doses absorbées qui peuvent atteindre jusqu'à 200 % pour les parois de certains organes, comme la vessie et le côlon gauche.

Enfin, il a été possible de développer un calcul de dose efficace dans un MRP qui n'est utilisé que chez l'homme (puisque son but est de diagnostiquer le cancer de la prostate). Dans ces cas, des stratégies de calcul des doses efficaces doivent être élaborées en tenant compte de ce type de situation.

Dans le chapitre 3, l'étalonnage d'un TEMP/TDM est effectué afin de déterminer le facteur d'étalonnage spécifique au ^{177}Lu. Ce facteur est utilisé pour estimer l'activité des structures segmentées point à point. Par la suite, des courbes d'activité-temps peuvent être générées.

Selon le constructeur de l'équipement, disposant chacun de son propre programme de dosimétrie, l'étalonnage de la TEMP/TDM doit être développé en mode acquisition planaire. Cependant, il a également été décidé de faire un mode acquisition TEMP.

Pour la sensibilité planaire, il est possible de conclure que sa variation, créant différentes régions d'intérêt, n'est pas significative entre 8 et 18 cm. La sensibilité est presque constante lorsque l'image entière est utilisée pour estimer le nombre de coups dans l'image.

Deux configurations de sources radioactives ayant des activités différentes ont été utilisées dans l'étude de sensibilité TEMP. En ce qui concerne les paramètres du protocole d'acquisition, seuls les temps par projections étaient différents. Dans le cas de la reconstruction, la quantité d'itérations, de sous-ensembles, de post-filtration et de corrections varie selon les effets des corrections tels que l'atténuation, la diffusion et la réponse du collimateur.

En ce qui concerne la géométrie de la source radioactive et du fantôme qui la contient, il a été conclu que pour deux configurations qui sont une source sphérique soit placée dans l'air, soit située au centre d'un fantôme rempli d'eau, le facteur de sensibilité ou d'étalonnage sera très similaire. En comparant ces résultats avec ceux obtenus avec une bouteille pleine d'eau (en essayant de simuler un rein), on peut dire que les différences de sensibilité ne sont pas significatives. Toutefois, dans les deux géométries, l'effet de volume partiel peut être présent, en particulier dans le cas de la source sphérique. Pour minimiser cet effet, une source radioactive de dimension plus importante peut être utilisée. Dans ce cas, les fantômes de volume supérieurs à 5 litres de volume peuvent être une bonne option.

Dans le cas du protocole d'acquisition, on peut conclure que pour les postes de travail dosimétriques où le facteur d'étalonnage n'est pas directement dépendant du temps, la variation de ce paramètre a peu d'impact. Mais il est souhaitable que le temps d'acquisition par projection soit le même que celui qui sera utilisé pour les patients. Dans notre cas également, le protocole d'acquisition utilisé a été élaboré à partir de ceux trouvés dans la littérature pour le même modèle de TEMP/TDM. Toutefois, l'analyse documentaire permet de constater qu'il n'existe pas de protocole clinique unique pour l'acquisition d'images de patients traités par le ^{177}Lu.

Dans le cas de la reconstruction d'images, l'approche initiale consistait à utiliser deux postes de travail, chacun utilisant tous les outils possibles pour mettre en œuvre les corrections disponibles. L'objectif initiale était de mesurer les variations du facteur d'étalonnage, qui pouvaient devenir importantes entre les deux postes de travail, pour le même type de reconstruction. Ceci est dû à l'algorithme de reconstruction mis en œuvre et aux corrections associées dans chaque station. De ce fait, il a été conclu que les images reconstruites dans un poste de travail doivent avoir leur propre facteur d'étalonnage afin d'effectuer des estimations dosimétriques.

Un aspect important est la création de la courbe d'étalonnage du TDM pour les postes de travail. Cette courbe est importante car elle permet d'effectuer la correction d'atténuation de l'isotope utilisée pour la quantification des images. Dans le cas du poste de travail d'Hermès, une courbe d'étalonnage bilinéaire a été établie, basée sur des nombres CT et des coefficients d'atténuation linéaire à 140 keV.

En cas d'augmentation du nombre d'itérations et de sous-ensembles (mises à jour), on peut conclure qu'au fur et à mesure de leur augmentation, la sensibilité augmente, étant donné que le nombre de coups se trouvant dans le même volume d'intérêt augmente, atteignant éventuellement un niveau où la sensibilité n'augmente plus. Cependant, deux effets sont présents : lorsque les mises à jour augmentent, le temps de reconstruction augmente considérablement et un artefact connu sous le nom de « *Gibbs-like* » est présenté, qui est associé à l'utilisation de la correction de réponse de collimateur pour un grand nombre de mises à jour. En principe, ce dispositif n'affecte pas le nombre total de coups, mais leur répartition.

Il a été possible de générer la courbe associée au coefficient de récupération, avec et sans activité de fond, avec et sans post-filtrage. Cette courbe a été générée pour caractériser la TEMP/TDM. Cependant, on constate que la gamme des volumes utilisés est réduite afin de pouvoir mieux étudier l'effet du volume partiel. Il serait souhaitable d'avoir une solution commerciale pour pouvoir étudier des volumes par exemple jusqu'à 100 ml.

Il a également été possible de voir l'effet du post-filtrage sur l'estimation de la sensibilité. Sans post-filtrage ou avec un filtre gaussien de 0,11 cm, les sensibilités sont pratiquement les mêmes, mais en utilisant un filtre gaussien de 1,0 cm, on peut voir une diminution significative des coups. Pour cette raison, il a été conclu qu'une reconstruction utilisant l'algorithme de reconstruction OSEM, incluant des corrections pour l'atténuation, la dispersion et la réponse du collimateur, avec 6 ou 8 itérations, 10 sous-ensembles et aucun post-filtrage, constitue un facteur d'étalonnage optimal pour la quantification.

La conclusion ci-dessus a été étudiée dans trois postes de travail dotés de logiciels dosimétriques, à savoir HDM d'Hermès, STRATOS de Phillips et PDOSE de Dosisoft. Afin d'étudier et d'évaluer la conclusion ci-dessus, on a conçu une expérience dont l'objectif était de déterminer le temps de résidence, en tenant compte uniquement de la décroissance physique d'une source contenue dans une bouteille, dans un fantôme. L'ensemble fantôme-bouteille étant une structure fixe, les positions de deux des cinq points de mesure ont été modifiées afin d'évaluer le registre rigide automatique des postes de travail. En parallèle, il a été possible de déterminer les activités pour les points de mesure dans chaque poste de travail en utilisant le facteur d'étalonnage pour la reconstruction avec 60 mises à jour. Trois conclusions ont été tirées de cette expérience : a) STRATOS a des difficultés avec le recalage des images pour les points où il y a eu des variations dans les positions de l'ensemble fantôme-bouteille, b) Le recalage des images HDM et PDOSE est satisfaisant et permet de corriger les variations de position de la bouteille (source radioactive), c) Les estimations d'activité pour chaque point de mesure sont satisfaisantes pour HDM et PDOSE, mais pas pour STRATOS, où l'emplacement du fantôme varie. Par conséquent, le calcul du temps de résidence pour HDM et PDOSE présente des différences relatives assez faibles (%), tandis que pour STRATOS, il est assez élevé. Cette expérience a permis de conclure que les images utilisées pour générer le facteur d'étalonnage doivent être traitées de la même manière que les images des patients, en termes d'acquisition et de reconstruction.

Dans le quatrième chapitre, pour le calcul de la dose absorbée par les patients avec le groupe de travail de l'Institut de Cancérologie de Montpellier (ICM), il a été convenu d'utiliser la reconstruction OSEM, avec 60 mises à jour, toutes les corrections et une post-filtrage de 0,11 cm. Le groupe ICM, indépendant et utilisant le DTK de Xeleris, a pu déterminer un facteur d'étalonnage différent de celui trouvé au Centre de Recherches en Cancérologie de Toulouse (CRCT) avec HROD d’Hermès.

Chaque centre a utilisé les données provenant de deux cycles de traitement de deux patients par ^{177}Lu-DOTATATE qui avaient des tumeurs gastro-entéropancréatiques. L'ICM a utilisé DTK pour effectuer l'analyse dosimétrique des données des deux patients. Le CRCT a utilisé les données reconstruites dans HROD pour effectuer des analyses dosimétriques dans HDM, STRATOS et PDOSE. De cette façon, il a été possible de comparer les résultats obtenus par chaque centre pour les quatre postes de travail.

Les flux de travail pour les quatre postes de travail sont similaires. Le recalage de toutes les images TEMP/TDM sont réalisées entre une image TEMP/TDM de référence et toutes les autres images TEMP/TDM. Les structures d'étude sont segmentées, cela peut être automatique ou manuel. Une propagation des structures segmentées de la TEMP/TDM de référence est faite vers les autres. Le facteur d'étalonnage est utilisé pour déterminer l'activité présente dans chaque structure segmentée. Des courbes d'activité-temps sont créées. Ces courbes sont intégrées pour déterminer l'activité cumulée ou le temps de résidence, ce qui permet enfin d’aboutir aux doses absorbées.

On peut conclure que tous les postes de travail peuvent effectuer un recalage rigide des images en utilisant l'ensemble du champ de vision. Il a été constaté que deux postes de travail fournissent à l'utilisateur des informations sur la matrice de transformation utilisée pour le recalage rigide. Peu d'entre eux peuvent développer un recalage élastique mais cette méthode n'a pas été utilisée. Chez DTK, STRATOS et HDM, le recalage rigide était automatique et les structures osseuses étaient généralement utilisées en tant que repères pour pouvoir effectuer cette étape. Dans le cas du PDOSE, le recalage rigide était également automatique, mais il pouvait être limité à un organe, ce qui permettait corriger les variations dans le positionnement des organes à chaque point de mesure. Aucun des postes de travail offre des outils pour le calcul de l'incertitude associée au processus du recalage.

Dans le cas de la segmentation automatique, les outils sur les postes de travail peuvent être suffisamment satisfaisants pour la dosimétrie. Certains postes de travail possèdent davantage d'outils que d'autres, cependant, déterminer quels outils sont plus importants et/ou nécessaires, dépend beaucoup de chaque utilisateur. La segmentation manuelle est en 2D et 3D c’est disponible et satisfaisant. Afin d'éviter l’utilisation de segmentations différents dans les différents postes de travail, l'idéal serait que tous permettent de charger des images de type « *DICOM RTStruc* ». Cependant, un seul d'entre eux permet l'importation et l'exportation de ce type d'images. Aucun des postes de travail n'offre d'outils pour évaluer l'incertitude associée au processus de segmentation d'une structure.

Le seul poste de travail qui permet d'abord la segmentation des structures et ensuite leur recalage est PDOSE. Il est probablement possible de réduire de cette façon les variations dans les positions des organes liés à un mauvais positionnement du patient ou par les mouvements des organes.

La propagation des structures, consiste simplement à copier et coller les images de la TEMP/TDM de référence dans les autres TEMP/TDM. Lors de l’exécution de ce processus, il peut être vérifié que les structures copiées ne correspondent pas aux mêmes structures dans d'autres points de mesure, ceci est dû au mauvais positionnement du patient et/ou aux mouvements de certains organes. Dans ce travail, il a été entrepris un déplacement des structures dans chaque point de mesure, mais tout en conservant le même volume total, ce qui signifie que la masse totale de la structure n'a pas varié. Aucune des stations ne permet d’associer ce processus a un calcul des incertitudes.

L'ajustement des courbes d'activité-temps était l'un des pas de la chaine dosimétrique qui diffère selon les postes de travail. DTK n'offre l'ajustement des données que par des moyens mono-exponentiels. STRATOS travaille uniquement selon la méthode des trapèzes, en considérant la décroissance physique (mono-exponentielle) du dernier point de mesure à l'infini. HDM offre un ajustement mono- et bi-exponentiel des données. PDOSE offre tout ce qui précède et même le réglage tri-exponentiel. Seul PDOSE dispose d'un outil permettant d'évaluer l'ajustement des données. Aucune des stations n'offre un outil qui tient compte du calcul de l'incertitude qui peut être associé à l'ajustement des données.

En ce qui concerne le calcul des doses absorbées, DTK et HDM effectuent le calcul dosimétrique au niveau de l'organe et exportent les résultats du temps de résidence vers OLINDA/EXM V1.0 et V2.0, respectivement. STRATOS calcule la dose absorbée, de voxel à voxel, en faisant un ajustement pour déterminer l'activité cumulée également de voxel à voxel. Enfin pour calculer la dose absorbée ce programme utilise un “kernel” qui a été calculé pour l'isotope étudié dans un milieu homogène infini (eau). Dans le cas du PDOSE, le calcul de la dose absorbée au niveau des organes est effectué en utilisant la méthode de dépôt local d'énergie, bien que d'autres outils soient disponibles. Dans le cas des données générées par PDOSE et STRATOS, les masses de chaque rein sont pondérées afin de pouvoir comparer les doses absorbées obtenues avec DTK et HDM.

Il a été conclu que trois paramètres étaient communs à tous les postes de travail : la masse des organes générée par leur segmentation, les temps de résidence et les doses moyennes absorbées.

Trois organes - le foie (y compris les métastases), la rate et les reins - ont été étudiés. Une correction de l'effet de volume partiel n'a pas été effectuée puisque pour ces trois organes, cet effet devrait être mineur en raison de la taille de chaque structure.

Il a été conclu que les masses des organes segmentés étaient très similaires pour chaque centre, ce qui a permis d'évaluer le travail effectué par leurs opérateurs.

L'évaluation du flux du travail peut être évalué en utilisant les résultats des temps de résidence, qu'étaient très similaires et du même ordre de grandeur pour tous les postes de travail de chaque organe. On constate également que les temps de résidence pour le deuxième cycle de traitements sont plus longs pour les reins et la rate des deux patients. Dans le cas du foie pour le patient masculin, il est le même que pour les autres organes, mais pour le patient féminin, il est réduit de près de 50%. On constate que pour STRATOS le calcul du temps de résidence des reins est beaucoup plus petit que celui obtenu avec les autres logiciels, pour le deuxième cycle de traitement, pour le patient masculin.

La méthode de dépôt d'énergie local mise en œuvre dans PDOSE génère des résultats de dose absorbée qui sont très similaires à ceux générés par les deux versions d'OLINDA. Le même effet doit se produire avec le « *kernel* » déterminé dans STRATOS, la contribution bêta doit être beaucoup plus importante que la contribution gamma, donc les doses absorbées obtenues avec ce logiciel sont comparables aux autres.

Dans le cas de la dose absorbée au niveau de la moelle osseuse, on obtient des résultats semblables à ceux d'autres études trouvées dans la littérature. Dans ce cas, il est possible de voir que la méthode développée fonctionne pour les deux patients, car ils peuvent avoir des similitudes avec les modèles de la CIPR en termes de masse et de volume. Ce qui est intéressant à propos de cette méthode, c'est qu'elle pourrait être mise en œuvre dans un service de médecine nucléaire où il n'y a pas de détecteur pour mesurer le corps entier du patient, comme c'est arrivé dans notre cas. Il est également conclu que près de 50% de la contribution à la dose absorbée dans la moelle osseuse est due au « *remainder* ». L'auto-irradiation est également importante, en fonction du patient, pouvant atteindre jusqu'à 50%. Notre méthodologie devrait être étudiée avec un plus grand nombre de patients et complétée par une dosimétrie sanguine afin d'établir une corrélation possible entre les deux méthodes.

D'autre part, il a été possible de trouver dans la littérature qu'il n'y a pas de correspondance entre les doses absorbées dans la moelle osseuse par la méthode sanguine et la méthode d'imagerie L_2 à L_4. Cependant, ces résultats ont été obtenus dans un petit groupe de patients (Beykan et al., 2018). On devrait s'attendre à davantage de données probantes pour un plus grand groupe de patients.

Dans le cadre de ce travail doctoral, certaines questions restent sans réponses, nous espérons donc pouvoir y donner suite par des études que nous développerons, par exemple :

- Nous prévoyons effectuer la dosimétrie pour les volontaires sains et des patients pour les trois MRP étudiés. Actuellement, nous attendons l'approbation finale des comités d'éthique nationaux/locaux et la révision des protocoles cliniques proposés par chaque centre de recherche.
- Nous espérons faire une publication où nous pourrons montrer les différences qui existent entre les deux versions d'OLINDA et IDAC 2.1, dans le cas de la dosimétrie de référence pour les nouveaux MRP.

- Nous espérons pouvoir estimer le facteur d'étalonnage à l'aide d'un mannequin de plus grand volume et comparer les résultats obtenus avec les autres géométries utilisées.
- En raison de la variation de la position de certains organes, il peut parfois être nécessaire de considérer une variation du volume d’intérêt à chaque point de mesure.
- En raison de la variation de la position de certains organes, l’utilisation du recalage d'image optimisé au niveau de chaque organe (disponible avec PDOSE) peut-être étudié en considérant deux cas : volume segmenté invariable, et volume segmenté variable, pour chaque point de mesure, donc, le calcul des temps de résidence doit être comparé pour les deux cas. A la suite des deux points précédents, les doses absorbées devraient être recalculées.
- Des comparaisons devraient également être faites entre d’autres méthodes de calcul de la dose absorbée au niveau des organes, telle que la convolution, disponible chez Dosisoft.
- De fait, certaines solutions dosimétriques (Dosisoft et STRATOS) permettent un calcul de la dose absorbée au niveau du voxel, par convolution ou en faisant l’hypothèse d’un dépôt local de l’énergie émise. On peut ainsi obtenir les histogrammes dose absorbée – volume (Dose Volume Histogrammes – DVH). De plus, ces résultats pourraient être comparés aux résultats obtenus à l'aide de simulations Monte-Carlo.
- Enfin, l'EANM a récemment soulevé la question de l'intégration du calcul d’incertitudes dans les protocoles cliniques. Cette question reste en suspens dans notre travail doctoral, étant donné qu'aucune des stations de travail étudiées ne permet d'évaluer l'incertitude dans les différentes étapes du protocole dosimétrique. Nous comptons toutefois orienter nos recherches en direction de l’estimation de la précision des résultats par propagation des incertitudes au long de la chaîne d’opérations qui mènent de la reconstruction des images à la détermination de la dose absorbée.

General conclusion and future perspectives

In this doctoral work, the MIRD formulation was analyzed. This formulation can be expressed in its simplest form through three variables - absorbed dose, cumulated activity and S value.

Each of these variables can be studied from a preclinical and clinical point of view. In each of these two areas, it was possible to understand the degree of complexity involved in the determination and its usage.

In the second chapter of this work, the estimation of absorbed doses and effective doses that can be used as reference in human beings is presented. This estimation was done for three new radiopharmaceuticals using preclinical data. In this case, the calculation of the cumulated activity implied a particular challenge for the type of information we received.

For example, in the case of the radiopharmaceutical studied with PET/CT images, eight volumes of interest, each with 16 measuring points were studied, which allowed to generate time-activity curves so as to identify easily the uptake and excretion phases of the radiopharmaceutical for certain organs. For several organs, it was possible to establish a biokinetic model, which described these two phases, but for others, despite having a good number of measurement points, it was not possible to establish a biokinetic model. In these cases, the trapezoid method was selected. This method can be considered as a conservative method since it can overestimate the cumulated activities at the time of the integration of the time-activity curve.

In the case of radiopharmaceuticals in which organ dissection was used, the number of measuring points was reduced (between three and four points) due to the number of animals sacrificed. In this experimental situation, the trapezoid method was optimal since there was no possibility of establishing a biokinetic model for the organs under study. Therefore, it can be expected that there is an overestimation of the cumulated activities at the time of the integration of the time-activity curve. For these two cases, the amount of volumes of interest used was between 13 and 14, considering the organs in the way of excretion. For one of the radiopharmaceuticals, a study was developed considering the bladder-voiding. The same study showed important differences in the results of absorbed doses when this consideration was not taken into account. From this point of view, it is concluded that considering the cumulated activities coming from the organs used as excretion pathways of the radiopharmaceuticals helped to show the absorbed doses received by other organs close to them.

In the case of these two radiopharmaceuticals, there was no calibration factor for the detector that was used to make the measurements of the studied organs. Hence, a methodology was developed to estimate the total number of counts in all the organs and the total activity injected.

On the other hand, the extrapolation of preclinical results to humans was performed by weighting organ masses between the two species. This method can create errors in residence times thereby inducing errors in the calculation of absorbed doses and effective doses between animals and humans. It can significantly increase or decrease the residence time values.

Regarding the use of the S-value provided by several software, it could be seen that the differences are mainly associated with the anthropomorphic models and the Monte Carlo codes. In the case of anthropomorphic models, differences in organ positions, dimensions, mass, volume and density can be observed. Differences have also been seen from stylized to voxelized models i.e. from models, which do not reflect a human being to models very close to the anatomy of a man or a woman. In case of the usage of Monte Carlo codes, the differences may be associated with the interaction of charged and uncharged particles with matter, in other words, the energy ranges associated with these particles, the energy spectra used and how they were generated, and so on. However, it is expected that in the most recent software (OLINDA/EXM V2.0 and IDAC 2.1), the differences in the Monte Carlo codes are less important.

It is expected that in the near future IDAC 2.1 (or its new versions) and OLINDA/EXM V2.0 (as its predecessor) will be used for absorbed and effective dose estimation as a reference for new radiopharmaceuticals. However, it will depend on the availability of the software and their approach to the ICRP recommendations. From this point of view, IDAC 2.1 takes the lead since it is a software that complies with all ICRP recommendations. On the other hand, OLINDA/EXM V2.0 does not comply with many of the recommendations of this institution. It is noteworthy that the weight radiation factor for alpha emissions is 5 instead of 20. In addition, organs such as skin, breasts are not available for the male model. Also, the weight factor for tissues such as ovaries, testes, prostate and ureters are different. The "*remainder*" definition in ICRP-133 is for 14 organs however in OLINDA/EXM V2.0, four organs namely the extrathoracic region, the lymphatic tissue, the muscle and the oral mucosa are not found. These differences in both software generate variations up to 200% for the walls of some organs such as the bladder and left colon in absorbed doses.

Finally, it was possible to develop an effective dose calculation in a radiopharmaceutical that is only used in men (since it is for prostate cancer). In these cases, effective dose calculation strategies must be developed considering this type of situation.

In chapter three, the calibration of a SPECT/CT is performed in order to determine the calibration factor for the ^{177}Lu. This factor is used to estimate the activity of the segmented structures point to point. Time-activity curves can then be generated.

According to the manufacturer, for the equipment having its own dosimetry program, the calibration of the SPECT/CT must be developed in planar acquisition mode. However, it was also decided to make a SPECT acquisition mode.

For planar sensitivity, it is possible to conclude that its variation creating different regions of interest is not significant between 8 and 18 cm. The sensitivity is almost constant when the whole image is used to estimate the number of counts.

Two configurations of radioactive sources with different activities were used in the SPECT sensitivity study. Regarding the parameters of the acquisition protocol, only the times per projection were different. In the case of reconstruction, the number of iterations, subsets, post-filtering and corrections for effects such as attenuation, scattering and collimator response were varied.

With respect to the geometry of the radioactive source and the phantom containing this source, it was concluded that for a spherical source placed in air and located in the center of a phantom filled with water, the sensitivity or calibration factor will be very similar between the two configurations. Comparing these results with those obtained with a bottle full of water (trying to simulate a kidney), the differences in sensitivity are not significant. However, in both geometries the partial volume effect may be present especially in the case of the spherical source. Hence, to minimize this effect, a larger radioactive source may be used. In this case, phantoms with volumes higher than 5 liters of volume can be a good option.

In the case of the acquisition protocol, it can be concluded that dosimetric workstations in which the calibration factor is not directly dependent on time, the variation of this parameter has little impact. However, it is desirable that the acquisition time per projection is the same as that to be used in patients. Also, in our case, the used acquisition protocol was developed based on literature for the same type of SPECT/CT. However, it can be observed from the literature review that there is no single clinical protocol for the acquisition of patient images who are treated with ^{177}Lu.

In the case of image reconstruction, the initial approach was to use two workstations, each using all possible tools to implement the available corrections. The initial idea when using the two workstations was to see how significant the variations in the calibration factor could be for the same type of reconstruction. Immediately, it could be determined that the calibration factors were very different between the two workstations. This was due to the reconstruction algorithm implemented and the associated corrections at each station. Due to this, it was concluded that the images reconstructed in a workstation must have its calibration factor in order to make dosimetric estimations.

An important aspect was the creation of the CT calibration curve for the workstations. This curve is important because it allows to make the attenuation correction for the isotope that is being used for the quantification of the images. In the case of the Hermes workstation, a bilinear calibration curve was established, based on CT numbers and linear attenuation coefficients at 140 keV.

It can be concluded that with the increasing number of iterations and subsets, the sensitivity increases, given that the number of counts found in the same volume of interest grows, possibly reaching a level where the sensitivity will no longer increase. However, two effects are presented: as the updates increase, the time for reconstruction increases considerably and an artifact known as "*Gibbs-like*" appeared, which is associated with the use of collimator response correction for a high number of updates. In principle, this artifact does not affect the total number of counts, but it does affect its distribution.

It was possible to generate the curve associated to the recovery coefficient, with and without background activity, with and without post-filtering. This curve was generated to characterize the SPECT/CT. However, it was possible to see that the range of volumes used was not enough to better study the effect of the partial volume. It would be desirable to have a commercial solution to be able to study volumes up to 100 ml for example.

It was also possible to see the effect of post-filtering on the estimation of sensitivity. Without post-filter and with a Gaussian post-filter set at 0.11 cm, the sensitivities are practically the same, but using a Gaussian filter of 1.0 cm decreases the number of counts significantly. Due to this, it was concluded that a reconstruction using the OSEM reconstruction algorithm, including corrections for attenuation, scattering and collimator response, with 6 or 8 iterations, 10 subsets and no post-filter provides an optimal calibration factor for quantification.

The above conclusion was studied in three workstations, namely HDM from Hermes, STRATOS from Phillips and PDOSE from Dosisoft. In order to study and evaluate the above conclusion, an experiment was designed in which the objective was the determination of the residence time, considering only the physical decay of a source contained in a bottle inside a phantom. As the phantom-bottle set was a fixed structure, the positions of two out of five measuring points were varied in order to evaluate the automatic rigid recording of the workstations. At the same time, it was possible to determine the activities for the measuring points in each workstation using the calibration factor for reconstruction with 60 updates. Three conclusions were generated from this experiments: a) STRATOS has difficulties in the registration of the images for the points where changes in the positions of the phantom-bottle set occurred, b) the registration of HDM and PDOSE images was satisfactory and the variations in the position of the bottle (radioactive source) could be corrected, c) the activity estimates for each measurement point are satisfactory for all three programs, except for STRATOS where there was a variation in phantom placement. Therefore, the residence time calculation for HDM and POSE have quite low relative differences (%), while for STRATOS it is quite high. From this experiment, it was possible to conclude that the images used to generate the calibration factor should be treated in the same way as the images of patients, in terms of acquisition and reconstruction.

In the fourth chapter, with the group of the Institute of Cancerology of Montpellier (ICM), it was agreed to use OSEM reconstruction, with 60 updates, all corrections and a 0.11 cm post-filter for the calculation of absorbed dose in patients. The ICM using DTK from Xeleris were able to determine a calibration factor that was different to the one found at the Toulouse Cancer Research Center (CRCT) using HROD from Hermes.

Each centre used information from two treatment cycles of two patients treated with ^{177}Lu-DOTATATE who had gastroenteropancreatic tumors. ICM used DTK to perform dosimetric analysis of the data from the two patients. CRCT used the reconstructed data in HROD to perform the dosimetric analysis in HDM, STRATOS and PDOSE. In this way, it was possible to cross-check the results obtained by each center for the four workstations.

It was also possible to determine that the four workstations have fairly similar workflows - the registration of all SPECT/CT images was performed between a reference SPECT/CT and all other SPECT/CT images. The study structures are segmented which could be automatic or manual, generally done at the reference SPECT/CT point. The segmented structures of the reference SPECT/CT were propagated to the other images. The calibration factor was used to determine the activity present in each segmented structure. Time-activity curves were created. These curves were integrated to determine cumulated activity or residence time. Finally, the absorbed doses were obtained.

It can be concluded that all workstations can perform a rigid registration of images using the entire field of view. It was found that two workstations provide information to the user about the transformation matrix used in the rigid registration. Few of them can develop an elastic registration but this method was not used. In DTK, STRATOS and HDM the rigid registration was automatic and generally the bone structures were used to be able to execute this work. In the case of PDOSE, the rigid registration was also automatic, but it could be restricted to an organ, which allowed the user to better correct the variations in the positioning of a patient's organs in each measuring point. None of the workstations offers two fundamental tools; one is associated with the calculation of uncertainty through the registration process and second is that it cannot analyze/correct retrospectively the registration that was used.

For automatic segmentation, the available tools on the workstations can be sufficiently satisfactory for dosimetry. Some workstations have more tools than others, however, establishing which tools are more important and/or necessary than others, depends a lot on each user. Manual segmentation in 2D and 3D is also available and satisfactory. To avoid segmentation in different workstations, the ideal would be that all allowed loading "*DICOM RTStruct*" images. However, only one of them allowed the import and export of this type of images. None of the workstations offered tools to evaluate the uncertainty associated in the process of segmentation of a structure.

The only workstation that allows first the segmentation of structures and then the registration of them is PDOSE. Probably in this way one can reduce the variations in the positions of the organs either by poor positioning of the patient or by movements of the organs.

The propagation of structures is simply to copy and paste the images of the reference SPECT/CT to the other SPECT/CT's. When performing this process, it can be verified that the copied structures do not correspond to the same structures at other points of measurement, which could be due to poor positioning of the patient and/or movements of some organs. In this work, it was permitted to move structures in each measuring point but the total volume of the structure was not varied which meant that the total mass of the structure was not varied. Uncertainties cannot be estimate for the propagation of structures among all workstations.

The fitting of the time-activity curves was one of the steps in the dosimetric chain which is different among the workstations. DTK only offers single-exponential data fitting. STRATOS only works the trapezoidal method (at voxel level) considering physical decay (by means of a mono-exponential) from the last measurement point to infinity. HDM offers mono- and bi-exponential fitting. PDOSE offers all the above and even the tri-exponential fitting. Only in PDOSE there is a tool to evaluate the goodness of fitting. None of the stations offers a tool that considers the uncertainty calculation associated to the fitting of the data.

Regarding the calculation of absorbed doses, DTK and HDM perform the dosimetric calculation at organ level followed by residence time results exportation to OLINDA/EXM V1.0 and V2.0, respectively. STRATOS calculates absorbed dose voxel to voxel, making a fitting to determine the cumulated activity voxel by voxel and further calculate the absorbed dose by using a voxel-kernel that was calculated for the isotope under study in a homogeneous medium (water). In the case of PDOSE, the calculation of absorbed dose is performed by using of the local energy deposition method at the level of the organ dosimetry, although other tools are available. In the case of the data generated by PDOSE and STRATOS, a weighting of the masses of each kidney is made in order to compare the absorbed doses obtained with DTK and HDM.

It was concluded that among all the workstations, three parameters were common - the mass of the organs generated by their segmentation, the residence times and the mean absorbed doses.

Three organs- the liver (including metastasis), the spleen and the kidneys were studied. A partial volume effect correction was not performed since for these three organs, this effect is expected to be minor due to the size of each structure.

It was concluded that the masses of the segmented organs were very similar for each centre, which allowed to evaluate the work done by their operators.

The evaluation of residence times begins to show results for the entire dosimetric workflow. They were very similar for all workstations for each organ. They were all in the same order of magnitude for all workstations. It can also be seen that the residence times for the second cycle of treatment was greater for the kidneys and spleen of both patients. In the case of the liver, for the male patient it was the same as for the other organs, but for the female patient it was reduced by almost 50%. It can be seen that for STRATOS, the calculation of kidney residence time was much smaller than that obtained with other software, for the second treatment cycle, for the male patient.

The local energy deposition method implemented in PDOSE generated absorbed dose results that were very similar to those generated by the two versions of OLINDA. The same results are obtained by using the voxel-kernel determined in STRATOS. The beta contribution is more important than the gamma contribution in order to generated the voxel-kernel; therefore, the absorbed doses obtained using this software were comparable to the other.

In the case of the absorbed dose at the level of the red bone marrow, our results are similar to other studies found in the literature. In this case, it was possible to see that the developed method works for both patients because there are similarities with the ICRP models in terms of mass and volume. This method that could be implemented in a nuclear medicine service where there are no detectors to perform whole-body measurements of the patient, as happened in this case. It was also concluded that the greatest contribution to the absorbed dose in the bone marrow was due to the "*remainder*" with almost 50%. Self-irradiation is also important, depending on the patient it can be close to 50% as well. Our methodology should be studied with a larger number of patients and also by considering a blood dosimetry in order to establish a possible correlation between the two methods.

Moreover, it has been found in the literature that there is no correspondence between the absorbed doses in bone marrow using a blood-sampling method and the L_2 to L_4 imaging method. However, these results were obtained in a small group of patients. More evidence should be expected in larger groups of patients (Beykan et al., 2018).

In the context of this doctoral work, some questions still remain unanswered, so we hope to be able to follow them up with studies that we will develop. This includes the following:

- As part of future work, we plan to perform dosimetry for healthy volunteers and patients for the three radiopharmaceuticals studied. Currently, we are waiting for the final approval from national/local ethics committees and the review of clinical protocols proposed by each research centre.
- We hope to make a publication where we can show the differences between the two versions of OLINDA and IDAC 2.1, in the case of reference dosimetry for the new radiopharmaceuticals.
- We hope to be able to estimate the calibration factor using a larger volume phantom and compare the results obtained with the other geometries used.
- Due to the variation in the position of some organs, it may sometimes be necessary to consider a variation in the volume of interest at each measurement point. The calculation of residence time must be different from what is done today.
- Due to the variation in the position of some organs, the use of optimized image registration at each organ (available with PDOSE) can be studied by considering two cases: invariable segmented volume, and variable segmented volume, for each measurement point. Therefore, the calculation of residence time must be compared for both cases. Following the two previous points, the absorbed doses should be recalculated.
- Comparisons should also be made between other methods of calculating absorbed dose, such as convolution, available at Dosisoft.
- In fact, some dosimetric solutions (Dosisoft and STRATOS) allow a calculation of the absorbed dose at the voxel level, by convolution or by assuming a local deposition of the emitted energy. This allows to obtain the absorbed dose - volume histograms (Dose Volume Histograms - DVH). In addition, these results could be compared to the results obtained using Monte Carlo simulations.

- Finally, EANM recently raised the issue of the integration of uncertainty calculation into clinical protocols. This question remains unresolved in our doctoral work, since none of the workstations studied allowed us to evaluate the uncertainty in the different stages of the dosimetry protocol. However, we intend to direct our research towards estimating the accuracy of the results by propagating uncertainties along the chain of operations that lead from image reconstruction to absorbed dose determination.

Organ masses for human and animals’ models

Table A.1. Organ masses (in grams) according to different references.

Organs	RADAR - OLINDA/EXM V2.0		ICRP 89		ICRP 23		OLINDA/EXM V2.0	
	Adult male	Adult female	Adult male	Adult female	Adult male	Adult female	Rat 300g	Mouse 35g
Adren-glands	14	13	14	13	14	14		
Brain	1450	1300	1450	1300	1400	1200	5.4	0.7
Eyes	15	15	15	15				
Breast		500	25	500	360	360		
GB-contents	58	48	58	48	62	50		
GB-wall	10	8	10	8	10	8		
Lcolon-contents	75	80	75	80	135	135	11.5	0.8
Lcolon-wall	150	145	150	145	160	160		
Sintest-contents	350	280	350	280	400	375	15.5	2.5
Sintest-wall	650	600	650	600	640	600		
Sto-contents	250	230	250	230	250	230	1.4	0.1
Sto-wall	150	140	150	140	150	140		
Rcolon-contents	150	160	150	160	220	210		
Rcolon-wall	150	145	150	145	210	200		
Recto-contents	75	80	75	80				
Recto-wall	70	70	70	70				
Heart-contetns	510	370	510	370	500	410	2.6	0.3
Heart-wall	330	250	330	250	330	240		
Kidneys	310	275.5	310	275	310	275	3.0	0.4
Liver	1800	1400	1800	1400	1800	1400	1.2	2.6
Lung	1200	950	1200	950	1000	800	0.9	0.1
Lng-Cont			0	0	0	0		
Muscle			29000	17500	28000	17000		
Esophagus	40	35	40	35	-	-		
Ovaries		11	0	11	11	11		
Prostate	17	1	17	0	-	-		
Pancreas	140	120	140	120	100	85	0.5	0.4
Skeleton	10500	7800	10450	7760	-	-		
R_Marrow	1170	900	1170	900	1500	1300		
C_Bone-V	4400	3200	4400	3200	4000	3000	22.1	3.0
T_Bone-V	1100	800	1100	800	1000	750		
Saliv-glands	85	70	85	70	-	-		
Skin	-	-	3300	2300	2600	1790		
Spleen	150	130	150	130	180	150	0.9	0.2
Testes	35	1	35	0	35	0	0.2	0.2
Thymus	25	20	25	20	20	20		
Thyroid	20	17	20	17	20	17	0.3	0.0
UB-contents	211	160	200	200	120	88,4	0.7	0.1
UB-wall	50	40	50	40	45	35,9		
Uterus	1	80	0	80	80	80		
Body	73000	60000	73000	60000	68831	56912	326	35.3

Materials and methods used for estimations with OLINDA/EXM V1.0

The residence times were used as input for OLINDA/EXM V1.0 according to the procedure described in Chapter 2 for this radiopharmaceutical.

Results for [^{18}F]FNM

In table A.2, organ masses for male and female dosimetric models used for mass scaling can be seen, also residence times used in OLINDA/EXM V1.0 after mass scaling are exhibits. Organs with highest residence times are brain, kidney, liver and lungs.

Table A.2. Organ masses for male dosimetric model and residence times (T) used in OLINDA/EXM V1.0 after mass scaling.

Target organ	M_{male} (g)	M_{female} (g)	T_{male} (h)	T_{female} (h)
Brain	1400	1200	2.12E-02	2.19E-02
Heart contents	500	410	9.48E-03	9.41E-03
Kidney	310	275	2.52E-02	2.70E-02
Liver	1800	1400	5.66E-02	5.33E-02
Lung	1000	800	3.48E-02	3.37E-02
Spleen	180	150	7.15E-03	7.21E-03
Stomach contents	250	230	6.41E-03	7.13E-03
Remainder	63391	52447	6.25E-01	6.26E-01
Total Body	68831	56912	-	-

Table A.3. shows results for the ADC and the CEDF per organ, for male and female dosimetric models from OLINDA/EXM V1.0. Organs with high ADC are stomach wall, kidneys, liver, lungs and spleen for both models. Mean effective dose was 4.65 x10^{-3} mSv/MBq and 5.73x10^{-3} mSv/MBq for the adult male and female models, respectively. This would correspond to effective dose of 1.63 mSv and 2.01 mSv, respectively, for an administrated activity of 350 MBq. For gallbladder, heart wall and testes under ICRP-60 there is not weighting tissue factor, also they do not contribute to the remainder.

Table A.3. Absorbed dose coefficients (ADC) and contribution to the effective dose factor (CEDF) results for adult male model from OLINDA/EXM V1.0.

Organ	Male		Female	
	ADC (mGy/MBq)	CEDF (mSv/MBq)	ADC (mGy/MBq)	CEDF (mSv/MBq)
Adrenals	4.66E-03	1.17E-05	5,91E-03	1,48E-05
Brain	4.23E-03	1.06E-05	5,09E-03	1,27E-05
Breasts	2.88E-03	1.44E-04	3,63E-03	1,81E-04
Gallbladder Wall	4.88E-03	-	5,73E-03	-
LLI Wall	3.72E-03	4.46E-04	4,68E-03	5,61E-04
Small Intetine	4.01E-03	1.00E-05	4,63E-03	1,16E-05
Stomach Wall	6.11E-03	7.33E-04	7,68E-03	9,21E-04
ULI Wall	4.01E-03	1.00E-05	5,03E-03	1,26E-05
Heart Wall	5.90E-03	-	7,15E-03	-
Kidneys	1.76E-02	4.39E-05	2,05E-02	5,12E-05
Liver	8.61E-03	4.30E-04	1,07E-02	5,36E-04
Lungs	7.83E-03	9.39E-04	9,68E-03	1,16E-03
Muscle	3.28E-03	8.19E-06	4,08E-03	1,02E-05
Ovaries	3.87E-03	7.74E-04	4,76E-03	9,52E-04
Pancreas	4.82E-03	1.20E-05	5,99E-03	1,50E-05
Red Marrow	3.27E-03	3.92E-04	4,02E-03	4,82E-04
Osteogenic Cells	5.01E-03	5.01E-05	6,55E-03	6,55E-05
Skin	2.55E-03	2.55E-05	3,17E-03	3,17E-05
Spleen	9.68E-03	2.42E-04	1,19E-02	2,96E-04
Testes	3.04E-03	-	-	-
Thymus	3.58E-03	8.96E-06	4,53E-03	1,13E-05
Thyroid	3.30E-03	1.65E-04	3,84E-03	1,92E-04
Urinary Bladder Wall	3.65E-03	1.83E-04	3,87E-03	1,94E-04
Uterus	3.90E-03	9.74E-06	4,72E-03	1,18E-05
Total Body	3.65E-03	-	4,55E-03	-
Total effective dose (mSv/MBq)	-	4.65E-03	-	5.73E-03

Results for [^{11}C]SAM

The mice remainder residence time was calculated as the sum of residence times for blood, muscles, bones and carcass. Therefore, the human remainder residence time considers same organs in OLINDA/EXM V1.0. Bladder contents with and without bladder voiding are also considered.

Table A.4 shows the human and mouse organ mass used for the scaling process as well as the residence times used for OLINDA/EXM V1.0. On the other hand, S-factor values can be observed for different organs.

The highest value for human residence time is for the bladder contents (without and without bladder voiding), also kidneys, liver + gallbladder contents, lungs, stomach contents exhibits high values.

Table A.4. Organ masses for male dosimetric model and residence times (T) used in OLINDA/EXM V1.0 after mass scaling.

Organ	M_{male} (g)	S-factor[a] (mGy/MBq-s)	M_{mouse} (g)	T_{male}(h)
Heart Wall	330	2.28E-04	0.1400 ± 0.010	5.33E-04
Kidneys	310	2.46E-04	0.4746 ± 0.047	1.06E-02
Liver + Gallbladder contents	1862		1.8355 ± 0.203	4.63E-03
Liver	1800	4.65E-05		4.48E-03
Gallbladder contents	62	6.39E-04[b]		1.54E-04
Lungs	1000	7.01E-05	0.2018 ± 0.012	3.71E-03
Spleen	180	4.08E-04	0.1109 ± 0.015	2.98E-04
Stomach contents	250	1.47E-04[b]	0.100[d]	1.67E-03
Intestines contents	755		3.300[d]	9.38E-04
Left colon contents (LLI)	135	2.43E-04[b]		1.68E-04
Small intestine contents (SI)	400	8.20E-05[b]		4.97E-04
Right colon contents (ULI)	220	1.57E-04[b]		2.73E-04
Bladder contents without bladder voiding	120[c]	1.87E-04[b]	0.1000[d]	1.52E-01
Bladder contents with bladder voiding	120	1.87E-04[b]	0.0900	6.10E-02
Remainder	64024	---	30.7023	1.11E-01[e]
Whole Body	68831	1.62E-06	36.8650 ± 2.010	-----

[a] S-factor refers to self–irradiation; [b] S-factor for gallbladder wall, stomach wall, LLI, SI, ULI wall and urinary bladder wall, considering their contents as a source; [c] Urinary bladder contents and urinary bladder wall masses for human model ICRP-23; [d] Mouse Stomach, intestines and bladder contents masses from OLINDA/EXM V2.0; [e] Remainder takes into account blood, muscles, bones and carcass.

Table A.5 shows the ADC and the CEDF, with and without the bladder voiding consideration. Organs showing high ADC are, urinary bladder wall, kidneys and uterus. Organs showing differences between 1.7 and 2.5 times in ADC are LLI wall, ovaries, testes, uterus and urinary bladder wall. For gallbladder, heart wall and testes under ICRP-60, there is not weighting tissue factor, also they do not contribute to the remainder.

The mean effective dose is 6.82x10^{-3} mSv/MBq and 3.32x10^{-3} mSv/MBq, without and with the bladder voiding consideration, respectively; corresponding to 2 times difference between the two methods. Considering CUDIM protocols the mean effective dose range is between 1.99–2.99 mSv, without bladder voiding and with bladder voiding, the effective dose ranged from 0.97–1.45 mSv.

Table A.5. Absorbed dose coefficient (ADC) and contribution to effective dose factor (CEDF) results for adult male model from OLINDA/EXM V1.0, with and without bladder voiding consideration.

Target Organ	**Without bladder voiding**		**With bladder voiding**	
	ADC (mGy/MBq)	**CED (mSv/MBq)**	**ADC (mGy/MBq)**	**CEDF (mSv/MBq)**
Adrenals	1.06E-03	5.31E-06	1.02E-03	5.11E-06
Brain	6.22E-04	3.11E-06	6.22E-04	3.11E-06
Breasts	6.25E-04	3.13E-05	6.18E-04	3.09E-05
Gallbladder Wall	1.44E-03	-	1.34E-03	-
LLI Wall	3.06E-03	3.67E-04	1.78E-03	2.13E-04
Small Intestine	1.79E-03	8.97E-06	1.31E-03	6.54E-06
Stomach Wall	1.78E-03	2.13E-04	1.71E-03	2.06E-04
ULI Wall	1.58E-03	7.92E-06	1.21E-03	6.07E-06
Heart Wall	8.68E-04	-	8.58E-04	-
Kidneys	9.86E-03	4.93E-05	9.78E-03	4.89E-05
Liver	1.16E-03	5.80E-05	1.11E-03	5.57E-05
Lungs	1.27E-03	1.52E-04	1.26E-03	1.52E-04
Muscle	1.24E-03	6.21E-06	9.22E-04	4.61E-06
Ovaries	2.78E-03	5.55E-04	1.60E-03	3.21E-04
Pancreas	1.08E-03	5.39E-06	1.03E-03	5.13E-06
Red Marrow	1.02E-03	1.23E-04	8.17E-04	9.80E-05
Osteogenic Cells	1.23E-03	1.23E-05	1.11E-03	1.11E-05
Skin	7.65E-04	7.65E-06	6.52E-04	6.52E-06
Spleen	1.04E-03	5.22E-06	1.00E-03	5.00E-06
Testes	2.10E-03	-	1.24E-03	-
Thymus	7.36E-04	3.68E-06	7.30E-04	3.65E-06
Thyroid	7.08E-04	3.54E-05	7.07E-04	3.53E-05
Urinary Bladder Wall	1.03E-01	5.15E-03	4.18E-02	2.09E-03
Uterus	5.45E-03	2.73E-05	2.68E-03	1.34E-05
Total Body	1.29E-03	-	9.82E-04	-
Total Effective Dose (mSv/MBq)	-	6.82E-03		3.32E-03

Results for [^{18}F]SFR101

The mice remainder residence time was calculated as the sum of residence times for blood, muscles, bones and carcass. Therefore, the human remainder residence time considers same organs in OLINDA/EXM V1.0.

Table A.6 shows the mass values from ICRP-23 used for mass scaling for both the dosimetric models and the S-factors for several organs available in OLINDA/EXM V1.0.

Table A.6. Mass values from ICRP-23 used for mass scaling for each organ in male/female dosimetric models and S-factors available in OLINDA/EXM V1.0.

Organ	Male		Female		
	Mass (g)	**S-factor[a] (mGy/MBq-s)**	**Mass (g)**	**S-factor[a] (mGy/MBq-s)**	**M_{mouse} (g)**
Brain	1400	4.62E-05	1200	5.28E-05	0.4090 ± 0.0731
Heart wall	330	1.54E-04	240	2.00E-04	0.1646 ± 0.0286
Kidneys	310	1.69E-04	275	1.83E-04	0.4204 ± 0.0425
Intestines contents	755		720		3.3000[c]
Left colon contents (LLI)	135	1.63E-04[b]	135	1.77E-04[b]	
Small Intestine Contents (SI)	400	5.48E-05[b]	375	6.61E-05[b]	
Right colon contents (ULI)	220	1.07E-04[b]	210	1.21E-04[b]	
Liver	1800	3.40E-05	1400	4.46E-05	1.8596 ± 0.2463
Lungs	1000	4.69E-05	800	5.93E-05	0.2193 ± 0.0319
Spleen	180	2.82E-04	150	3.39E-04	0.0963 ± 0.0285
Stomach contents	250	1.03E-04[b]	230	1.19E-04[b]	0.1000[c]
Bladder contents	120	1.31E-04[b]	88.4	1.85E-04[b]	0.1000[c]
Remainder	62686	1.28E-06	51808.6	1.60E-06	28.2063[d]
Whole body	68831	---	56912	---	34.8755 ± 3.4749

[a] S-factor refers to self-irradiation; [b] S-factor for LLI wall, SI wall, ULI wall, stomach wall and urinary bladder wall considering their contents as a source; [c] Mouse Stomach, intestines and bladder contents masses from OLINDA/EXM V2.0; [d] Remainder takes into account blood, muscles, bones and carcass.

Residence times used in OLINDA/EXM V1.0 are included in table A.7. Organs with highest values are intestines contents, liver and stomach contents.

Absorbed and effective dose values for adult male and female dosimetric models from OLINDA/EXM V1.0 are listed in table A.8. In this case, LLI wall, SI wall and ULI wall show high ADC values, probably associated with the excretion path of the radiopharmaceutical. The mean effective dose obtained from OLINDA/EXM V1.0 using the male and female dosimetric models is 6.55x10^{-3} μSv/MBq and 8.77x10^{-3} μSv/MBq, respectively. Considering CUDIM protocols the mean effective dose is 2.29 mSv and 3.07 mSv, for the male and female dosimetric models, respectively.

Table A.7. Residence times (T) used for dosimetric estimations in OLINDA/EXM V1.0.

Organ	**T_{male}(h)**	**T_{female}(h)**
Brain	2.37E-04	2.46E-04
Heart wall	9.67E-05	8.51E-05
Kidneys	4.84E-03	5.19E-03
Intestines contents	1.96E-01	2.27E-01
Left colon contents (LLI)	3.50E-02	4.26E-02
Small Intestine Contents	1.04E-01	1.18E-01
Right colon contents (ULI)	5.71E-02	6.62E-02
Liver	5.69E-02	5.35E-02
Lungs	2.25E-03	2.18E-03
Spleen	5.19E-05	5.23E-05
Stomach contents	2.24E-02	2.49E-02
Bladder contents	4.65E-03	4.15E-03
Remainder	3.90E-02	3.90E-02

Table A.8. Absorbed dose coefficient (ADC) and contribution to effective dose factor results (CEDF) for adult male model from OLINDA/EXM V1.0.

	Male		**Female**	
Organ	**ADC (mGy/MBq)**	**CEDF (mSv/MBq)**	**ADC (mGy/MBq)**	**CEDF (mSv/MBq)**
Adrenals	1.46E-03	3.65E-06	1.91E-03	4.78E-06
Brain	8.92E-05	2.23E-07	1.13E-04	2.82E-07
Breasts	3.96E-04	1.98E-05	5.17E-04	2.59E-05
Gallbladder Wall	3.81E-03	-	5.24E-03	-
LLI Wall	2.29E-02	2.74E-03	3.04E-02	3.65E-03
Small Intestine	2.35E-02	5.87E-05	3.22E-02	8.04E-05
Stomach Wall	9.85E-03	1.18E-03	1.28E-02	1.54E-03
ULI Wall	2.65E-02	6.63E-04	3.50E-02	8.75E-04
Heart Wall	7.97E-04	-	1.07E-03	-
Kidneys	4.55E-03	1.14E-05	5.55E-03	1.39E-05
Liver	7.80E-03	3.90E-04	9.78E-03	4.89E-04
Lungs	9.26E-04	1.11E-04	1.22E-03	1.46E-04
Muscle	9.66E-04	2.42E-06	1.32E-03	3.29E-06
Ovaries	4.91E-03	9.83E-04	7.22E-03	1.44E-03
Pancreas	2.13E-03	5.32E-06	2.84E-03	7.11E-06
Red Marrow	1.33E-03	1.60E-04	1.75E-03	2.10E-04
Osteogenic Cells	8.15E-04	8.15E-06	1.13E-03	1.13E-05
Skin	4.47E-04	4.47E-06	5.92E-04	5.92E-06
Spleen	1.27E-03	3.16E-06	1.70E-03	4.25E-06
Testes	5.30E-04	-	-	-
Thymus	3.80E-04	9.50E-07	4.98E-04	1.24E-06
Thyroid	2.35E-04	1.17E-05	2.90E-04	1.45E-05
Urinary Bladder Wall	3.63E-03	1.82E-04	4.76E-03	2.38E-04
Uterus	3.43E-03	8.58E-06	4.92E-03	1.23E-05
Total Body	1.48E-03	-	2.00E-03	-
Total Effective Dose (mSv/MBq)	-	6.55E-03		8.77E-03

Figure A.1 shows reconstructed images using all correction methods, without post-filter, for different updates (iterations*subsets), for a spherical source placed in the centre of a phantom filled with water and without background activity. All profiles are for the same position in the "y-axis" for each image on the second column of the figure. Gray values in these profiles are related to the number of counts present in each pixel of the line.

As the number of updates increases, a discontinuity of the profile can be seen, which may be related to Gibbslike artifacts (for updates higher than 80). Moreover, as the number of updates increases, the spheres become clear and well defined. Also, the maximal number of counts remains constant as the number of updates increases.

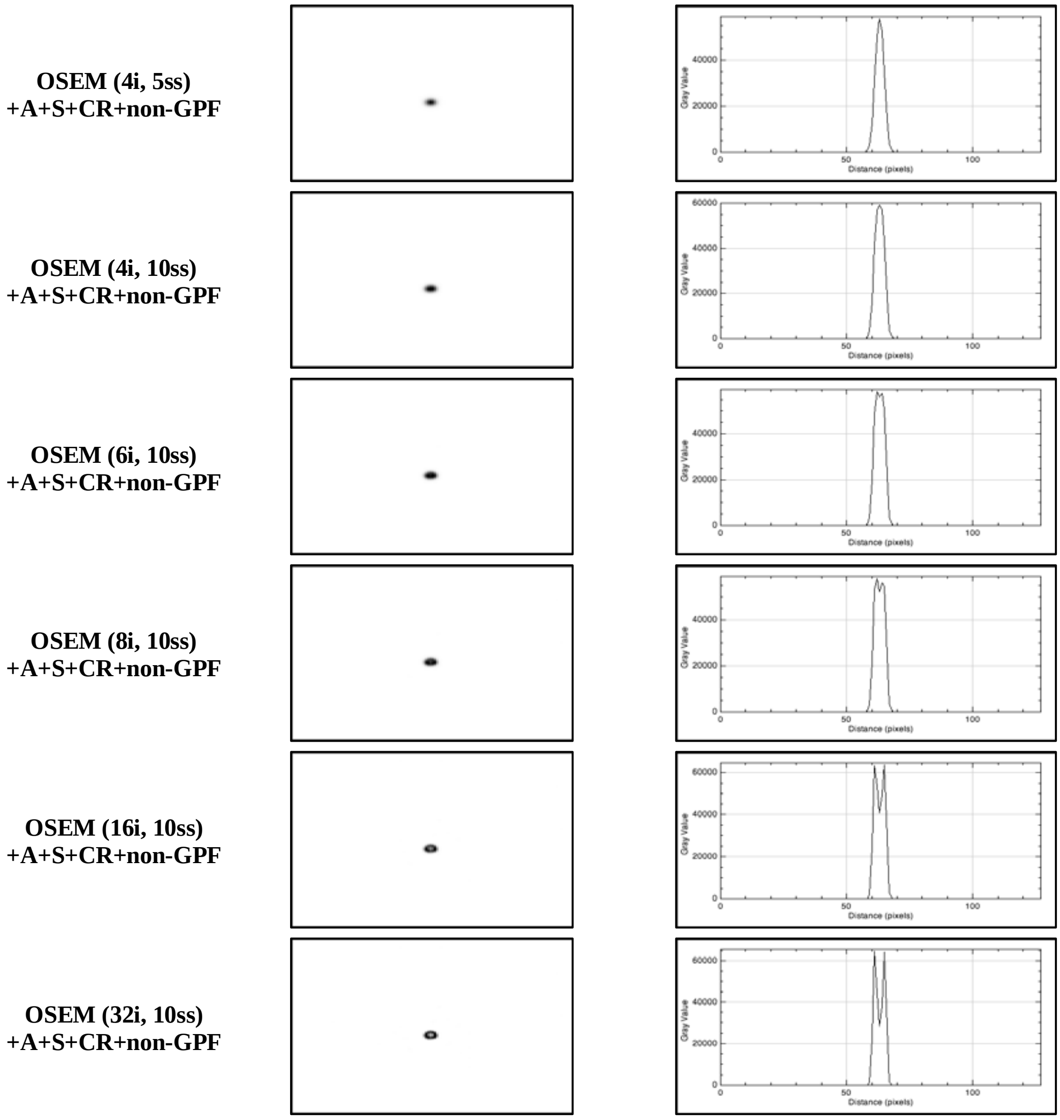

Figure A.1: OSEM reconstructed images of a source in the centre of a phantom filled with water without background activity using attenuation, collimator response and scatter corrections and non-Gaussian post-filter. Also, line-profile across the sphere source.

Figure A. 2 is similar to figure A.1 but using the Gaussian post-filter set at 1.0 cm, for different updates (iterations*subsets), for a spherical source placed in the centre of a phantom filled with water and without background activity is shown. As the number of update increases, the discontinuity in the profile starts to appear at 320 updates.

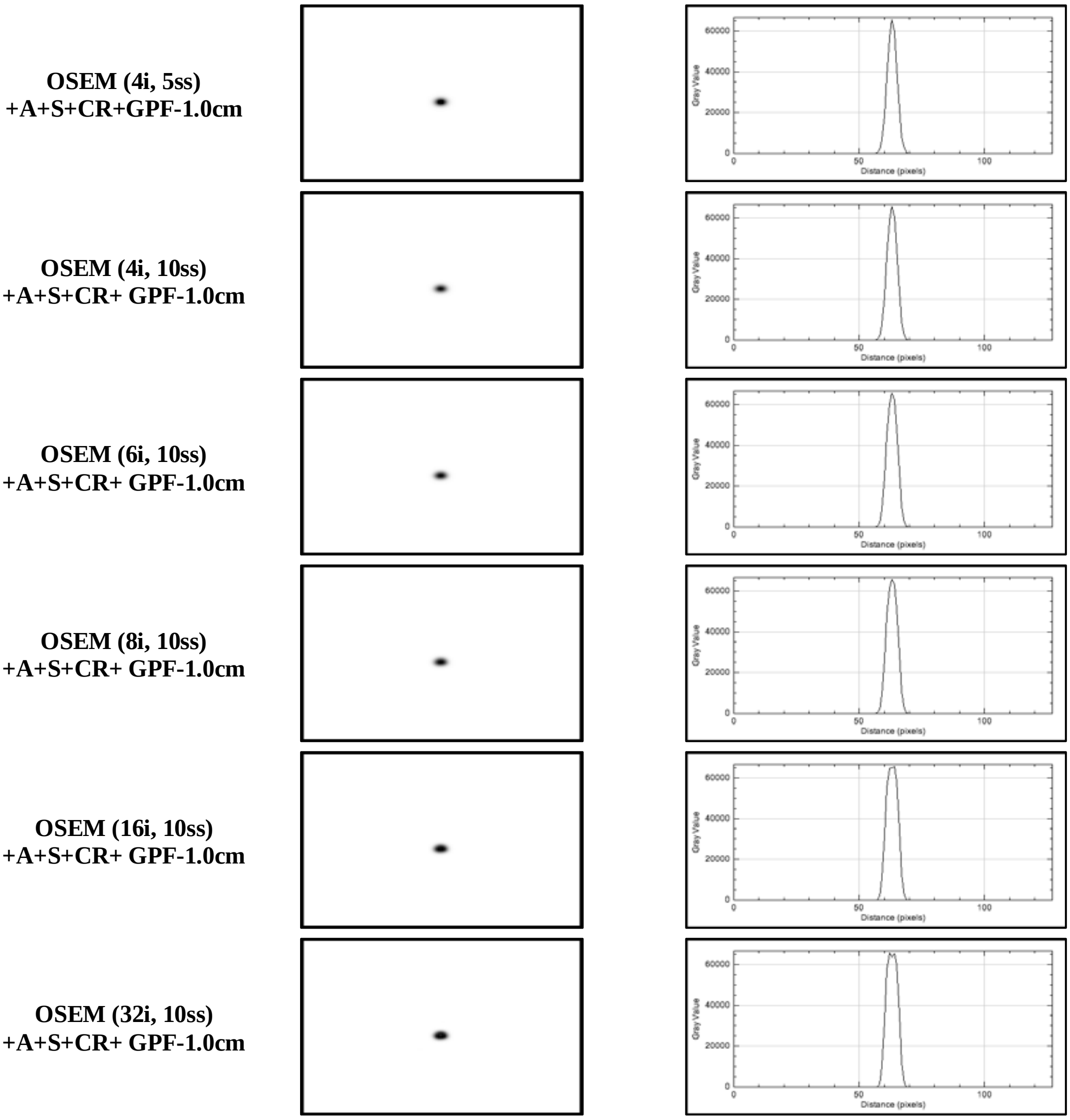

Figure A.2: OSEM reconstructed images of a source in the centre of a phantom filled with water without background activity using attenuation, collimator response and scatter corrections and Gaussian post-filter set at 1.0 cm. Also, line-profile across the sphere source.

Figure A.3 shows results for OSEM reconstructed images of a phantom without background activity, using all correction methods and non-Gaussian post-filter. All images are for the same slice of the reconstructed phantom. Same figure shows profiles generated drawing a line across the biggest sphere source; all profiles are for the same position in the “y-axis” for each image, on the second column of the figure. Gray values in these profiles are related to the number of counts present in each pixel of the line. As the number of updates increases more clearly and well defined all spheres can be seen, also the maximal number of counts in the profile decreases as the number of updates increases. The same discontinuity showed in figure A.1 can be seen for updates higher than 80.

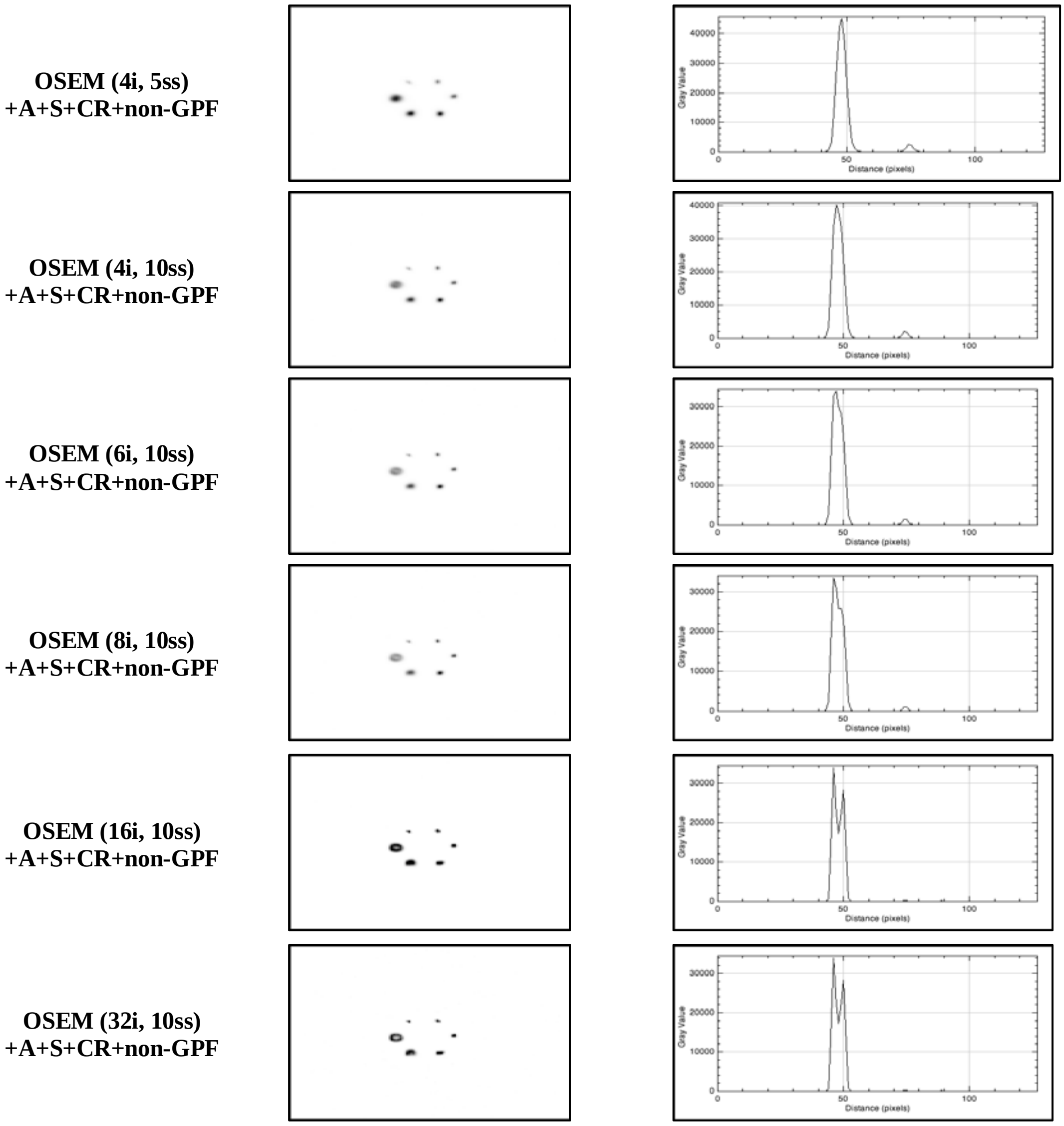

Figure A.3: OSEM reconstructed images of phantom without background activity using attenuation, collimator response and scatter corrections and non-Gaussian post-filter. Also, line-profile across the biggest sphere source.

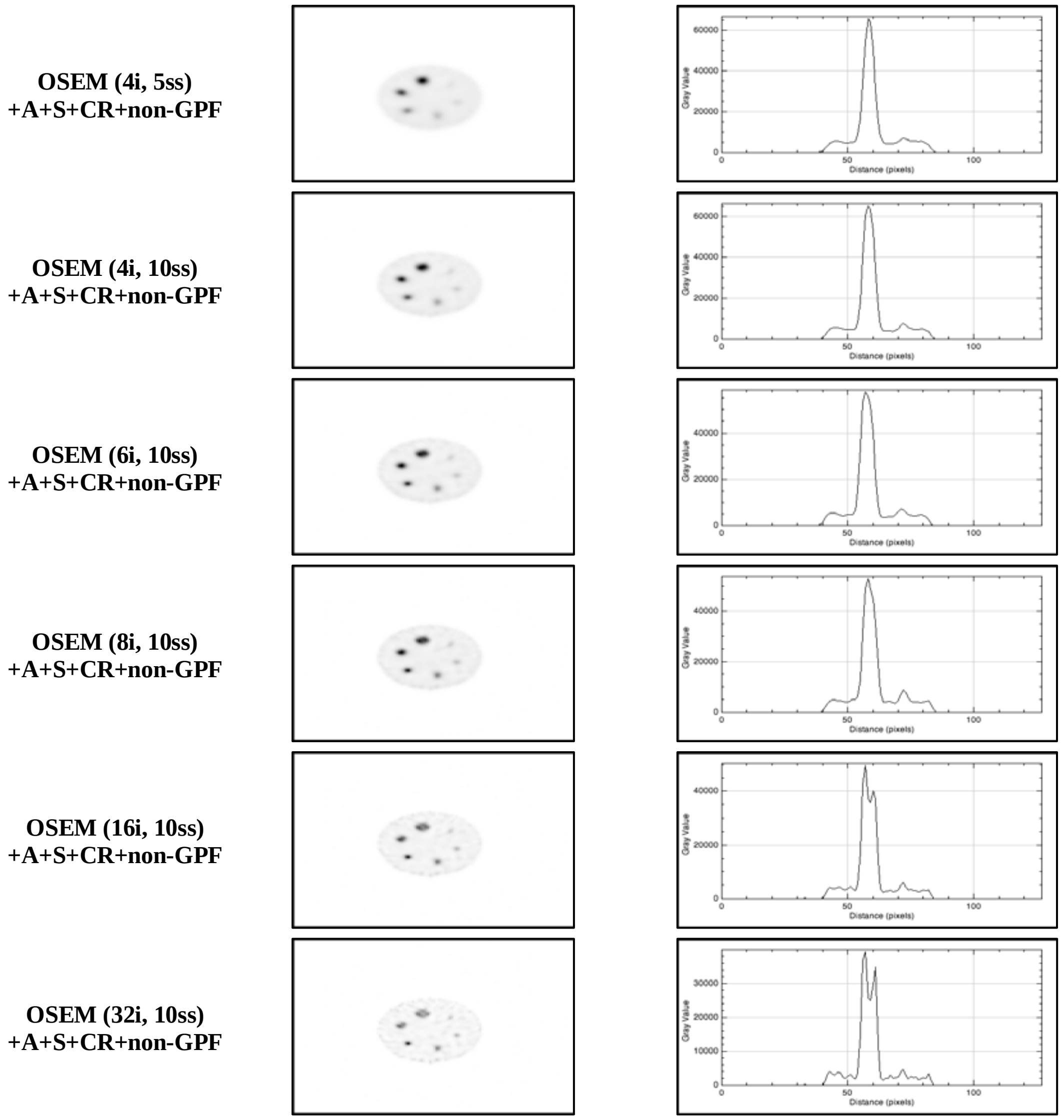

Figure A.4: OSEM reconstructed images of phantom with background activity using attenuation, collimator response and scatter corrections and non-Gaussian post-filter. Also, line-profile across the biggest sphere source.

On the other hand, figure A.4 shows results for OSEM reconstructed images of a phantom with background activity, using all correction methods and non-Gaussian post-filter. All images are for the same slice of the phantom reconstruction. Also, profiles were generated drawing a line across the biggest sphere source. Here as the number of updates increases all spheres can be seen more clearly and well defined, also contrast is improved and for 320 updates the image of the phantom looks “less smooth” comparing to the one at 20 updates.

Looking at the generated profiles, which are coming from the same position in the “y-axis” for each image on the second column, as previously shown, gray values in these profiles are related to the number of counts present in each pixel of the line. Here one can see that as the number of updates increases the maximal number of counts in the profile decreases and the same discontinuity showed in figure A. 1 can be seen for updates higher than 80, however, the level of discontinuity with background activity is not as significant as it was shown without background activity.

A

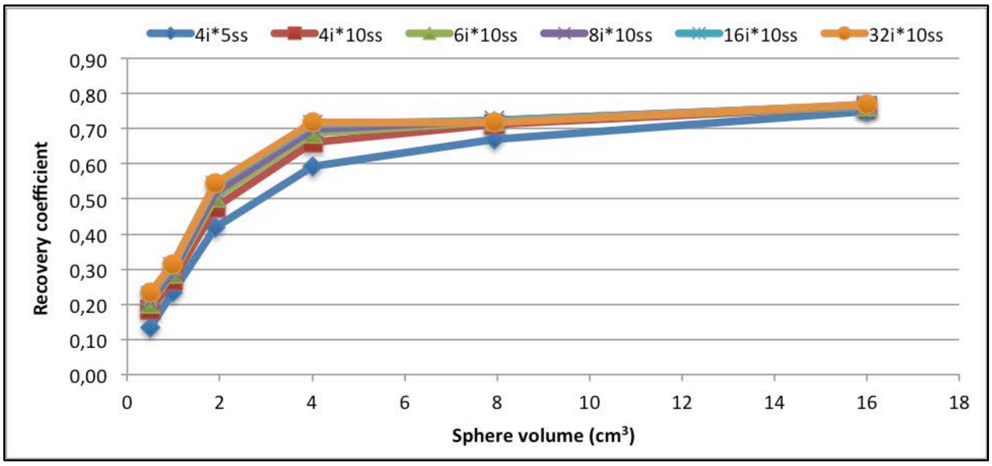

B

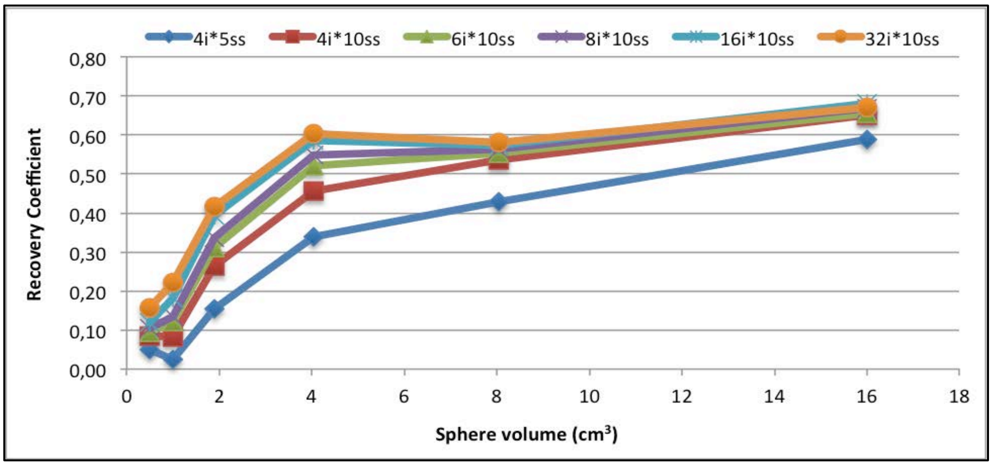

Figure A.5: Recovery coefficient for OSEM reconstructed images of a phantom using attenuation, collimator response and scatter corrections with Gaussian post-filter 1.0 cm. A: without background activity. B: with background activity.

Figure A.5, shows the recovery coefficient results using a phantom with and without background activity, with Gaussian post-filter set at 1.0 cm. In both cases, images were reconstructed using OSEM, applying all correction methods. For figure A.5.A, as the number of updates increase, the recovery coefficient increase, for updates equal to 60, the recovery coefficient reaches 65% for the 4 ml sphere and 80% for the 16 ml sphere, for updates equal to 320 the recovery coefficient varies from 68% to 77% for the same sphere volumes. In the case of figure A.5.B, for the 2 ml sphere the recovery variation varies between 16% and 42%, for the 4 ml sphere its variation is between 34% and 60%, for the 8ml sphere its variation is between 43% and 58 %, for the 16 ml sphere its variation is between 59% and 67%.

These values were generated just to benchmark the SPECT/CT system in the case of using a similar reconstruction method.

Table A.9. Organ mass (g) results for female patient for each workstation.

Organ/Software	First treatment cycle					
	DTK	HDM	STRATOS	PDOSE	Mean (g)	Standard deviation
Liver	1643.0	1656.5	1560.3	1639.3	1624.8	43.6
Spleen	109.2	103.0	112.4	99.0	105.9	6.0
Kidneys	273.0	271.8	279.3	270.8	273.7	3.8
Organ/Software	Second treatment cycle					
	DTK	HDM	STRATOS	PDOSE	Mean (g)	Standard deviation
Liver	1643.0	1551.3	1476.6	1540.6	1552.9	68.6
Spleen	116.6	103.1	108.1	98.2	106.5	7.8
Kidneys	281.0	260.6	294.0	266.1	275.4	15.1

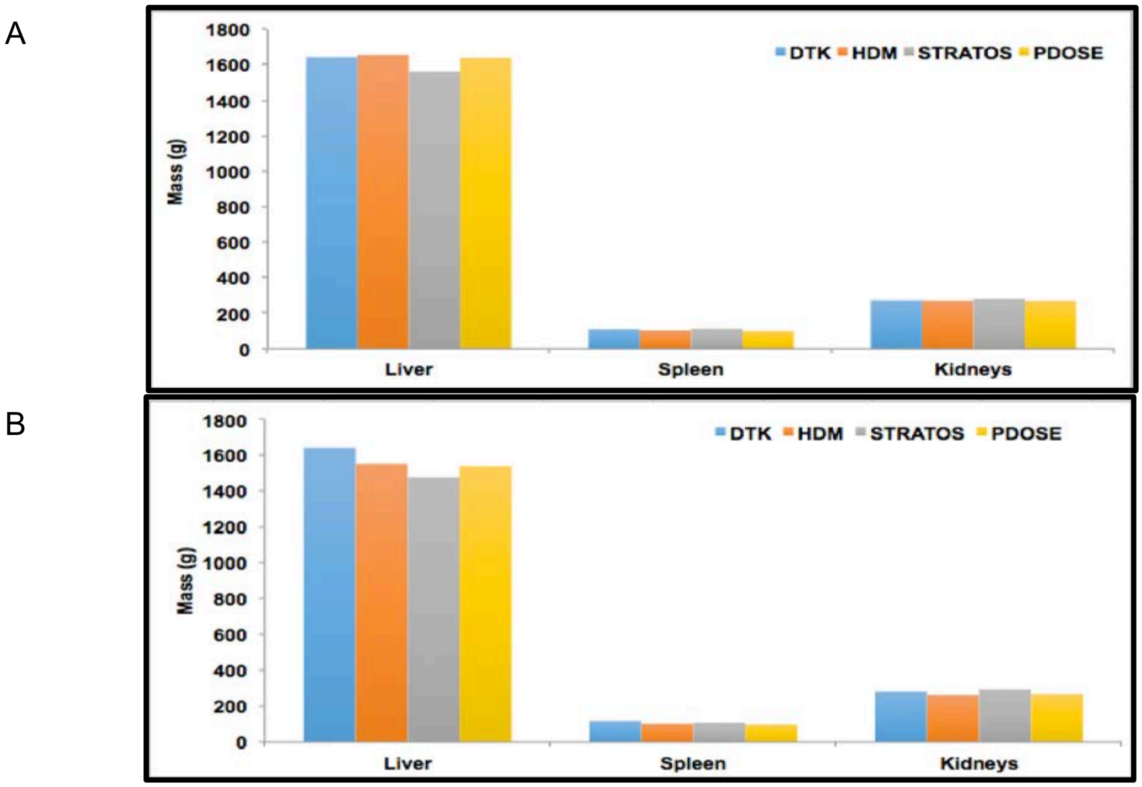

Figure A.6: Mass for liver, spleen and kidneys. Female patient, A: first treatment, B: second treatment. Own creation.

Table A.10. Residence times (h) results for female patient for each workstation.

Organ/Software	First treatment cycle					
	DTK	HDM	STRATOS	PDOSE	Mean (h)	Standard deviation
Liver	39.0	45.7	41.7	45.2	42.9	3.2
Spleen	0.6	0.8	0.6	0.7	0.7	0.1
Kidneys	1.1	1.6	1.6	1.6	1.5	0.2
Organ/Software	**Second treatment cycle**					
	DTK	**HDM**	**STRATOS**	**PDOSE**	**Mean (h)**	**Standard deviation**
Liver	21.0	24.3	24.7	24.8	23.7	1.8
Spleen	0.9	0.9	0.9	0.9	0.9	0.1
Kidneys	1.5	1.7	1.9	1.7	1.7	0.2

Table A.11. Mean absorbed dose (Gy) results for female patient for each workstation.

Organ/Software	First treatment cycle					
	DTK	HDM	STRATOS	PDOSE	Mean (Gy)	Standard deviation
Liver	14.5	17.8	17.5	16.9	16.6	1.5
Spleen	3.6	4.5	3.4	4.3	3.8	0.5
Kidneys	2.5	3.7	3.6	3.7	3.3	0.6
Organ/Software	**Second treatment cycle**					
	DTK	**HDM**	**STRATOS**	**PDOSE**	**Mean (Gy)**	**Standard deviation**
Liver	7.8	10.0	10.7	10.0	9.5	1.2
Spleen	4.6	5.1	5.0	5.9	4.9	0.6
Kidneys	3.2	4.0	4.2	4.1	3.8	0.4

Table A.12. Organ mass (g) results for male patient for each workstation.

Organ/Software	**First treatment cycle**					
	DTK	**HDM**	**STRATOS**	**PDOSE**	**Mean (g)**	**Standard deviation**
Liver	1208.4	1397.6	1383.3	1366.0	1338.8	87.9
Spleen	244.9	239.6	254.4	234.0	243.2	8.7
Kidneys	482.0	390.8	466.2	408.9	437.0	44.0
Organ/Software	**Second treatment cycle**					
	DTK	**HDM**	**STRATOS**	**PDOSE**	**Mean (g)**	**Standard deviation**
Liver	1282.6	1303.9	1304.9	1306.3	1299.4	11.3
Spleen	259.7	239.9	272.4	234.5	251.6	17.6
Kidneys	483.0	402.7	473.6	410.2	442.3	41.8

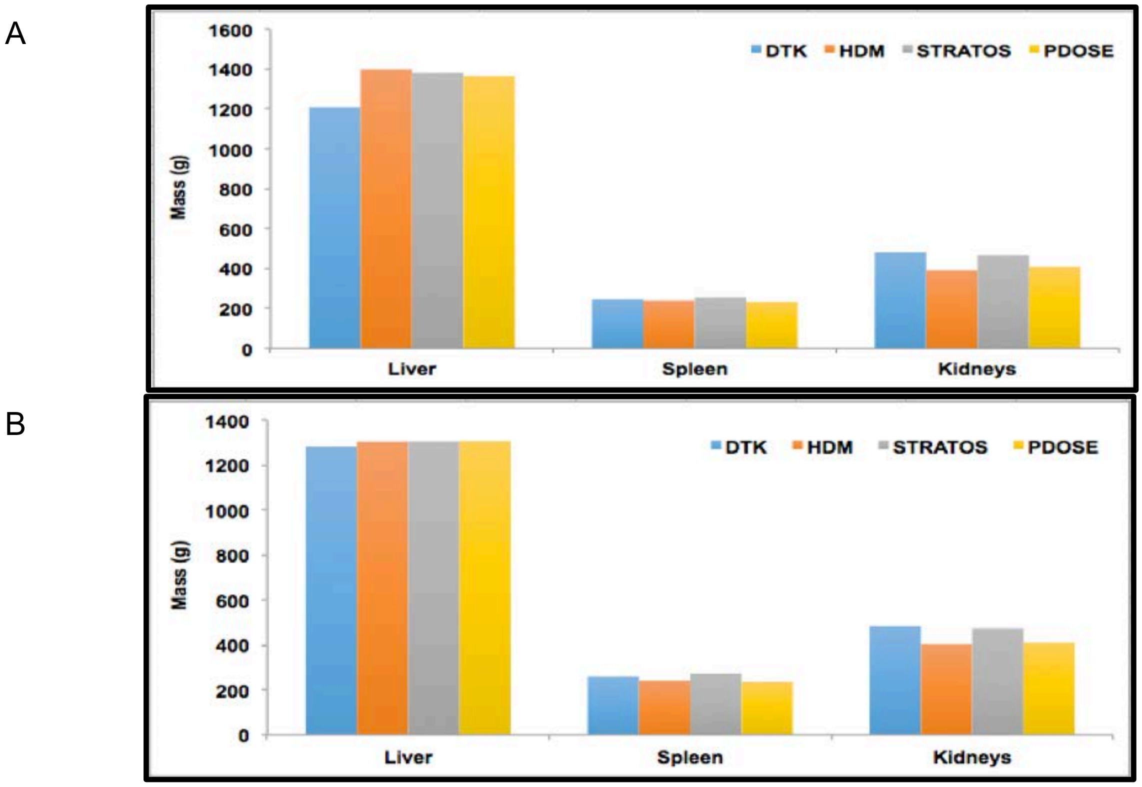

Figure A.7: Mass for liver, spleen and kidneys. Male patient, A: first treatment, B: second treatment. Own creation.

Table A.13. Residence times (h) results for male patient for each workstation.

Organ/Software	First treatment cycle					
	DTK	HDM	STRATOS	PDOSE	Mean (h)	Standard deviation
Liver	1.9	2.8	3.2	2.7	2.7	0.6
Spleen	1.2	1.6	1.7	1.5	1.5	0.2
Kidneys	1.4	1.5	1.9	1.7	1.6	0.2
Organ/Software	**Second treatment cycle**					
	DTK	**HDM**	**STRATOS**	**PDOSE**	**Mean (h)**	**Standard deviation**
Liver	2.6	3.2	3.1	3.0	3.0	0.3
Spleen	2.1	2.2	1.9	2.1	2.1	0.1
Kidneys	1.9	2.0	0.9	2.0	1.7	0.5

Table A.14. Mean absorbed dose (Gy) results for male patient for each workstation.

Organ/Software	First treatment cycle					
	DTK	HDM	STRATOS	PDOSE	Mean (Gy)	Standard deviation
Liver	1.0	1.1	1.5	1.2	1.2	0.2
Spleen	2.9	4.7	4.3	4.0	4.0	0.8
Kidneys	1.7	2.5	2.6	2.5	2.3	0.4
Organ/Software	**Second treatment cycle**					
	DTK	**HDM**	**STRATOS**	**PDOSE**	**Mean (Gy)**	**Standard deviation**
Liver	1.2	1.3	1.5	1.4	1.4	0.1
Spleen	4.9	6.6	4.4	5.6	5.3	0.9
Kidneys	2.3	3.3	1.2	3.0	2.3	1.0

Journal papers

Santoro L, Mora-Ramirez E, Trauchessec D, Chouaf S, Eustache P, Pouget JP, Kotzki PO, Bardiès M, Deshayes E. ***“Implementation of patient dosimetry in the clinical practice after targeted radiotherapy using [^{177}Lu-[DOTATO,Tyr3]-octreotate]”***. EJNMMI Research. 2018; 8:103.

Zoppolo F, Mora-Ramirez E, Reyes AL, Vasilskis E, Paolino A, Porcal W, Oliver P, Savio E, Bardies M, Engler H. ***“Biological and dosimetric evaluation of [^{11}C]S-adenosyl methionine as a potential agent for prostate cancer diagnosis”***. Cancer Research Frontiers. 2018;4(1):27-44. DOI:10.17980/2018.27.

Kreimerman I, Mora-Ramirez E, Reyes AL, Bardies M, Savio E, Engler H. ***“Dosimetry and toxicity studies of the novel sulfonamide derivative of Sulforhodamine 101([^{18}F]SRF101) at a preclinical level”***. Curr. Radiopharm. 2019;12(1): 40-48. DOI: 10.2174/1874471011666180830145304.

Salabert A-S, Mora-Ramirez E, Beaurain M, Alonso M, Fontan C, Tahar HB, Boizeau ML, Tafani M, Bardiés M, Payoux P. ***“Evaluation of [^{18}F] FNM biodistribution and dosimetry based on whole-body PET imaging of rats”***. Nucl. Med. Biol. 2018;59:1–8. DOI: 10.1016/j.nucmedbio.2017.12.003

Estrada-Lobato E., Alonso-Farto J.C., De Haro-Del Moral F.J., Cerci J.J., Rodriguez-Perez J.L., Vazquez-Peña E., Godinho F., Mora-Ramirez E., Tinoco-Mezquita F., Mut-Bastos F., Savio-Quevedo E.O., Penedo-Ojea M., Ramirez-Quijada R., ***“Sesion Medicina Nuclear”***, Radioproteccion, 87: 34-39, 2017.

International conferences

Kayal G, Chauvin M, Mora-Ramirez E, Struelens L, Bardiès M. (Abstract). **Modelling SPECT auto-contouring acquisition for 177Lu Molecular RadioTherapy (MRT) using new developments in GATE/GEANT4**. MCMA, Montreal, Canada, 17-21 June 2019. Oral Presentation by Gunjan Kayal.

Mora-Ramirez E, Cassol E, Ocampo-Ramos JC, Chouaf S, Trauchessec D, Pouget P, Kotzki P, Santoro L, Deshayes E, Bardiès M. (**Abstract – OP-557). "Comparsion between PLANET®Dose and OLINDA/EXM V2.0 in organ-based absorbed doses estimations for patients treated with Lutathera®"**. Eur J Nucl Med Mol Imaging. 2018, 45 (Suppl 1): S180. Oral presentation.

Leek F, Gregory R, Newbold K, Verburg FA, Luster M, Schurrat T, Lassmann M, Eberlein U, Buck AK, Lapa C, Bardiès M, Mora-Ramirez E, Vallot D, Courbon F, Vija L, Flux G. (**Abstract – EP-0166). "The MEDIRAD multi-national I-131 Dosimetry study for thyroid ablation and adjuvant therapy"**. Eur J Nucl Med Mol Imaging. 2018,45 (Suppl 1): S359. Poster presentation.

Mora-Ramirez E, Ocampo-Ramos JC, Cassol E, Stiles B, Chouaf S, Trauchessec D, Pouget P, Kotzki P, Santoro L, Deshayes E, Bardiès M. (**Abstract – EP-0170). "Red Marrow dosimetry without whole-body measurements for patients treated with Lutathera®"**. Eur J Nucl Med Mol Imaging. 2018,45 (Suppl 1): S361. Poster presentation.

Savio E, Kreimerman I, Mora-Ramirez E, Reyes A, Bardiès M, Engler H. (**Abstract – EP-0836).** "**Toxicological and dosimetric assessement of a ^{18}F-Sulforhodamine 101 derivative as a novel radiotracer for PET imaging of astrocytosis**". Eur J Nucl Med Mol Imaging. 2018,45 (Suppl 1): S638. Poster presentation.

Mora-Ramirez E, Santoro L, Trauchessec D, Chouaf S, Deshayes E, Pouget P, Kotzki P, Bardiès M. (**Abstract – EP-0887). "SPECT/CT calibration using clinical dosimetry workstations for peptide receptor radionuclide therapy (PRRT) in patients treated with 177Lu-DOTATATE"**. Eur J Nucl Med Mol Imaging. 2017,44 (Suppl 1): S809. Poster presentation.

Mora-Ramirez E, Santoro L, Trauchessec D, Chouaf S, Deshayes E, Pouget P, Kotzki P, Bardiès M. (**Abstract – EP-0888). "Dosimetric estimations using commecial workstations for peptide receptor radionuclide therapy (PRRT) in patients treated with 177Lu-DOTATATE"**. Eur J Nucl Med Mol Imaging. 2017,44 (Suppl 1): S810. Poster presentation.

Estrada-Lobato E, Alonso-Farto JC, De Haro-Del Moral FJ, Cerci JJ, Rodriguez-Perez JL, Vazquez-Peña E, Godinho F, Mora-Ramirez E, Tinoco-Mezquita F, Mut-

Bastos F, Savio-Quevedo EO, Penedo-Ojea M, Ramirez-Quijada R, **“Sesion Medicina Nuclear”**, Radioproteccion, 87: 34-39, 2017. <u>Oral presentation</u>.

National conferences

Mora-Ramirez E, Cassol E, Santoro L, Chouaf S, Trauchessec D, Pouget P, Kotzki P, Deshayes E, Bardiès M. ***"*Comparaison des estimations de dose absorbée à l'organe obtenues avec PLANET®Dose et OLINDA/EXM V2.0 chez des patients traités par radiopeptidothérapie (RPT) au Lutathera®*"***. 57$^{\text{èmes}}$ journées scientifiques de la SFPM, Toulouse, France, 13-15, June 2018. Oral presentation.

Mora-Ramirez E, Cassol E, Santoro L, Chouaf S, Trauchessec D, Pouget P, Kotzki P, Deshayes E, Bardiès M. **"Comparison of organ-based absorbed doses estimations by using PLANET®Dose and OLINDA/EXM V2.0 in patients with peptide receptor radionuclide therapy (PRRT) treated with Lutathera®"** (Abstract-60). Physica Medica, 2018, 56 (Suppl 1) : 34.

Mora-Ramirez E, Santoro L, Trauchessec D, Chouaf S, Pouget P, Kotzki P, Deshayes E, Bardiès M. ***"Absorbed dose calculation in patients treated with 177Lu-DOTATATE for peptide receptor radionuclide therapy".*** *2nd* Workshop SFPM: Bridging the gap between imaging and therapy. Fort-Mahon, France, 10-13 September 2017. Oral presentation.

Mora-Ramirez E, Bardiès M. "***Absorbed dose estimation from preclinical biokinetic data using different commercially available fitting software".*** 1st Workshop SFPM: Radiotherapies modelling, Luz Saint Sauveur, France, 21-24. September 2016. Oral presentation.

Agradecimientos

Primero que todo agradecer al todo poderoso por dejarme llegar a este momento de mi vida, algo con lo que soñé por muchos años y por fin se hace realidad gracias a él. A la virgencita de los Ángeles por cuidarme en este camino.

A mi bella esposa, Viviana Meoño Alvarado, GRACIAS por ayudarme en tantas cosas, por ser mi amiga, mi confidente, por aceptar compartir esta aventura en Toulouse. Gracias macha, te amo mucho, te estoy eternamente agradecido.

A mi hijo, Alejandro Mora Cruz, has sido una de las fuentes de inspiración más grandes en mi vida para seguir siempre adelante. Te amo nano.

A mi madre, mis hermanos, mi hermana, mi tía Gis y el resto de mi familia, gracias por estar siempre a mi lado. Los amo mucho.

A la familia Meoño-Alvarado, Don Mario, Doña Lidieth, Monica, Marito, Mil gracias por todo, les estoy eternamente agradecido.

Quiero agradecer profundamente al Ph.D. Ralph García Vindas y a la M.Sc. Patricia Mora Rodríguez por pensar en mi para poder realizar estos estudios en aras de poder colaborar con en el proyecto Ciclotrón – Radiofarmacia – PET/CT de la Universidad de Costa Rica. Gracias por su confianza y apoyo.

A las Asambleas de la Escuela de Física y de la Escuela de Tecnologías de Salud, al Sistema de Estudios de Postgrado (SEP) y a la Oficina de Asuntos Internacionales de la Universidad de Costa Rica, por apoyarme con la beca de estudios, por todas las gestiones que se realizaron para que yo pudiera estar acá.

A la Dra. Isabel Berrocal Gamboa, al M.Sc. José Carvajal Mejías y al Lic. Mario Meoño Alvarado, que me sirvieron como fiadores ante la Universidad de Costa Rica, gracias por toda su confianza y apoyo. Les estoy eternamente agradecido.

Al Institut Français d’Amerique Centrale (IFAC) a todo el personal que ahí trabaja, les agradezco por la beca que se me brindo. Un agradecimiento especial a doña Yadira Vargas, por su apoyo incondicional durante estos estudios.

Quiero agradecer de todo corazón a mi tutor Manuel Bardiès, por aceptarme en su equipo de trabajo, por darme la oportunidad de poder desarrollar los estudios doctorales. Gracias por todo Manu, he aprendido francés con un buen acento, he aprendido mucho de la cultura francesa y he podido apreciar lo hermoso que es este país. Espero haber retribuido con mucho trabajo toda la confianza que depositaste en mi. Para mi tu eres un gran maestro y ejemplo académico a seguir, te estaré eternamente agradecido.

A todos los miembros permanentes del equipo, a Marie-Claude Bordage por siempre aceptar una buena taza de café y darme el soporte necesario en lo referente a la administración francesa universitaria. A Emmanuelle Cassol por todas esas horas donde pudimos discutir de diversos temas de medicina nuclear, no solo los relacionados a la tesis, aprendí mucho de esas conversaciones. A Luc Simon, a Laure Vieillevigne gracias por estar ahí, el equipo no seria igual sin ustedes. A todos los otros miembros del equipo gracias.

A todo el personal administrativo del CRCT, en especial a Sébastien Gibert, Laurence Granier y Marie-Hélène Lalaux, gracias por toda la ayuda que me brindaron durante mi estancia.

A Anne-Sophie Salabert mil gracias por toda la confianza depositada en mi para poder desarrollar los cálculos dosimétricos del fármaco que se desarrolló en el CHU-PURPAN. Estoy eternamente agradecido contigo.

Al servicio de Medicina Nuclear del Institut de Cancérologie de Montpellier (ICM), en especial a Lore Santoro y Emmanuel Deshayes, por toda la amabilidad que tuvieron conmigo durante mi estancia en el servicio. Gracias por darme la oportunidad de trabajar con ustedes para mi fue todo un honor, un placer y un gran aprendizaje, les estaré eternamente agradecido. A Soufiane Chouaf y Dorian Trauchessec por toda la ayuda que me brindaron durante este trabajo.

A Dr. Eduardo Savio, Dra. Florencia Zoppolo, Dra. Ingrid Kreimerman y todo el equipo del CUDIM por darme la oportunidad de realizar los cálculos dosimétricos de los dos fármacos

desarrollados en su centro, para mi fue todo un honor y placer colaborar con ustedes. Estoy eternamente agradecido con ustedes.

A Sara Beilla GRACIAS por todo el apoyo que me diste acá, fuiste como un ángel para mi, me ayudaste muchísimo cuando más lo necesitaba, siempre estaré en deuda contigo. Gracias por todos tus consejos. Un gran abrazo.

A Sara Marcatili, gracias por todo el tiempo dedico a atender mis preguntas, gracias por los consejos brindados.

A Antonis Tsologiannis, gracias compartir tus ideas conmigo. Un gran abrazo.

A Gustavo Costa gracias por darme consejos para acomodarme acá en Toulouse y tranquilizarme en algunos momentos difíciles. Gracias por ensenarme a ver de una manera diferente el café. Gracias por toda la ayuda que me diste con GATE. Un gran abrazo.

A Richard Brown, gracias por ser el vegetariano que eres, por escucharme y por los consejos que me diste, gracias por recibirme en tu casa, me sentí como en la mía, gracias por todo mi amigo. Un gran abrazo.

A Frederic Chatrie, gracias por enseñarme a esquiar, por tus consejos, tu ayuda. Un gran abrazo.

A Jonathan Tranel, gracias por siempre pensar en mi para hacer una caminata, de verdad que disfrute mucho de los paisajes por los que pudimos caminar. Gracias por toda ayuda.

A Julien Bordes, gracias por hacerme sentir como en casa, mi hermano francés, por escucharme, por todos los consejos que me diste y por mostrarme un poco de la cultura francesa. Un gran abrazo.

A Tony Younes, mi hermano Libanes, gracias por todo, especialmente por las conversaciones en el CRCT, por las risas y los buenos chistes, por también hacerme sentir en casa, por escucharme, darme tus consejos y por mostrarme un poco de la cultura libanesa. Un gran abrazo.

A Maxime Chauvin, gracias por todo lo que he podido aprender de ti, por compartir tantos buenos momentos y buenas conversaciones. Gracias por tus enseñanzas de Python y GATE. Un gran abrazo.

A Ana Rita Pereira, gracias por escucharme, por los consejos que me diste y por toda la ayuda que me brindaste.

A Juan Camilo Ocampo Ramos, Parce, mi hermano colombiano, gracias por las risas y los buenos chistes, por todas las conversaciones que tuvimos, no solo las académicas, todas fueron muy provechosas, te estoy eternamente agradecido, aprendí muchísimo de ti. Un gran abrazo.

A Joey Labour, espero poder celebrar dentro de poco la finalización de tus estudios. Un gran abrazo.

A Gunjan Kayal, mi hermana de India, gracias por compartir tu cultura, la comida, por escucharme y todos tus consejos, espero poder celebrar dentro de poco la finalización de tus estudios. Un gran abrazo.

A Jerémy Lester y Alex Vergara, gracias por todos los momentos compartidos.

A todas esas personas formidables que pude conocer del cuarto piso del CRCT (Salvatore, Sabina, Maha, Carlos, Clara, Laura, Vincent, Mme. Weulersse, Léa), gracias por todos los momentos compartidos.

A mis queridos compatriotas Maria, Salome, Estefanny, Esteban Vargas, Esteban González, Esteban Muñoz, Sebastien, Alfonso, Kerry, Aaron, Juan Jose, Miguel, Jean-Carlo Augusto y a mis queridos amigos franceses Muriel, Olivier, Clara et Benoit……..PURA VIDA!!!!!!.

Dosimetría de radiofármacos en terapia dirigida con radionúclidos

Resumen

La medicina nuclear es una especialidad médica en la cual una de sus aplicaciones es estudiar la fisiología de los órganos y el metabolismo de diversos tipos de tumores. Productos farmacéuticos marcados con radio-nucleídos (radio-fármacos) son estudiados a nivel pre-clínico antes de ser usados en seres humanos. Roedores son generalmente utilizados para estudiar la biocinética del trazador en un grupo de órganos predefinidos. La extrapolación de los resultados de estos estudios de animales a humanos provee una estimación del comportamiento de los radio-fármacos y de la irradiación entregada clínicamente. Tres nuevos radiofármacos fueron desarrollados, uno en Francia (CHU-Hôpital Purpan) y dos en Uruguay (CUDIM). Dos con el objetivo de estudiar el cerebro y uno para el diagnóstico de cáncer de próstata. En este trabajo, la extrapolación de los resultados preclínicos es presentada, las dosis absorbidas y efectivas son estimadas utilizando los programas OLINDA/EXM V1.0, V2.0 e IDAC2.1. Las diferencias entre los resultados de cada programa son discutidas.

A nivel clínico, los protocolos dosimétricos incluyen la determinación del factor de calibración, la segmentación, el registro, el ajuste de las curvas y el cálculo de dosis absorbida. En este trabajo, la calibración desarrollada a un SPECT/CT es presentada utilizando diferentes fuentes de calibración y diferentes geometrías. La influencia del método de reconstrucción en la determinación del factor de calibración y las curvas de factor de recuperación son mostradas.

Por otro lado, se comparan cuatro programas comerciales basándonos en información clínica de dos pacientes con tumores gastro-entero-pancreáticos de origen neuroendocrino tratados con ^{177}Lu-DOTATATE. Dos ciclos de tratamiento por cada paciente fueron usados para estimar tiempos de residencia para los riñones, hígado, bazo, médula ósea y cuerpo entero. El cálculo de las dosis absorbidas se desarrolló inicialmente utilizando OLINDA/EXM V1.0, V2.0, ajustando las masas de cada órgano/tejido. En el caso de la médula ósea, se presenta una novedosa metodología para estimar la dosis absorbida sin necesidad de contar con mediciones de cuerpo entero. Se logra ver que el registro de las imágenes tiene un impacto en la determinación de la dosis absorbida. Los resultados son calculados empleando una herramienta que permite el registro independientemente de cada órgano y no de toda la imagen del campo de visión.

Diferentes algoritmos de cálculo fueron usados para determinar la dosis absorbida entregada a los pacientes, por ejemplo, el modelo de esferas de OLINDA/EXM V2.0, los métodos de convolución y depósito local de energía de PLANET®Onco Dose de Dosisoft. Los resultados encontrados con las diferentes herramientas son comparados y discutidos.

Palabras clave: Dosimetría, terapia dirigida con radionúclidos, medicina nuclear


COSTA RICA,
SIEMPRE
ESTAS EN MI
MENTE Y EN
MI CORAZON